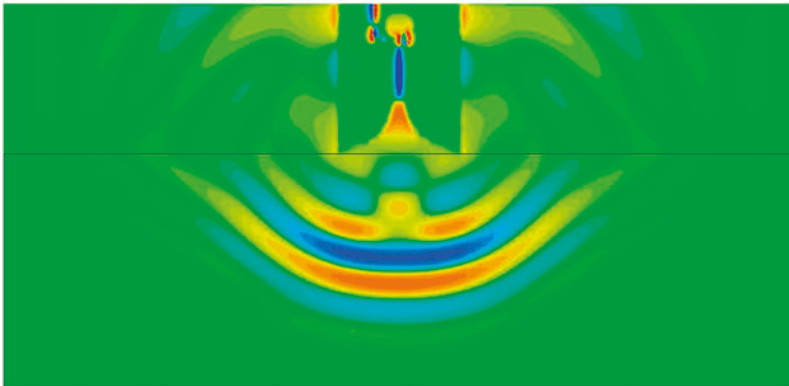


# Analysis and Design of Antennas and Algorithms for Near-Field Sensing

Davide Comite





Collana Studi e Ricerche 86

# SCIENZE E TECNOLOGIE

# Analysis and Design of Antennas and Algorithms for Near-Field Sensing

*Davide Comite*



SAPIENZA  
UNIVERSITÀ EDITRICE

2020

Copyright © 2020

**Sapienza Università Editrice**

Piazzale Aldo Moro 5 – 00185 Roma

[www.editricesapienza.it](http://www.editricesapienza.it)

[editrice.sapienza@uniroma1.it](mailto:editrice.sapienza@uniroma1.it)

Iscrizione Registro Operatori Comunicazione n. 11420

ISBN 978-88-9377-142-9

DOI 10.13133/9788893771429

Pubblicato a giugno 2020



Quest'opera è distribuita  
con licenza Creative Commons 3.0  
diffusa in modalità *open access*.

Impaginazione/layout a cura di: Davide Comite

In copertina: Davide Comite, *Simulazione numerica del campo elettrico irradiato da un'antenna Vivaldi*.

*Non al denaro, non all'amore,  
né al cielo.*



# Table of contents

Preface	XI
PART I – INTERFACIAL PROPAGATION	
Introduction	3
1. Radiation from Line Source	5
1.1. Radiation from interfacial line source	5
1.2. Numerical solution of the integrals	9
2. Radiation from Short Dipole	15
2.1. Vertical electric dipole	15
2.1.1. Electric field in air	20
2.1.2. Electric field in the ground	22
2.1.3. Asymptotic solution	23
2.1.4. Numerical solution	24
2.2. Horizontal electric dipole	25
2.2.1. Asymptotic solution	33
2.2.2. Numerical solution	35
2.3. Radiation from a half-wavelength dipole	39
PART II – GROUND PENETRATING RADAR	
Introduction	45
3. GPR Antennas	49
3.1. Introduction	49
3.2. Monopole	50

3.3. Simple and loaded dipoles	51
3.3.1. Printed folded dipole	53
3.4. Bow-tie antenna	55
3.5. Printed Vivaldi antenna	56
4. Experimental and Numerical GPR Setups	61
4.1. GPR laboratory setup	61
4.1.1. Measurements on metallic objects	63
4.1.2. Measurements on dielectric objects	65
4.2. Depth estimation of shallow targets	68
4.3. Customized numerical setup	70
4.4. Depth estimation on the numerical data	75
4.5. Numerical setup for 3D surveys	80
5. GPR Early-Time Technique	95
5.1. Introduction	95
5.1.1. Complex trace analysis	100
5.2. Laboratory scale experiments	103
5.3. Numerical setup	107
5.3.1. Air/ground waves analysis	109
5.4. Parametric analyses	113
5.4.1. Numerical analysis on alternative parameters	117
5.4.2. Numerical model of a GPR commercial system	119
5.4.3. Numerical analysis of the loss effects	123
5.4.4. Frequency domain elaboration	125
5.5. Conclusion	127

## PART III – INVERSE PROBLEMS

Introduction	131
6. Microwave Tomography	135
6.1. Scattering equation	135
6.1.1. Contrast function	141
6.1.2. Half-space 2D scattering equations	142
6.2. Ill-posedness and nonlinearity	143
6.2.1. Born approximation	146
6.3. Microwave tomographic algorithm	147

6.4. Reconstruction of PEC scatterers	149
6.4.1. Inversion with experimental data	153
6.4.2. Inversion with numerical data	155
6.5. 3D microwave tomographic algorithm	158
6.5.1. Dyadic Green function for a homogeneous medium	159
6.5.2. Dual-pol tomographic algorithm	161
6.6. Inversion with 3D numerical data	163
6.7. Conclusion	167
7. Advanced Microwave Tomography	169
7.1. Introduction	169
7.2. 2D numerical model of the incident field	170
7.3. Spectral performance analysis	173
7.4. Reconstruction of PEC scatterers	181
7.5. Reconstruction of dielectric scatterers	185
7.6. Contact less configuration	187
7.7. Non-ideal effects	189
7.7.1. Error on the permittivity estimation	189
7.7.2. Inhomogeneous ground medium	191
7.7.3. Surface roughness	193
7.8. Multipath effects	197
7.9. 3D numerical model of the incident field	200
7.9.1. Metallic cube	201
7.9.2. Dielectric cube	203
 PART IV – RECONFIGURABLE LEAKY-WAVE ANTENNAS	
Introduction	209
8. Modal Analysis of a Wire-Medium Loaded Structure	213
8.1. Introduction	213
8.2. Field matching technique	216
8.2.1. TM modes	217
8.2.2. TEM mode	218
8.2.3. Generalized structure	219
8.2.4. Multi-modal Bloch analysis	223
8.3. Results for a closed structure	225

8.3.1. Transverse field configuration	229
8.4. Equivalent network for an air/WM interface	232
8.4.1. Input impedance for the equivalent 3-port network	235
8.4.2. Model validation of the closed structure	237
8.5. Input impedance of a wire medium slab	241
8.6. Open structure	244
8.7. Leaky-mode equalization	249
9. Radiative Analysis of Wire-Medium Loaded Antennas	253
9.1. Introduction	253
9.2. Far field via reciprocity	253
9.2.1. Line source excitation	255
9.2.2. Vertical electric dipole	264
9.3. Wire-medium slab	268
9.3.1. TEM suppression	273
9.4. Conclusion	275
 PART V – NON-DIFFRACTING BEAMS	
Introduction	279
10. Higher Order Bessel Beams	281
10.1. Non-diffracting beams	281
10.2. Generalized field with invariant section	283
10.3. Far-field evaluation	284
10.3.1. Derivation of the first term	285
10.3.2. Derivation of the second term	289
10.3.3. Radiation formula for the case $n = 1$	290
10.4. Radiation formula for a $n$ th-order Hankel function	290
10.5. Radiation formula for a Bessel function	291
10.6. Aperture field	293
10.7. RLSA antenna design	294
10.7.1. Optimization procedure	299
10.8. Numerical results	301
10.8.1. Feeding design	304
List of Publications	305
Bibliography	311

# Preface

This thesis collects the main results of the Author's three-year Ph.D. in Electromagnetics and Mathematical Models for Engineering at 'Sapienza' University of Rome, under the tutoring of Prof. Alessandro Galli. Four months of that period have been spent as Visitor Scholar at the University of Rennes 1, Rennes, France, under the tutoring of Profs. Ronan Sauleau, Mauro Ettorre and Guido Valerio. The dissertation mostly deals with the analysis and design of different kind of antennas and related propagation features, concerning a wide set of sensing applications. Specific attention has been given to Ground Penetrating Radar (GPR) by developing an ad-hoc full-wave numerical setup based on a commercial CAD software, with the aim of analyzing some important electromagnetic issues involving both the radiative system of this instrument and the post-processing procedures on the collected data. Even though the overall activity is rather heterogeneous, most of the topics that have been considered are related to the *near-field* region of the relevant electromagnetic fields. The work is divided into five chapters and is mainly focused on new techniques and relevant results rather than on well-established instruments and approaches. Nevertheless, attention has been paid to provide the Reader with the essential background information useful to easily deal with the original material presented here. To better emphasize the state-of-art of the considered topics extensive references to previous works have been inserted; in addition, throughout the work some references to published journal and conference papers have been highlighted to further guide through later advances on these topics.

Part I deals with the propagation of an electromagnetic pulse at the interface between two half-spaces. The results outlined and discussed

are not only interesting for themselves but are also useful for the rest of the work. Indeed, an interfacial short dipole can be seen in first approximation as the simplest model for a GPR system. Its solution can be faced analytically but only for observation points placed in far-field region of the considered source. Thus, to characterize the electromagnetic field produced at the interface a numerical solution has been carried out, giving also the possibility of extensively analyzing the region of space near the transmitting short dipole (typically at distances less than one wavelength) where the receiving antenna of a GPR system is usually located. A numerical model of a more realistic antenna has been carried out as well, suitably sampling a half-wavelength dipole by means of equispaced short dipoles.

Part II deals with the numerical characterization of GPR systems for geophysical and planetary applications. In particular, attention is devoted to the design of free-space and ground-coupled antennas, that will be exploited later to conduct numerical analysis in various realistic scenarios. A full-wave model of the GPR system designed in the framework of the ExoMars mission on Mars has been developed as well. Moreover, in collaboration with the Earth and Space applied physics laboratory of 'Rome Tre' University an ad-hoc experimental setup has been exploited to conduct GPR measurements by means of commercial systems. It is important to note that the overall activity developed in this part of the work mainly aims at analyzing the capability of these systems to detect, locate, and reconstruct dielectric and metallic targets buried in the shallow portion of the considered soil, i.e., in the near-field region of the considered antenna. Finally, a novel and potentially very interesting technique for fast and low-cost estimation of the electromagnetic parameters of shallow soils has been investigated; a reliable and efficient full-wave model of a commercial GPR system has been designed and a comparative set of numerical and experimental studies have been developed.

In the first section of Part III a well-known and established imaging procedure based on the solution of a linearized inverse problem has been described and applied on the numerical data developed in Part II, and also to some significant experimental radargrams. This activity has been carried out in collaboration with the Institute of Electromagnetic Sensing of the Environment at the National Research Council of Naples (IREA-CNR) and it has been mainly aimed at extensively investigating the capability of GPR systems to reconstruct the main features of

metallic and dielectric targets having dimension comparable with the dominant probing wavelength and buried in the near-field region of the considered antenna. To introduce the Reader to this kind of algorithm, the overall approach has been shortly summarized by starting from the formulation of the scattering problem. Hence, the concept of ill-posed and non-linearity for an inverse problem has been described. The second part of this activity contains an original advanced implementation of the microwave tomographic algorithm just described. Basically, a new approach capable to take into account the real far- and near-field distribution radiated by the considered antenna has been designed and implemented; thus, the reconstruction obtained with the novel imaging procedure has been compared with those obtainable with the conventional procedure, considering both a simple 2D scalar scenario as well as a more involved 3D vectorial implementation.

Part IV deals with a different topic focused on the study of advanced antenna systems. It has been mainly developed in collaboration with the researchers of the 'Electromagnetic Field 1' Lab, at the Department of Information Engineering, Electronic and Telecommunication of this University, and considers the design of a reconfigurable leaky-wave antenna based on planar geometry. Modal properties of both closed and open structures made by a Fabry-Perot cavity antennas have been extensively studied, both with analytical and full-wave approaches. In particular, the radiative properties of a parallel-plate waveguide having the upper wall made by a periodic high impedance surfaces and excited with simple sources have been analyzed through a suitable implementation based on the reciprocity theorem. In this context a novel and efficient equivalent transverse network for this kind of structures has been developed, considering a wire-medium slab symmetrically inserted inside the structure with the aim to suppress spurious radiation due to the TEM mode as well as to higher order TM leaky modes, keeping substantially unchanged radiation of the  $TM_1$  mode. The results have been validated by means of multi-modal Bloch analysis of a macro-cell, that in turns has been solved through a full-wave approach with a commercial code. A very good agreement has been obtained on a geometry suitably designed to provide omni-directional conical patterns with very wide angular scanning ranges and reconfigurable features of polarization.

Part V, whose topics have been investigated at the University of Rennes 1, treats the design and optimization of a novel antenna capable to focus the near-field distribution of the radiated field. This represents a

very attractive feature for a wide variety of applications such as imaging, diagnostics and wireless power transfer. Non-diffracting solutions of the scalar wave equation are typically named Bessel beams, and the possibility of generating this particular configuration by means of radial waveguides has been investigated in the past years. More recently, thanks to a customized optimization algorithm, the capability of a Radial Line Slotted Antenna (RLSA) to focus energy in a limited region of space has been also investigated. In particular, slot positions and dimensions required to generate a zero-order Bessel beam on a certain plane in the near-field region have been suitably determined. By following the interesting results achieved so far, in this thesis the possibility of designing and focus a higher-order Bessel beam showing an azimuthal phase variation is evaluated; this allows us to produce an orbital angular momentum (OAM) beam, of recent great interest at radio frequencies. Indeed, OAM may be capable, among other applications, of an increased capacity of communication channels, and enhanced remote sensing.

The list of references and publications conclude the work.

PART I

INTERFACIAL PROPAGATION



# Introduction

Since many decades, wave excitation and propagation in planar layered media has been one of the most intensely studied topics in electromagnetics (see [1]-[6]). In addition to the quite straightforward and elegant mathematical formulations of the problem ([1, 2]) and of relevant numerical analyses, such structures have been proved to be of great interest in a wide range of applications. In the last decade, the interest in this topic renewed, due to the great amount of research related to fast and reliable numerical codes. Generally speaking, when an elementary source is placed at an interface between air and one or more dielectric layers (possibly lossy), a canonical issue commonly named *Sommerfeld's problem* is defined [7],[8]. Since early years of 20<sup>th</sup> century this problem has been widely faced [9]-[16] aiming at analytically evaluating the far-field produced by antennas placed on the Earth surface. For some specific cases efficient and elegant closed-form expression have been obtained [9]-[11], that were very useful for the solution of communication problems. On this topic, a well-known controversy related to the presence of a wrong sign in the seminal paper of Sommerfeld also arose. More recently, two review articles [17, 18] have been published, giving a complete description of the problem and of the related issues.

In the second half of the 20<sup>th</sup> century various authors were interested in the evaluation of the far field produced in a dielectric half-space by an interfacial dipole [19, 20], but only in the Seventies two important papers [21, 22] investigated the possibility of determining electrical properties of low-loss soil and to detect its subsurface stratification for environments moderately transparent to electromagnetic waves, naming this procedure *radio interferometry depth-sounding*. In particular, this half-

space solutions has shown that an interface modifies the directionality of the antenna and that a regular interference pattern is present in the surface fields around the source. These two works paved the way for the development of the Ground Penetrating Radar, as it is understood today. Indeed, in the following years both the engineering and geophysical communities extensively analyzed the far-field behavior of horizontal simple or loaded dipoles over an interface [23]-[25]; in addition, the possibility of modeling the interaction between a transmitting and a receiving dipole on a dielectric soil was also investigated [26]-[29]. It is interesting to note that a time-domain characterization of the far field produced by an interfacial dipole has been also proposed in various papers [30]-[32].

To the Author's knowledge, very few works have attempted in some way to analyze the near-field distribution generated by an interfacial short dipole. A first contribution was described in [33], where an FDTD code was developed to provide a temporal sketch of the pulse radiated near a dipole placed at the interface between two media. It is important to note that this topic represents a natural extension of the Sommerfeld's problem, briefly introduced at the beginning of this section.

On this basis, in the following we propose a numerical solution of this problem to describe the near-field distribution produced by interfacial elementary sources, aiming at gaining valuable information on the behavior of the electromagnetic field with respect to the electrical parameters of the medium and to the position of the antennas on the surface. We start from a typical formulation of the problem at hand, proposed in [34], solving the relevant integrals in the complex plane by developing an ad-hoc MatLab code. The results have been validated in the far field region by considering an asymptotic solution of the problem already available in literature. A more realistic basic antenna configuration has been also synthesized by suitable sampling a horizontal half-wavelength dipole through  $n$  short dipoles. A number of interesting information have been obtained, which have proved to be useful for some topics investigated in the second and the third part of this thesis.

# 1. Radiation from Line Source

## 1.1. Radiation from interfacial line source

The simplest ideal scenario to model standard GPR surveys can be seen as made by two half-spaces, i.e., by two indefinite flat, isotropic, homogeneous, non-dispersive and non-magnetic media, having two different values of the dielectric permittivity, namely  $\varepsilon_1$  and  $\varepsilon_2$  for the upper and lower half-space, respectively. Almost always throughout this work  $\varepsilon_1 = \varepsilon_0$ , representing a vacuum free space medium. Consequently, at least in first approximation, the geometry of the problem at hand can be considered as two-dimensional (2D) and a line current placed at the interface can be assumed as an ideal source of an electromagnetic signal. As is known, the first 2D problem extensively studied and analyzed, which models a wave impinging on an inhomogeneous medium, was that of reflection and refraction of a plane wave on a flat interface. It was solved and published for the first time by Fresnel in 1823. In particular, a primary wave made by an incident plane wave on the interface was considered and the direction of the refracted and reflected waves were simply evaluated defining the well-known Snell's laws. In the following we are going to consider a cylindrical wave radiating from an elementary source placed exactly or at a certain distance  $h$  from an interface. Even though this 2D problem can be modeled by a simple scalar Helmholtz equation, it cannot be solved by means of the method of separation of variables, because of the additional boundary condition that have to be enforced along the interface. Consequently, a spectral domain method will be exploited here, which reduces the problem of finding a solution to a complex integration. [35, 36]. To formulate the problem mathematically, we introduce a Cartesian coordinate system  $(x, y, z)$

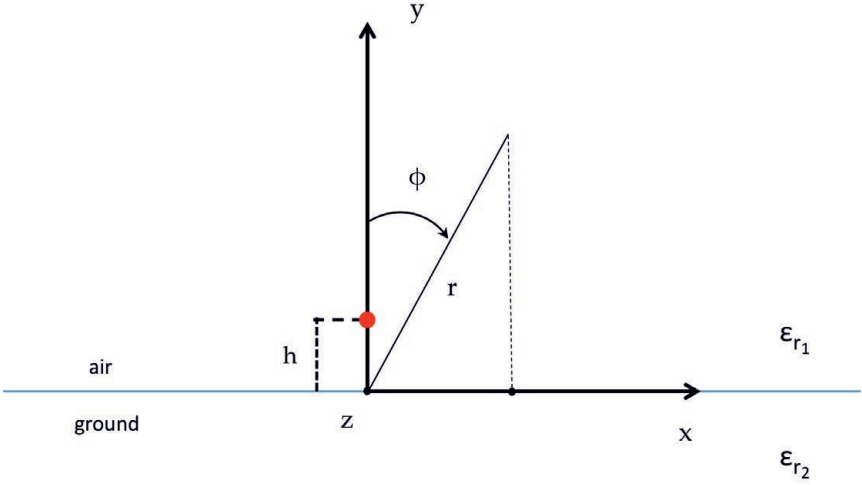


Fig. 1.1. Line source (red dot) placed at a distance  $h$  from the interface of two dielectric media represented by  $\epsilon_1$  and  $\epsilon_2$ , respectively.

wherein the  $z$  axis lies along the extension of the line source; as shown in Fig. 1.1 the plane of the interface is given by  $y = 0$ . By starting from the Maxwell's curls equations, thanks to the 2D approximation ( $\partial/\partial z = 0$ ), we can write

$$\frac{\partial E_z}{\partial y} = -j\omega\mu H_x \quad (1.1)$$

$$\frac{\partial E_z}{\partial x} = j\omega\mu H_y \quad (1.2)$$

$$\frac{\partial E_y}{\partial x} - \frac{\partial E_x}{\partial y} = -j\omega\mu H_z \quad (1.3)$$

$$\frac{\partial H_z}{\partial y} = j\omega\epsilon E_x \quad (1.4)$$

$$\frac{\partial H_z}{\partial x} = -j\omega\epsilon E_y \quad (1.5)$$

$$\frac{\partial H_y}{\partial x} - \frac{\partial H_x}{\partial y} = J_z + j\omega\epsilon E_z \quad (1.6)$$

Now, by grouping these six equations in two independent sets, namely transverse magnetic with respect to  $z$  ( $TM^z$ , having as non-null components  $E_z, H_x$  and  $H_y$ ) and transverse electric with respect to  $z$  ( $TE^z$ , having as non-null components  $H_z, E_x$  and  $E_y$ ), we can see that those not containing components of the electric field in the  $z$ -direction (i.e.,

$TE^z$ ) are source-free, consequently the only possible solution of this set of equations consists of the null field. Hence we can write

$$H_z = E_x = E_y = 0. \quad (1.7)$$

To solve for  $TM^z$  fields we can put equations (1.1) and (1.5) in equation (1.6), thus by recalling that  $J_z = I_0\delta(x)\delta(y)$  we have

$$H_x = -\frac{1}{j\omega\mu} \frac{\partial E_z}{\partial y} \quad (1.8)$$

$$H_y = \frac{1}{j\omega\mu} \frac{\partial E_z}{\partial x} \quad (1.9)$$

$$\frac{\partial^2 E_z}{\partial x^2} + \frac{\partial^2 E_z}{\partial y^2} + k^2 E_z = j\omega\mu I_0\delta(x)\delta(y) \quad (1.10)$$

where  $\mu = \mu_0$  everywhere,  $k^2 = k_0^2 = \omega^2\mu_0\epsilon_0$  for  $y > 0$  and  $k^2 = n^2k_0^2$  for  $y < 0$ . Next, by combining the *spectral representation* and the *Green function* [35] we can easily find the solution of (1.10). Specifically, by enforcing the Sommerfeld radiation conditions and recalling the spectral representation of the operator  $\partial^2/\partial x^2$  [35]

$$\delta(x - x') = \frac{1}{2\pi} \int_{-\infty}^{\infty} e^{jk_x(x-x')} dk_x \quad (1.11)$$

multiplying both sides of (1.11) by  $E_z(x', y)$  and integrating over  $(-\infty, \infty)$  on  $k_x$  we obtain the *spatial Fourier transform pair*

$$\begin{aligned} E_z(x, y) &= \frac{1}{2\pi} \int_{-\infty}^{\infty} \hat{E}_z(k_x, y) e^{jk_x x} dk_x \\ \hat{E}_z(k_x, y) &= \int_{-\infty}^{\infty} E_z(x, y) e^{-jk_x x} dx. \end{aligned} \quad (1.12)$$

Hence, by taking the Fourier transform of both side (1.10) we can write

$$\frac{\partial^2 \hat{E}_z(k_x, y)}{\partial y^2} + k_y^2 \hat{E}_z(k_x, y) = j\omega\mu I_0\delta(y) \quad (1.13)$$

where  $k_y = \pm\sqrt{k^2 - k_x^2}$ . It is important to note here that for the upper half-space ( $y > 0$ )  $k^2 = k_0^2$  and we can denote  $\hat{E}_z$  by  $\hat{E}_{z_1}$ , whereas for the lower half-space ( $y < 0$ )  $k^2 = k_e^2 = n^2k_0^2$  and we consider  $\hat{E}_{z_2}$  in place of  $\hat{E}_z$ . Since  $E_z$  must satisfy the radiation condition for  $y = -\infty$  and  $y = \infty$ , by solving the associate Green function problem, we can show (see [35, 36]) that solutions of (1.13) must have the following form

$$\begin{aligned} \hat{E}_{z_1} &= Ae^{-j\sqrt{k_0^2 - k_x^2}y} & \text{for } y > 0 \\ \hat{E}_{z_2} &= Ae^{j\sqrt{k_e^2 - k_x^2}y} & \text{for } y < 0 \end{aligned} \quad (1.14)$$

thus the constant  $A$  is taken to be the same in both expressions because  $E_z$  must be continuous across the interface, and for  $y = 0$  we must have  $E_{z_1} = E_{z_2}$ .

To find the value of  $A$  we should integrate equation (1.13) with respect to  $y$  from  $-\Delta y$  to  $\Delta y$ , consequently it is easily shown [36] that for  $\Delta y \rightarrow 0$  we get

$$A = \frac{j\omega\mu_0 I}{2\pi} \frac{1}{j\sqrt{k_0^2 - k_x^2} + j\sqrt{k_e^2 - k_x^2}}. \quad (1.15)$$

Finally, equations (1.14) and (1.15) completely define the electric field in both the half-spaces, thus substituting and transforming back to the spatial domain we can write

$$E_{z_1}(x, y) = \frac{j\omega\mu_0 I}{2\pi} \int_{-\infty}^{\infty} \frac{e^{-j\sqrt{k_0^2 - k_x^2}y}}{j\sqrt{k_0^2 - k_x^2} + j\sqrt{k_e^2 - k_x^2}} e^{jk_x x} dk_x \quad \text{for } y > 0 \quad (1.16)$$

$$E_{z_2}(x, y) = \frac{j\omega\mu_0 I}{2\pi} \int_{-\infty}^{\infty} \frac{e^{j\sqrt{k_0^2 - k_x^2}y}}{j\sqrt{k_0^2 - k_x^2} + j\sqrt{k_e^2 - k_x^2}} e^{jk_x x} dk_x \quad \text{for } y < 0. \quad (1.17)$$

We cannot obtain, for these integrals, a closed-form solution for every point of the space surrounding the line source. However, as shown in [36], an exact evaluation is possible for points along the interface ( $y = 0$ ). To gain a description of  $E_z$  out of the interface we can resort to an asymptotic evaluation of the integrals, as shown again in [36]. Incidentally, to determine the far field distribution of the line source may be most convenient to use the cylindrical coordinates  $(\rho, \phi)$ ; consequently, by putting  $x = \rho \cos \phi$  and  $y = \rho \sin \phi$  in equations (1.16) and (1.17) we obtain the sought integral representation of  $E_{z_1}$  and  $E_{z_2}$ . For  $k_0\rho \rightarrow \infty$  and  $0 \leq \phi \leq \pi$  it is possible to get the following expression

$$E_{z_1_{farfield}} = \frac{\omega\mu_0 I}{\sqrt{2\pi}} \frac{1}{(n^2 - 1)} (\sin^2 \phi - \sin \phi \sqrt{n^2 - \cos^2 \phi}) \frac{e^{jk_0\rho - j\frac{\pi}{4}}}{\sqrt{k_0\rho}} \quad (1.18)$$

while, for  $k_e\rho \rightarrow \infty$  and  $0 \leq \phi \leq \phi_c$  (where  $\phi_c$  is the critical angle defined as  $\cos \phi_c = 1/n$ ) we obtain

$$E_{z_2a_{farfield}} = -\frac{\omega\mu_0 I}{\sqrt{2\pi}} \frac{n}{(n^2 - 1)} (n \sin^2 \phi + \sin \phi \sqrt{1 - n^2 \cos^2 \phi}) \frac{e^{jnk_0\rho - j\frac{\pi}{4}}}{\sqrt{nk_0\rho}} \quad (1.19)$$

Finally, for  $k_c \rho \rightarrow \infty$  and  $-\phi_c \leq \phi \leq 0$  and  $-\pi \leq \phi \leq -\pi + \phi_c$  we have

$$E_{z2b_{farfield}} = -\frac{\omega \mu_0 I}{\sqrt{2\pi}} \frac{n}{(n^2 - 1)} (n \sin^2 \phi + j \sin \phi \sqrt{n^2 \cos^2 \phi - 1}) \frac{e^{jnk_0 \rho - j\frac{\pi}{4}}}{\sqrt{nk_0 \rho}} \quad (1.20)$$

These formulas give the possibility of obtaining an immediate description of the far field radiated by a line source placed at an interface between two dielectric media. Just as an example in Fig. 1.2 the behavior of the  $E_z$  component with respect to  $\phi$  angle (measured starting from the horizontal axis) has been reported. Specifically, the pattern in the upper

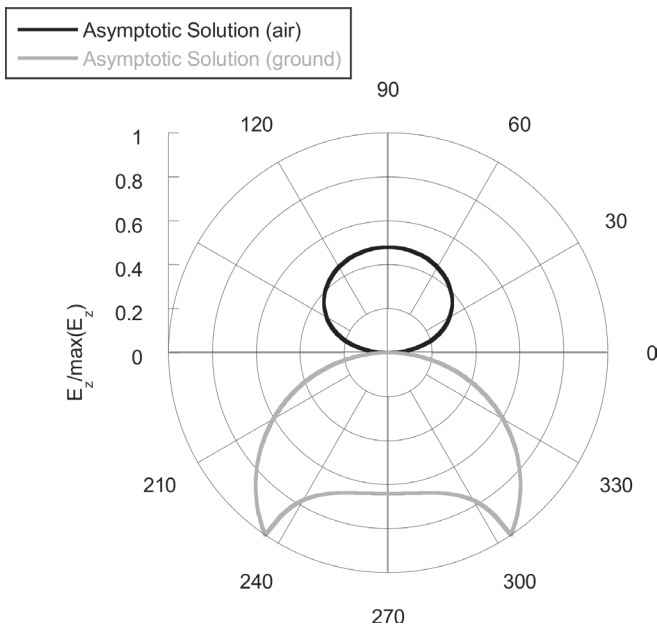


**Fig. 1.2.** Far field pattern for an interfacial line source, whose lower medium has a permittivity  $\epsilon_r = 3.2$  (lower medium air) for a frequency  $f = 1$  GHz.

medium, whose index of refraction is less than that of the lower one, has a single lobe with a maximum normal to the interface. The pattern in the subsurface region has two peaks separated symmetrically by a minimum. An interesting physical interpretation of such a behavior has been given in [36].

## 1.2. Numerical solution of the integrals

As highlighted in the previous section, the integrals modeling the electromagnetic field radiated by a line source placed at an interface

between two dielectric media cannot be evaluated in closed form. Even though an asymptotic solution is available, in the framework of GPR application we usually need to characterize the electromagnetic field in the region surrounding the antenna, both at the interface and in the lower medium. In particular, a detailed description of the signal which propagate along the interface and on the direct path between the transmitting and receiving antenna of a GPR system may be of paramount importance for some applications. Just as an example, the characterization of the time-domain pulse collected by the receiving antenna can provide some pieces of information regarding the electrical properties of the lower medium. In this framework, different techniques have been analyzed; we will give a wide description of the state of art and of future perspectives of this activity in next sections. Since an interfacial line source can be seen as an elementary antenna of a GPR system (actually the simplest possible source), we are very interested in the analysis of the spatial behavior of the radiated electromagnetic field. Even though here we are operating in the frequency domain, by suitable sampling the Fourier transform of the time-domain pulse transmitted by an ideal system, we can easily synthesize the signal radiated by a GPR antenna. To characterize the electric field a numerical solution of the integrals (1.16) and (1.17), representing the solution of the problem at hand, will be given. Basically, by means of an ad-hoc customized MatLab routine we have implemented a solution of the involved integrals in the complex plane, reported in the following for convenience.

$$E_{z_1}(x, y) = \frac{j\omega\mu_0 I}{2\pi} \int_{-\infty}^{\infty} \frac{e^{-j\sqrt{k_0^2 - k_x^2}y}}{j\sqrt{k_0^2 - k_x^2} + j\sqrt{k_e^2 - k_x^2}} e^{jk_x x} dk_x \quad \text{for } y > 0 \quad (1.21)$$

$$E_{z_2}(x, y) = \frac{j\omega\mu_0 I}{2\pi} \int_{-\infty}^{\infty} \frac{e^{j\sqrt{k_0^2 - k_x^2}y}}{j\sqrt{k_0^2 - k_x^2} + j\sqrt{k_e^2 - k_x^2}} e^{jk_x x} dk_x \quad \text{for } y < 0. \quad (1.22)$$

It is worth to note that both these integrals are made by a complex exponential term (i.e.,  $e^{jk_x y}$ ) that is always oscillating for  $k_x$  ranging from  $-\infty$  up to  $\infty$ , and by a term decaying as  $\frac{1}{\sqrt{k_x}}$ , which in turns not converge at all. Anyway, considering these two terms together allows the integral to converge, even in a very fast way since the term  $e^{\pm j\sqrt{k_0^2 - k_x^2}y}$

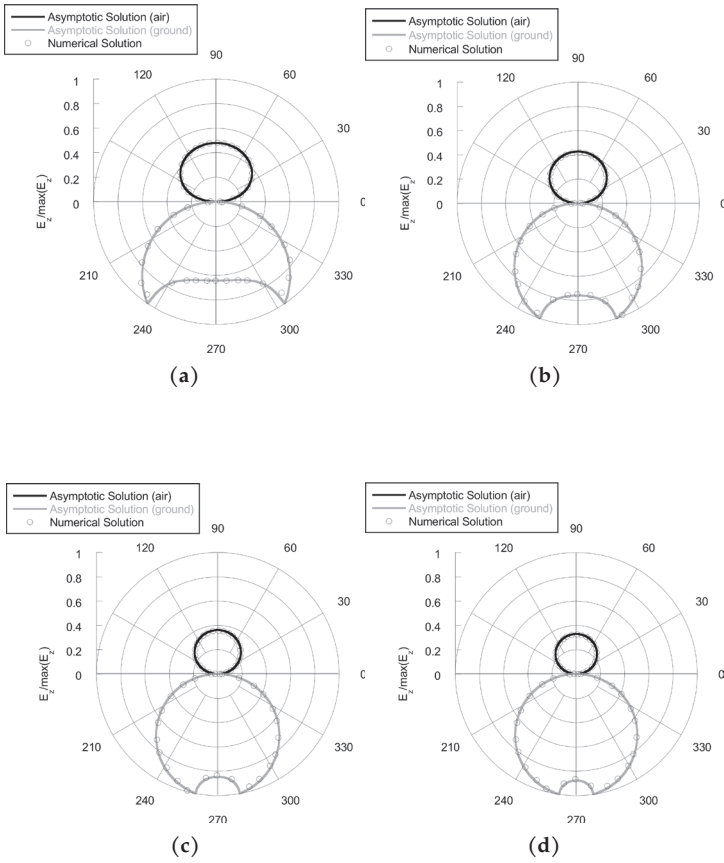


**Fig. 1.3.** Comparison between numerical (gray circles) and asymptotic far-field patterns (solid lines) for different values of the permittivity of the lower medium (a)  $\epsilon_r = 3.2$ , (b)  $\epsilon_r = 10$ , (c)  $\epsilon_r = 30$ , (d)  $\epsilon_r = 50$ .

has a real exponential for  $k_x > k_0$ . Incidentally, by plotting the behavior of the kernel of the integral at hand we would see that the fundamental contribution to the sought solution is given by values of  $k_x$  ranging between  $-k_0$  and  $k_0$ , allowing to stop the numerical integration at a value of  $k_x = \pm 5k_0$ . Let us point out, finally, that the kernel of the integral shows two pairs of branch cut, given by the square roots at the denominator and respectively placed at  $k_x = \pm k_0$  and  $k_x = \pm k_e$ . Consequently, we have to suitably choose the right Riemann surface, deforming the integration path in the complex plane [2].

To give a validation of the results obtained by means of our customized integration routine, a comparison between the asymptotic model previously introduced has been reported. In particular, in Fig. 1.3 the numerical results carried out by putting  $\rho = 10\lambda$  inside the integral are in excellent agreement with those obtained by means of the asymptotic solution (based on the method of the stationary phase).

Being the code validated, we can analyze the behavior of the electric field in the near-field region, by considering typical distances where a transmitting and a receiving GPR can be placed. In Fig. 1.4 a field map at two distances, equal to  $\lambda/2$  and  $\lambda$ , have been reported, considering also three different values for the permittivity of the background medium. As for the far-field case, even though it is not so intuitive and clearly predictable, the field is more confined inside the lower medium, while inside the upper one it becomes less and less strong.

Furthermore, in Fig. 1.5 more detailed behaviors of the electric field for a number of permittivity values of the lower medium have been reported. A particular good sensitivity of the field in air is observed with respect to different values of  $\epsilon_r$ , ranging from 2 up to 50, that paves the way to some interesting applications, when a bistatic GPR system is exploited to radiate and collect waves propagating along the interface of two half-spaces.

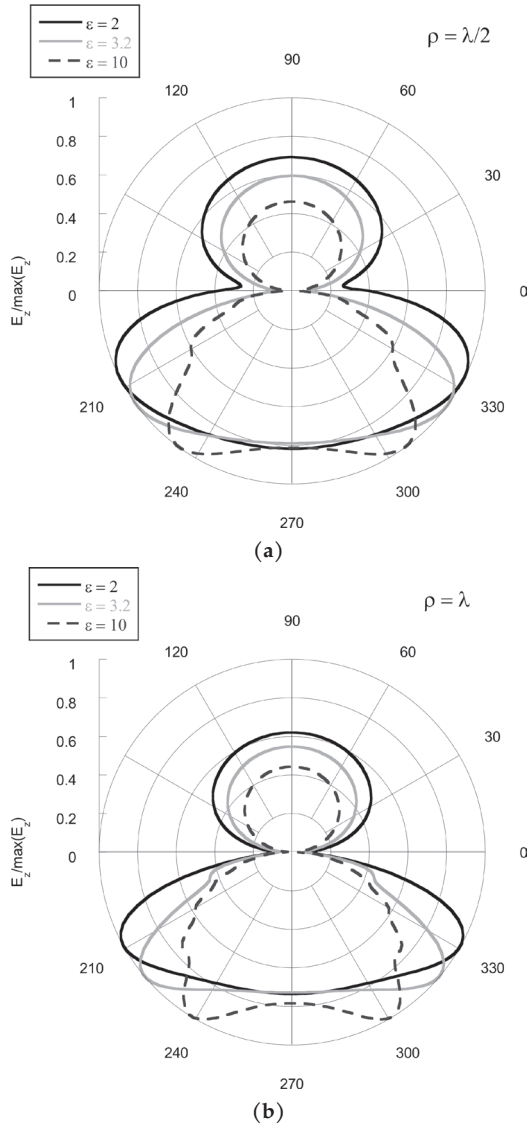


**Fig. 1.4.** (a) Numerical near field for  $\rho = \lambda/2$  and for different values of the permittivity (b) Numerical near field for  $\rho = \lambda$  and for different values of the permittivity.

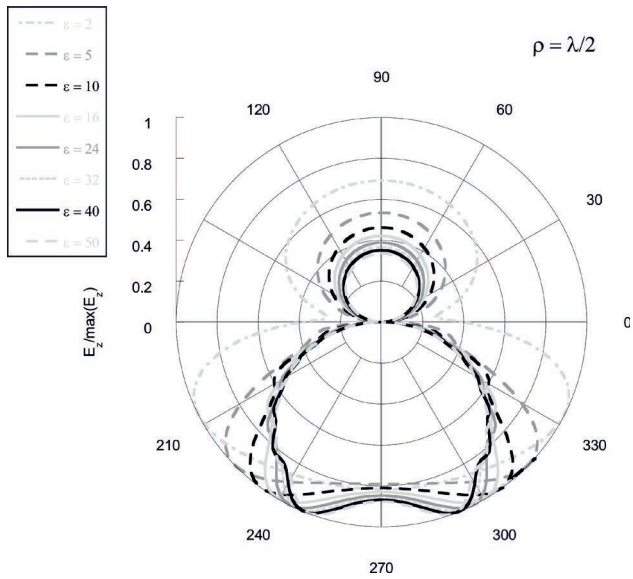


Fig. 1.5. Near-field distribution of an interfacial line source for a number of permittivity values (see legend).

## 2. Radiation from Short Dipole

### 2.1. Vertical electric dipole

In this section the radiation generated by a vertical electric dipole (VED) placed at an interface between two half-spaces will be analyzed. Even though such a configuration is not coherent with respect to typical GPR surveys, where transmitting and receiving antenna in most cases are ground-coupled horizontal dipoles, it is useful to give valuable information about the physics and mathematics background lying behind these kinds of problems. Moreover, the solution outlined in the following is a bit less complicate from an analytical viewpoint; the geometry of the scenario at hand shows an azimuthal symmetry, allowing to make simpler the involved vectorial problem and to develop the computational issue in more convenient conditions. The electromagnetic field radiated by an interfacial VED can be described by the Hertz vector  $\boldsymbol{\pi}$ , whose rectangular components must satisfy the scalar wave equation

$$\nabla^2 \pi_z + k^2 \pi_z = -\frac{J_z}{j\omega\epsilon_0}, \quad (2.1)$$

the current carried by the electric dipole of equivalent length  $L$ , located at  $\mathbf{r}'$  is given by

$$J_z = IL\delta(\mathbf{r} - \mathbf{r}') \quad (2.2)$$

where for convenience we let

$$\frac{IL}{j\omega\epsilon_0} = 1. \quad (2.3)$$

The dipole is located at  $z = h$  in air, where the wave number is  $k$ , whilst the wave number in the ground medium is  $k_e$ .

In air ( $z > 0$ ) we can write

$$\nabla^2 \pi_z + k^2 \pi_z = -\delta(\mathbf{r} - \mathbf{r}') \quad (2.4)$$

whereas in the ground ( $z < 0$ ), since there are no sources, we have

$$\nabla^2 \pi_z + k_e^2 \pi_z = 0. \quad (2.5)$$

The boundary condition at  $z = 0$  (i.e., electric and magnetic fields continuous across the boundary) together with the radiation conditions give a complete mathematical description of the problem at hand. A way to solve equations (2.4) is to consider the solution as a sum of the *primary* and *secondary wave*. The former is the wave radiated from the dipole in an infinite space in absence of the boundary showing the correct singularity at the location of the antenna; the latter represents the effects of the boundary and has no singularity in the point where the antenna is located.

The Hertz potential representing the primary wave is given by

$$\pi_p = \frac{e^{-jk|\mathbf{r}-\mathbf{r}'|}}{4\pi|\mathbf{r}-\mathbf{r}'|} \quad (2.6)$$

which is, as expected, the free space Green function. Since the problem shows a cylindrical symmetry, to satisfy the boundary conditions it is useful to express (2.6) in terms of cylindrical waves (see Fig. 2.1) that have the same radial wave number in air and in the ground, thus we get

$$\frac{1}{\rho} \frac{\partial}{\partial \rho} \left( \rho \frac{\partial}{\partial \rho} \right) \pi_p + \frac{1}{\rho^2} \frac{\partial^2}{\partial \phi^2} \pi_p + \frac{\partial^2}{\partial z^2} \pi_p + k^2 \pi_p = -\frac{\delta(\rho - \rho') \delta(\phi - \phi') \delta(z - z')}{\rho}. \quad (2.7)$$

Expanding  $\pi_p$  in a Fourier series in  $\phi$  and using the Fourier Bessel transform (cylindrical equivalence of the usual Fourier transform) the solution of the considered equation is reported in the following (further details can be found in [34])

$$\pi_p = \frac{1}{4\pi} \sum_{m=-\infty}^{\infty} e^{-jm(\phi-\phi')} \int_0^{\infty} J_m(k_\rho \rho) J_m(k_\rho \rho') e^{-jk_z |z-z'|} \frac{k_\rho}{jk_z} dk_\rho = \quad (2.8)$$

where  $k_\rho^2 + k_z^2 = k^2$ . Equation (2.8) is equivalent to (2.6) but is written in terms of cylindrical waves with propagation constant  $k_\rho$ . In particular, when the antenna is located at  $\rho' = 0$  and  $z' = 0$ , equations (2.8) becomes

$$\pi_p(\rho, z) = \frac{1}{4\pi} \int_0^\infty J_0(k_\rho \rho) e^{-jk_z |z-z'|} \frac{k_\rho}{jk_z} dk_\rho. \quad (2.9)$$

It is very interesting to note that the cylindrical wave approach allows us to expand the field above and below the boundary in terms of the same wave number  $k_\rho^2$ , hence we are able to satisfy the boundary conditions at any  $\rho$ .

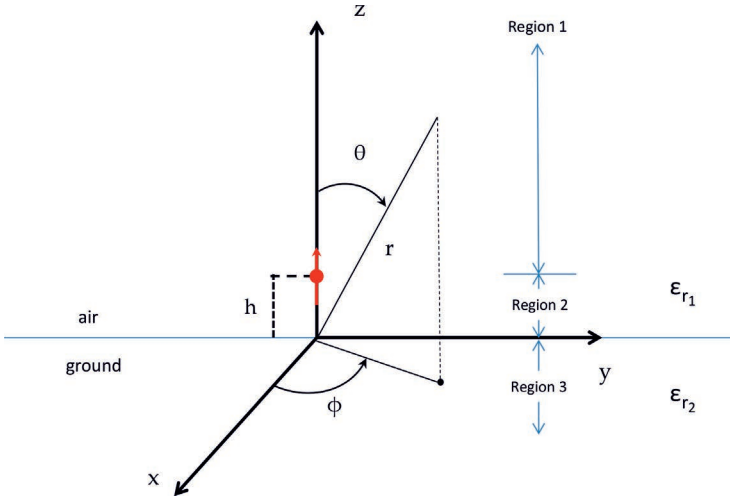


**Fig. 2.1.** Vertical short dipole in a spherical coordinate system placed at a distance  $h$  from the surface.

Considering the problem depicted in Fig. 2.1 we know that in air (region 1), the  $z$ -component of the Hertz potential satisfies equation (2.4). As introduced previously,  $\pi_z$  can be written as the sum of the primary wave  $\pi_p$  and the scattered wave  $\pi_s$

$$\pi_z = \pi_p + \pi_s. \quad (2.10)$$

For the primary wave in region 1 we can write

$$\pi_p(\rho, z) = \frac{1}{4\pi} \int_0^\infty J_0(k_\rho \rho) e^{-jk_z(z-h)} \frac{k_\rho}{jk_z} dk_\rho \quad (2.11)$$

while in region 2

$$\pi_p(\rho, z) = \frac{1}{4\pi} \int_0^\infty J_0(k_\rho \rho) e^{-jk_z(h-z)} \frac{k_\rho}{jk_z} dk_\rho. \quad (2.12)$$

The difference in the exponents of the kernel of the integrals (2.11) and (2.12) represents the singularity at  $z = h$ . It is now important to note

that the scattered wave does not have singularity in  $z = h$  and must satisfy homogeneous wave equation. Thus, for both regions 1 and 2 we can write

$$\pi_s(\rho, z) = \frac{1}{4\pi} \int_0^\infty R(k_\rho) J_0(k_\rho \rho) e^{-jk_z(z+h)} \frac{k_\rho}{jk_z} dk_\rho \quad (2.13)$$

where  $R(k_\rho)$  is an unknown function that will be determined by applying the boundary conditions. In region 3 the primary wave is not present and thus the scattered wave must satisfy an homogeneous wave equation

$$\nabla^2 \pi_s + k_e^2 \pi_s = 0 \quad (2.14)$$

whose solutions, following the same procedure outlined previously, can be written as

$$\pi_s(\rho, z) = \frac{1}{4\pi} \int_0^\infty T(k_\rho) J_0(k_\rho \rho) e^{+jk_{z_e}z - jk_z h} \frac{k_\rho}{jk_z} dk_\rho \quad (2.15)$$

where again  $T(k_\rho)$  is an unknown function that depends on the boundary conditions; the relation for the wave numbers suitably changes  $k_\rho^2 + k_{z_e}^2 = k_e^2$ . As usual, the choice of  $-jqz$  instead of  $+jqz$  is made to represent an outgoing wave in the  $+z$  direction satisfying the *radiation conditions*. Analogously,  $-jq_e z$  represent an outgoing wave in the  $z$ -direction (in both case  $q$  and  $q_e$  are in the fourth quadrant). The outlined integral expression for  $\pi_s$  and  $\pi_p$  in regions 1,2 and 3 represent a complete expression of the field; it remains only to enforce the boundary conditions at the interface. Because of the symmetry of the problem the only tangential components of the electric and magnetic field are  $E_\rho$  and  $H_\phi$ . Therefore recalling the connections between EM fields and the Hertz potential [37], it holds

$$\begin{aligned} E_\rho &= \frac{\partial^2}{\partial \rho \partial z} \pi_z \\ H_\phi &= -j\omega \varepsilon \frac{\partial}{\partial \rho} \pi_z \end{aligned} \quad (2.16)$$

and we can write

$$E_\rho^{(2)} = E_\rho^{(3)} \quad H_\phi^{(2)} = H_\phi^{(3)}. \quad (2.17)$$

where  $E_\rho^{(2,3)}$  and  $H_\phi^{(2)}$  are the relevant components of the electric and

magnetic field in region 2 and 3 respectively. Since the boundary conditions must be enforced at  $z = 0$  and for any  $\rho$ , we can write

$$\frac{\partial}{\partial \rho} \left[ \frac{\partial}{\partial z} \pi_z^{(2)} - \frac{\partial}{\partial z} \pi_z^{(3)} \right] = 0 \quad (2.18)$$

$$\frac{\partial}{\partial \rho} \left[ \pi_z^{(2)} - n^2 \pi_z^{(3)} \right] = 0 \quad (2.19)$$

and we finally have

$$\frac{\partial}{\partial z} \pi_z^{(2)} = \frac{\partial}{\partial z} \pi_z^{(3)} \quad (2.20)$$

$$\pi_z^{(2)} = n^2 \pi_z^{(3)} \quad (2.21)$$

where of course  $\pi_z^{(2)}$  and  $\pi_z^{(3)}$  are the Hertz potential in regions 2 and 3 respectively. By considering this conditions and equation (2.11), (2.12), (2.13) and (2.15), recalling that  $\pi_z = \pi_p + \pi_s$ , in  $z = 0$  it is possible to obtain the sought expression for the function  $R(k_\rho)$  and  $T(k_\rho)$ . Indeed, after some algebra we get

$$R(k_\rho) = \frac{n^2 k_z - k_{ze}}{n^2 k_z + k_{ze}} \quad (2.22)$$

$$T(k_\rho) = \frac{2k_z}{n^2 k_z + k_{ze}}. \quad (2.23)$$

It is finally important to mention that the remaining components of the electric field can be obtained by differentiation of the scalar Hertz potential [37], as highlighted in the following

$$E_z = \frac{\partial^2}{\partial z^2} \pi_z + k^2 \pi_z \quad (2.24)$$

$$E_\rho = \frac{\partial^2}{\partial \rho \partial z} \pi_z \quad (2.25)$$

$$H_\phi = -j\omega\epsilon \frac{\partial}{\partial \rho} \pi_z \quad (2.26)$$

In the next sections all the component of the electric field will be evaluated and a numerical solution of the involved integrals will be outlined in order to carried out a comprehensive study of the electric field radiated by a vertical short dipole placed at the interface between two homogeneous lossless dielectric media.

### 2.1.1. Electric field in air

In air (i.e., for  $z > 0$ ) considering equations (2.11) and (2.12) the Hertz potential can be written as follows

$$\pi_s(\rho, z) = \frac{e^{-jk|r-r'|}}{4\pi|r-r'|} + \frac{1}{4\pi} \int_0^\infty R(k_\rho) J_0(k_\rho \rho) e^{-jk_z(z+h)} \frac{k_\rho}{jk_z} dk_\rho; \quad (2.27)$$

since we want to carried out a numerical solution of the electric field we consider here a plane-wave expression of the primary wave, that basically allows us to save time in the numerical evaluation of the equivalent integral expression.

By considering equations (2.10) and (2.24) for the  $z$  component of the electric field we can write

$$E_z = \frac{\partial^2}{\partial z^2} \pi_p + \frac{\partial^2}{\partial z^2} \pi_s + k^2 \pi_p + k^2 \pi_s \quad (2.28)$$

while for the  $\rho$  component we have

$$E_\rho = \frac{\partial^2}{\partial \rho \partial z} \pi_p + \frac{\partial^2}{\partial \rho \partial z} \pi_s; \quad (2.29)$$

basically, to write the final expression for electric field we have to calculate the second derivatives of  $\pi_p$  and  $\pi_s$ . To do this, it is convenient to express  $\pi_p$  in cylindrical coordinates as

$$\pi_p = \frac{e^{-jk|\sqrt{\rho^2+z^2}-h|}}{4\pi|\sqrt{\rho^2+z^2}-h|} \quad (2.30)$$

and to introduce two different cases, considering separately  $\sqrt{\rho^2+z^2} > h$  and  $\sqrt{\rho^2+z^2} < h$ .

#### 1. First case: $\sqrt{\rho^2+z^2} > h$

Considering equation (2.28) we can write

$$\begin{aligned} E_z = & \frac{\partial^2}{\partial z^2} \frac{e^{-jk(\sqrt{\rho^2+z^2}-h)}}{4\pi(\sqrt{\rho^2+z^2}-h)} + k^2 \frac{e^{-jk(\sqrt{\rho^2+z^2}-h)}}{4\pi(\sqrt{\rho^2+z^2}-h)} + \\ & \frac{1}{4\pi} \int_0^\infty R(k_\rho) J_0(k_\rho \rho) (-q) e^{-jk_z(z+h)} \frac{k_\rho}{j} dk_\rho + \\ & \frac{k^2}{4\pi} \int_0^\infty R(k_\rho) J_0(k_\rho \rho) e^{-jk_z(z+h)} \frac{k_\rho}{jk_z} dk_\rho \end{aligned} \quad (2.31)$$

Here for the sake of brevity the second derivative of the first term has not been reported. Hence, recalling equation (2.29) we can write

$$E_\rho = \frac{\partial^2}{\partial \rho \partial z} \pi_p + \frac{\partial^2}{\partial \rho \partial z} \pi_s \quad (2.32)$$

and finally we have

$$E_\rho = \frac{1}{4\pi} \frac{\partial^2}{\partial \rho \partial z} \frac{e^{-jk(\sqrt{\rho^2+z^2}-h)}}{(\sqrt{\rho^2+z^2}-h)} + \frac{1}{4\pi} \int_0^\infty R(k_\rho) J_1(k_\rho \rho) e^{-jk_z(z+h)} k_\rho dk_\rho \quad (2.33)$$

Again, the second derivative has not been reported.

## 2. Second case: $\sqrt{\mathbf{a}^2 + \mathbf{z}^2} < \mathbf{h}$

Recalling again equation (2.29)

$$E_z = -\frac{\partial^2}{\partial z^2} \frac{e^{+jk(\sqrt{\rho^2+z^2}-h)}}{4\pi(\sqrt{\rho^2+z^2}-h)} - k^2 \frac{e^{+jk(\sqrt{\rho^2+z^2}-h)}}{4\pi(\sqrt{\rho^2+z^2}-h)} + \frac{1}{4\pi} \int_0^\infty R(k_\rho) J_0(k_\rho \rho) (-q) e^{-jk_z(z+h)} \frac{k_\rho}{j} dk_\rho + \frac{k^2}{4\pi} \int_0^\infty R(k_\rho) J_0(k_\rho \rho) e^{-jk_z(z+h)} \frac{k_\rho}{jk_z} dk_\rho \quad (2.34)$$

Here for the sake of brevity the second derivative of the first term has not been presented. Recalling again that

$$E_\rho = \frac{\partial^2}{\partial \rho \partial z} \pi_p + \frac{\partial^2}{\partial \rho \partial z} \pi_s \quad (2.35)$$

in the second region we can finally write

$$E_\rho = -\frac{1}{4\pi} \frac{\partial^2}{\partial \rho \partial z} \frac{e^{-jk(\sqrt{\rho^2+z^2}-h)}}{(\sqrt{\rho^2+z^2}-h)} + \frac{1}{4\pi} \int_0^\infty R(k_\rho) J_1(k_\rho \rho) e^{-jk_z(z+h)} k_\rho dk_\rho \quad (2.36)$$

where once again the second derivative has not been explicitly reported for space limitation.

Considering together equations (2.31), (2.33), (2.34) and (2.36), explicitly evaluating the remaining second derivatives and suitably performing the complex integrations, we can evaluate the electric field radiated by a VED in the upper medium for every radial distance and, most of all, also in the near-field region of the considered elementary interfacial source.

### 2.1.2. Electric field in the ground

By considering equations 2.24 and recalling that in the ground only the secondary wave is present we can write

$$E_z = \frac{1}{4\pi} \int_0^\infty T(k_\rho) J_0(k_\rho \rho) (-k_{z_e}^2) e^{+jk_{z_e}z - jk_z h} \frac{k_\rho}{jk_z} dk_\rho + \frac{1}{4\pi} \int_0^\infty T(k_\rho) J_0(k_\rho \rho) e^{+jk_{z_e}z - jk_z h} \frac{k_\rho}{jk_z} dk_\rho \quad (2.37)$$

whilst referring to equation (2.29) for the  $\rho$ -component we get

$$E_\rho = \frac{1}{4\pi} \int_0^\infty T(k_\rho) J_1(k_\rho \rho) (-k_{z_e}) e^{+jk_{z_e} z - jk_z h} \frac{k_\rho^2}{jk_z} dk_\rho. \quad (2.38)$$

In conclusion, by solving the integrals in equations (2.37) and (2.38) in the complex plane, we can also evaluate the electromagnetic field in the lower dielectric medium.

### 2.1.3. Asymptotic solution

As for the 2D case, the integrals involved in the description of the field radiated by horizontal line source do not admit a closed-form solution for every points of the space surrounding the antenna. Anyway, by exploiting the theory of asymptotic expansion of double integrals [2], it possible to obtain a simple formula describing radiation far from the source. To handle the far-field zone, which will have the form of a spherical wave, it is convenient to introduce a spherical coordinate system  $(r, \theta, \phi)$ , thus the following relations hold true

$$\begin{aligned} x &= r \sin \theta \cos \phi \\ y &= r \sin \theta \sin \phi \\ z &= r \cos \theta \end{aligned} \quad (2.39)$$

with  $0 \leq \theta \leq \pi$  and  $0 \leq \phi < 2\pi$ . As outlined in [38], in the far field region only the  $\theta$  component of the electric field is different from zero; under the asymptotic solution of the involved integrals, radiation in the upper half-space ( $z < 0$ ) can be simply described by this expression

$$E_{1\theta} = \frac{-jI_0}{2\pi} \eta_0 \frac{n^2 k_0 \sin \theta \cos \theta}{n^2 \cos \theta + \sqrt{n^2 - \sin^2 \theta}} \frac{e^{jk_0 r}}{r} \quad (2.40)$$

where  $\eta_0 = \sqrt{\mu_0/\epsilon_0}$  is the free space impedance,  $I_0$  is the total current flowing on the dipole, and  $k_0$  and  $k_e$  are the wave numbers in the upper and lower half-spaces, respectively, as introduced in the previous chapter. In the subsurface region ( $z < 0$ ) for  $k_0 \rho \rightarrow \infty$  and  $\pi - \theta_c \leq \theta < \pi$  we have

$$E_{2\theta} = \frac{jI_0}{2\pi} \eta_0 \frac{n^2 k_0 \sin \theta \cos \theta}{n \sqrt{1 - n^2 \sin^2 \theta} - \cos \theta} \frac{e^{jk_e r}}{r} \quad (2.41)$$

whereas, for  $k_0 \rho \rightarrow \infty$  and  $\pi/2 \leq \theta < \pi - \theta_c$

$$E_{2\theta} = \frac{I_0}{2\pi} \eta_0 \frac{n^2 k_0 \sin \theta \cos \theta}{n \sqrt{n^2 \sin^2 \theta - 1} + j \cos \theta} \frac{e^{jk_e r}}{r}. \quad (2.42)$$

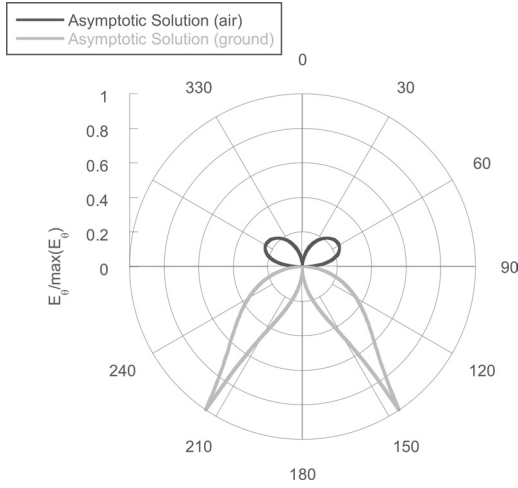


Fig. 2.2. Far field radiated by an interfacial vertical short dipole, whose lower medium has a permittivity equal to  $\epsilon_r = 3.2$ .

In Fig. 2.2 a plot of  $E_\theta$  for a fixed value of the permittivity of the ground medium has been reported. Generally speaking, the radiation pattern is quite different from that of a free-space short dipole; two main lobe are clearly visible in both upper and lower medium and a null at the interface along the dipole axis has been obtained.

#### 2.1.4. Numerical solution

To get a solution in each point of the space surrounding the antenna and have the possibility of analyzing the electromagnetic field also in the near-field region, a numerical solution of the involved integrals is requested. As for the 2D case, outlined in the previous sections, here by means of a customize MatLab routine a solution in the complex plane of the integrals at hand has been also developed. The general procedure is standard and is based on the Gaussian-Kronrod adaptive quadrature formula; attention should be paid to the choice of the right Riemann surface and on the adopted convergence criteria. Incidentally, kernels of the involved integral are made by an oscillating (i.e.,  $J(k_\rho \rho)$ ) contribution and by a complex exponential term (i.e.,  $e^{-j\sqrt{k_0^2 - k_z^2}(z+h)}$ ), which becomes real for  $k_z > k_0$  allowing once again for a fast convergence.

Numerical results obtained with the customized routine have been validated by means of the asymptotic formula introduced in the previous section. Specifically, in Fig. 2.3 the far-field behavior for a vertical short

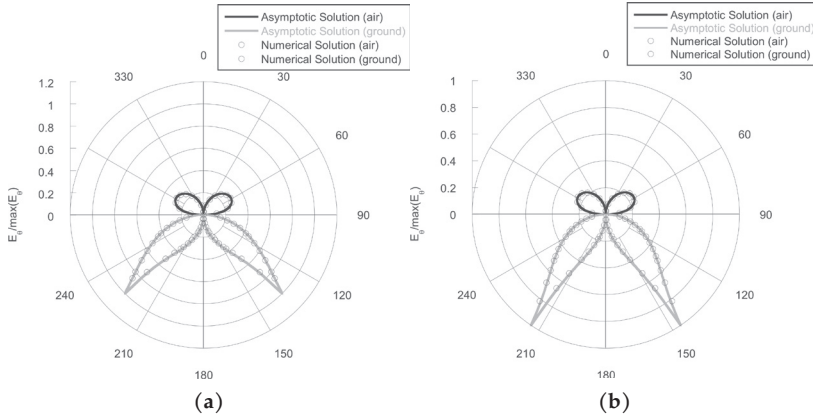


**Fig. 2.3.** Comparison between numerical and asymptotic far field pattern: (a)  $\epsilon_r = 2$  (b)  $\epsilon_r = 3.2$ .

dipole on a dielectric medium whose permittivity is equal to  $\epsilon_r = 3.2$  is presented. The relevant results are in excellent agreement, confirming the accuracy of the proposed numerical solution.

## 2.2. Horizontal electric dipole

In this section, following the same procedure outlined so far, the electromagnetic field radiated by horizontal electric dipole (HED) will be carried out. Since the geometry of the problem at hand lacks the azimuthal symmetry, the radiation will be not azimuthally uniform. Additionally, we will discover that on the surface of the considered half-space most of the energy is radiated in the direction of the dipole axis. This is clearly in contrast with the behavior of the same antenna in free space, where the radiation is in the direction perpendicular to the axis (i.e., at broadside). It is important to remind that analyzing the performance of a HED may provide useful information for a number of GPR applications. Indeed, such a configuration represents the simplest three-dimensional (3D) source of the electromagnetic pulse and the only one capable to lead to closed-form expression of the radiated field. An important practical application case is the radiation from buried antennas (underground, in ice or submerged in water); indeed, in this case it can be shown that the horizontal dipole is most effective and that the VED is an ineffective radiator [34]. Following the same scheme of the previous section, the field radiated may be seen as the sum of

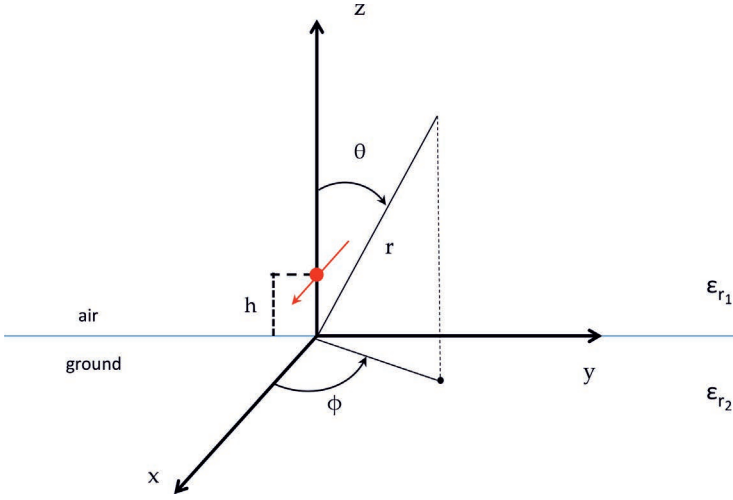


Fig. 2.4. Horizontal short dipole in spherical coordinate system.

a *primary* and *secondary* wave, respectively represented again by two Hertz potentials (i.e.,  $\pi_p$  and  $\pi_s$ ).

Let us consider a dipole located at a distance  $h$  from the surface and oriented in the  $x$  direction. Again, the primary field can be easily obtained from the  $x$ -component of the Hertz potential  $\pi$

$$\nabla^2 \pi_x + k^2 \pi_x = -\frac{J_x}{j\omega\epsilon_0} \quad (2.43)$$

with  $J_x = I_x L \delta(\mathbf{r} - \mathbf{r}')$ . The primary field is then given by

$$\begin{aligned} \pi_p &= \frac{e^{-jk|\mathbf{r}-\mathbf{r}'|}}{4\pi|\mathbf{r}-\mathbf{r}'|} = \\ &= \frac{1}{4\pi} \int_0^\infty J_0(k_\rho \rho) e^{-jk_z|z-h|} \frac{k_\rho}{jk_z} dk_\rho, \end{aligned} \quad (2.44)$$

as usual, in the following the term  $I_x L / j\omega\epsilon_0$  for convenience will be omitted (fixed equal to 1). Analogously, the secondary field in the air and in the ground is given by

$$\begin{aligned} \pi_{x_{s1}}(\rho, z) &= \frac{1}{4\pi} \int_0^\infty R(k_\rho) J_0(k_\rho \rho) e^{-jk_z|z+h|} \frac{k_\rho}{jk_z} dk_\rho & \text{for } z > 0, \\ \pi_{x_{s2}}(\rho, z) &= \frac{1}{4\pi} \int_0^\infty T(k_\rho) J_0(k_\rho \rho) e^{+jk_z z - jk_z h} \frac{k_\rho}{jk_z} dk_\rho & \text{for } z < 0. \end{aligned} \quad (2.45)$$

Generally speaking, a complete description of the electromagnetic field (non-separable in TM and TE cases) requires two scalar functions. Thus, in addition to  $\pi_{x_{s_1}}$  and  $\pi_{x_{s_2}}$  we need another scalar potential. A convenient choice, which was first introduced by Sommerferld in its seminal paper [8], is the  $z$  component  $\pi_z$ . With regards to the boundary condition, the tangential electric fields  $E_x$  and  $E_y$  and the tangential magnetic fields  $H_x$  and  $H_y$  must be continuous at the interface (i.e.,  $z = 0$ ); however, these conditions must be recast in terms of  $\pi_x$  and  $\pi_z$ . By considering that

$$\begin{aligned}\mathbf{E} &= \nabla(\nabla \cdot \boldsymbol{\pi}) + k^2 \boldsymbol{\pi} = \mathbf{E}_1 + \mathbf{E}_2 \\ \mathbf{H} &= j\omega\epsilon \nabla \times \boldsymbol{\pi}\end{aligned}\quad (2.46)$$

it possible to deduce the following boundary conditions (further details can be found in [34])

$$\text{Continuity of } E_x \rightarrow \pi_{x_1} = n^2 \pi_{x_2} \quad (2.47)$$

$$\text{Continuity of } E_y \rightarrow \frac{\partial}{\partial x} \pi_{x_1} + \frac{\partial}{\partial z} \pi_{z_1} = \frac{\partial}{\partial x} \pi_{x_2} + \frac{\partial}{\partial z} \pi_{z_2} \quad (2.48)$$

$$\text{Continuity of } H_x \rightarrow \pi_{z_1} = n^2 \pi_{z_2} \quad (2.49)$$

$$\text{Continuity of } H_y \rightarrow \frac{\partial}{\partial z} \pi_{x_1} = n^2 \frac{\partial}{\partial z} \pi_{x_2}. \quad (2.50)$$

By enforcing equations (2.47) and (2.50) we can determine the unknown functions in the integral equations (2.45)

$$R(k_\rho) = \frac{k_z - k_{z_e}}{k_z + k_{z_e}} \quad (2.51)$$

$$T(k_\rho) = \frac{2k_z}{n^2 k_z + n^2 k_{z_e}}. \quad (2.52)$$

In addition, equation (2.48) assesses a link between the  $x$ -component of  $\boldsymbol{\pi}$  and its  $z$ -component

$$\frac{\partial}{\partial z} (\pi_{z_1} - \pi_{z_2}) = \frac{\partial}{\partial z} (\pi_{x_2} - \pi_{x_1}) \quad (2.53)$$

thus, from equations (2.45), after evaluating the derivative with respect to  $x$ , we can write the following expression for the  $z$ -components of the

Hertz potential

$$\begin{aligned}\pi_{z_{s_1}}(\rho, z) &= \frac{\cos\phi}{4\pi} \int_0^\infty A(k_\rho) J_1(k_\rho \rho) e^{-jk_z(z+h)} k_\rho^2 dk_\rho & \text{for } z > 0, \\ \pi_{z_{s_2}}(\rho, z) &= \frac{\cos\phi}{4\pi} \int_0^\infty B(k_\rho) J_1(k_\rho \rho) e^{+jk_z z - jk_z h} k_\rho^2 dk_\rho & \text{for } z < 0,\end{aligned}\tag{2.54}$$

where

$$A(k_\rho) = -\frac{2}{k^2} \frac{k_z - k_{z_e}}{n^2 k_z + k_{z_e}}\tag{2.55}$$

$$B(k_\rho) = -\frac{2}{n^2 k^2} \frac{k_z - k_{z_e}}{n^2 k_z + k_{z_e}}.\tag{2.56}$$

Let us recast the first of equations (2.46) as follow

$$\mathbf{E} = \nabla(\nabla \cdot \boldsymbol{\pi}) + k^2 \boldsymbol{\pi} = \mathbf{E}_1 + \mathbf{E}_2,\tag{2.57}$$

and let us consider the first term of its right side. In Cartesian coordinates we can write

$$\mathbf{E}_1(x, y, z) = \nabla(\nabla \cdot \boldsymbol{\pi}) = \nabla(\nabla \cdot (\pi_x \mathbf{x}_0 + \pi_z \mathbf{z}_0)) = (\mathbf{x}_0 E_{x_1} + \mathbf{z}_0 E_{y_1} + \mathbf{z}_0 E_{z_1})\tag{2.58}$$

while in cylindrical coordinates we have

$$\mathbf{E}_1(\rho, \phi, z) = \nabla(\nabla \cdot \boldsymbol{\pi}) = \nabla(\nabla \cdot (\pi_x \mathbf{x}_0 + \pi_z \mathbf{z}_0)) = (\mathbf{x}_0 E_\rho x_1 + \mathbf{z}_0 E_\phi x_1 + \mathbf{z}_0 E_z x_1)\tag{2.59}$$

By developing the expression of the gradient of the divergence in equation (2.58) we get

$$\mathbf{E}_1 = \mathbf{x}_0 \left( \frac{\partial^2 \pi_x}{\partial x^2} + \frac{\partial^2 \pi_z}{\partial x \partial z} \right) + \mathbf{y}_0 \left( \frac{\partial^2 \pi_x}{\partial y \partial x} + \frac{\partial^2 \pi_z}{\partial y \partial z} \right) + \mathbf{z}_0 \left( \frac{\partial^2 \pi_x}{\partial z \partial x} + \frac{\partial^2 \pi_z}{\partial y^2} \right)\tag{2.60}$$

whereas for the expression in cylindrical coordinates (2.58) we have

$$\begin{aligned}\mathbf{E}_1 &= \mathbf{x}_0 \left( \cos^2 \phi \frac{\partial^2 \pi_x}{\partial \rho^2} + \cos \phi \frac{\partial^2 \pi_z}{\partial \rho \partial z} \right) + \\ &\quad \mathbf{y}_0 \left( \cos \phi \sin \phi \frac{\partial^2 \pi_x}{\partial \rho^2} + \sin \phi \frac{\partial^2 \pi_z}{\partial \rho \partial z} \right) + \\ &\quad \mathbf{z}_0 \left( \cos \phi \frac{\partial^2 \pi_x}{\partial \rho \partial z} + \frac{\partial^2 \pi_z}{\partial z^2} \right); \end{aligned}\tag{2.61}$$

for the three components of the electric field we can write

$$E_{x_1} = \cos^2 \phi \frac{\partial^2 \pi_x}{\partial \rho^2} + \cos \phi \frac{\partial^2 \pi_z}{\partial \rho \partial z} \quad (2.62)$$

$$E_{y_1} = \cos \phi \sin \phi \frac{\partial^2 \pi_x}{\partial \rho^2} + \sin \phi \frac{\partial^2 \pi_z}{\partial \rho \partial z} \quad (2.63)$$

$$E_{z_1} = \cos \phi \frac{\partial^2 \pi_x}{\partial \rho \partial z} + \frac{\partial^2 \pi_z}{\partial z^2}. \quad (2.64)$$

Therefore the following derivatives of the integral expression of the potential (see (2.45) and (2.54)) must be evaluated

$$\begin{array}{ll} 1. \frac{\partial^2 \pi_x}{\partial \rho^2} & 3. \frac{\partial^2 \pi_z}{\partial \rho \partial z} \\ 2. \frac{\partial^2 \pi_x}{\partial \rho \partial z} & 4. \frac{\partial^2 \pi_z}{\partial z^2} \end{array} \quad (2.65)$$

To simplify the discussion of the next developments, two different cases will be considered, one for  $z > 0$  and one for  $z < 0$ .

### 1. First case: $z > 0$

We have that

$$\begin{aligned} \pi_x(\rho, z) = & \frac{1}{4\pi} \int_0^\infty J_0(k_\rho \rho) e^{-jk_z|z-h|} \frac{k_\rho}{jk_z} dk_\rho + \\ & \frac{1}{4\pi} \int_0^\infty R(k_\rho) J_0(k_\rho \rho) e^{-jk_z|z+h|} \frac{k_\rho}{jk_z} dk_\rho \end{aligned} \quad (2.66)$$

and

$$\pi_z(\rho, z) = \frac{\cos \phi}{4\pi} \int_0^\infty A(k_\rho) J_1(k_\rho \rho) e^{-jk_z(z+h)} k_\rho^2 dk_\rho \quad (2.67)$$

#### • $z > h$

Under this condition we have that  $(z - h) > 0$ ; if also  $h > 0$  we can assume that  $|z + h| = (z + h)$  of course under this condition we cannot place the short dipole in the second half-space; however, for our purposes (modeling GPR surveys) this represents an acceptable limitation, and allows us to suppress the absolute value in the exponential term of the

previous integrals. Consequently, the involved integral can be recast as follows

$$\begin{aligned}\pi_{x_{s_1}}(\rho, z) &= \frac{1}{4\pi} \int_0^\infty J_0(k_\rho \rho) e^{-jk_z(z-h)} \frac{k_\rho}{jk_z} dk_\rho \\ &\quad + \frac{1}{4\pi} \int_0^\infty R(k_\rho) J_0(k_\rho \rho) e^{-jk_z(z+h)} \frac{k_\rho}{jk_z} dk_\rho\end{aligned}\quad (2.68)$$

Now, recalling that  $J'_n(z) = -J_n(z) + \frac{n}{2} J_{n+1}(z)$ , we have

$$\begin{aligned}\frac{\partial J_0(k_\rho \rho)}{\partial \rho} &= -k_\rho J_1(k_\rho \rho) \\ \frac{\partial^2 J_0(k_\rho \rho)}{\partial \rho^2} &= \frac{\partial(-k_\rho J_1(k_\rho \rho))}{\partial \rho} = k_\rho \left[ k_\rho J_2(k_\rho \rho) - \frac{J_1(k_\rho \rho)}{\rho} \right]\end{aligned}\quad (2.69)$$

For the first derivative of (2.65) we can finally write

$$\begin{aligned}\frac{\partial^2 \pi_x}{\partial \rho^2} &= \frac{1}{4\pi} \int_0^\infty \left[ k_\rho J_2(k_\rho \rho) - \frac{J_1(k_\rho \rho)}{\rho} \right] e^{-jk_z(z-h)} \frac{k_\rho^2}{jk_z} dk_\rho + \\ &\quad + \frac{1}{4\pi} \int_0^\infty R(k_\rho) \left[ k_\rho J_2(k_\rho \rho) - \frac{J_1(k_\rho \rho)}{\rho} \right] e^{-jk_z(z+h)} \frac{k_\rho^2}{jk_z} dk_\rho\end{aligned}\quad (2.70)$$

In order to evaluate the second derivative of (2.65) we firstly write

$$\begin{aligned}\frac{\partial \pi_x}{\partial z} &= \frac{1}{4\pi} \int_0^\infty -J_0(k_\rho \rho) e^{-jk_z(z-h)} k_\rho dk_\rho + \\ &\quad + \frac{1}{4\pi} \int_0^\infty R(k_\rho) J_0(k_\rho \rho) e^{-jk_z(z+h)} k_\rho dk_\rho\end{aligned}\quad (2.71)$$

thus

$$\begin{aligned}\frac{\partial^2 \pi_x}{\partial \rho \partial z} &= \frac{1}{4\pi} \int_0^\infty J_1(k_\rho \rho) e^{-jk_z(z-h)} k_\rho^2 dk_\rho + \\ &\quad + \frac{1}{4\pi} \int_0^\infty R(k_\rho) J_1(k_\rho \rho) e^{-jk_z(z+h)} k_\rho^2 dk_\rho\end{aligned}\quad (2.72)$$

- $\mathbf{z} < \mathbf{h}$

We have that

$$\begin{aligned}\pi_x(\rho, z) &= \frac{1}{4\pi} \int_0^\infty J_0(k_\rho \rho) e^{jk_z(z-h)} \frac{k_\rho}{jk_z} + dk_\rho \\ &\quad \frac{1}{4\pi} \int_0^\infty R(k_\rho) J_0(k_\rho \rho) e^{-jk_z(z+h)} \frac{k_\rho}{jk_z} dk_\rho\end{aligned}\quad (2.73)$$

thus

$$\begin{aligned}\frac{\partial^2 \pi_x}{\partial \rho^2} &= \frac{1}{4\pi} \int_0^\infty \left[ k_\rho J_2(k_\rho \rho) - \frac{J_1(k_\rho \rho)}{\rho} \right] e^{jk_z(z-h)} \frac{k_\rho^2}{jk_z} dk_\rho + \\ &\quad \frac{1}{4\pi} \int_0^\infty R(k_\rho) \left[ k_\rho J_2(k_\rho \rho) - \frac{J_1(k_\rho \rho)}{\rho} \right] e^{-jk_z(z+h)} \frac{k_\rho^2}{jk_z} dk_\rho\end{aligned}\quad (2.74)$$

To evaluate also in this case the second derivative of (2.65) we firstly write

$$\begin{aligned}\frac{\partial \pi_x}{\partial z} &= \frac{1}{4\pi} \int_0^\infty J_0(k_\rho \rho) e^{jk_z(z-h)} k_\rho dk_\rho + \\ &\quad \frac{1}{4\pi} \int_0^\infty R(k_\rho) J_0(k_\rho \rho) e^{-jk_z(z+h)} k_\rho dk_\rho\end{aligned}\quad (2.75)$$

thus

$$\begin{aligned}\frac{\partial^2 \pi_x}{\partial \rho \partial z} &= \frac{1}{4\pi} \int_0^\infty -J_1(k_\rho \rho) e^{jk_z(z-h)} k_\rho^2 dk_\rho + \\ &\quad \frac{1}{4\pi} \int_0^\infty R(k_\rho) J_1(k_\rho \rho) e^{-jk_z(z+h)} k_\rho^2 dk_\rho.\end{aligned}\quad (2.76)$$

Regarding to the remaining derivative of equation (2.65) no condition on the vertical position of the dipole has to be enforced. Therefore, they can be easily calculated in the following way:

$$\frac{\partial \pi_z}{\partial z} = \frac{\cos \phi}{4\pi} \int_0^\infty A(k_\rho) J_1(k_\rho \rho) (-jk_z) e^{-jk_z(z+h)} k_\rho^2 dk_\rho \quad (2.77)$$

recalling that

$$\frac{\partial J_1(k_\rho \rho)}{\partial \rho} = \left[ \frac{J_1(k_\rho \rho)}{\rho} - k_\rho J_2(k_\rho \rho) \right] \quad (2.78)$$

we have

$$\frac{\partial^2 \pi_z}{\partial \rho \partial z} = \frac{\cos \phi}{4\pi} \int_0^\infty -jq A(k_\rho) \left[ \frac{J_1(k_\rho \rho)}{\rho} - k_\rho J_2(k_\rho \rho) \right] e^{jk_z(z+h)} k_\rho^2 dk_\rho, \quad (2.79)$$

whereas for the last derivative we can simply write

$$\frac{\partial^2 \pi_z}{\partial z^2} = \frac{\cos \phi}{4\pi} \int_0^\infty -k_z^2 A(k_\rho) J_1(k_\rho \rho) e^{-jk_z(z+h)} k_\rho^2 dk_\rho. \quad (2.80)$$

## 2. Second case: $z < 0$

In this case for  $x$ -component of the Hertz potential it holds

$$\pi_x = \frac{1}{4\pi} \int_0^\infty T(k_\rho) J_0(k_\rho \rho) e^{jk_{ze}z - jk_z h} \frac{k_\rho}{jk_z} dk_\rho \quad (2.81)$$

and for the first and second derivative of (2.65) we can write

$$\frac{\partial^2 \pi_x}{\partial \rho^2} = \frac{1}{4\pi} \int_0^\infty T(k_\rho) \left[ k_\rho J_2(k_\rho \rho) - \frac{J_1(k_\rho \rho)}{\rho} \right] e^{jk_{ze}z - jk_z h} k_\rho^2 dk_\rho \quad (2.82)$$

$$\frac{\partial^2 \pi_x}{\partial \rho \partial z} = -\frac{1}{4\pi} \int_0^\infty T(k_\rho) J_1(k_\rho \rho) e^{jk_{ze}z - jk_z h} \frac{k_\rho^2 k_{ze}}{k_z} dk_\rho \quad (2.83)$$

respectively. Finally for the  $z$ -component it holds

$$\pi_z = \frac{\cos \phi}{4\pi} \int_0^\infty B(k_\rho) J_1(k_\rho \rho) e^{jk_{ze}z - jk_z h} k_\rho^2 dk_\rho \quad (2.84)$$

and for the remaining derivative of (2.65) we can write

$$\frac{\partial^2 \pi_z}{\partial z^2} = -\frac{\cos \phi}{4\pi} \int_0^\infty k_{ze}^2 B(k_\rho) J_1(k_\rho \rho) e^{jk_{ze}z - jk_z h} k_\rho^2 dk_\rho \quad (2.85)$$

$$\frac{\partial^2 \pi_z}{\partial \rho \partial z} = \frac{\cos \phi}{4\pi} \int_0^\infty B(k_\rho) \left[ \frac{J_1(k_\rho \rho)}{\rho} - k_\rho J_2(k_\rho \rho) \right] jk_{ze} e^{jk_{ze}z - jk_z h} k_\rho^2 dk_\rho. \quad (2.86)$$

Once that all the derivatives in equations (2.65) are known, it is possible to obtain the electric field  $\mathbf{E}_1$  presented in (2.61); thus, to evaluate the electric field radiated by a HED, expressed by equation (2.57), it remains only to add the  $\mathbf{E}_2$  field, whose calculation is straightforward. As final comment, it is very interesting to note that the field given by  $\pi_z$ , as expected, is directional because of the  $\cos \phi$  factor in equations (2.54).

### 2.2.1. Asymptotic solution

As for both the line source and VED sources, once again the integrals modeling the problem cannot be solved analytically and a closed-form solution for each point of space is not available. An asymptotic method provides a simple and accurate solution far from the source, that is of course very useful for communication problem, wherein one is interested to evaluate the electromagnetic field produced in a very remote point. However, for the case at hand, since the problem is no more azimuthally symmetric, in the analytical expression we also find a dependency on the azimuthal angle (i.e.,  $\phi$ ); additionally, as shown below, the far-field distribution is described by two components of the electric field, namely  $E_\theta$  and  $E_\phi$ .

For the field in the upper medium (labeled with the subscript 1) for  $z > 0$  we can write

$$E_{1\theta} = \frac{jI_0k_0}{2\pi}\eta_0 \left[ \frac{\cos^2\theta}{\cos\theta + \sqrt{n^2 - \sin^2\theta}} - \sin^2\theta \cos\theta \frac{\cos\theta - \sqrt{n^2 - \sin^2\theta}}{n^2 \cos\theta + \sqrt{n^2 - \sin^2\theta}} \right] \cos\phi \frac{e^{jk_0r}}{r} \quad (2.87)$$

$$E_{1\phi} = \frac{-jI_0k_0}{2\pi}\eta_0 \frac{\sin\phi \cos\theta}{\cos\theta + \sqrt{n^2 - \sin^2\theta}} \frac{e^{jk_0r}}{r} \quad (2.88)$$

In the subsurface region ( $z < 0$ , subscript 2) for  $k_0\rho \rightarrow \infty$  and  $\pi - \theta_c \leq \theta < \pi$  we have

$$E_{2\theta} = \frac{jnI_0k_0}{2\pi}\eta_0 \left[ \sin^2\theta \cos\theta \frac{\sqrt{1 - n^2 \sin^2\theta} + n \cos\theta}{n\sqrt{1 - n^2 \sin^2\theta} - \cos\theta} - \frac{\cos^2\theta}{\sqrt{1 - n^2 \sin^2\theta} - n \cos\theta} \right] \cos\phi \frac{e^{jnk_0r}}{r} \quad (2.89)$$

$$E_{2\phi} = \frac{jnI_0k_0}{2\pi}\eta_0 \frac{\sin\phi \cos\theta}{\sqrt{1 - n^2 \sin^2\theta} - n \cos\theta} \frac{e^{jnk_0r}}{r} \quad (2.90)$$

whereas, for  $k_0\rho \rightarrow \infty$  and  $\pi/2 \leq \theta < \pi - \theta_c$

$$E_{2\theta} = \frac{jnI_0k_0}{2\pi}\eta_0 \left[ \sin^2\theta \cos\theta \frac{\sqrt{n^2 \sin^2\theta - 1} - jn \cos\theta}{n\sqrt{n^2 \sin^2\theta - 1} + j \cos\theta} + j \frac{\cos^2\theta}{\sqrt{n^2 \sin^2\theta - 1} + jn \cos\theta} \right] \cos\phi \frac{e^{jnk_0r}}{r} \quad (2.91)$$

$$E_{2\phi} = \frac{nI_0k_0}{2\pi}\eta_0 \frac{\sin\phi \cos\theta}{\sqrt{n^2 \sin^2\theta - 1 + jn \cos\theta}} \frac{e^{jnk_0r}}{r} \quad (2.92)$$

In Fig. 2.5 and 2.6 two plots of the normalized module of the electric field (i.e.,  $|E|$ ) for two fixed values of the permittivity of the ground medium have been reported.

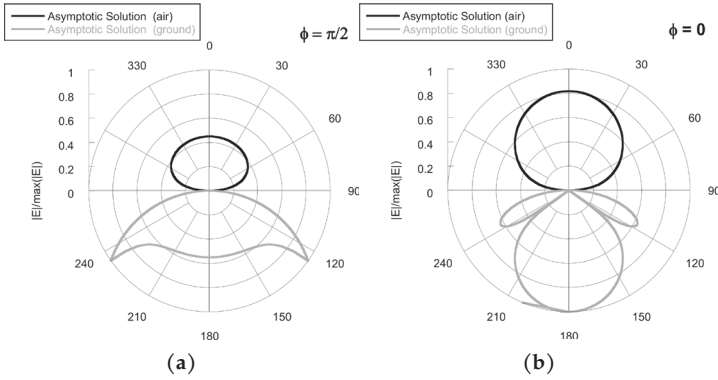


Fig. 2.5. Far field radiated by horizontal short dipole placed on a dielectric medium with permittivity  $\epsilon_r = 1.5$ . (a) plane  $\phi = \pi/2$ , (b) plane  $\phi = 0$ .

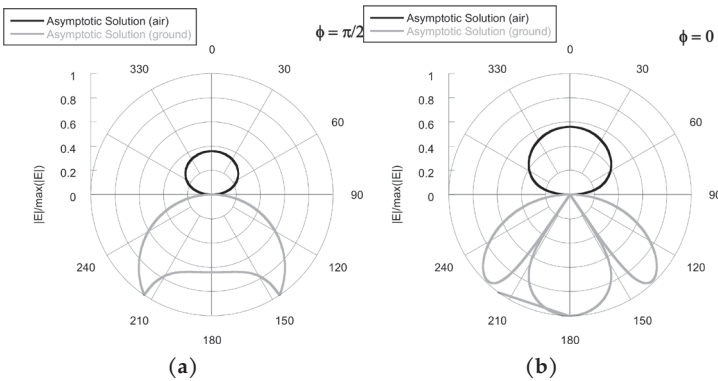


Fig. 2.6. Far field radiated by horizontal short dipole placed on a dielectric medium with permittivity  $\epsilon_r = 3.2$ . (a) plane  $\phi = \pi/2$ , (b) plane  $\phi = 0$ .

In this case the pattern has a null at the interface, whereas in the upper half-space a single lobe with a maximum normal to the interface has been obtained. Additionally, in the lower medium, in the plane normal to the interface and containing the dipole, the pattern has three lobes,

whereas in the plane normal to the interface and normally bisecting the dipole, the pattern has two maxima located symmetrically about a minimum.

### 2.2.2. Numerical solution

As discussed in previous sections, the possibility of analyzing the electric field radiated by HED placed at the interface of two dielectric half-spaces is highly desirable. Indeed, by following the same procedure outlined for a VED, we are once again able to numerically characterize the electric field in every point of the space surrounding the antenna. The involved integrals are basically the same, thus the numerical procedure outlined for the previous case is still valid. As usual, we propose a validation of our customized MatLab routine by comparing the numerical far-field pattern with those carried out asymptotically. Specifically, in Fig. 2.7 results obtained for a dielectric medium having a permittivity  $\varepsilon_r = 2$  have been reported for two principal planes, namely  $\phi = \pi/2$  and  $\phi = 0$ . In Fig. 2.8, instead, a comparison for larger values of the

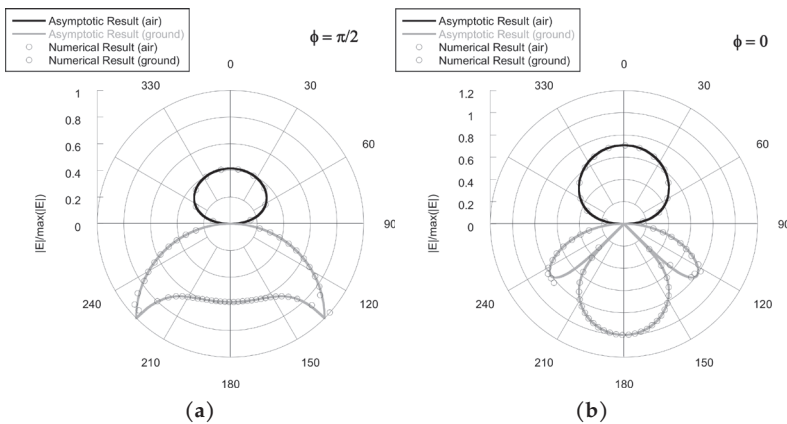


Fig. 2.7. Comparison between numerical and asymptotic results for an interfacial horizontal short dipole. (a)  $\varepsilon_r = 2$ , plane  $\phi = \pi/2$ , (b)  $\varepsilon_r = 2$ , plane  $\phi = 0$ .

permittivity, on the principal plane  $\phi = \pi/2$ , has been shown. The results are in excellent agreement for all the considered values, fully confirming the accuracy of the proposed numerical implementation.

It is important to recall that we have now available a powerful instrument to conduct comprehensive analysis on the near-field distribution produced by an interfacial short dipole; it represents a simple and reli-

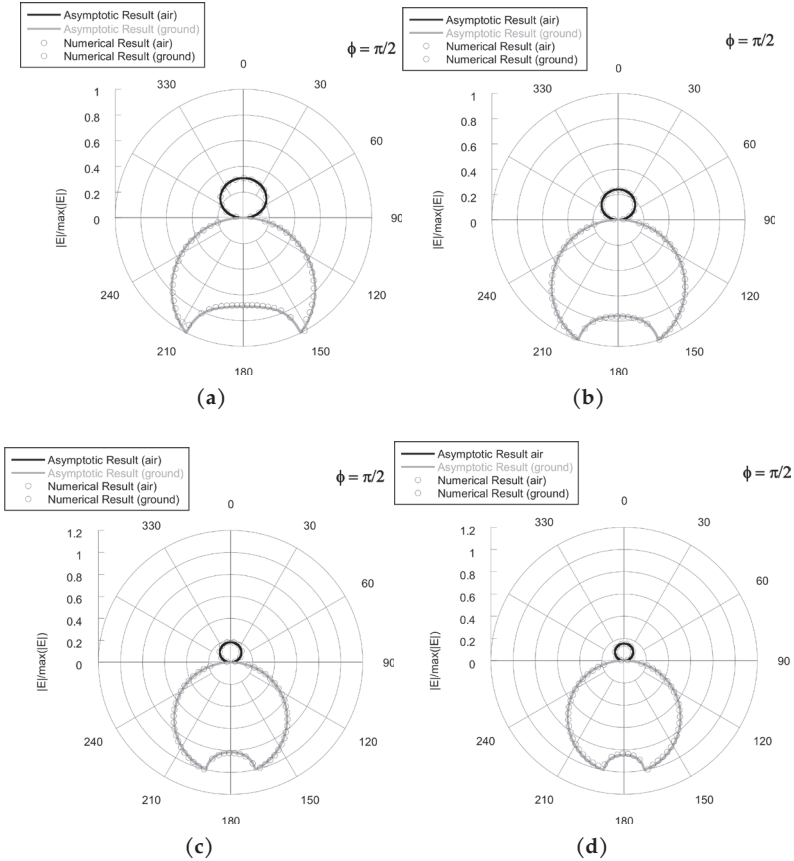
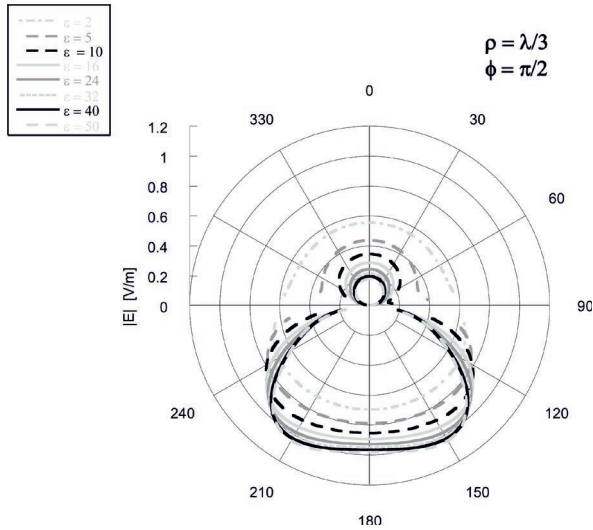


Fig. 2.8. Comparison between numerical and asymptotic far field pattern (a)  $\epsilon_r = 5$ , (b)  $\epsilon_r = 10$ , (c)  $\epsilon_r = 20$ , (d)  $\epsilon_r = 30$ .

able mathematical model for a realistic antenna of a GPR system.

Specifically, in the following, we focus our attention on the near field radiated on the  $\phi = \pi/2$  plane, since we are interested in synthesizing a simple mathematical model for a transmitting and receiving antenna of a more complex system. As an example in Fig. 2.9 the near-field distributions ( $E$ -field module in V/m,  $I_0 = 1$  A/m, equivalent length  $L = 0.1$  mm, frequency  $f = 1$  GHz) for a number of permittivity values, ranging from  $\epsilon_r = 2$  up to  $\epsilon_r = 50$ , at a radial distance from the source equal to  $\lambda/3$  have been shown. The behavior of the radiated field is extremely interesting: for increasing values of the dielectric constant the electric field becomes stronger in the lower medium. Besides, the



**Fig. 2.9.** Near-field distribution of a short dipole for a number of permittivity values ( $h = 0$  cm).

field in air shows a very interesting sensitivity to the  $\epsilon_r$  variation, even for observation point close to the surface where a receiving antenna could be located. The same behavior can be observed in Fig. 2.10, where the problem has been solved for the same parameters considered previously but observing the field at a distance equal to  $\lambda/2$ . Specifically the sensitivity of the electric field in air is still clearly visible. In the next sections we will go back on this attractive feature, and extensive analysis on the possibility of exploiting such a sensitivity to produce an estimation of the soil parameters by means of GPR systems will be investigated.

In the numerical results shown so far we have always placed the dipole just on the surface; this since asymptotic solution of the integral solving the problem requires  $h = 0$  in the formulation. This value has been also kept for the far- and near-field numerical results. In Fig. 2.11 the angular distribution of the electromagnetic field on the plane  $\phi = \pi/2$  for  $h = 1$  cm has been reported. It is interesting to note that this position is more suitable to represent realistic GPR configurations; the behavior of the electric field remains unchanged and a good sensitivity of the field in air with respect to the permittivity variations is still clearly visible.

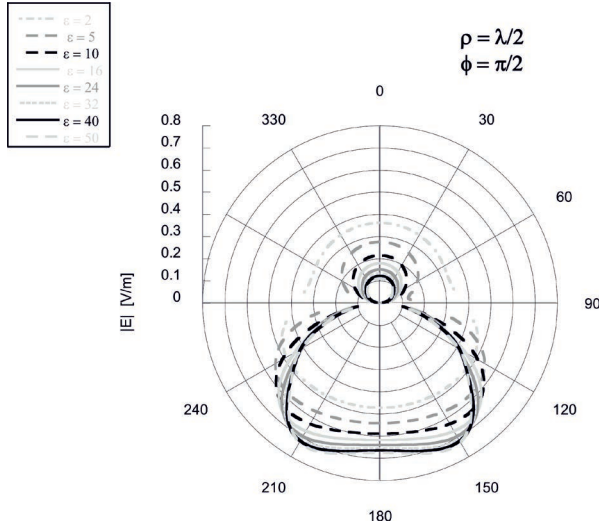


Fig. 2.10. Near field distribution of a short dipole for a number of permittivity values for  $h = 0$  cm and  $\rho = \lambda/3$ .

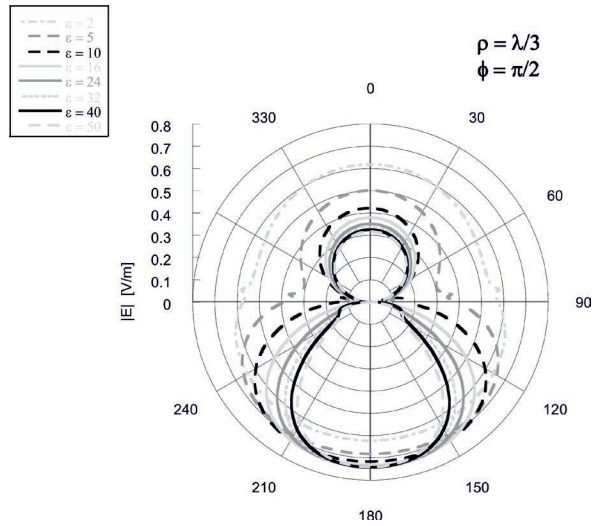
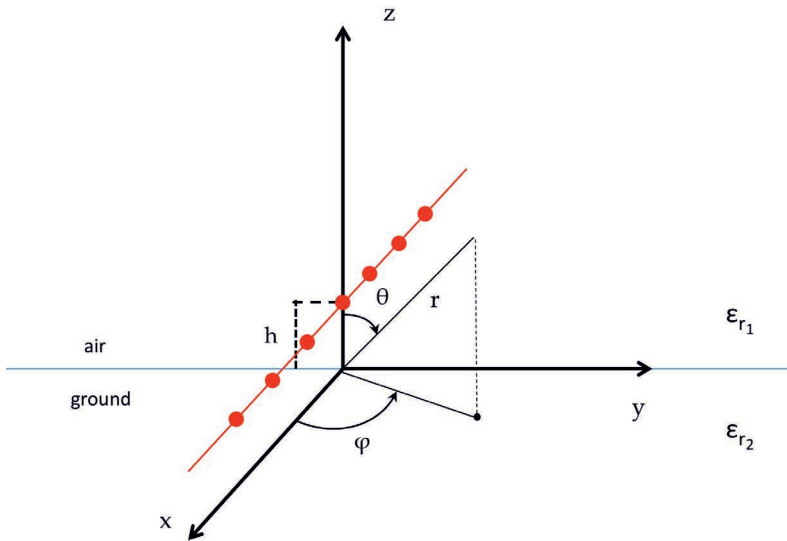


Fig. 2.11. Near-field distribution of a short dipole for a number of permittivity value for  $h = 0$  cm and  $\rho = \lambda/2$ .

### 2.3. Radiation from a half-wavelength dipole

So far the near-field distribution generated by elementary sources placed on a flat interface has been analyzed. The obtained results are very interesting for themselves, but also because two horizontal electric dipoles placed at distance  $d$  represent a simple mathematical model for a ground-coupled GPR systems. To make our model even more realistic, in this section we synthesize a half-wavelength dipole (HWD) as a transmitting device. Basically, we consider this kind of antenna as made by a suitable number of short horizontal dipoles, as shown in Fig. 2.12. Since a spatial sampling has been introduced, the number of



**Fig. 2.12.** A horizontal interfacial half-wavelength dipole in a spherical coordinate system synthesized by considering a suitable number of short dipoles (red dots on the red line).

short dipoles representing our HWD should be suitably designed. In particular, being  $\lambda$  the selected central wavelength of the radiated pulse (corresponding to a carrier frequency  $f_c$ ), at least a step  $s = \lambda/10$  has been considered. To validate our code in Fig. 2.13 and 2.14 a comparison between the far-field pattern of a free-space short dipole and of a half-wavelength dipole for a fixed frequency  $f = 1$  GHz have been reported [39]. A pattern obtained with our numerical implementation of a HWD by sampling with  $n = 3$  and  $n = 9$  short dipoles is shown as well. They are equi-spaced as shown in Fig. 2.12 and are represented by gray circles and gray squares, respectively. Already for  $n = 9$  (see Fig. 2.13) the

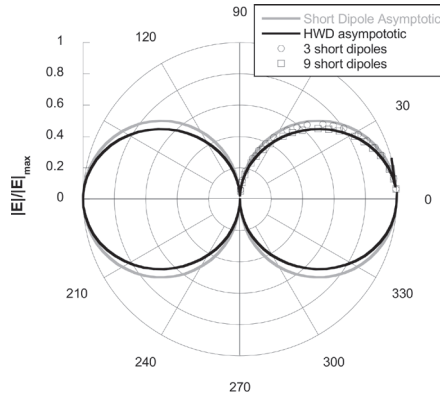
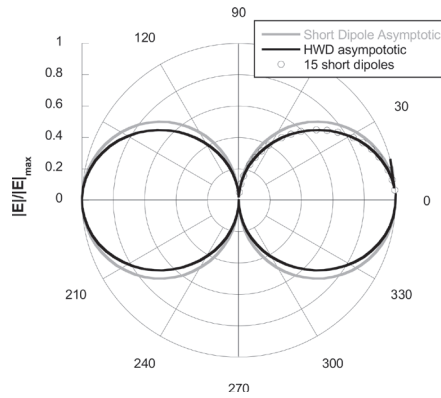


Fig. 2.13. Far-field patterns for a free-space short dipole (SD), a HWD and the results obtained with its discretized model. See label for the relevant details.

pattern is converging while the results obtained for  $n = 15$  (see Fig. 2.14) confirm the accuracy of the proposed novel implementation.

In Fig. 2.15 a numerical result obtained by considering as input waveform a modulated Gaussian pulse having a bandwidth of 1 GHz around a carrier frequency  $f_c = 1$  GHz is reported. The signal received by an interfacial short dipole is synthesized exploiting our frequency-domain code for a suitable number of frequency and transforming back in the time domain. A quite high permittivity for the lower medium is considered to allow for the separation of two different contribution (i.e., air and ground wave, see part II of this thesis for further details). Our numerical results are in excellent agreement with those obtained with an ad-hoc full-wave solution of the considered scenario. Some visible slight differences are possibly due to the different model of excitation of the Gaussian pulse and to the finite thickness of the dipole's radius that is requested in the discretized model of the full-wave solution. This frequency-domain code is very interesting not only for itself but because it can also represent a valuable and efficient alternative whenever a representation of the near-field distribution of the electromagnetic field radiated by a realistic antenna on a lossy and dispersive medium is requested. Indeed, full-wave solutions with ad-hoc implementation on CAD tools could become computationally very heavy when a certain degree of dispersion have to be considered in the model of the lower half-space.



**Fig. 2.14.** Far-field patterns for a free-space SD, a HWD and the results obtained with its discretized model for  $n = 15$ . See label for the relevant details.

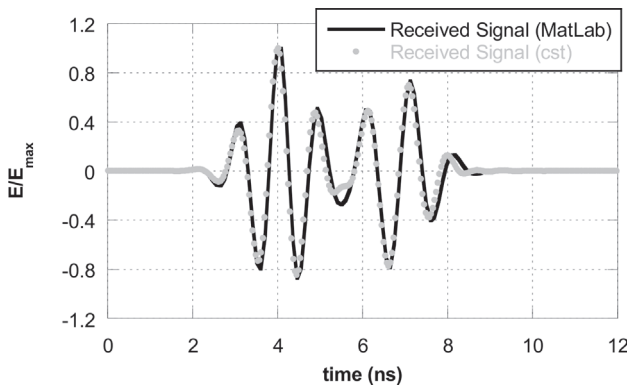


**Fig. 2.15.** Comparison between two Gaussian pulses (bandwidth 0.5 - 1.5 GHz) received by a short dipole when a transmitting half-wavelength dipole is placed on a flat interface between two dielectric media as in Fig. 2.12 ( $\epsilon_{r1} = \epsilon_0$  and  $\epsilon_{r2} = 36$ ). Solid black line represents the signal radiated by our numerical model of the HWD, whereas the gray circles represent a validation of the model developed through a full-wave solution.



PART II

GROUND PENETRATING RADAR



# Introduction

Ground Penetrating Radar (GPR) is a well-established geophysical technique, widely used for shallow subsurface exploration. It has become indispensable for a wide variety of geophysical, civil and forensic applications, as it can provide fast and reliable information on the investigated subsoil by simply analyzing the reflected signal generated whenever the transmitted electromagnetic wave encounters discontinuities or buried objects. Antennas, electronic systems, and post-processing algorithms must be suitably designed depending on the considered scenario and application. In the last years this technique has also gathered large interest of the planetary and space community, and nowadays is by far considered the most promising electromagnetic method for planetary subsurface explorations. Dry and cold geological materials forming planets, satellites and comets usually allow for good penetration of low- and high-frequency electromagnetic waves. This was proven for the first time in 1972 by the Apollo 17 mission, where two different experiments involving subsurface radio propagation were tested. After this pioneering attempt, only in 1990s, also thanks to various improvements in GPR technology, a new strong interest towards such a geophysical instrument was induced. Indeed, several payloads for the Mars subsurface investigation with GPR were proposed and developed. Among those, the European Space Agency (ESA) selected MARSIS (Mars Advanced Radar for Subsurface and Ionosphere Sounding), a multi-frequency coherent orbiting GPR [40] operating at few MHz, while NASA selected SHARAD (SHallow RADar), a similar subsurface radar operating at higher frequency (20 MHz) [41]. Both the instruments have been shown to be capable to deeply penetrate the Martian subsoil and to detect in-

interfaces between the bottom of polar deposits and bedrocks. Specifically, MARSIS has been able to go beyond 4 km of the planet crust and SHARAD has produced extraordinary high resolution images of the Martian polar caps.

In the meantime, in 2007, the Japan Aerospace Exploration Agency (JAXA) launched its first mission on the Moon. The spacecraft SELENE was equipped with a 5 MHz GPR (named Lunar Radar Sounder - LRS), able to operate for weeks performing extensive subsurface exploration of the lunar crust. Also, a surface penetrating radar, CONSERT (Comet Nucleus Sounding Experiment by Radiowave Transmission), is part of the payload of the Rosetta mission, whose lander (Philae) touched down after ten years from its launch toward the comet just in these days. The 90 MHz bi-static radar will investigate the internal structure of the comet nucleus. Finally, in the framework of JUICE (JUperiter ICy moons Explorer) mission, a 9 MHz GPR, named RIME (Radar for Icy Moon Exploration), has been chosen as the main geophysical instrument to sound Jupiter's moons to a depth of about 9 Km. In this planetary contest, ground-based GPR has the same potentialities of its orbiting counterpart, as it can access the subsurface and retrieve qualitative and quantitative information on its composition and eventually on the presence of scatterers of different materials and dimensions; in fact, this would not be possible through traditional imaging systems or spectrometers, that can only analyze the visible surface. At present, several GPR systems have been proposed by the scientific community for a planetary mission, but only two have been selected: one on-board the EXOMARS rover, named WISDOM (Water Ice Subsurface Deposit Observation on Mars), and one on-board of the 2020 NASA Mars rover, named RIMFAX (Radar Imager for Mars' Subsurface Experiment). The activity of this part of thesis, outlined in the next chapters, is closely related to the project of the WISDOM GPR. It has been developed in collaboration with the Earth and Space applied physics laboratory of the 'Rome Tre' University, with financial support provided by the Italian Space Agency (ASI). Since the main goal of the mission will be to drill and analyze the subsurface of the 'red planet', to find evidence on past or present biological life, a rover equipped with various instruments has been designed. A wide-band GPR, whose operative bandwidth ranges from 0.5 to 3 GHz, has been also considered, with the main goal to detect shallow hard rocks whose presence could dramatically damage the drilling system. For these reasons, a realistic model of the operating

environment is implemented and described in this investigation through a full-wave electromagnetic simulator, which has shown to be capable to take into account the main features of the real antenna system and of the radiated signal. The flexibility and efficiency of this numerical approach has allowed for the analysis of a great variety of configurations. The background is modeled based on data from recent explorations, while various kinds of embedded scatterers are considered with different geometrical and physical characteristics. In addition, thanks to an in-house laboratory setup, the simulated results have been compared with ad-hoc GPR measurements performed on basalt rocks buried in a mixture of glass beads, as analogue of a dry sandy Martian soil. A very good agreement between theoretical and experimental results has been found, thus validating the proposed numerical approach. This research, accurately outlined in the next sections, has provided useful and reliable information concerning the prediction of the scattering effects from buried objects in the environment where the ExoMars rover will operate.



## 3. GPR Antennas

### 3.1. Introduction

One of the most important components of a commercial or prototypical GPR is the radiating system. The choice among possible solutions and configurations is strictly related to the application and to the main goal of the relevant GPR survey. Even though this kind of instrument belongs to the broad class of RADAR (RAdio Detection and Ranging) systems, typically it radiates an electromagnetic pulse in the subsoil. To optimize the transmitted energy and to minimize reflections and multipaths between the air and ground interface, for many applications the GPR antenna is placed as near as possible to the probed material, i.e., it works in *ground-coupled* configuration. This means that not all the configurations investigated and usually employed for antennas working in the free-space can be exploited or at least partially re-adapted. To find a complete description of the most common antennas employed for geophysical surveys one can refer to [42] and [43]; typically, the choice of models and topologies is related to the requirement about the operative bandwidth. Indeed, to obtain the requested range resolution and a good signal penetration, it is highly desirable to design an antenna capable to provide a fractional bandwidth larger than 40 %, around the carrier frequency, which should be lower than about 1.5 GHz. Unfortunately, as it is known, the lower is the operative frequency more difficult is to obtain large bandwidth. This means that a trade-off between depth penetration and range resolution must be always faced. It is clear at this point that simple resonant antennas are usually not able to provide the desired performances, and consequently more advanced solutions and configurations should be addressed. In the next sections, as a first

step for the implementation of a virtual scenario for general-purpose GPR surveys, different kind of antennas will be designed and simulated by means of a commercial CAD tool, providing in the various cases matching and radiative features for the proposed numerical model.

### 3.2. Monopole

The first kind of antenna was designed during the master's degree thesis of the Author with the aim to reproduce the operational bandwidth and the physical dimension of a commercial systems, already available for measurements in a laboratory environment. It has been derived by suitable scaling and re-adapting a prototype designed and measured in [44].

In particular, to acquire simulated data as consistent as possible with those measured and to compare the synthetic imaging results with those obtained through our experimental setup, a pair of wide-band printed monopole antennas having bandwidth similar to the one nominally used for a commercial GPR system were designed and simulated. As shown in Fig. 3.1, our numerical model is fed by a coplanar waveguide; two different prototypes have been implemented, one operating in monostatic condition (Fig. 3.1(a)) and one for bistatic surveys (Fig. 3.1(b)). In both cases the input port of the proposed antenna is fed with a Gaussian pulse whose spectrum ranges between 0.5 and 1.5 GHz (defined among frequencies having 10 % of its maximum amplitude); it is generated as the modulation of a pulse through 1 GHz sinusoid. A parametric analysis allow us to optimize the geometric dimension of the metalization, the dielectric constant and the thickness of the substrate to obtain an impedance matching lower than -10 dB inside all the operational

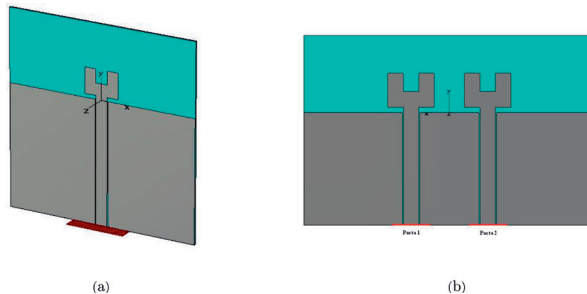


**Fig. 3.1.** Printed monopole antenna fed with a coplanar waveguide in monostatic (a) and bistatic (b) configuration.

bandwidth. As an example in Fig. 3.2(a) the return loss of the proposed

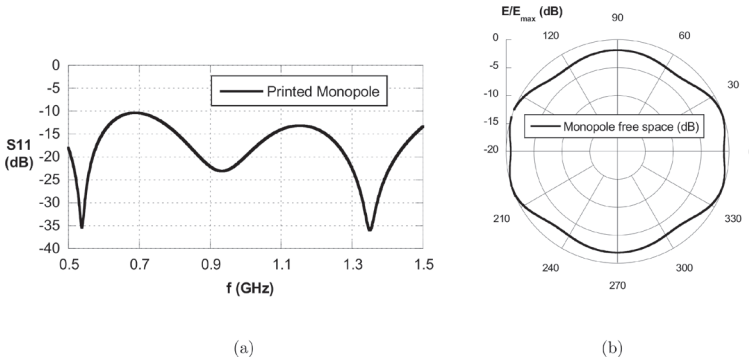


**Fig. 3.2.** (a) Reflection coefficient at the input port of the antenna; (b) Radiation pattern in polar coordinates on the  $xz$  plane.

monostatic antenna (shown in Fig. 3.1(a)) has been presented. The black solid curve is below  $-10$  dB for all the expected frequency range, confirming the potentialities of the proposed full-wave approach. In Fig. 3.2(b) the normalized 2D far-field pattern on the  $xz$  plane (see Fig. 3.2(a) for the relevant coordinate system) for the monostatic antenna working in free-space configuration has been also reported. As expected, the behavior is rather omnidirectional and symmetric, as that of a cylindrical half-wavelength dipole. It is important to note that the performances of the same antenna will be heavily influenced by the presence of a dielectric interface; however, to test our numerical model in effective operation conditions, a further optimization step can be introduced to re-adapt the geometry and preserve the requested performances.

### 3.3. Simple and loaded dipoles

A simple antenna that could be theoretically considered to radiate an electromagnetic pulse into a dielectric half-space is, of course, a cylindrical half-wavelength dipole. As is well-known, it is made by a metallic cylinder whose radius is much more smaller than the operating wavelength; it can be fed at the center through ideal gap source, as shown in Fig. 3.3(a). Even though the geometry is simple and easy to design, it belongs to the family of the resonant antenna showing a rather narrow bandwidth behavior. In particular, in Fig. 3.3(b) the return loss has been reported for a dipole having length  $l = 15$  cm (thus resonant around  $\approx 1$  GHz) inside a bandwidth ranging from 0.5 GHz up to 1.5

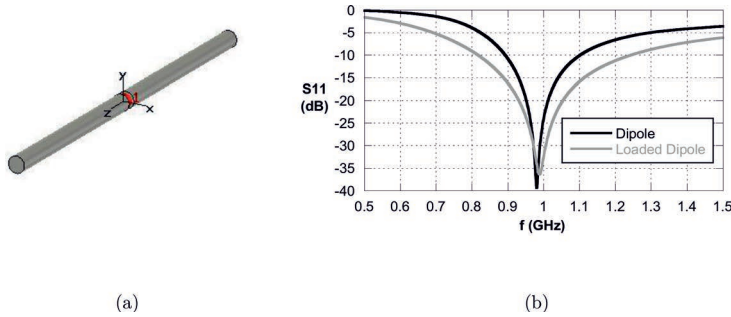


**Fig. 3.3.** (a) Numerical model of a cylindrical half-wavelength dipoles. (b) Impedance matching inside the considered operation bandwidth; the  $S_{11}$  of a simple dipole is compared with one loaded by means of a Wu-King profile.

GHz. As expected, a quite narrow fractional bandwidth, equal to about 20%, has been obtained.

The most effective way to produce wider operational bandwidth with this kind of antennas requires the implementation of a load profile along the dipole's arms. From a theoretical viewpoint, the electric currents, excited thanks to a voltage gap, propagates along the metalization up to the discontinuities, where they are partially reflected: this phenomenon is continuously repeated as far as the current completely lapses going to zero. Even though most of the input energy is radiated in the free space, this behavior produces a prolonged time signal and consequently a narrower bandwidth for the radiated pulse. However, by introducing a resistively load profile along the dipole's arm, the flowing currents can be progressively dissipated along its path toward the end of the metalization, where it can assume very low values (ideally zero). Namely, if no currents reach the end of the dipole's arm the reflected signal cannot be excited and the pulse remains shorter in time.

By starting from Maxwell's equations, as demonstrated for the first time in [45], the optimum profile for the current flowing on a cylindrical dipole of length  $L$  is given by the following equation

$$I(z) = C(L - |z|)e^{-jk_0|z|}. \quad (3.1)$$

This represents a current traveling in the direction of increasing  $|z|$ , that is, from the generator towards both the ends of the two arms. By suitably elaborating this equation it is possible to evaluate the relevant

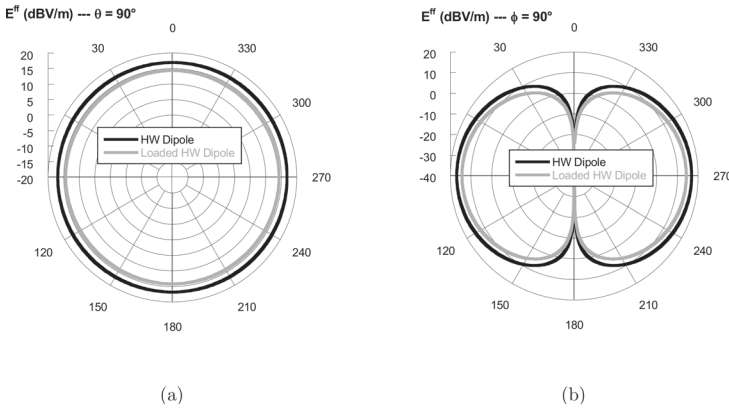


**Fig. 3.4.** Radiative features of the considered half-wavelength dipoles. (a) Two-dimensional far field pattern on the  $xy$  plane ( $\theta = 90^\circ$ ), (b) Two-dimensional far field pattern on the  $yz$  plane ( $\phi = 90^\circ$ ).

resistive profile implementable on the considered antenna. In particular, for a half-wavelength structure whose profile is discretized with  $N$  total resistors, we get this equation to express the value of the  $n$ -th resistive load

$$R(n) = \frac{L}{2A\sigma_0} \frac{\log[(L-2)(n-1)\Delta]}{L-2n\Delta} \quad (3.2)$$

being  $\sigma_0$  the conductivity of the metal,  $A$  the cross-section of the radiating arms and  $\Delta$  the size of the discretization step. In Fig. 3.3(b) the return loss obtained by implementing the Wu-King profile along the virtual model of the considered dipole has been reported. A comparison with that generated by a simple non-loaded structure demonstrates the improvement achievable in term of fractional bandwidth, that is grown here from 20% to nearly 40%. In Fig. 3.4 a comparison for the far-field pattern in two principal planes for our dipoles is also reported. As expected, the angular dependence of the radiated field is not affected by the resistive profile, but a lower intensity patterns has been obtained for the loaded structure. Indeed, the presence of shunt resistances causes energy dissipation of ohmic nature, that in turn gives rise to a lower radiation efficiency.

### 3.3.1. Printed folded dipole

A folded dipole is an evolution of the half-wavelength dipole obtained by connecting its two ends with additional arms (see Fig. 3.6) [39]. It has been proposed in the past to provide a simple and effi-

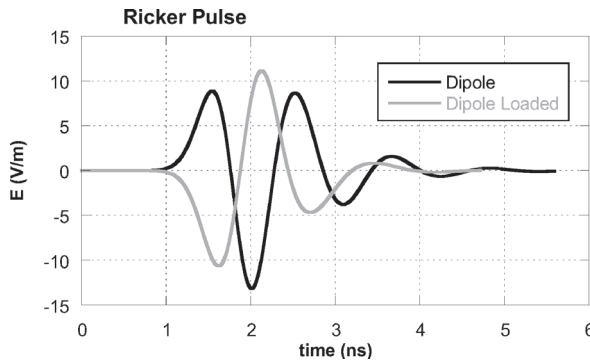


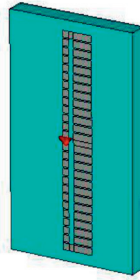
Fig. 3.5. Comparison between the Ricker pulse radiated by simple and resistively loaded dipole.



Fig. 3.6. Numerical model of a cylindrical folded dipole. One of the two arms is suitably cut to allow for the introduction of an idealized voltage gap.

cient way to widen the operational bandwidth of this class of antennas. If the additional wire has the same diameter and cross-section as the dipole, two nearly identical radiating currents are generated; the resulting far-field emission pattern is nearly identical, but at the resonance frequency its input impedance is four times the radiation resistance of a single-wired dipole. This is because for a fixed amount of power, the total radiating current is equal to twice the current in each wire. The folded dipole usually is therefore well matched to 300-Ohm balanced transmission lines. Since the bandwidth of a resonant antenna is larger for growing section of the metalization, a folded dipole has also a wider bandwidth with respect to that of a single dipole.

Very often to satisfy design constraints on weight and dimensions requested by specific applications, a cylindrical loaded folded dipole shown in Fig. 3.6 can be transformed in a printed version, as shown in Fig. 3.7. In particular, the configuration at hand has been suitably optimized to obtain an excellent impedance matching inside an operational



**Fig. 3.7.** Simulated model of a printed loaded folded dipole, optimized to obtain a very wide operational bandwidth.

bandwidth ranging from 0.6 up to 1.9 GHz. It is important to note that the width of both two arms have been suitably designed and discretized to introduce a resistive profile. Incidentally, the search of the optimum values for all the resistances constituting the profile requires a rather complex optimization scheme: for this reason an automatic procedure has been suitably developed, capable to parametrically change at each step the value of the shunt resistance constituting the loading profile. In conclusion, in Fig. 3.8 the optimized return loss has been presented,

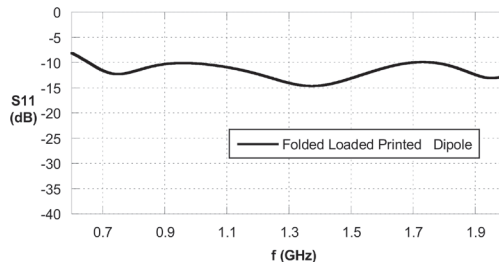


**Fig. 3.8.** Return loss of the printed loaded folded dipole shown in Fig. 3.7.

whose profile is just below the desired threshold of -10 dB, inside all the considered frequency range.

### 3.4. Bow-tie antenna

As discussed previously, by widening the section of the metalization of the considered class of antennas, one can effectively improve its impedance bandwidth. By starting from a simple printed dipole and progressively enlarging the end of its two arms, as shown in Fig. 3.9(a),

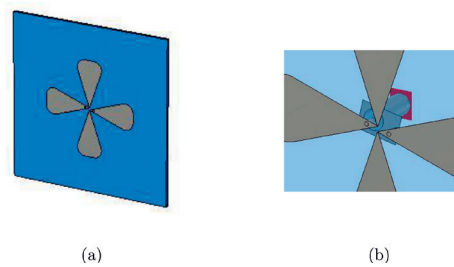


**Fig. 3.9.** Printed bow-tie antenna in dual-pol configuration. (a) Virtual model of the overall structure, (b) sketch of the coaxial cable designed to excite the proposed structure from the back.

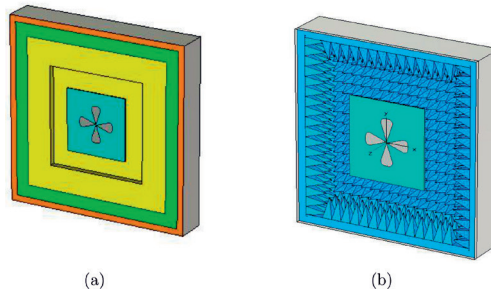


**Fig. 3.10.** Shielded dual-pol printed bow-tie antenna. (a) Shielding made by three materials having different conductivity and permittivity values, (b) shielding made by homogeneous pyramidal shape.

it is possible to obtain a so-called bow-tie antenna (dual polarized for this specific case) [39]. This type of antennas shows wider bandwidth with respect to simple printed dipole, indeed they can be also seen as the printed version of a biconical antennas [39], that is a broad-band antenna made of two roughly conical metalization. Just to give an example about the excitation system for this kind of element, in Fig. 3.9(b) a coaxial cable suitably designed on our CAD tool has been highlighted.

### 3.5. Printed Vivaldi antenna

As discussed in the introduction of this chapter, the main scientific objectives of the planned ExoMars mission are to search for evidence of past and present life on Mars and to characterize the composition of its shallow subsurface. To do this, a rover equipped with a drill capable to

sample the subsurface down to a depth of approximately 2 m has been designed [46]. To obtain information about the nature of the subsurface along the rover path before drilling, a presence on board of a GPR system is highly desirable, being its main goal that to explore the first 3 m of the soil with a vertical resolution of few centimeters, in accordance with the objectives and expected capabilities of the drill. Extensive surveys will help identifying the location of sedimentary layers, where organic molecules are the most likely to be found and well preserved. As usual, the design requirements of the antenna system are driven by both scientific objectives of the experiment and accommodation issues associated with its integration on a remotely operated rover. The requisite resolution of few centimeters and a penetration depth of more than 2 m call for a frequency range of about 500 MHz–3 GHz; a fully polarimetric antenna system is also highly recommended to study depolarization effects. The two-channel GPR system needs an antenna design that takes into account two perpendicular linearly polarized transmitting antennas and two co- and cross-polar oriented antennas for reception. In addition, mass, volume, and protection requirements preclude the use of absorbing material and shielding. As a consequence, the antenna pattern of each element must be carefully focused on the ground. Ideally, the radiation pattern should be wide in the rover path direction, so that point-like reflectors are visible over relatively long distances, while the cross-path pattern should be narrow. The gain function should increase with frequency in order to compensate the frequency-dependent free-space loss encountered at higher frequencies and also to partially account for the gain functions of the electronic systems. These and other constraints like EMC requirements, as well as pattern deformation due to radiation coupling effects with the rover structure, has led to an antenna that is based on a Vivaldi configuration [47], [48]. In this section, as in the previous case, a virtual model developed on a commercial CAD tool will be described. Basically, this kind of antenna, proposed for the first time in [49], belongs to the wide family of traveling-wave antennas. In his printed version it is made by an exponentially shaped metalization placed on a thin substrate. In Fig. 3.11(a) a virtual model of a printed Vivaldi has been reported. It is designed to work inside an operational bandwidth going from 0.5 up to 3 GHz and has dimensions of about  $25 \times 20$  cm. As shown in Fig. 3.11(b) it is fed by a microstrip line having variable sections and terminated with a shaped radial stub. These degrees of freedom, together with the circular shape etched on the met-

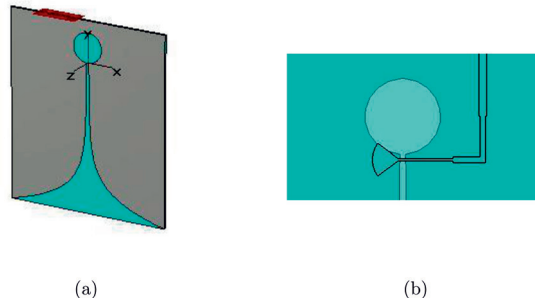


**Fig. 3.11.** Virtual model of a printed Vivaldi antenna fed with a microstrip line. (a) monostatic model radiating linear polarize fields, (b) Back view of the virtual model; a microstrip with variable section loaded with a radial stub is clearly visible.

alization have been suitably optimized to obtain an excellent impedance matching. Indeed in Fig. 3.12(a) the return loss for this antenna has been presented inside the considered frequency range: the black curve shows the result obtained for a free-space configuration, whereas the gray one shows the results for the structure further optimized to work in ground-coupled configuration, close to a medium having permittivity equal to about 3.2. In both cases an excellent performance has been obtained, confirming the potentialities offered by this kind of structure. Finally, in Fig. 3.12(b) the far-field pattern in the  $xy$  principal plane has been reported as well, showing a good directive behavior. In conclusion, in Fig. 3.13 the same antenna designed to work in dual-pol configuration is reported. It represents a prototype satisfying technical and geometrical constraints as indicated in [46]; in the next chapter it will be extensively used to produce numerical data in a virtual Martian scenario.

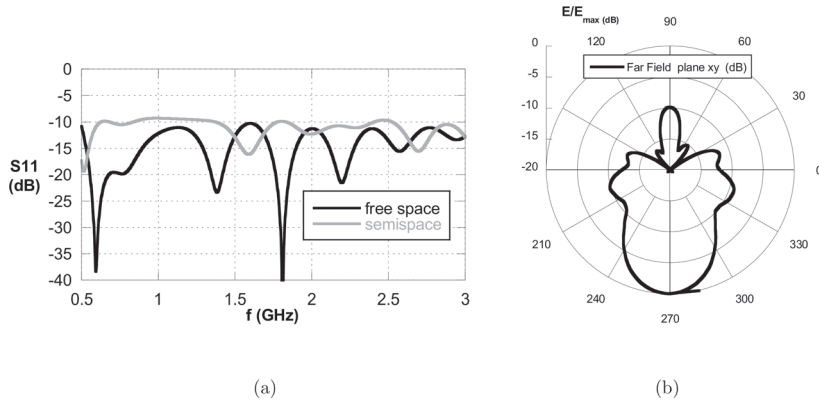


**Fig. 3.12.** (a) Impedance matching for the proposed linear polarized Vivaldi antenna. (b) Two-dimensional far field pattern for the considered antenna on the  $xy$  principal plane. Copyright © 2017, IEEE.

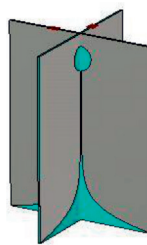


**Fig. 3.13.** Virtual model of a printed Vivaldi antenna working in dual-pol configuration. It is fed by two microstrips with variable sections suitably modified to satisfy the geometrical constraints.



## 4. Experimental and Numerical GPR Setups

### 4.1. GPR laboratory setup

A laboratory setup was exploited in order to acquire experimental GPR data to be further processed and inverted, as will be shown in the next chapters. The setup is constituted by a box made of fiberglass, having approximate dimensions  $150 \times 100 \times 30$  cm (length, width, and height, respectively), which can be filled by different background materials. In the case at hand, a mixture of glass beads was chosen as hosting material, which can be regarded as an analogue of a sandy soil [51]. The electromagnetic features of this material, which is nonmagnetic and with negligible losses, were investigated independently through a Time Domain Reflectometry (TDR) analysis [52, 53, 54].

Such an instrument allowed us to fix the relative dielectric permittivity of the glass beads equal to 3.2 [54]. Measurements were performed using the commercial GPR device 'PulseEkko Pro' manufactured by Sensors and Software Inc. [50] and equipped with a pair of dipoles antennas having a 1 GHz bandwidth around the nominal central frequency of 1 GHz. In the measurements, the GPR antenna system was moved along the length of the box at the soil smooth interface, in a multi-bistatic configuration having an offset between the Tx/Rx antennas of about 19 cm (center to center). A view of the laboratory experimental setup is given in Fig. 4.1. In Fig. 4.3 a zoom on the GPR Tx/Rx antennas placed on the ground surface is reported.

This controlled laboratory setup has been extensively used to conduct GPR surveys both on metallic and dielectric object, that can be buried at different depth from the surface. Typically these scatterers have dimensions comparable with the probing wavelength and are placed at depth

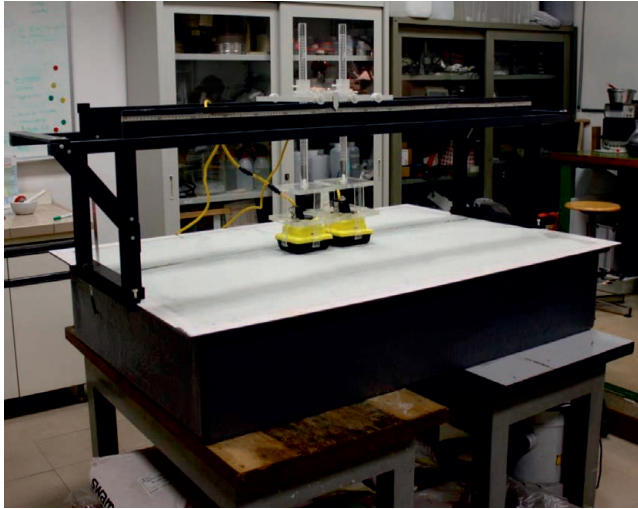


Fig. 4.1. View of the GPR laboratory experimental setup: the artificial sand box, filled with a ground medium in which scatterers are buried. Copyright © 2013, Elsevier B.V.

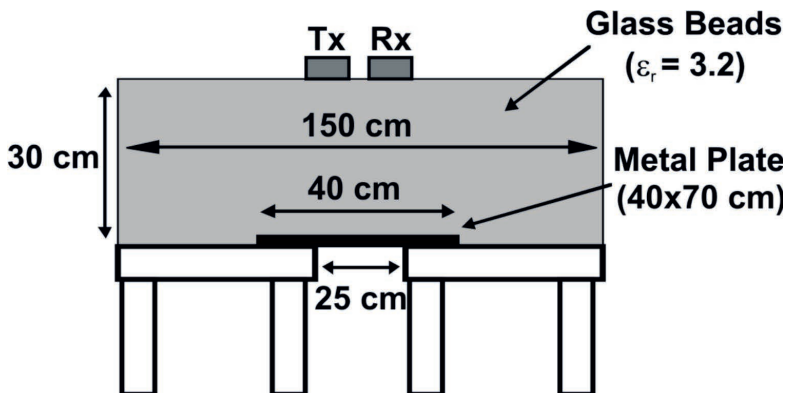
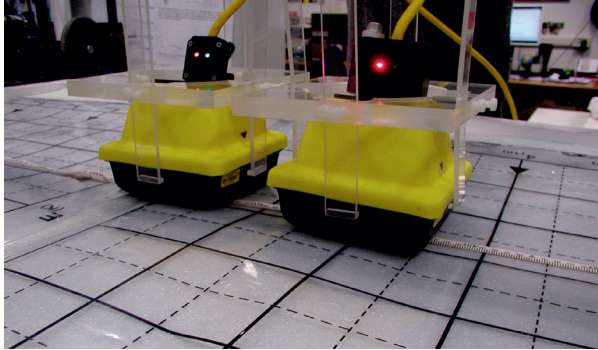


Fig. 4.2. The laboratory setup used in this work for the analysis of metallic and dielectric scatterers buried in a host medium. Side view of the setup positioned on a pair of wooden tables. The metallic plate has been inserted for calibration purposes and is removed during the measurements. Copyright © 2013, Elsevier B.V.



**Fig. 4.3.** The commercial GPR instrument with coupled Tx/Rx antennas for the measurements at the interface.

<b>Object</b>	<b>Geometry</b>
Cube	Side: 9 cm
Sphere	Radius 9 cm
Cone	Base diameter: 9 cm; height: 10 cm
Pyramid	Base: $9 \times 9$ ; height: 10 cm
Cylinder	Diameter: 5 cm; height: 10 cm
Parallelepiped	Base: $5 \times 5$ ; height: 10 cm

**Tab. 4.1.** Geometry of the objects investigated experimentally.

of 9 cm, that makes indeed the overall problem very challenging.

#### 4.1.1. Measurements on metallic objects

In order to account for the case of electromagnetic non-penetrable (metallic-type) scatterers, GPR measurements were carried out by the Author with the help of some colleagues of the Earth and Space applied physics laboratory of the ‘Rome Tre’ University on targets made of hard wood wrapped with aluminum foils. In particular, several targets having canonical geometries and size comparable in terms of the dominant probing wavelength (i.e.,  $\lambda = 30$  cm for  $f_c = 1$  GHz) were considered. The details of the tested geometries are given in Table 4.1.

The objects were located at a fixed depth from the air/sand interface, that is 9 cm with respect to the upper face or top point of the metallic targets, according to their geometry. In Fig. 4.4 a picture showing some of the probed targets on the surface of our glass beads has been reported;

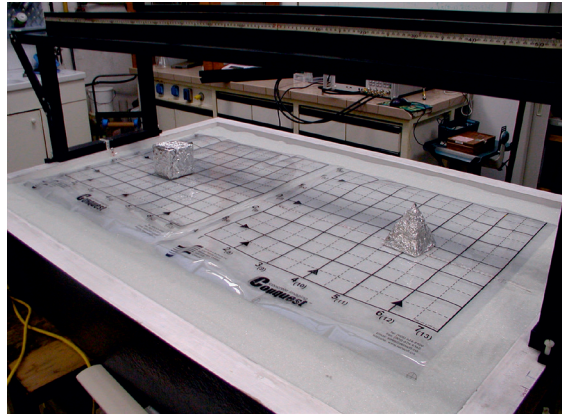
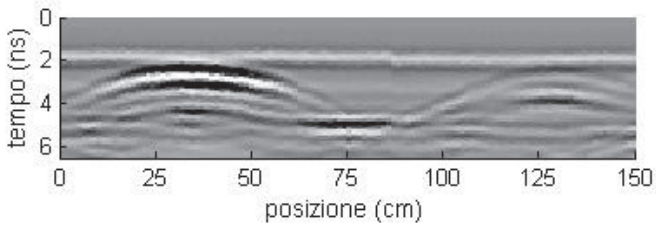


Fig. 4.4. Experimental setup showing metallic targets in the position where they are buried.

in particular the cube was located on the left of the major length of the box and a square-based pyramid was on the right side at a distance of about 80 cm. The row GPR outcomes are given under the usual form of radar B-scan sections or 'radargrams' [42]. These are generated here by transmitting a Gaussian-type pulse from each position along the survey line and collecting the signal scattered by the buried objects from the receiving antenna.

As an example, Fig. 4.5 shows a measured radargram: the effects of different wave contributions appear according to well-established classifications (i.e., direct and reflect waves) [42, 43]. In particular, the first received event is a 'direct wave', which travels straightforwardly from Tx towards Rx antenna. This effect is partly limited by the shielding and by the directional features of the radiators and, when the background has rather homogeneous characteristics, as in the case at hand, it can be dropped out from the output data, with the so-called 'background removal' procedure [42, 43]. Such a processing step gives rise to a cleaner pattern mainly focused on the scattering contributions arising from the buried targets. Further, the roughly hyperbolic events visible in the radargram of Fig. 4.5 are produced by the main 'scattered wave' and clearly emphasize the presence of the buried objects. It is worth noting a lighter and slightly delayed hyperbolic event for the pyramid, if compared to the cube response, which is related to the lower scattering cross section of the tip wedge with respect to a flat side. Additional backscattered contributions appearing in Fig. 4.5 can be associated to the



**Fig. 4.5.** Example of a measured GPR radargram in the sand box. The radar signatures are due to different metallic buried scatterers placed along the major length of the box: a cube (on the left) and a pyramid (on the right). Details on the physical parameters chosen are provided in the main text. Copyright ©2013, reproduced courtesy of The Electromagnetics Academy.

bottom interface of the sand box. In particular, being the box located on two lateral wooden tables and air-suspended in its central part (see Fig. 4.2, where a metal plate has been inserted only for preliminary measurements), the reflection effect is particularly visible in the central region due to the strong dielectric contrast occurring between sand and air. The measured radargrams are available for all the canonic targets reported in Tab. 4.1, however for sake of brevity only the most significant results have been described here; they will be reconsidered in the part III of this work, where an imaging procedure will be introduced and applied to GPR numerical and experimental data.

#### 4.1.2. Measurements on dielectric objects

Metallic objects are non-penetrable by the electromagnetic radiation and generate a very strong backscattered signals; this means that they are relatively easily detectable and can be considered as limit case with respect to typical dielectric scattered buried in natural scenarios. Indeed, with regard to planetary exploration, very often the main goal of a GPR system consists in detecting and localizing dielectric hidden targets or interfaces; consequently, it is essential to refer to the contrast between the permittivity of the background medium with respect to that of the buried scatterer. Since this part of the present thesis aims at characterizing performances of a GPR in a Martian scenario, we will consider in the following some measurements developed by colleagues of the Earth and Space applied physics laboratory of the 'Rome Tre' University on basalt rocks (relative dielectric constant  $\epsilon_r = 6.7$ ) with dimension comparable to the probing wavelengths, buried in the shallow region of a subsoil with permittivity of  $\epsilon_r = 3.2$ , that, as outlined in the previous section,

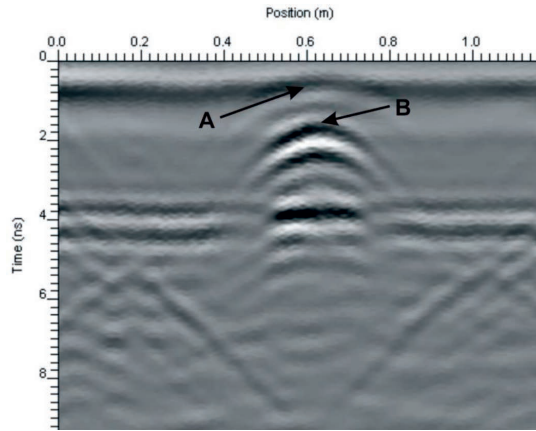


**Fig. 4.6.** Measured radar cross sections for a basalt block buried at 5 cm in the sand box, obtained with the PulseEKKO Pro GPR. The vertical axis indicates the two-way travel time (ns), and the horizontal axis shows the position (m) along the longitudinal profile of the box. Copyright © 2013, Elsevier B.V.

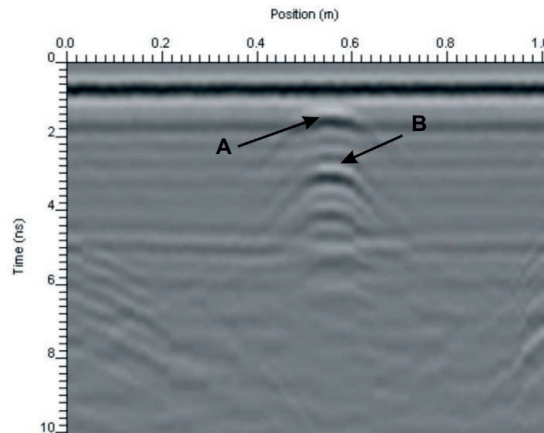


**Fig. 4.7.** Measured radar cross sections for a basalt block buried at 5 cm in the sand box, obtained with the Noggin GPR. The vertical axis indicates the two-way travel time (ns), and the horizontal axis shows the position (m) along the longitudinal profile of the box. Since the Tx/Rx antenna separation and size are different for the two GPRs, the target position (m) with respect to Fig. 4.17 does not coincide. Copyright © 2013, Elsevier B.V.

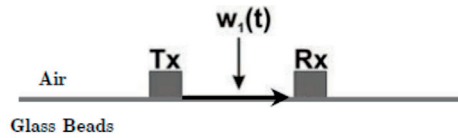


Fig. 4.8. Wave propagating along the direct path between transmitting and receiving antenna on the interface between air and glass beads.

represents an analogue of a region of the Martian sandy soil. Specifically, attention was devoted here to finite-size three-dimensional dielectric targets: the basalt block of quasi-regular shape (with a flat upper face of about  $12 \times 9$  cm and a thickness of about 8 cm) was buried in the center of the box (see Fig. 4.1) at three different depths, i.e., with the top of the rock at 5, 10, and 20 cm from the air/sand interface. For each rock position, a 2D radar cross section was acquired with a step size of 1 cm along the major axis of the dielectric box through two different commercial GPRs, namely the PulseEKKO Pro and the Noggin systems [50], choosing a time window equal to 30 ns and a stacking of 4. The relevant results for a depth  $d = 5$  cm from the surface are shown in Fig. 4.6 and 4.7 for the PulseEKKO pro and Noggin Systems, respectively. Both these GPRs are manufactured by Sensors & Software, Inc., working at central frequency of 1 GHz. Two well-separated hyperbolic events are clearly visible now as the dielectric object is penetrable: the first one is related to the top face of the basalt rock, while the second one is generated from the bottom face, after that the radiation has propagated inside the object with a different velocity. It is worth noting that the configuration under analysis is quite challenging: our rock is buried in the near-field region of the considered antenna and its dimension is comparable with the dominant wavelength of the transmitted pulse ( $\lambda = 30$  cm). In addition, both systems have a small offset (with respect to  $\lambda$ ): for these reason the air-ground wave interference results quite strong. Indeed, in Fig. 4.6 and 4.7 the scattered hyperbola is overlapping with the direct wave ( $w_1(t)$  in the schematic view of Fig. 4.8), making the depth estimation procedure quite involved. In the next section, by starting from this measured radargrams, the capability to estimate the depth of these shallow targets will be investigated.

## 4.2. Depth estimation of shallow targets

In various important applications, GPR instruments are demanded to operate in particularly challenging conditions, e.g., for the detection of variously sized and shaped buried rocks in the shallow planetary subsurface, with close Tx/Rx antennas placed at the soil interface (as for the mentioned ESA 'ExoMars' mission, having a GPR on board an on-site rover). In such cases, this instrument should be able to properly locate scatterers at depths where the usual far-field operation could no longer be fulfilled and the relevant performance heavily depends on various physical parameters. Based on proper processing of the measured radargrams described in the previous section, the depth of shallow subsurface rocky blocks in a sandy soil has been estimated in connection with different GPR features. The validity of the results has been checked with suitable reference data provided by the Earth and Space applied physics laboratory group, taking into account various critical setup parameters (host medium features, geometrical and physical characteristics of the inclusions, GPR operating wavelengths, antenna separation, etc.). Helpful and reliable criteria can be achieved for proper design of such type of instruments in future planetary missions.

The main purpose of our analysis here has been focused on the evaluation of the accuracy limits in predicting the depth of basaltic blocks in connection with different GPR systems, particularly in the case of rather superficial rocks. To this aim, the basaltic block considered in the previous section (roughly cubic with 10-cm side and  $\epsilon_r = 6.7$ ) has been buried at different depths  $d$  from the surface (see section 4.1.2 for further details). Based on the output of the received signals, the depth of the top of the rock has been estimated, for both GPR systems, by suitably evaluating the time delay  $\tau_{GPR}$  between the direct wave (straight traveling from Tx to Rx antenna at velocity  $v_{dw}$ ,  $w_1(t)$  in Fig. 4.9) and the reflected wave (going from Tx to the scatterer and back to Rx at velocity in the host medium  $v_h$ ,  $w_2(t)$  in Fig. 4.9). By following elementary geometric considerations, the estimated distance  $d_{est}$  can be expressed as

$$d_{est} = \frac{1}{2} \sqrt{\left(\tau_{GPR} + \frac{s}{v_{dv}}\right)^2 + v_h^2 - s^2}. \quad (4.1)$$

These values have then been tested through comparisons with ad-hoc reference results made available by our colleagues, estimated by combining a-priori information on the physical location of the rock and on

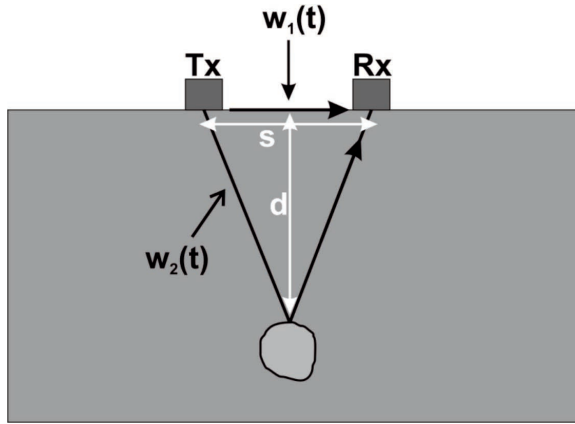


**Fig. 4.9.** Possible paths of the electromagnetic signal in a schematized GPR scenario. Copyright © 2013, Elsevier B.V.

Actual Depth (cm)	$\tau_{TDR}$ (ns)	$\tau_{GPR}$ (ns)	$d_{est}$ (cm)
$5 \pm 2$	$0.6 \pm 0.1$	$0.6 \pm 0.1$	$5 \pm 0.1$
$10 \pm 2$	$1.0 \pm 0.1$	$1.0 \pm 0.1$	$10 \pm 0.2$
$20 \pm 2$	$2.0 \pm 0.2$	$2.0 \pm 0.1$	$20 \pm 1$

**Tab. 4.2.** Comparisons between theoretically predicted (TDR-based) and experimental values of time delays to evaluate different depths of a basalt block in a sandy soil with the PulseEkko Pro GPR commercial systems (offset between Tx and Rx antenna equal to 19 cm).

the wave velocity in the host material already calculated with TDR (the travel time  $\tau_{TDR}$  is in this case calculated through the minimum path of reflected wave from Tx to Rx antenna). The results of this analysis are summarized in Tab. 4.2 and 4.3, where we present comparisons between the actual and the estimated depths of the scatterer evaluated by means of the two GPR instruments. Both radars show good accuracy (within the uncertainties deriving from the error linear propagation formula [55]). The slight systematic overestimation of Noggin values is related to the presence of a sled in the antenna case.

Among various interesting aspects, attention has to be paid to the resolution limits of the measurements as the scatterer becomes closer to the surface (thus buried in the near field region of the considered antenna), since in these cases the rock could not properly intersect the bistatic ‘footprint radius’ [57], which depends in a rather complex

Actual Depth (cm)	$\tau_{TDR}$ (ns)	$\tau_{GPR}$ (ns)	$d_{est}$ (cm)
$5 \pm 2$	$0.5 \pm 0.1$	$0.7 \pm 0.1$	$7 \pm 1$
$10 \pm 2$	$1.0 \pm 0.1$	$1.3 \pm 0.1$	$12 \pm 2$
$20 \pm 2$	$2.2 \pm 0.2$	$2.4 \pm 0.1$	$22 \pm 1$

**Tab. 4.3.** Comparisons between theoretically-predicted (TDR-based) and experimental values of time delays to evaluate different depths of a basalt block in a sandy soil with the Noggin GPR commercial systems (offset between Tx and Rx antenna equal to 7 cm).

way on the other physical and geometrical parameters of the setup (operating wavelengths, antenna features, shielding and separation of the instrument from one side, dimensions and depth of the target from the other). It is seen that in these cases the usual far-field patterns of the antennas are no longer met and the detection could occur in general near-field conditions. For these reasons, a theoretical investigation of these involved behaviors based on rigorous full-wave simulated tests allows us to make clear important criticalities in the GPR operation, as will be addressed in the next sections.

### 4.3. Customized numerical setup

In order to provide further reference GPR data useful for testing performances GPR systems and to produce a wide set of data to test conventional and advanced inversion procedures, the scattering problem widely discussed in the previous sections was simulated by taking advantage of a flexible numerical setup. In particular, the commercial electromagnetic time-domain CAD tool ‘CST Microwave Studio’ [56] was used to simulate scenarios similar to the laboratory setup described and discussed in the previous sections. This software allow us to carry out efficient and reliable full-wave numerical solutions of the considered scenario to accurately study and analyze features and performances of the proposed ground-coupled antennas. In addition, the involved phenomena characterizing the electromagnetic propagation of different waves detected by the receiving antenna of a GPR can be analyzed with flexible parameterization. As the simplest configuration, an environment made of a two layers was considered. The first one is made by air, while the second one is given by a dielectric material representing the hosting soil used in the experiments. Accordingly, such a material is non-magnetic, lossless and has a relative dielectric permittivity equal to

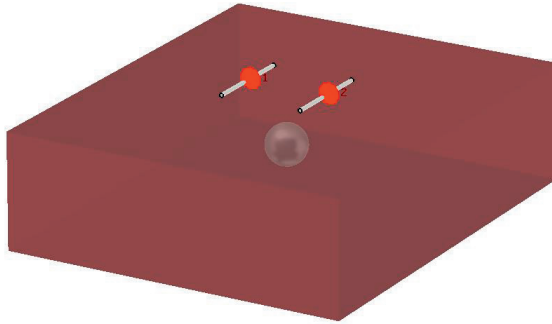


**Fig. 4.10.** GPR Numerical setup designed on CST made by two half-wavelength dipoles fed by a gap-voltage and placed at the interface between the air and dielectric medium. A metallic sphere has been also inserted representing a possible buried object to detect, locate and reconstruct.

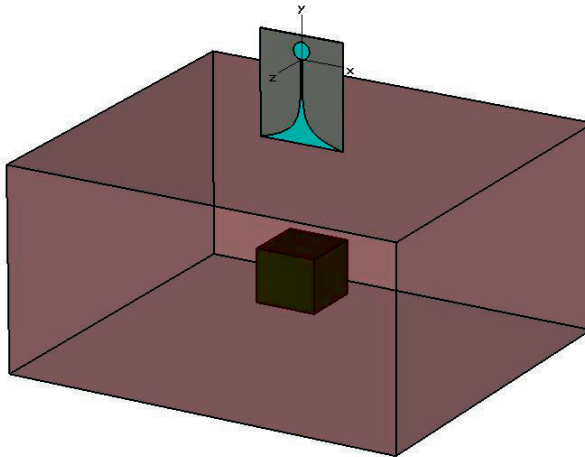


**Fig. 4.11.** GPR Numerical setup designed with CST made by a printed Vivaldi antenna fed by a waveguide port and placed at the interface between the air and dielectric medium. A basalt cube has been also inserted representing analogue to those considered during the measurement campaign.

3.2. Moreover, since the irregularities of the sandy interface occurring in the experimental setup are small with respect to the wavelengths of the probing signals and considering that the smooth surface is flattened by the GPR movements, a flat air/sand interface was simulated.

In this environment, perfect electric conductor (PEC) or dielectric objects can be inserted in locations similar to those considered during the experiments (about 10 cm deep from the interface). The overall dimensions of the simulated region are 80 cm length, and 50 cm in width and depth. The region is discretized by means of a hexahedral mesh, whose elements have size less than  $\lambda/15$ ,  $\lambda$  being the smaller wavelength in the considered frequency range (that is dependent by the considered antenna). Perfect-matched-layer (PML) boundary conditions have been imposed on the side walls and the bottom of the simulated environment, leading to an ideal absence of reflections (homogeneous half-spaces). This choice allowed us to efficiently reduce the dimensions of the simulation region and also to focus our attention exclusively on the scattering effects of the buried targets. Therefore, the simulations differ a bit from the experiments, which take also into account the reflection from the bottom of the box. It is anyway worth noting that the simulation tool gives the possibility of considering several and complex scenarios with affordable computational efforts. The Tx/Rx antennas are usually placed on the soil surface, sweeping along the longer planar direction with step of 3 cm in a bistatic configuration having a fixed offset of 19 cm, i.e., the same as for the PulseEkko Pro system occurring in the laboratory measurements. The simulated setup is exemplified in Fig. 4.10, and Fig. 4.11 gives a view of the numerical environment including dielectrics, scatterers, and two different antenna system; Fig. 4.12 shows a typical simulated waveform of the GPR transmitted signal. At each position on the surface, the Tx antenna radiates a pulse and at the output port of the Rx antenna a signal, including the back-scattered wave from the objects, is gathered. Thus, a gray-scale 2D 'simulated radargram' for the investigated domain can be generated. Suitable signal processing is anyway needed to properly emphasize the scattering effects. In particular, as said, the time-domain output signal is generally made by a first contribution guided by the soil/air interface along the linear path between Tx and Rx antennas. This 'undesired signal' (direct wave) is followed at a later time by the 'useful signal' (scattered wave) from the buried target. Under the described assumptions, the direct wave can be considered as the same for any position along the observation

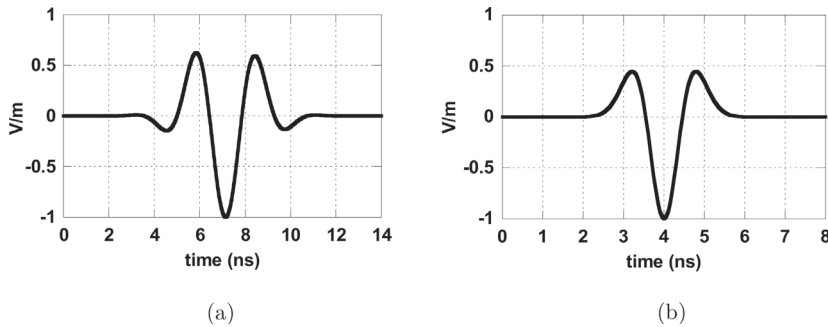


Fig. 4.12. Simulated waveforms of the GPR transmitted signal: (a) Modulated Gaussian Pulse, (b) Ricker pulse, i.e. second derivative of a baseband Gaussian pulse.

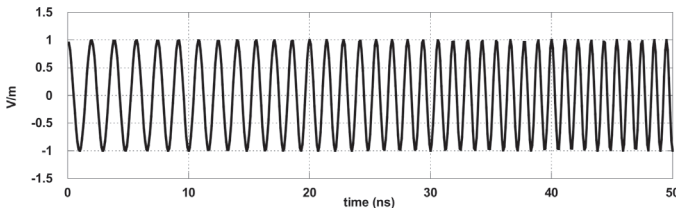
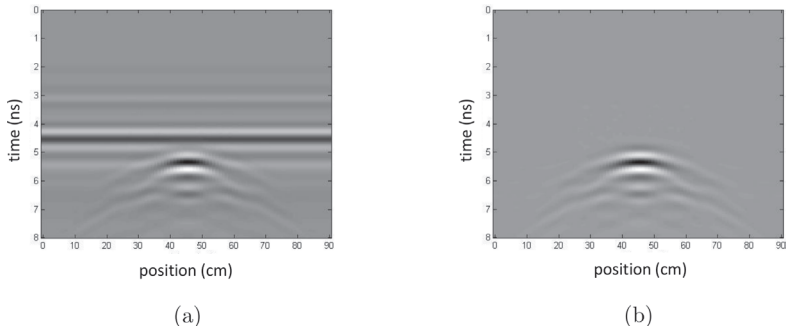
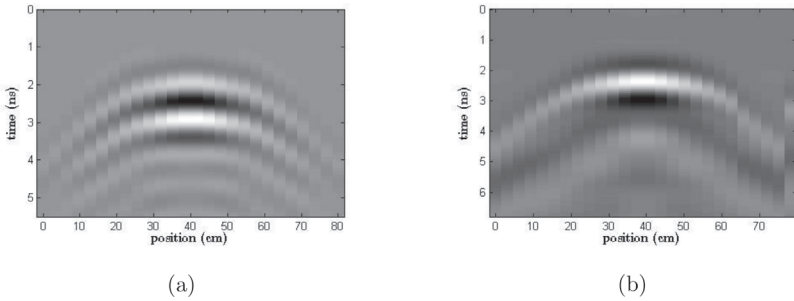


Fig. 4.13. Time-domain representation of a truncated chirp pulse.

domain and can be evaluated numerically with a suitable simulation of the Tx/Rx GPR signal performed in the absence of any scattering object. Then, to improve the detectability of the targets by emphasizing the relevant scattering contributions with respect to undesired signals, the direct wave has been subtracted numerically from each collected trace. An example of a simulated radargram, generated according to the numerical procedure described above, is shown in Fig. 4.14 for a buried PEC cube with 9-cm side, illuminated with the Vivaldi antenna shown in Fig. 4.11 and presented in section ???. Specifically, in Fig. 4.14(a) the result obtained before the background removal is shown. The direct wave is here particularly strong, due to the limited shielding between Tx/Rx antennas in the implementation. The wave scattered by the target produces, indeed, approximately hyperbolic curves partially masked by the direct wave. In Fig. 4.14(b), the radargram after the background removal is given. In this figure, only the scattered echo from the cube is present and the top of the diffraction curve is now clearly visible. It is seen that the echoes from the lateral sides of the block are weaker than the echoes from its top. This is an expected outcome, being the scattering from the top of the cube mainly due to strong reflection by a flat



**Fig. 4.14.** GPR radargrams obtained with the simulation setup: (a) complete pattern for a buried PEC cube including direct and reflected waves; (b) pattern for the scattered field after background removal.



**Fig. 4.15.** Numerical radargram obtained with our customized setup with two alternative input waveforms after the operation of background removal. (a) Gaussian modulated pulse, (b) Ricker Pulse.

interface, while the scattering from the side walls is related to diffracted fields spread over wider angles. Again to compare the scattering event generated by considering alternative input waveforms, in Fig. 4.15 two numerical radargrams obtained illuminating the buried object with a bistatic monopole antenna, as that describe in section 3.2, have been reported. In particular, in Fig. 4.15(a) and 4.15(b) the GPR outcomes obtained respectively with a Gaussian and a Ricker pulse for a PEC cube buried again at 9 cm from the surface have been shown. As expected, the shapes of the scattered hyperbolas are clearly different: as a general comment it is possible to state that a slightly better range resolution for the Ricker waveform, due to a reduced number of oscillation of the time-domain radiated waveform, in turns related to different spectral content of the two signals, has been obtained. In conclusion in Fig. 4.16 results produced by putting as input waveform a time-domain chirp

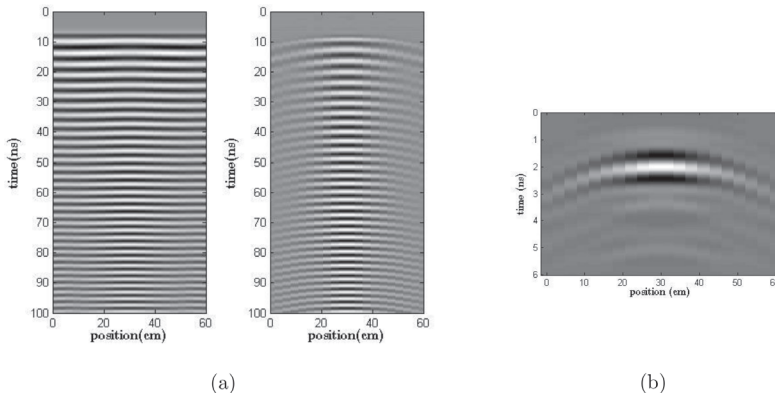


**Fig. 4.16.** Numerical radargram obtained with our customized setup with a time domain chirp signal as input waveform after the operation of background removal; (a) chirp signal before compression, (b) hyperbolic event produce by a chirp signal after a matched filtering operation.

signal (pulse compression rate equal to 100) is reported. A comparison of Fig. 4.16(a), representing the signal after the operation of pulse compression (i.e., processed through a matched filter), with Fig 4.15 allowing to identify an improved resolution obtained with the chirp pulse, that anyway introduces noticeable complications of the involved electronic systems.

#### 4.4. Depth estimation on the numerical data

The experimental results on the GPR detectability of shallow inclusions were also compared to simulated results derived with our numerical setup, that has shown to be particularly suitable for solving electromagnetic problems modeling GPR scenario. Here the implementation was extended in order to simulate the operation of the commercial GPR antenna systems introduced in the previous sections, considering in particular dissimilar mutual Tx/Rx spacing and also different signal waveforms. The simulations were specified for the same host medium (electromagnetic model of silica glass beads) with schematized included blocks (electromagnetic model of basalt), at variable depths. Even though the CAD implementation allows us to suitably account also for both ohmic and dispersion features of the media, in the operating frequency range under consideration it is seen that the overall performance is not sensitively affected. As already shown in the previous section, the simulated numerical results for the scattering problems can be given in

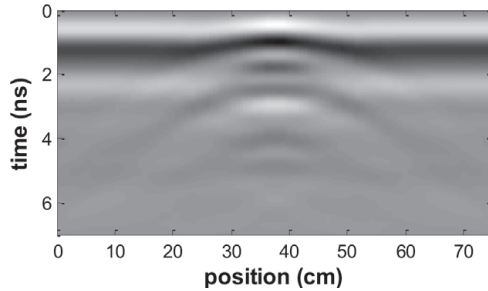


**Fig. 4.17.** Numerical radar cross sections for a basalt block buried at 5 cm in the sand box. The vertical axis indicates the two-way travel time (ns), and the horizontal axis shows the position (cm) along the longitudinal profile of the box. The antenna features are the same of the PulseEkko Pro, in the absence of reflections from the boundaries of the box; the reference starting time in the plots of this simulated results is set as that of the experimental measurements of Fig. 4.6.

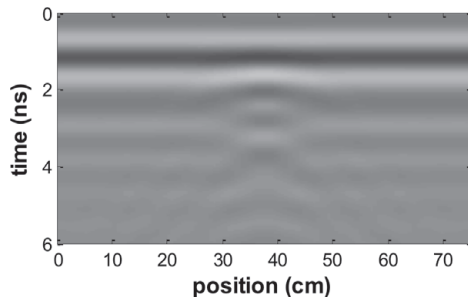


**Fig. 4.18.** Numerical radar cross sections for a basalt block buried at 5 cm in the sand box. The antenna features are the same of the Noggin, in the absence of reflections from the boundaries of the box; the reference starting time in the plots of this simulated results is set as that of the experimental measurements of Fig. 4.7.

the form of radar sections by plotting the collected time signal on a gray scale.

In particular, Fig. 4.17 shows synthetic cross sections in the same scattering conditions as presented in Fig. 4.6 (buried basalt block in the air/glass-bead environment), for a GPR systems simulating the PulseEkko device. In addition, the cross sections shown in Fig. 4.18 represent those obtained by the virtual model of the Noggin instruments. Both numerical radargrams have been evaluated focusing the simulation on the effect due to the buried scatterer only (i.e., perfect matching conditions are considered on the region boundaries). An even more 'realistic' comparison is shown in Fig. 4.19, where the synthetic cross section (for the PulseEkko case) takes also into account the reflections

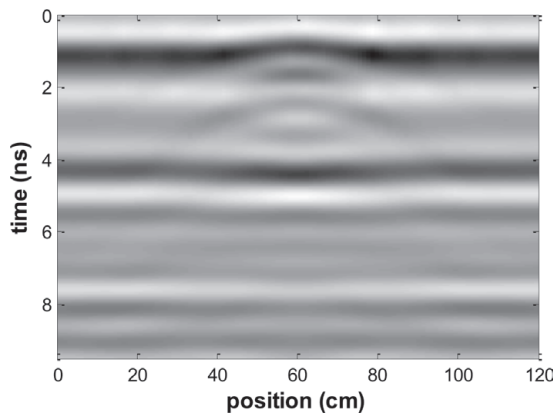


**Fig. 4.19.** Numerical radar cross sections in more realistic condition for a basalt block. The antenna features are the same of the PulseEkko Pro; the reference starting time in the plots of this simulated result is set as that of the experimental measurements of Fig. 4.6. Copyright © 2013, Elsevier B.V.

due to the discontinuities caused by the bottom and the lateral walls of the filled box (assuming an outside air region). The effect of the echo from the bottom is now evident. It is noted that, in the numerical results, the amplitude of the reflected wave with respect to the direct one can be different from what measured, since the shielding and coupling characteristics of the simulated and of the real antennas are quite different. This aspect will be commented further in connection with the next results focused on the single signal traces. Nonetheless, the simulated events match quite well the measured ones in terms of shape and location of the various reflections, emphasizing also some expected discrepancies related to the two different GPR systems as regards the signal waveforms.

To make clearer the role of the direct and reflected waves for the revealed waveform, it is useful to explore the single traces of the signal acquired by the receiver as a function of time. An example of simulation, for a fixed central position of the GPR antenna, is given in the following for the cases under analysis. The received signals (voltage vs. time) for the simulated Noggin GPR system are presented for different depths of the considered basalt block in the sandy soil, buried at 10 cm and 5 cm in Fig. 4.20 and 4.21, respectively. Note that, due to the lack of precise information on the features of the real GPR antennas (radiation patterns, mutual coupling, shielding, etc.), the wave contributions in the simulations have been properly tuned by imposing the ratio of the

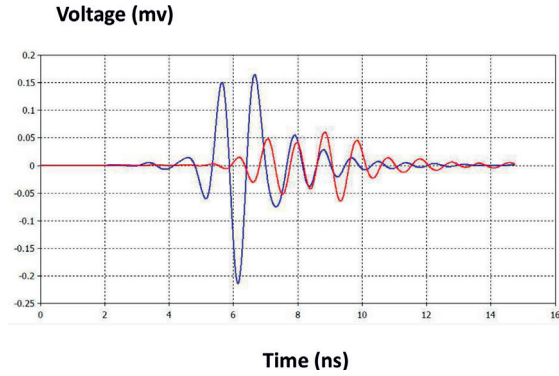


**Fig. 4.20.** Simulated traces of the received voltage signals vs. time for a GPR configuration similar to Noggin, with the basalt block buried at a depths  $d = 10$  cm (direct wave: blue curve; reflected wave: red curve). Copyright © 2013, Elsevier B.V.

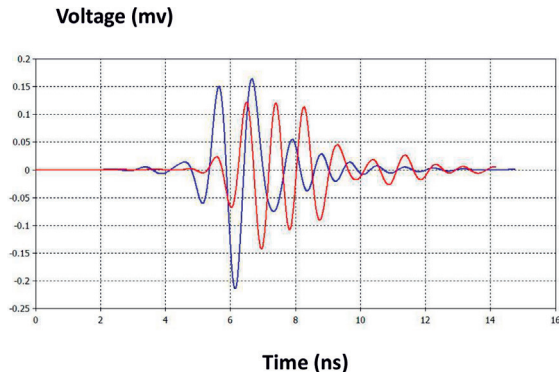


**Fig. 4.21.** Simulated traces of the received voltage signals vs. time for a GPR configuration similar to Noggin, with the basalt block buried at a depth  $d = 5$  cm (direct wave: blue curve; reflected wave: red curve). Copyright © 2013, Elsevier B.V.

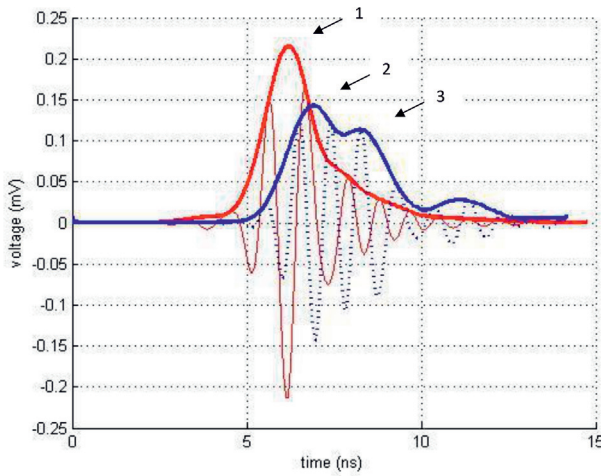


**Fig. 4.22.** Simulated traces of the received voltage signals vs. time for a GPR configuration similar to Noggin, with the basalt block buried at  $d = 5$  cm: patterns of the signal envelopes of the direct (blue curve) and scattered (red curve) waves, emphasizing through the relevant peak positions (arrows 1, 2, and 3) the possibility of correct evaluation of both location and height of the target. Copyright © 2013, Elsevier B.V.

reflected to the direct wave equal to the one observed in the relevant experimental data. From these numerical results, it is seen that, as the target depth becomes lower, the reflected wave tends to be more superimposed to the direct wave, but anyway distinguishable.

Fig. 4.22 considers again the minimal depth of 5 cm, showing the behavior of the envelopes of the signals: in this way it can be straightforwardly calculated the time delay between the peak of the direct wave and the first peak of the scattered wave (see arrows 1 and 2 in Fig. 4.22), the latter corresponding to the first maximum reflection due to the upper side of the block. It is found a very good agreement between this simulated time delay and the one effectively measured with Noggin GPR ( $\tau_{GPR}$ ), which are actually the same (0.7 ns). This gives rise to a possible alternative numerical evaluation of the depth of the scatterer, that comes out equal to 7 cm from the simulation (to be compared with the analogous  $d_{est} = 7 \pm 1$  cm from measurement and  $d = 5 \pm 2$  cm from theory, as results from Tab. 4.3). For other target depths ( $d = 10$  and  $d = 20$  cm) the matching between simulated and experimental time delay remains still very good. Moreover, the envelope form of the scattered contribution of Fig. 4.22 allows us to give an independent evaluation also of the height of the target, by calculating the time delay  $\Delta t$

between its first and second peak (see arrows 2 and 3 in Fig.4.22), which is linked to the backscattering of the upper and lower walls of the basalt block (see also the experimental counterpart in Fig. 4.7). From this calculation ( $\Delta t = 1.31$  ns from simulation and  $\Delta t = 1.38$  ns from measurement), the numerical evaluation of the height of the block comes out equal to 7.6 cm, to be compared to the experimental one,  $9 \pm 2$  cm, and to the already-established theoretical value,  $8 \pm 2$  cm 4.3. An overall excellent agreement of the results is found from measurements compared to theory and simulations as well. It should be noted, for these last results, that the clear identification of peaks in the numerical traces is easily possible due to absence of significant environmental distortion and noisy effects in the simulated results. It would be a more critical procedure if applied to the experimental data discussed previously, where the estimation through the proposed cross-correlation approach can lead to more robust and accurate results. Nevertheless, for ‘noisy’ cases, it is easily possible to apply the same cross-correlation procedure to simulated data as well.

#### 4.5. Numerical setup for 3D surveys

In order to have a wide set of 3D data to be efficiently processed for imaging purposes, the ‘forward’ scattering problem is analyzed by suitable extending our numerical implementation on the time-domain CAD tool. Once again this software enables us to explore different realistic complex GPR scenarios with affordable computational efforts and excellent accuracy. The investigated domain consists again of two half-spaces media separated by a flat interface, representing an air/soil environment, in which various types of scatterers can be buried. The GPR system can be simulated with various types of antennas both in bistatic and in monostatic configurations, as already discussed in section 4.3. In order to keep the GPR system as simple as possible in the analysis of the imaging performance, in the present study a monostatic configuration is chosen, with the antenna placed at the interface between air and ground (a wide-band printed monopole antenna, already described in section 3.2). The numerical GPR environment under analysis is shown in the 3-D view in Fig. 4.23.

The antenna scanning domain at the interface is sketched in the top view of Fig. 4.24, with the numbering of the scanning lines, the grid points for gathering synthetic data, and the proper coordinate

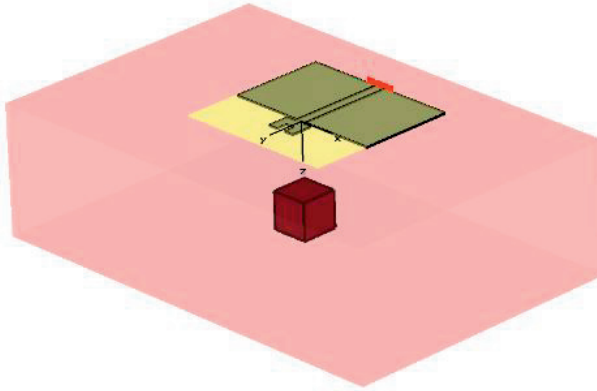


**Fig. 4.23.** The basic GPR setup analyzed by means of the CAD tool for the forward scattering problem: 3-D view of the simulation environment, including a wide-band printed monopole antenna placed on the air/ground interface and a buried scatterer. Copyright © 2013, Hindawi Publishing Corporation, <https://doi.org/10.1155/2013/610389>.

system. In accordance with the specifics of a GPR instrument such as the PulseEkko Pro [50], the simulated system is fed with an input Gaussian-like signal having a spectrum between 0.5 and 1.5 GHz, generated as the modulation of a pulse through a 1 GHz sinusoid: this waveform is shown by the time-domain trace of Fig. 4.25(a), with the relevant frequency spectrum of Fig. 4.25(b). The matching characteristics of the antenna in the considered operational range are summarized once again through the return loss (RL), i.e., the magnitude of the antenna scattering reflection coefficient in dB, vs. frequency  $f$ . It is seen from Fig. 4.26 that the RL curve for our antenna in realistic operating conditions (i.e., located at the interface of the air/ground external environment) lies in the range of interest well below the typical matching threshold of -10 dB, as desired. The far-field radiative features of the antenna, again operating in the air/ground environment, are described by means of the radiation patterns, as already done in section 3.2 for the antenna working in free space. The pair of examples of Fig. 4.27 show the polar-form plots vs. the elevation angle  $\theta$ , for the two principal planes,  $\phi = 0^\circ$  or  $xz$  plane (left) and  $\phi = 90^\circ$  or  $yz$  plane (right), at the central frequency of the spectrum ( $f = 1$  GHz). In both cases it is noticed that, as expected, the distribution is no longer rather omni-directional, but the radiation is mainly more focused in the ground dielectric region than in the air, with a certain forward squint of the main lobe (around

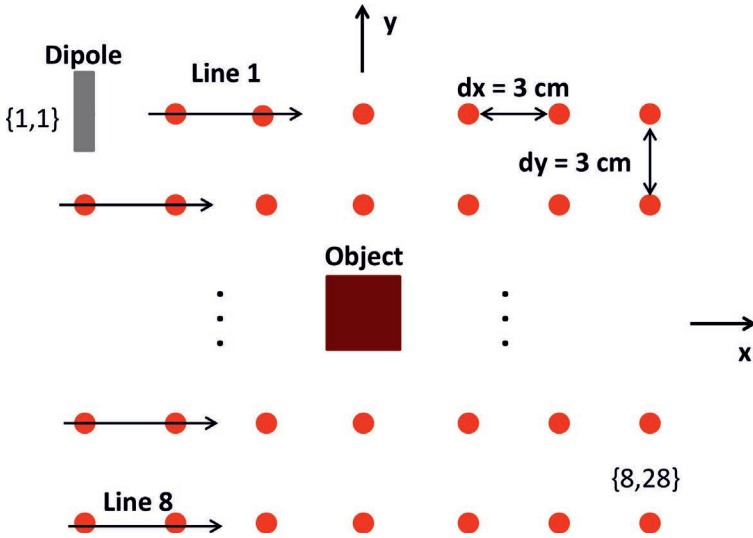


Fig. 4.24. Top view of the antenna scanning domain at the interface, with the coordinate system, the grid points, and the numbering of the scanning lines. Copyright © 2013, Hindawi Publishing Corporation, <https://doi.org/10.1155/2013/610389>.

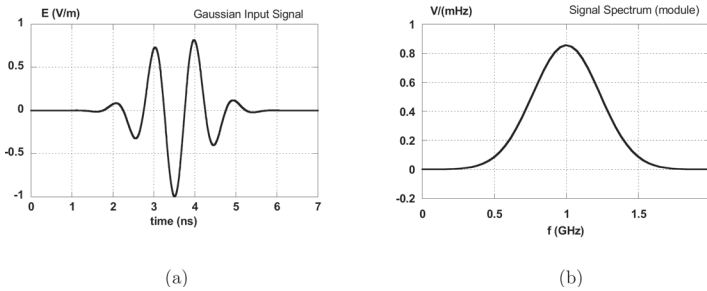


Fig. 4.25. (a) Simulated waveform of the GPR transmitted signal vs. time (ns); (b) Amplitude of the transmitted signal vs. frequency  $f$  (GHz).

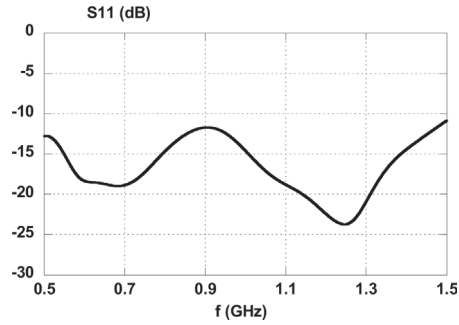


Fig. 4.26. Behavior of the antenna return loss (magnitude of the reflection coefficient in dB) vs. frequency  $f$  (GHz) in the matching range.

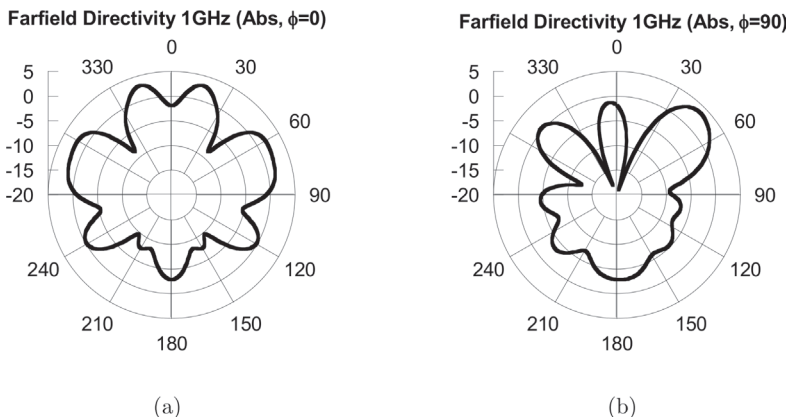
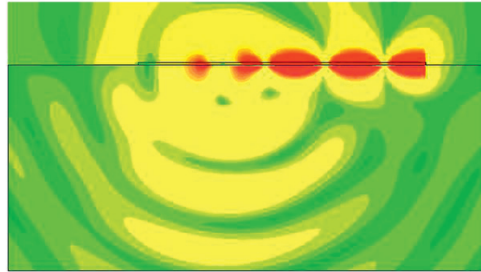


Fig. 4.27. Antenna radiation patterns vs. elevation angle  $\theta$  in polar form, in the  $\phi = 0^\circ$  (left) and the  $\phi = 90^\circ$  (right) planes (fixed central frequency  $f = 1$  GHz).



**Fig. 4.28.** Section view for a fixed  $x$  (central  $yz$  plane) of the magnitude of the electric-field distribution generated by the antenna at the interface in near-field conditions (same fixed frequency  $f = 1.0$  GHz). Copyright ©2013, Hindawi Publishing Corporation, <https://doi.org/10.1155/2013/610389>.

$45^\circ$  in the  $\phi = 90^\circ$  plot) due to the asymmetry of the radiating printed element with respect to the central plane  $xz$ . Since in general the GPR system will not operate in far-field conditions, it is also important to have precise information on the actual radiation in the near field. The CAD tool can compute the distribution of the fields in the volume of interest close to the antenna at the interface. A section view in the  $yz$  plane ( $x$  fixed) of the magnitude of the electric field for our antenna in the two half-spaces (air/ground) environment is illustrated by the color plot of Fig. 4.28, for a fixed frequency (again at the central frequency  $f = 1$  GHz).

In this picture it is clearly emphasized the spatial focusing of the near-field radiation, as already observed in the far-field radiation patterns as well. As said, this piece of information on the field distribution is particularly significant since in our cases the shallow scatterers will just be located in such near-field region. Once again various targets can be buried in the ground medium, at the same depth considered in the previous sections (9 or 10 cm). In the forward problem, shape, size, depth, and electromagnetic parameters of the scatterer are fixed. In each simulation of the CAD tool, after the signal is launched by the antenna, the scattering effect of such a target is evaluated by means of the time-domain trace of the received signal, which is due to the scattering from the buried object. It is reminded that our choice for an interfacial antenna allows us to eliminate most of the signal reflection due to the media discontinuity; in addition to this, as already described in previous

sections, absorbing boundary conditions have been implemented in order to avoid any further reflection effect from the surfaces enclosing the 3-D investigation domain. The numerical evaluations of the received signal traces are repeated in a multi-monostatic configuration, i.e., for a number of positions of the antenna with respect to the fixed target inside a 2-D rectangular domain (area on the  $xy$  interface plane at  $z = 0$ ), scanning along the  $x$  direction for different parallel lines by changing  $y$ , in a way similar to the actual measurements performed by a GPR instrument. In the numerical results presented here the scanning step along  $x$  is fixed at 3 cm; the number of points along  $x$  is  $N_x = 28$ , for an overall investigated length of 81 cm. The distance between parallel lines along  $y$  is also fixed at 3 cm; the number of lines along  $y$  is  $N_y = 8$ , for an overall width of 21 cm (refer to the sketch of Fig. 4.23 for the investigated grid, the relevant numbering of the lines, and the antenna position). Each time-domain trace of the received signal is therefore available in the  $28 \times 8 = 224$  points of a grid with unit cell  $3 \times 3$  cm (the relevant distance between grid points compared to the free-space wavelength at the central frequency being equal to  $0.1\lambda$ ). As already done so far, the results of the time-domain traces giving the amplitude of the scattered wave received by the antenna is plotted in the form of B-scan radargrams (time delay of the received signal vs.  $x$  scan position, in gray-scale form for its intensity).

The environment in the simulations presented here is chosen again as air (vacuum) for the upper medium and as a 'dry sandy soil' ( $\epsilon_r = 3.2$ ,  $\mu_r = 1$ ,  $\sigma = 0$ ) for the lower medium. In order to emphasize the effects of different radar cross sections, the buried scatterers are chosen of cubic and spherical shapes and can have different electromagnetic contrasts: specifically, computation is presented here for  $\epsilon_r = 6.7$  (basalt block) and for  $\epsilon_r = 1$  (air cavity). The effects of the dimensions can be also analyzed, e.g., with possible different cubic sides or sphere diameters. Finally, also the influence of the scatterer location can be considered, choosing variable depths  $d$  under the surface ( $d$  being the distance of the top point of the target from the air/sand interface). It is reminded that, as for the 2D analysis, the characteristic dimensions of the scatterers are generally comparable to the wavelengths of the signal (of the order of 10 cm in the medium) and are illuminated in near-field conditions. First examples of the GPR synthetic radargrams are shown in Fig. 4.29 for a cubic basalt scatterer of 10 cm side and buried 10 cm deep in the sand (practically the same already considered in 2D configuration);

specifically, each of Fig. 4.29 refers to B-scans vs.  $x$  for all the scan lines along  $y$ , reading each row from left to right. The scattering events, emphasized by the received-signal amplitudes in grey scale, present expected hyperbolic shapes along  $x$ . It is seen that, considering also the squint effect of the monopole antenna and its relevant orientation in the scanning process (see Fig. 4.23), the reflection effect correctly appears to be in general lower for the upper  $y$  positions (i.e., line 1), where radiation is not properly focused on the target, and sensitively increases as the antenna scans towards the center (i.e., line 5), where the scattering effect is maximal; at lower  $y$  positions (i.e., line 8) the effect is higher with respect to the upper  $y$  position (line 1) due to the asymmetric squinted illumination. It is also observed that the position in time of the main upper and lower hyperbolic events are fully consistent with the traveling speed of the signal scattered by the upper and the lower sides of the penetrable object. The echoes from the lateral sides of the block are also present, even if weaker than those from its top: this is related to the fact that the scattering from the top of the cube is mainly due to strong reflection by a flat interface and edge points, while the scattering from the side walls is related to diffracted fields spread over wider angles. In order to illustrate the specific differences that can be observed in the synthetic radargrams depending on the shape of the scatterer, Fig. 4.30 presents the results for a basalt sphere of radius 5 cm, being all the other parameters fixed as in Fig. 4.29. Again, Fig. 4.30 shows B-scans for parallel lines with different  $y$  (lines no. 1, to 8, reading each row from left to right). By using the same gray-scale as in Fig. 4.29 for the received signal intensity, it is clearly seen that the reflection events from the sphere are generally less strong than the cube, as expected from the reduced scattering effect of the round shape with respect to the flat and wedged shapes. The different radar cross section of the two geometries affects in part also the time delays in which the maxima of the scattered waves are found.

The effect of different electromagnetic contrast has also been evaluated through the radargram forms.

The results of Fig. 4.31 refer to the case of a cube as in Fig. 4.29 (same dimensions and location) but having permittivity of a vacuum (representing an air cavity in the sandy soil): again, sub-figures show the B-scans for eight different lines (no. 1 to 8, reading each row from left to right), with the relevant amplitudes in gray scale. Even if in this case the scattering effect is related to a target which is less dense than

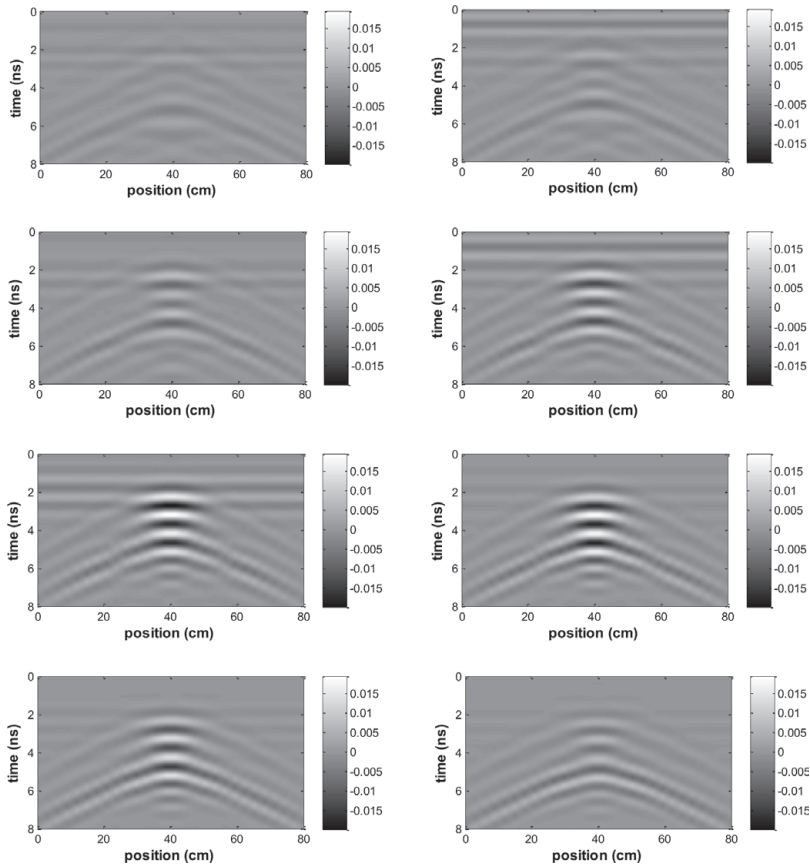


Fig. 4.29. GPR B-scan synthetic radargrams from our numerical setup for a basalt cube of 10 cm side, buried 10 cm deep from an air/sand interface (details on the other physical parameters are in the main text). Grey-scale received-signal amplitude in time vs. longitudinal scanning position along  $x$ , for three parallel lines at different  $y$ . Each figure can be associated to the scan line reading each row from left to right. The scatterer is located in a central position along  $x$ . Copyright © 2013, Hindawi Publishing Corporation, <https://doi.org/10.1155/2013/610389>.

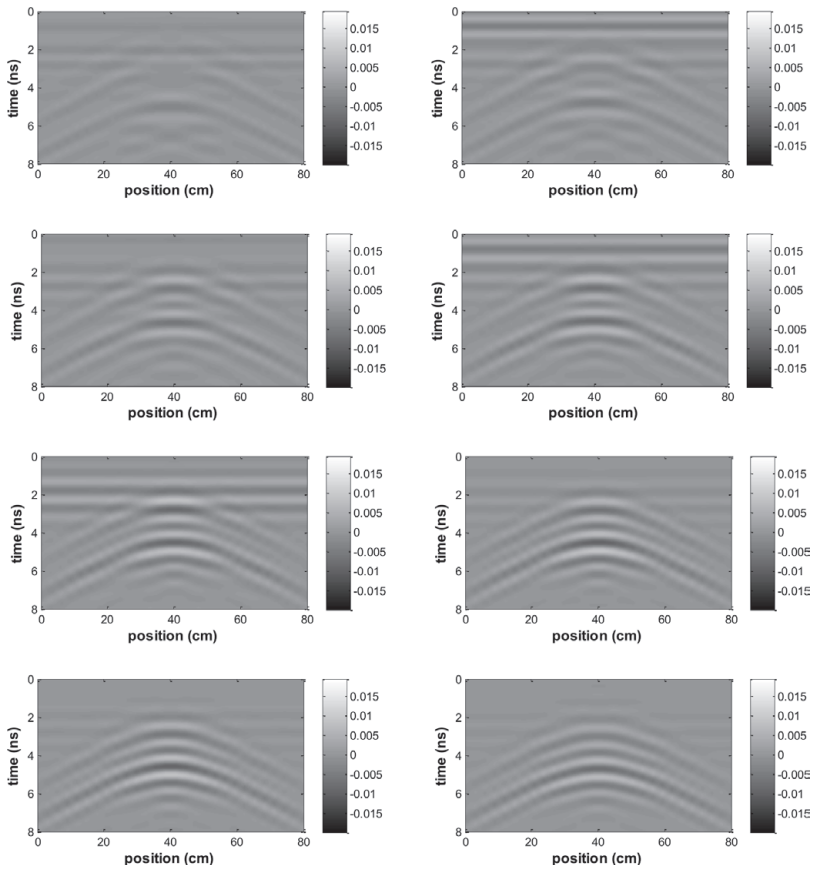
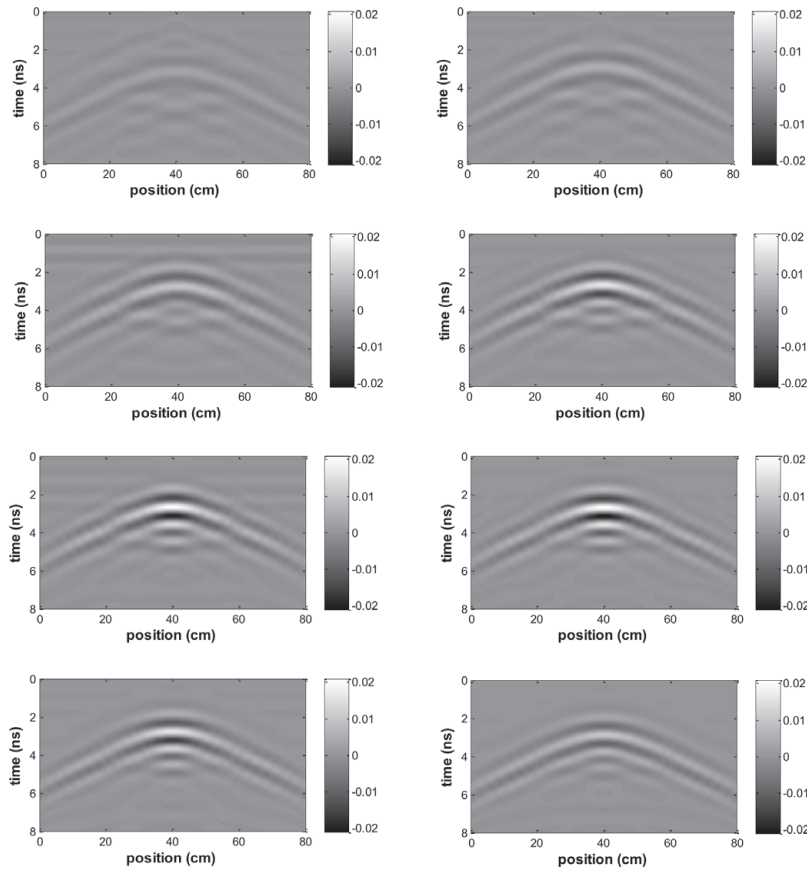


Fig. 4.30. GPR B-scan synthetic radargrams for a basalt sphere of 5 cm radius, buried 10 cm deep from an air/sand interface. Grey-scale received-signal amplitude in time vs. longitudinal scanning position along  $x$ , for eight parallel lines at different  $y$ . Each figure can be associated to the scan line reading each row from left to right. The scatterer is located in a central position along  $x$ . Copyright © 2013, Hindawi Publishing Corporation, <https://doi.org/10.1155/2013/610389>.



**Fig. 4.31.** GPR B-scan synthetic radargrams for a vacuum cube of 10 cm side, buried 10 cm deep from an air/sand interface. Grey-scale received-signal amplitude in time vs. longitudinal scanning position along  $x$ , for eight parallel lines at different  $y$ . Each figure can be associated to the scan line reading each row from left to right. The scatterer is located in a central position along  $x$ .

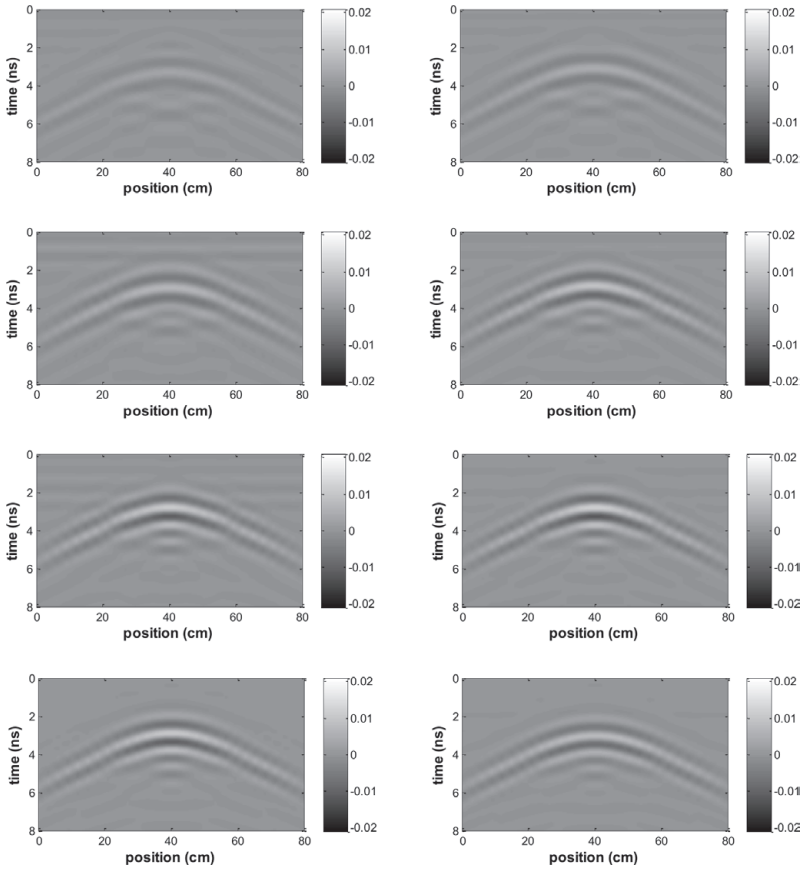
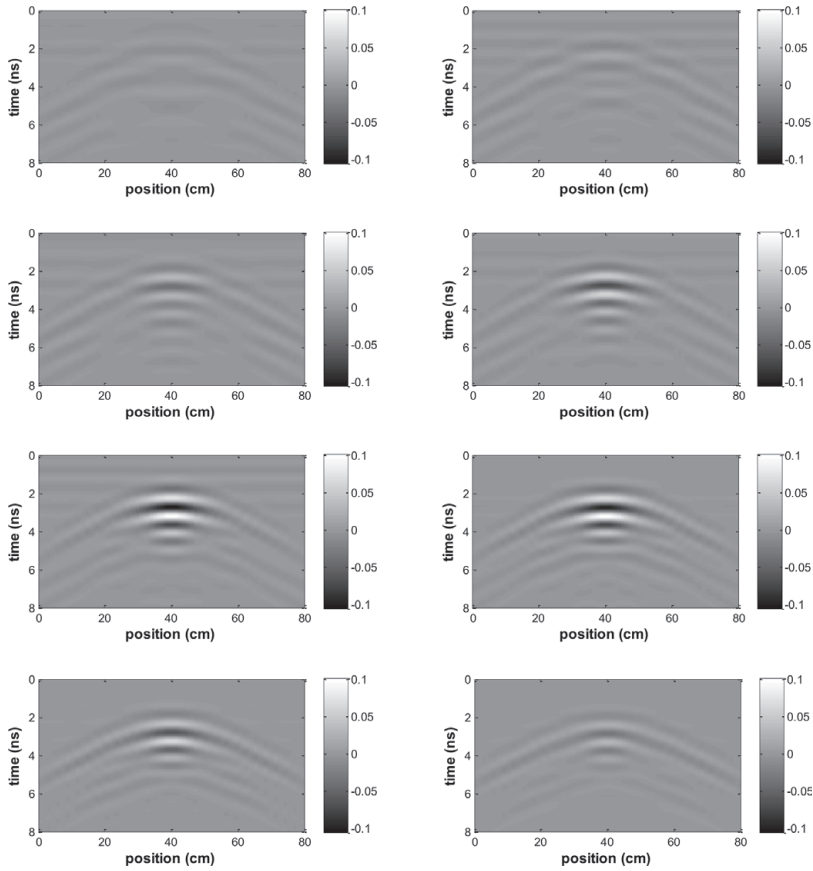
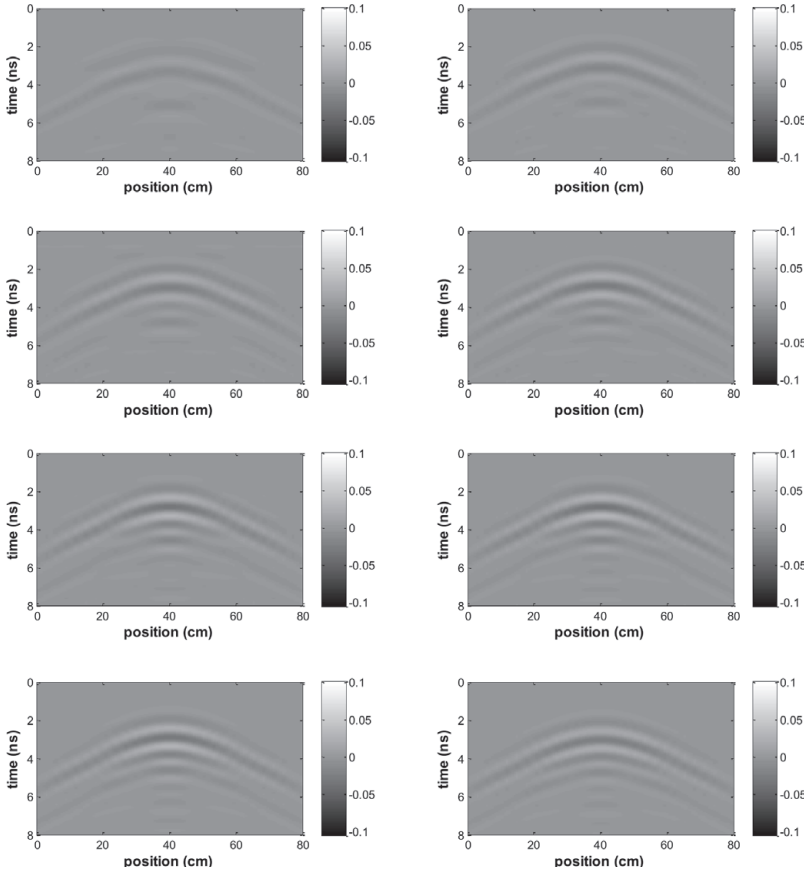


Fig. 4.32. GPR B-scan synthetic radargrams for a vacuum sphere of 5 cm radius, buried 10 cm deep from an air/sand interface. Grey-scale received-signal amplitude in time vs. longitudinal scanning position along  $x$ , for eight parallel lines at different  $y$ . Each figure can be associated to the scan line reading each row from left to right. The scatterer is located in a central position along  $x$ .



**Fig. 4.33.** GPR B-scan synthetic radargrams for a PEC cube of 10 cm side, located in a central position along  $x$  and buried 10 cm deep from an air/sand interface. The grey-scale received-signal amplitude in time are presented as in Fig. 4.29.



**Fig. 4.34.** GPR B-scan synthetic radargrams for a PEC sphere of 5 cm radius, located in a central position along  $x$  and buried 10 cm deep from an air/sand interface. The gray-scale received-signal amplitude in time are presented as in Fig. 4.30.

the outer host environment (sand), the radargrams of Fig. 4.31 appear quite similar to the ones of Fig. 4.29. Actually, from a careful analysis of the single-trace numerical data (not reported explicitly here for brevity), it is seen that the main reflection hyperbolic event, due to the upper side of the cube, is in general slightly stronger for the vacuum cube than for the basalt one. This is related to the fact that the reflection amounts in the hosting medium (sand) are different for the two scattering materials, being greater for vacuum than for basalt: in fact, for the sand/basalt case the magnitude of the reflection coefficient for a normally incident plane wave is about 0.35, while for the sand/air case the magnitude is about 0.5. Furthermore, the thickness of the scattered hyperbola appears to be different for the two objects (greater for the basalt than for the vacuum cube), due to the propagation velocity  $v$  of the wave transmitted through the penetrable scatterers ( $v$  being lower in the basalt than in the vacuum), which generates a dissimilar composition with the wave scattered from the bottom of the target. This influenced also the resolution of the pulse propagating inside the vacuum material, where the wavelength is greater than in the outer environment being here the medium more dense. The results of Fig. 4.32 refer to the case of a sphere having permittivity of a vacuum, buried in the sand: dimensions and location are the same as in Fig. 4.30. Sub-figures show the B-scans of the usual eight lines (no. 1 to 8, reading each row from left to right), with the same grey scale of Fig. 4.31. It is seen that the distinctive features already commented for the vacuum cube can be applied to the vacuum sphere as well. Even if the scattering effects are confirmed to be less significant for the sphere if compared to the equivalent cube, it is again observed that the main reflection hyperbolic event is in general slightly stronger for the vacuum sphere than for the equivalent basalt one. From all the shown synthetic radargrams (Figs. 4.29 to 4.32) it is seen that certain amounts of spurious signal occur ('flat' events found around 2 ns), due to slight reflections at the input port of the antenna, whose matching features in the operational bandwidth are affected also by the presence of nearby dielectric discontinuities. These spurious contributions are particularly visible when the basalt scatterer is in the closest position with respect to the antenna, whilst the undesired signals become almost invisible particularly for the vacuum targets located far from the antenna (see, e.g., Fig. 4.32).

The three-dimensional direct problem has also considered for the same cube and sphere made by perfect electric conductor. Antenna and

grid configurations are the same as in Fig. 4.23 and 4.24. In particular, the results of Fig. 4.33 refer to a PEC cube with dimension and location as in the previous pictures. Again the reflection effect correctly appears to be lower for the upper  $y$  positions (i.e., line 1), where the radiation is not focused on the target, and increases while the antenna scans towards the center of the domain where the flat metallic face is fully intercepted; at lower  $y$  positions (i.e., line 8) the effect is higher with respect to the upper position due to asymmetric illuminations. It is important to note that, in accordance with the strong scattered signal generated by a metallic object, the gray scale considered in this case is different with respect to those of Figs 4.29 and 4.31, being indeed more than ten times larger. Since the object is non-penetrable a well defined hyperbola event is clearly visible, being also well compact and shorter in time.

Fig. 4.34, finally, presents a result for the same metallic sphere considered so far, being parameters and configurations fixed as in Fig. 4.33. To allow direct comparison between the hyperbolas generated by the metallic cube, the gray-scale has been fixed at the same interval. As expected, the intensity of the non-penetrable curved shaped is generally lower but follows the same patterns as in the previous cases (minimum for upper position of the antenna along  $y$  directions and maximum at the central position).

From this analysis it is seen that all such synthetic data concerning the forward scattering problem appear to be pretty consistent and regular, so that they are particularly suitable to be processed by an efficient inversion algorithm, as discussed in part III of this thesis.

## 5. GPR Early-Time Technique

### 5.1. Introduction

Over the past few decades, significant advances have been done in the development of geophysical methods to investigate and characterize the shallow subsurface by means of non-invasive procedures [21, 22, 42]. A number of different techniques have been investigated in order to characterize the electromagnetic parameters of the considered medium at different depths. Specifically, GPR has shown to be one of the best options in terms of spatial resolution, fast acquisition time, extension of the investigated area and repeatability of measurements. As discussed previously, this system employs high-frequency electromagnetic waves, which in low-loss and non-magnetic soils respond primarily to the bulk dielectric permittivity of the medium. Consequently, as the permittivity of liquid water is much larger than other geologic constituents, a GPR instruments can be highly suited for measuring the volumetric water content [59].

More generally, quantitative evaluations of electromagnetic properties of materials is an important goal for a wide area of applications. In this chapter, the capability to estimate physical soil properties in a fast and non-invasive way through GPR surveys will be addressed. By starting from a novel alternative GPR method for monitoring electromagnetic (EM) parameters directly below the air/soil interface, firstly introduced in [63]-[65], numerical and experimental studies will be described to assess the theoretical background and to provide additional reliable information on the effective potentialities of the proposed approach.

Typically, surface GPR technique exploits a transmitting (Tx) and receiving (Rx) antenna positioned at the interface between air and di-

electric ground medium; the most common operational mode is the so-called *common offset* reflection profiling [42]. Basically, for this kind of survey, the Tx and Rx antenna are placed at a constant offset (i.e., constant separation) distance and are moved along a survey line to map reflection from underground vs. position. The system is usually moved along the scan line at a uniform step size between two sounding locations. This procedure is repeated multiple times and a typical raw output is obtained displaying on a horizontal axis the position of the system on the surface and on the vertical axis the travel time of the collected signal. As shown in the previous chapter, reflection events are originated from a contrast in the EM properties of different medium, typically due to the presence of an interface or a buried object. The *common mid-point* (CMP) survey collects reflection data while Tx and Rx antenna are moved apart about a fixed location, sequentially and with a certain step, allowing the separation of different events of the field, i.e., *direct air wave*, *direct ground wave*, and *subsurface reflection* (see Fig. 5.1, where all the main GPR events have been highlighted). Very often, CMP sounding is primarily used to obtain an estimate of the radar signal velocity with respect to depth in the ground by simply varying the antenna separation at a fixed location, thus measuring the change of the two-way travel time of the reflected signal. Consequently, by increasing the horizontal distance at a constant rate, variations of the two-way travel time can be used to calculate EM wave velocities, as well as the depth of a reflector (further details can be found in [42, 43]).

In reflection methods a GPR transmits EM waves into the soil, hence moisture content can be retrieved by analyzing the travel time of the wave reflected at an interface. Anyway, as is well known, this approach requires good signal penetration and the presence of a subsurface dielectric interface that yields clear GPR reflections. Another commonly used approach is the so called ‘ground-wave method’, which can be applied for soil EM characterization when no shallow reflectors are present. The ground wave must be recognized in the collected data using a multi-offset GPR acquisition configuration, and its velocity can be determined from the slope of the linear relationship between the antenna separation and the ground-wave travel times. However, this slope is not always well defined, when, as an example, near-surface heterogeneities are present. Additionally, the method is time-consuming and the information on soil permittivity may be averaged only over a large horizontal distance. The ground-wave method can be also used

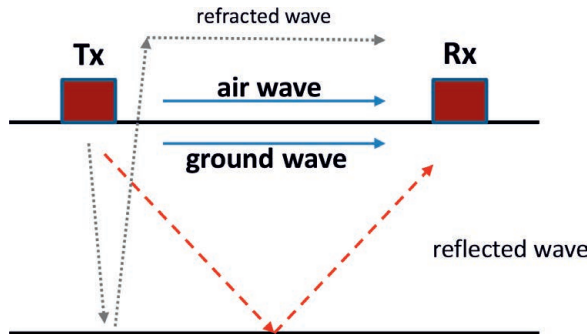


Fig. 5.1. GPR waves at the receiving antenna for a ground-coupled bistatic system.

with a single-offset configuration; even though this method is more attractive with respect to CMP surveys, because it gives the possibility of performing faster acquisition, it is affected by some uncertainties related to the potential difficulty of separating the ground-wave arrival from the clutter of critically refracted and reflected waves. Moreover, it might be difficult to choose the proper antenna separation for which air-ground waves are always well separated for a wide range of soil water content (i.e., a wide range of soil permittivity), which can be encountered in large field measurements. In addition, for all the proposed cases one has to take into account that the range of influence on the considered signal attributes depends on the wavelength, which in turn is a function of the dielectric properties of the analyzed soil [58]. Consequently the region of influence depends itself on the moisture content, making an accurate evaluation of the investigated area rather involved.

When working in bistatic configuration, in addition to the signal reflected by an object (or more generally by an interface) buried in the ground under analysis, one has to consider also the signal which propagates along the direct path between the transmitting and receiving antenna. This contribution travels at a velocity that is not well specified and has a value that ranges between the free-space velocity of the wave and that in the medium. As shown in [21, 68] such a signal is composed by a complex superimposition of the air wave and the ground wave. In single-offset configuration, for a fixed carrier frequency, these two waves arrive totally separated at the receiving antenna, i.e., they do not interfere, only if the permittivity of the material and/or the distance between the antenna is large enough. Just as an example, we can find

Material	Static Conductivity $\sigma_s$ (mS/m)	Relative Permittivity $\epsilon_r$
Air	0	1
Dry Clay	1–100	2–20
Wet Clay	100–1000	15–40
Dry Concrete	1–10	4–10
Wet Concrete	10–100	10–20
Freshwater	0.1–10	78–8
Freshwater ice	0–1	3
Seawater	4000	81–88
Seawater ice	10–100	4–8
Dry Sand	0–1	3–5
Wet Sand	0.1–10	10–30
Dry Sandy Soil	0.1–100	4–6
Wet Sandy Soil	10–100	15–30
Dry Clayey Soil	0.1–100	4–6
Wet Clayey Soil	100–1000	10–15
<b>Average Soil</b>	5	16

**Tab. 5.1.** Typical values of relative permittivity (real component) and static conductivity for common subsurface materials for quasi-static conditions ( $f = 100$  MHz). For further detail see [43].

that with an offset between Tx-Rx antenna equal to about 10 cm and for a dominant wavelength in free-space of 30 cm, such a separation is clearly visible when the lower medium has a relative dielectric constant larger than 20 (see Table 5.1 for indication on typical values of most common materials). In this particular condition the ground wave can be easily exploited to estimate the signal velocity in the material, to extract the value of the permittivity and therefore the water content [59, 62]. It is worth to note that even though this technique is quite simple and easy to implement, it can work only in specific condition, providing an estimation of the water content mediated on relatively wide areas, that, as already introduced, is also influenced by the penetration depth of the ground wave in the medium under analysis. However, the obtainable accuracy is usually evaluated by comparing the relevant results with other more traditional and well-established technique, such as Time Domain Reflectometry (TDR) and gravimetric measurements.

Generally speaking, when the permittivity of the probed medium is lower than 20 (i.e., for a great number of common media) and working

with offsets that are sufficiently large, the first signal arriving at the receiver is the combination of the direct and ground waves. On this basis, more recently, a new radar approach named Early-Time Technique has also been proposed in [63]; it is based on the amplitude analysis of the early-time portion of the GPR collected waveform, using a fixed-offset ground-coupled antenna configuration where the separation between transmitting and receiving antenna is of the order of the dominant pulse wavelength. Indeed a number of studies, particularly in the last decades, observed systematic variations of the GPR direct-wave peak-to-peak amplitude with the degree of saturation of concrete [59, 60, 61]. Actually, it is expected that changes in amplitude, shape, and time duration of the GPR received signals should occur, since the ground-coupled antenna parameters are sensitively affected by the electromagnetic properties of the underlying media and the overall environment. A number of laboratory experiments supported such indications, emphasizing different cases in which the ground-medium dielectric constant and conductivity manifestly influence the characteristics of the first direct signal in simple GPR configurations. In particular, with close ground-coupled antennas, a high degree of correlation was found between the shallow-soil permittivity and the instantaneous amplitude of that portion of the signal where the air and ground waves partially overlap and are not still clearly separated (that is just referred early time signal or 'ETS' in short). It was experimentally tested that dielectric-constant variations affect amplitude, shape and duration of the first-arrival GPR signals, whereas changes in soil conductivity mainly alter their amplitude [63, 64]. However, there is a complex dependence of the signal properties on the GPR scenario that can be chosen, involving the type and radiative properties of the antennas, the setup geometry (e.g., the location of the Tx/Rx elements), the characteristics of the transmitted signal waveform and relevant frequency spectrum, the EM contrast of the media, and their dispersion and loss effects. If an effective quantitative assessment of the technique is searched for, it looks therefore essential to investigate such problem extensively by means of accurate EM numerical approaches.

Theoretical analyses could confirm these overall behaviors, even though a number of significant approximations and simplifications were necessarily required in the EM problem modeling. Indeed, some details have been recently examined in [65], where under certain hypotheses and conditions, a solution of the frequency-domain integral modeling the problem has been introduced. In particular, also a closed-form

solution of the inverse Fourier transform requested to go back in the time domain has been presented. Basically, introducing strong approximation on the operative frequency and on the distance between transmitting and receiving antenna, the follow closed form expression connecting the instantaneous amplitude of the direct wave with soil EM parameters has been obtained

$$A_{air-wave} = \frac{\sqrt{\varepsilon_0\mu_0}}{2\pi(\varepsilon_2 - \varepsilon_0)d^2} \quad (5.1)$$

$$A_{air-wave} = \frac{\sqrt{\varepsilon_1\mu_0}}{2\pi(\varepsilon_2 - \varepsilon_0)d^2} e^{-\frac{1}{2} \frac{\sqrt{\mu_0}}{\sqrt{\varepsilon_1}} \sigma_1 d}$$

where  $\sigma_1$  and  $\varepsilon_2$  are the conductivity and the permittivity of the medium under analysis and  $d$  is the antenna separation. It is interesting to note that the exponential term in the second equation expresses the evanescent nature of the ground wave, moving away along the direction normal to the surface. Incidentally, in this work also information about the portion of the time-domain signal that is more suitable to correlate with the EM parameters has been discussed. In particular, it has been found that the first positive half cycle of the ET signal may represent the best choice for the instantaneous amplitude evaluation, allowing us to maximize the SNR and minimizing interferences from reflection caused by shallow interfaces.

Equations (5.1), showing an inverse relationship between the early-time amplitude and the soil permittivity, will be further investigated in the following by extensively developing a simulation setup of a realistic scenario. By means of a suitable implementation on a commercial CAD tool, wide-ranging efficient surveys will be conducted; this enables us to identify which are the more revealing signal attributes able to give predictable correlation with the ground permittivity and conductivity values, and also if alternative and more accurate functional relations can be outlined among the involved parameters. Novel reliable information are thus achieved on the effective potentiality of the ETS technique for various geophysical applications.

### 5.1.1. Complex trace analysis

The amplitude information on the collected pulse can be extracted from the ET signal through a so-called complex trace analysis; it can be applied to computing both the average value over a selected time window or more simply the instantaneous value at a fixed time. This

method is based on the Hilbert transform, that basically is defined as the imaginary part of a time domain signal whose negative part of the spectrum has been suppressed. Namely, being  $s(t)$  a time domain signal (for the case at hand it will be the GPR trace), we define  $S_a(f)$  as the spectrum of  $s(t)$  with a suppressed negative frequency contribute; transforming back in the time domain we introduce the so-called *analytic signal*, that is related to the starting signal as follow [66]

$$s_a(t) = s(t) + jh(t) \quad (5.2)$$

here  $h(t)$  is the Hilbert transform of  $s(t)$ . Generally speaking, discarding negative frequency components of the involved signals does not cause a loss of information, but induces us to deal with a complex-valued function. This procedure makes certain attributes of the signal more accessible and facilitates the derivation of modulation and demodulation techniques. As long as the manipulated function has no negative frequency components (i.e., it is still analytic), the conversion from complex back to real can immediately obtained discarding the imaginary part. Additionally, since  $s_a(t)$  is a complex signal, it can be expressed in polar for as

$$s_a(t) = A(t)e^{j\phi(t)} \quad (5.3)$$

where

$$\begin{aligned} A(t) &= |s_a(t)| = \sqrt{s^2(t) + h^2(t)} \\ \phi(t) &= \angle s_a(t) \end{aligned} \quad (5.4)$$

These functions are respectively called the instantaneous *amplitude envelope* and instantaneous *phase* of the starting signal  $s(t)$ . Specifically, the instantaneous envelope is usually a slow varying function, ranging from zero and the maximum amplitude of the collected trace, containing information on the true resolution of the data.

In Fig. 5.2(a-b) a typical GPR waveform is reported. The bold line highlight the portion of the signal that can be considered and related to the EM properties of the probed medium. In addition, in Fig. 5.2(c-d) the relevant instantaneous envelope have been reported: the averaged value of the bold portion or more simply the instantaneous value can be considered and elaborated to estimate permittivity and conductivity of the investigated medium.

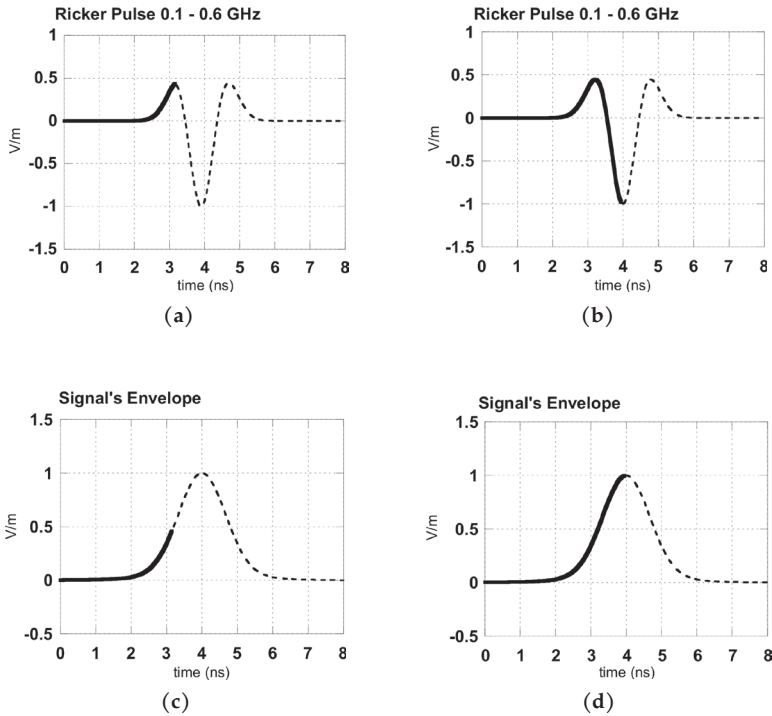


Fig. 5.2. Typical GPR signals gathered for ETS analysis. (a) Ricker waveform vs. time, with its 'onset' (bold line in the picture on the left) and 'first half cycle' (bold line in the picture on the right); (b) relevant instantaneous 'envelope amplitude', again for the 'onset' (left) and 'first half cycle' trace (right). Copyright © 2017, IEEE.

## 5.2. Laboratory scale experiments

As discussed so far, the ET approach is based on the amplitude analysis of the first portion of the GPR waveform using a fixed-offset ground-coupled antenna configuration, where the Tx and Rx antennas are separated by a distance comparable with the dominant wavelengths of the transmitted signal. In this section some results obtained by changing in a controllable way the electromagnetic conductivity of the probed medium will be presented; measurements carried out with controllable variations of the permittivity are not yet available, but some interesting results developed in an open test site have already been described in [64]. Indeed, the change of the permittivity of the medium under analysis through a reliable and low-cost method requires rather complicated procedures, whereas, as will be outlined in the follow, it has been possible to merely control the conductivity variations by acting on the potassium-chloride concentration (KCl) of a porous material.

The data presented in the following were collected again by colleagues of the Earth and Space applied physics laboratory of the 'Rome Tre' by using a bistatic radar unit manufactured by Sensors and Software Inc., equipped with 1 GHz shielded antennas and having 7 cm center-to-center antenna separation. The analyses were performed in a specifically designed laboratory-scale test site (see Fig. 5.3), to remove all the factors that can affect the antenna/material coupling (e.g., large-scale roughness of the surface, lateral inhomogeneities in the solid matrix, lateral permittivity variation), except for the influence of the electric conductivity whose effects are specifically investigated. To this purpose, measurements were performed on a homogeneous porous material, a  $0.35 \text{ m} \times 0.35 \text{ m} \times 0.17 \text{ m}$  box filled with glass beads (the same medium for the analysis described in the chapter, having bead radius ranging to  $400 - 800 \mu\text{m}$ ), saturated with deionized water, changing every time the potassium-chloride (KCl) concentration (i.e., the conductivity) and measuring variations using TDR, as illustrated in Fig. 5.4. For this purpose data were acquired using a three-pronged probe having a rod length of 15 cm. The probe was connected through a  $50 \Omega$  coaxial line to a Tektronix 1502C cable tester (Tektronix, Inc.), which applies a step function wave front and measures the signal reflected by the impedance discontinuities. The TDR data give minimum and maximum conductivities of  $0.0061 \pm 0.0004 \text{ S/m}$  and  $0.21 \pm 0.01 \text{ S/m}$ , respectively, as shown in Fig. 5.5, where the conductivity values are presented with respect to



**Fig. 5.3.** An experimental laboratory setup for the analysis of ETS features, developed at the applied geophysical lab of 'Roma Tre' University. An air/dielectric environment is investigated by means of a simple commercial GPR system with interfacial fixed close antennas. The ground dielectric constant and conductivity can be changed in controllable ways. Copyright © 2016, IEEE.



**Fig. 5.4.** TDR measurement setup to control the conductivity variation due to change on the KCl concentration. Copyright © 2017, IEEE.

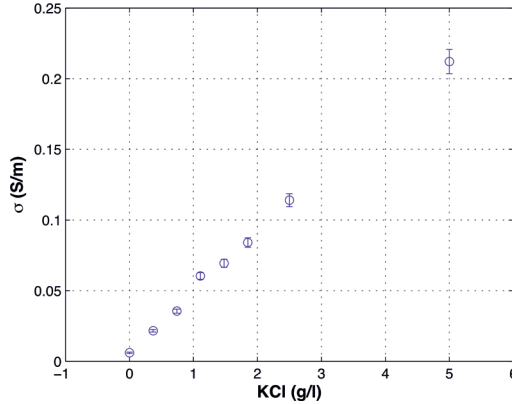


**Fig. 5.5.** The TDR-derived electrical conductivity as a function of salt (KCl) concentrations in a porous sandy soil, for all the measurements. Copyright © 2016, IEEE.

the saline concentration applied to the porous material. Through the use of the same instrument, for each set of measurement, it has also been verified that the relative dielectric constant does not significantly change, being always almost equal to  $\epsilon_{r_{TDR}} = 28.9 \pm 0.3$ . This averaged value of the TDR-derived permittivity was also compared with that derived through the GPR survey, which was determined from the two-way travel (TWT) time according to standard procedures. It is important to note that at the bottom of the test site a metal sheet was placed (clearly visible in Fig. 5.3) to precisely detect the arrival of the GPR reflected signals. Therefore, to extract the permittivity information from the collected data, the cross-correlation function between the direct and reflected wavelet envelopes [67] has been calculated, determining a permittivity average value of  $\epsilon_{r_{GPR}} = 29 \pm 2$ .

As already discussed in section 5.1.1 a robust method for extracting the early-time amplitude information is through the use of the complex trace analysis. As an example in Fig. 5.6 a single collected trace is presented together with its instantaneous envelope; also the signal reflected from the bottom of the medium under analysis is clearly visible and well positioned in time with respect to two-way path in the glass beads medium. Again, in Fig. 5.7 the traces collected for different values of the conductivity variation has been presented. It is observed that, as  $\sigma$  increases, the overall signal mainly decreases in its amplitude, even though the sensitivity of such variations does not look very high. To

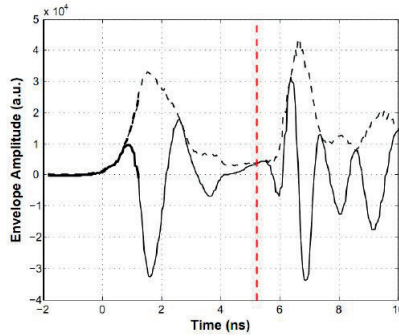


Fig. 5.6. Example of a GPR acquired trace (solid line) and relevant envelope amplitude (dashed line). The bold portion of the curve represents the first half-cycle, while the reflection from the bottom of the investigated medium is highlighted by the red dashed line. Copyright © 2016, IEEE.

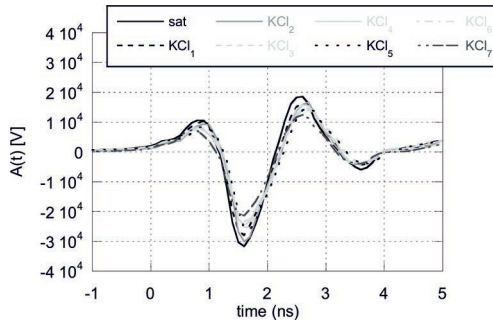


Fig. 5.7. GPR traces collected by the receiving antenna for different KCl concentrations (i.e., conductivities), with our the experimental setup. In the legend the term ‘sat’ refers to the deionized water, while KCl<sub>1</sub> to KCl<sub>7</sub> refer to the lowest and the highest value of the potassium-chloride concentration. Copyright © 2017, IEEE.

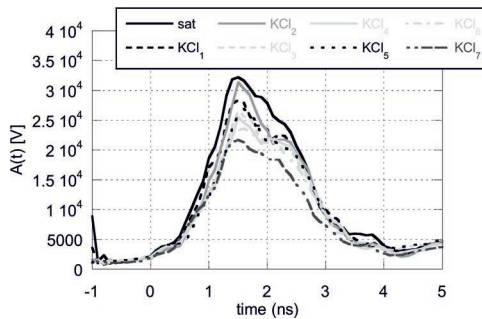


Fig. 5.8. Relevant instantaneous envelope for the signals presented in Fig. 5.7. Copyright © 2016, IEEE.

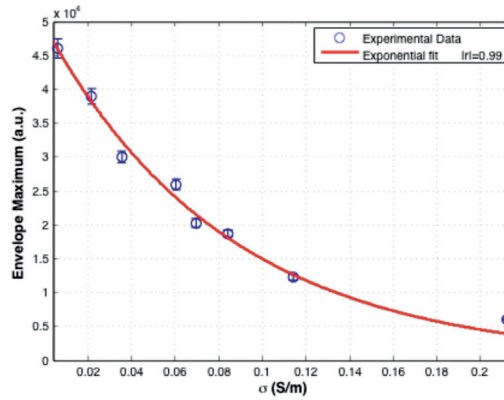
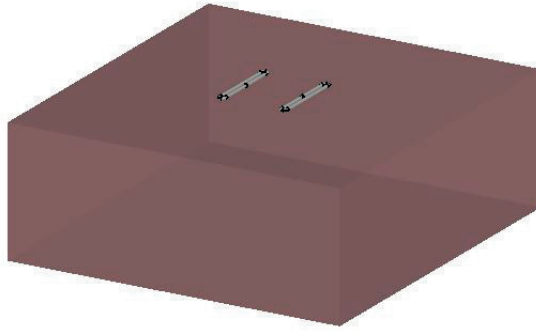


Fig. 5.9. Maximum envelope value of the reflected wave as a function of the corresponding conductivity values derived from the TDR measurements. The curve is the exponential data fitting. Copyright © 2016, IEEE.

better understand the variation of the instantaneous amplitude of the collected traces, in Fig. 5.8 the relevant envelopes with respect to the signal presented in Fig. 5.7 have been shown. As expected, this analysis allows for clearer detection of the early-time signal features (see Fig. 5.2). To quantitatively compare these data, the degree of the exponential correlation between the GPR averaged envelope maximum of the first half-cycle and the TDR-derived conductivities has been estimated: an exponential function clearly represents both the experimental data ( $r = 0.95$ ), and the simulated data ( $r = 0.99$ ). The variations of the electrical properties of the material can be also cross-checked by analyzing the reflected wave from the investigated medium bottom. Fig. 5.9 shows the exponential attenuation that conductivity causes in the GPR wave propagation.

### 5.3. Numerical setup

To develop an effective quantitative assessment of the proposed novel technique, it looks essential to extensively investigate the problem by means of accurate EM numerical techniques. As discussed in the introduction, this issue is faced mainly here by developing a synthetic setup based on an efficient and accurate implementation of a full-wave time-domain CAD simulator, CST Microwave Studio as already used in previous chapter. In this way, systematic and comprehensive parametric analyses are possible, aimed at establishing rigorously the functional



**Fig. 5.10.** The synthetic setup based on a EM software tool. Implementation of a GPR system for the simulation of ETS. The scenario consists of two half-space media (e.g., an air/soil environment, described by the EM parameters  $\epsilon_r, \mu_r, \sigma$ ) where a close fixed bistatic ground-coupled Tx/Rx antenna system is located. Standard or resistively loaded folded dipoles are chosen in this case to simulate a commercial GPR antenna system.

relations between the ground-soil permittivity features and the most significant ETS attributes. In the basic GPR configuration of our interest, we are referring to a two half-space environment (that is generally air for the upper medium and an unknown dielectric for the lower medium), with a fixed ground-coupled Tx/Rx antenna system having electrically small mutual separation (in terms of dominant signal wavelengths). Specifically, our synthetic setup (see a sketch in Fig. 5.10 and section 4.3) allows us to design a bistatic antenna, to choose the input signal waveforms and, above all, to vary the probed medium EM parameters (including loss and dispersive effects too). Thus, thanks to this suitable implementation of the EM software tool, in conjunction with the experimental experience gained for this kind of approach, it has been possible to extensively analyze our numerical problem. Since, as emphasized, we are interested in deeply analyzing the effects of the antenna position and of the various involved physical parameters with respect to the fundamental features of the received signals in quick and flexible way, this numerical approach gives us the possibility of several efficient, versatile, and inexpensive analyses. In the next subsection, we will begin from the analysis of the collected trace obtained by suitable changing the distance between Tx and Rx antenna, in order to roughly understand what are the configuration that provide a clear overlap between the air and ground wave. Indeed, as discussed in section 5.1, this represents an essential requirement to extract reliable information from the instantaneous amplitude of the early time signal.

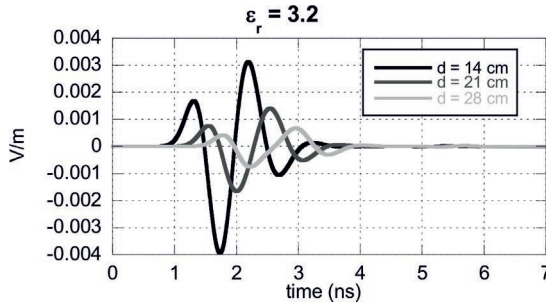


**Fig. 5.11.** Received signal for the numerical model of the GPR surveys.  $\epsilon_r = 3.2$  is fixed, variable offset is considered (see label). It is clearly visible that the air-ground waves are always overlapping. Copyright © 2016, IEEE.

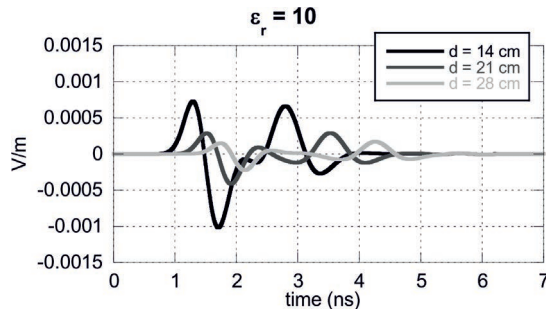


**Fig. 5.12.** Received signal with our numerical model.  $\epsilon_r = 10$  for various antenna offset distances, ranging from  $d = 14$  cm to  $d = 28$  cm (see label). It is clearly visible that already starting from the lower distances, the air-ground waves are always separated. Copyright © 2016, IEEE.

### 5.3.1. Air/ground waves analysis

When an electromagnetic pulse is transmitted by a source placed at an interface between dielectric media, since the wave velocity depends on the permittivity of the medium, in a certain position and for a fixed time two different wavefronts may be distinguishable. However, if the permittivity or the offset is not large enough, this two contribute may be still overlapping. The main goal of this section consists in giving some quantitative information about this issue. A first representative example of a simulated configuration is shown in 5.11 where various collected signals have been reported for  $\epsilon_r = 3.2$  (as usual, a common value for dry soils, equal to the glass beads used in the laboratory setup) and three different offsets of the antenna system. It very interesting to note that even for  $d = 28$  cm (light gray in the picture), a single well-defined pulse is visible, indicating that the two waves are still overlapping. In

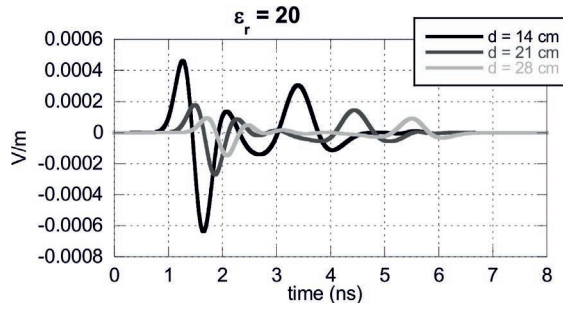


Fig. 5.13. Received signal with our numerical model.  $\epsilon_r = 20$  for various antenna offset distances, ranging from  $d = 14$  cm to  $d = 28$  cm (see label). It is clearly visible that now the air-ground waves are always separated. Copyright © 2016, IEEE.

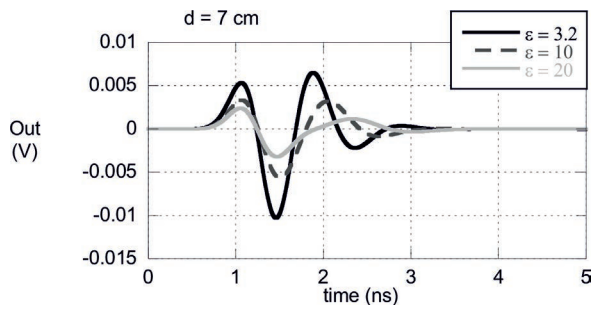
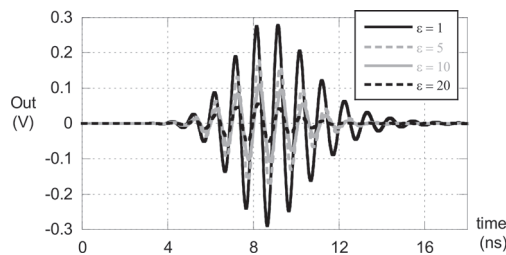


Fig. 5.14. Received signal for the numerical model of the commercial GPR antenna. For  $d = 7$  cm and  $\epsilon_r$  ranging from 1 to 20 the air-ground wave are always overlapping. Copyright © 2016, IEEE.

the following figures (5.12, 5.13), the same configurations have been considered for larger value of the soils permittivity: starting from  $d = 14$  cm the two signals are already clearly separated and are also inversely polarized, as demonstrated and discussed in [68].

For all the presented plot, progressive shape variations of the waveforms are clearly visible. Also, the main distinctive feature of this technique, that is the overall decreasing of the ETS amplitude as  $\epsilon_r$  increases, is anyway confirmed. Fig. 5.14, instead, summarizes the behavior for  $d = 7$  cm, showing different traces for the values of dielectric constant considered so far (i.e.,  $\epsilon_r = 3.2, 10$  and  $20$ ). The influence of  $\epsilon_r$  on the collected waveforms is clearly visible: even for the largest value (i.e.,  $\epsilon_r = 20$ , light gray curve), no separation for the two contributes is detected and the ETS attributes can be quite clearly revealed.

As expected, the results shown in this section allow us to state that for distances between Tx and Rx antenna less than the relevant wavelength (equal to 30 cm for this case,  $d = 7$  cm thus  $d \sim \lambda/4$ ), the collected waves are always fully overlapping, even for rather large values of the dielectric constant. Consequently, in the next section we will always consider this offset as starting value, that is actually the one exploited for the available GPR commercial systems. As anticipated by the experimental analysis, these results give us a first numerical confirmation that the ETS features are strongly dependent on the permittivity variations and on the location of both transmitting and receiving antennas.



**Fig. 5.15.** Simulation results of ETS for a ground-coupled radar system having Tx/Rx  $\lambda/2$  dipoles designed at the central frequency  $f = 1$  GHz (dipoles fixed with mutual offset  $d = 7$  cm and elevation above the interface  $h = 1$  cm), using a suitable Gaussian modulated pulse as an input signal. The waveforms of the output signal (V) vs. time (ns) for a number of different  $\epsilon_r$  of the ground medium have been presented (see labels).

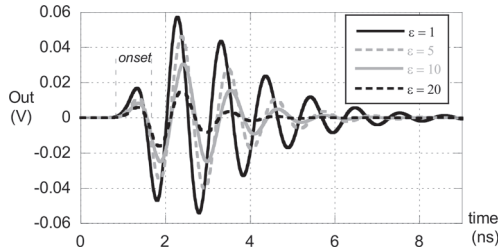


**Fig. 5.16.** As in Fig. 5.15 but applying a Ricker pulse as input signal. Again the waveforms of the output signal (V) vs. time (ns) for a number of different  $\epsilon_r$  of the ground medium have been presented (see labels).

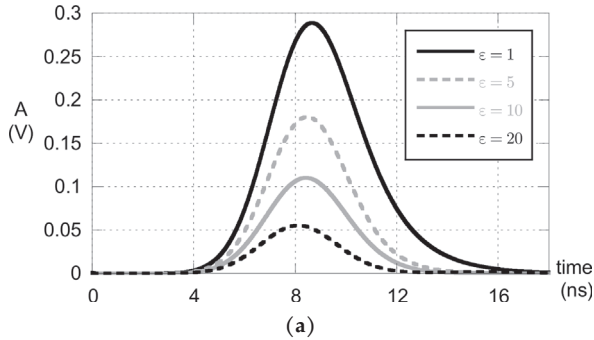


**Fig. 5.17.** Relevant overall signal amplitude envelope of the received signal  $A$  (V) vs. time (ns) for a Gaussian pulse as input signal. Copyright © 2016, IEEE.

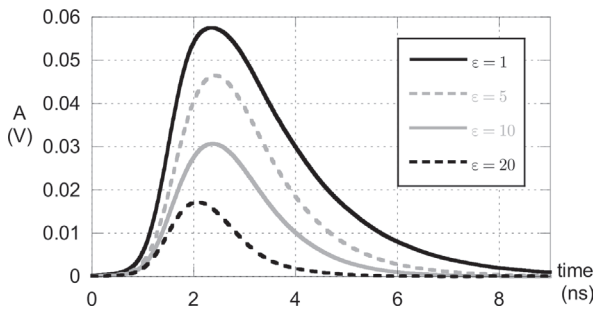


**Fig. 5.18.** Relevant overall signal amplitude envelope of the received signal  $A$  (V) vs. time (ns) for a Ricker pulse as input signals. Copyright © 2016, IEEE.

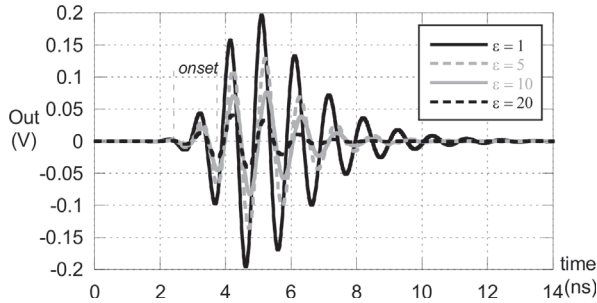


**Fig. 5.19.** Collected signals for a modulated Gaussian pulse ( $f_c = 1$  GHz,  $BW = 0.5$  GHz,  $d = 7$  cm) and different values of the permittivity (see legend).

#### 5.4. Parametric analyses

The choice of the input signal waveforms is also related to the characteristics of the antenna type. In connection with the time-domain waveform and relevant spectral features of the chosen signal (Ricker, Gaussian pulse, etc.), the antenna frequency characteristics have to be evaluated in terms of input matching (return loss) and field distribution (radiation patterns).

These aspects are further complicated because in our scenarios the system typically works in inhomogeneous environments (i.e., the antenna features can be sensitively modified by the ‘loading’ due to the interfacial ground medium) and the radiation pattern is not as regular as in far-field conditions (the Tx/Rx antennas can be strongly coupled through involved near-field effects). As an example, we report the ETS characteristics simulated for a pair of typical pulse signals used in GPR instruments: a Gaussian modulated pulse in Fig. 5.15, and a Ricker pulse in Fig. 5.16.

Both the received signal and relevant amplitude attribute are displayed, as different ground dielectric constant  $\epsilon_r$  are chosen for a fixed antenna geometry (see relevant figure captions). In order to emphasize the influence of the antenna type, these results are derived for a Tx/Rx system based on a pair of half-wavelength dipoles (at a center frequency  $f = 1$  GHz and an overall bandwidth  $BW = 1$  GHz as well). The fact that such radiating elements are basically resonant (if not properly improved in terms of bandwidth through proper loading or other techniques, see Chapter 3 for more details) is emphasized by marked ‘ringing’ behaviors of the gathered time-domain waveforms in both cases (see again Figs. 5.15 and 5.16).

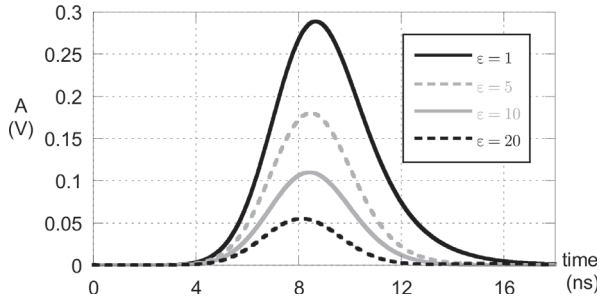


**Fig. 5.20.** Instantaneous envelope of the received signals (modulated Gaussian pulse,  $f_c = 1$  GHz, BW = 0.5 GHz,  $d = 7$  cm) and different values of the permittivity (see legend).

In Fig. 5.17 and 5.18 the relevant instantaneous envelope amplitude have been reported of the two set of signals presented in Figs. 5.15 and 5.16 to better highlight the sensitivity of the signal amplitude with respect to the permittivity of the probed medium. As expected, at a first glance it is clearly visible that the amplitude decreases for increasing values of the permittivity with a non-linear behavior. This is fully in agreement with the frequency-domain analysis on the near-field distribution developed in Chapter 1 for interfacial elementary sources.

Just as a further example in Figs. 5.19 and 5.20 the signals and the relevant envelopes obtained by considering as excitation a Gaussian pulse having the same carrier frequency but a different bandwidth have been presented. All the considerations made previously are confirmed.

After having examined various fundamental issues so far neglected in the analysis of ETS approach, we focus now our attention on the distinctive feature of the method, that is the functional relationships between ETS amplitude and dielectric constant. Based on our synthetic model, in the following we illustrate various behaviors of different ETS attributes as a function of  $\epsilon_r$  (the range of values spans continuously between 1 and 20). In particular, Fig. 5.21 reports the results for the Ricker pulse, whereas Fig. 5.22 for the Gaussian modulated pulse.

According to the standard definitions and procedures on ETS (see Fig. 5.2 and related comments) and referring to the relevant figure captions, for both Figs. 5.21 and 5.22, different signal attributes are displayed, considering the ETS amplitudes of the ‘onset’ (‘OA’) and of the first ‘envelope’ (‘EA’), both for its ‘maximum’ (‘M-’) and for its ‘average’ values (‘A-’). In Fig. 5.23 and 5.24 also the influence of the offset  $d$  is

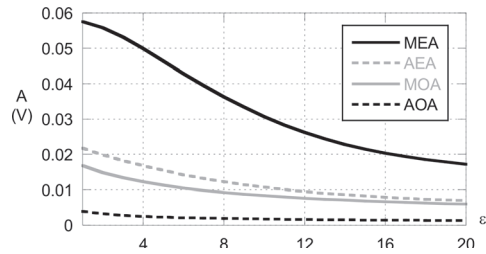


**Fig. 5.21.** MEA and MOA for a fixed distance between Tx-Rx antenna (Ricker pulse,  $d = 7$  cm). Copyright © 2016, IEEE.

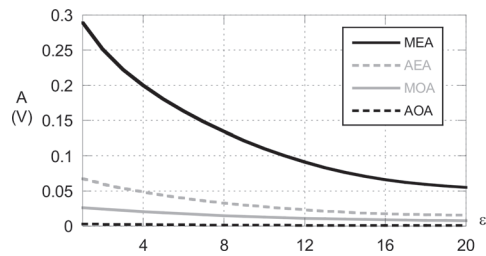


**Fig. 5.22.** MEA and MOA for a fixed distance between Tx-Rx antenna (Gaussian pulse,  $d = 7$  cm). Copyright © 2016, IEEE.

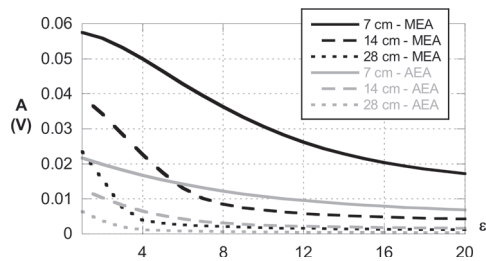


**Fig. 5.23.** MEA and MOA for a various distances between Tx-Rx antenna (see legend, Ricker pulse,  $h = 1$  cm).

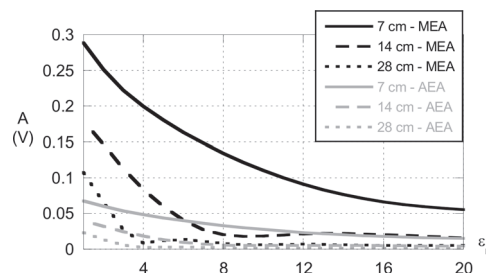


**Fig. 5.24.** MEA and MOA for a various distances between Tx-Rx antenna (see legend, Gaussian pulse,  $h = 1$  cm).

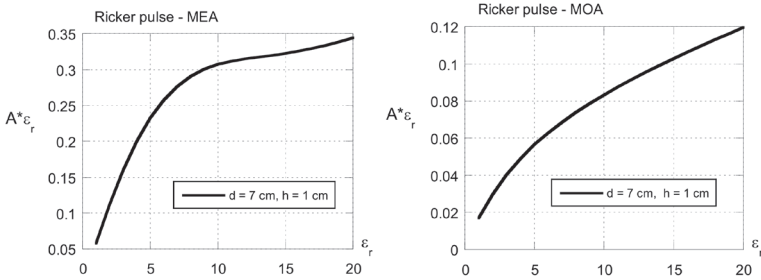


**Fig. 5.25.** Behavior of the maximum envelope amplitude with respect to permittivity variations (Ricker pulse,  $h = 1$  cm). It is clearly visible that for the considered range the link is not linear. Copyright © 2016, IEEE.

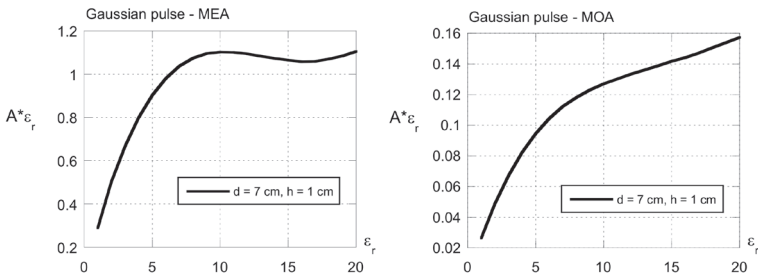


**Fig. 5.26.** Behavior of the maximum envelope amplitude with respect to permittivity variations (Gaussian pulse,  $h = 1$  cm). As for the Fig. 5.25 in the considered range the link is not linear. Copyright © 2016, IEEE.

also taken into account (different curves for  $d = 7, 14, 28$  cm).

As a basic comment, it is seen that, even though an inverse relationship between early-time amplitudes and permittivity always occurs, the actual functional dependence between these quantities is not related to the simple formulas [65] presented in equations (5.1). In particular, the dependence of any ETS amplitude  $A$  on  $\epsilon_r$  is not a simple inverse proportionality (i.e., of the type  $1/\epsilon_r$ ). This can be verified by plotting as in Fig. 5.25 and Fig. 5.26 the quantity  $A \cdot \epsilon_r$  as a function of  $\epsilon_r$  and noting that this curve is not at all a constant. Only for the envelope peak of ETS and for quite high values of dielectric constant (greater than 10) this simple rule can be seen approximately useful.

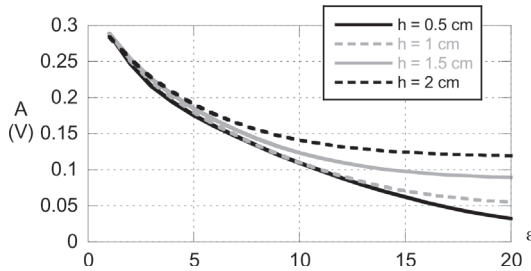


**Fig. 5.27.** Behavior of the maximum envelope amplitude with respect to permittivity variations for different height of the antenna from the interface (Gaussian pulse,  $d = 7$  cm). It is clearly visible that the MEA, for higher value of  $\epsilon_r$ , is sensitive to the value of  $h$ . Copyright © 2016, IEEE.

#### 5.4.1. Numerical analysis on alternative parameters

Various additional issues, so far quite disregarded but that can instead suitably accounted for in our analysis, are further addressed in this section. One of the significant aspects is the ETS sensitivity with respect to Tx/Rx antenna location. In addition to their offset, even though in ground-coupled configurations the antennas are very closed to the interface, another variable geometrical parameter that can deeply affect the features of the received signal is the vertical height (elevation)  $h$  of the antennas from the surface. Indeed, the waveforms are very sensitive even to small elevation from the ground, due to the presence of undesired excitation of spurious reflections. From the analytical side this problem is rather complicated and in our context we show just some numerical representative effects of this issue. An example of the degree of influence of the antenna elevation  $h$  on the ETS attributes is calculated in Fig. 5.27. It is seen that the curves of the amplitude maintain an overall typical decaying behavior as  $\epsilon_r$  increases, and in general tend to rise as  $h$  is raised as well (the interval for  $h$  is here from 0.5 to 2 cm). This interesting property, related to different coupling effects close to the interface, can be suitably interpreted: for low values of the permittivity the dominant wavelength of the transmitted pulse is still large enough to ‘see’ the antenna as perfectly coupled to the ground, whereas as  $\epsilon_r$  increases the distance  $h$  from the surface is not more negligible and the amplitude of the collected signal can be sensitive even to small variations of the distance. Anyway, this qualitative information could be very useful in order to improve the overall understanding of the problem at hand. Additional studies have also been carried out in order to evaluate

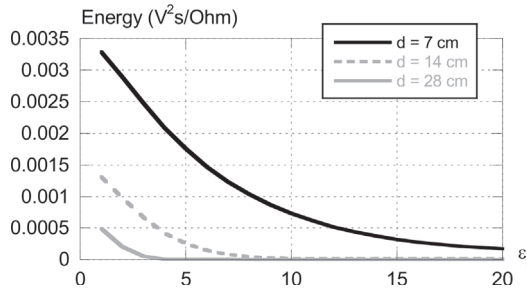


Fig. 5.28. Behavior of the signal energy with respect to permittivity variations for different antennas separation (Gaussian pulse,  $h = 1$  cm). Copyright © 2017, IEEE.

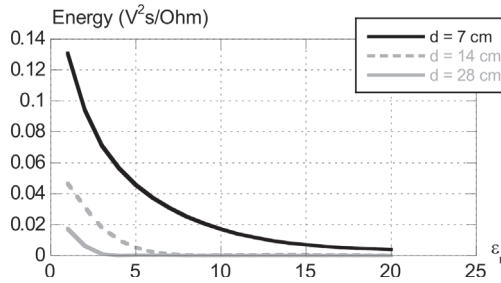
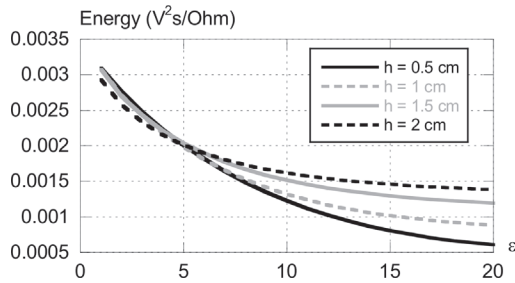
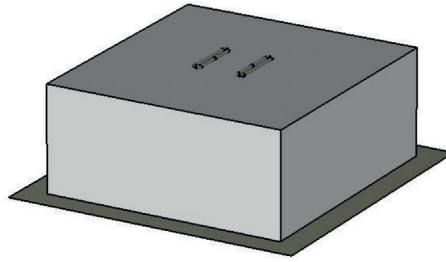


Fig. 5.29. Behavior of the signal energy with respect to permittivity variations for different antennas separation (Ricker pulse,  $h = 1$  cm).

attributes that are alternative with respect to the time-domain amplitude of ETS. Among these, for instance, the overall ETS energy has been evaluated and correlated to the dielectric constant. An example of this behavior is reported in Fig. 5.28 and 5.29, respectively for a Gaussian and a Ricker pulse. The dependence of the signal energy on the dielectric constant is qualitatively similar to what already recognized, even though the rate of decaying is different, as expected. In particular, it is confirmed that the antenna offset  $d$  is rather critical, since the amount of energy is quickly decaying when the mutual distance of the antennas raises significantly. As already reported in Fig. 5.27, it is interesting to analyze the behavior of the signal energy with respect to the antenna distance from the interface. In Fig. 5.30 again a parametric analysis has been considered, showing as expected that for lower values of the permittivity the energy is not sensitive to the distance, whereas starting from  $\epsilon_r = 6$ , the dominant wavelength becomes small enough to 'see' even small value of  $h$ .



**Fig. 5.30.** Behavior of the signal's energy with respect to permittivity variations for different height of the antenna from the interface (Gaussian pulse,  $d = 7$  cm).



**Fig. 5.31.** The synthetic setup based on a EM software tool. Implementation of a GPR system for the simulation of ETS. The scenario under analysis consisting of two half-space media (e.g., an air/soil environment, described by the EM parameters  $\epsilon_r, \mu_r, \sigma$ ) where a close fixed bistatic ground-coupled Tx/Rx antenna system is located. Resistively loaded folded dipoles are chosen in this case to simulate a commercial GPR antenna system, as that of Fig. 5.3. Copyright © 2016, IEEE.

#### 5.4.2. Numerical model of a GPR commercial system

By starting from the numerical setup described in the previous sections and comprehensively tested to develop numerical analysis on the Early-Time technique, an ad-hoc numerical model of a GPR commercial system has been suitably designed. As already discussed in Chapter 3, most of standard GPR systems are equipped with simple cylindrical or printed dipoles. However, in order to improve the impedance bandwidth, even though this kind of solutions entails a loss of efficiency and consequently of penetration depth, a certain distribution load along the profile has been considered. Thanks to an ad-hoc design and a comprehensive optimization procedure, a very good results shown in Fig. 5.32 has been obtained, where also the gathered numerical trace (solid lines), evaluated in the already presented experimental scenario (dashed lines), is shown and compared. If we take into account that

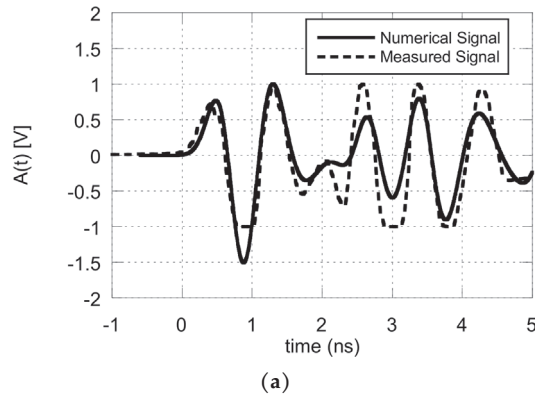


**Fig. 5.32.** Behavior of a time-domain signal waveform measured by the GPR in the experimental configuration of Fig. 5.31, emphasizing the direct wave (ETS contribution) and the first reflected wave due to the presence of a bottom metal sheet. The measured traces are in dashed lines. The received waveform (signal voltage amplitude  $A$  vs. time  $t$ ), given by a Ricker pulse in an air/sand environment and a metallic reflecting surface on the bottom of the enclosing box. Copyright © 2016, IEEE.

a number of uncertainties and idealization are present (related to the incomplete knowledge of the specifics of the commercial instrument), the agreement between experiments and simulations looks excellent. Indeed the received traces are very well superimposed, as regards time location and amplitude of the ripples, both for the direct ETS portion and for the reflected contribution. In Fig. 5.33, the matching between measured and simulated frequency spectrum of the signal is also remarkable. It is worth to note that the commercial instrument considered so far is, as said, a TR1000 system manufactured by Sensors&Software, equipped with a fixed offset bistatic antenna ( $d = 7$  cm,  $f_c = 1$  GHz). Nevertheless, also other GPRs, belonging to the same series, have been numerical designed and tested. Having available an accurate and efficient model of the considered GPR bistatic system, various numerical analyses have been carried out, by introducing parametric variation of the most important involved quantities and of the electromagnetic properties of the dielectric half-space.

A first general result that confirms the theoretical basis introduced and discussed in the previous section is reported in Fig. 5.34.

Specifically, parametric simulations changing the dielectric constant of the probed medium ( $\epsilon_r$  variable from 1 to 20 in step of a unity) have been shown. To make clearer the presentation of the picture, only a

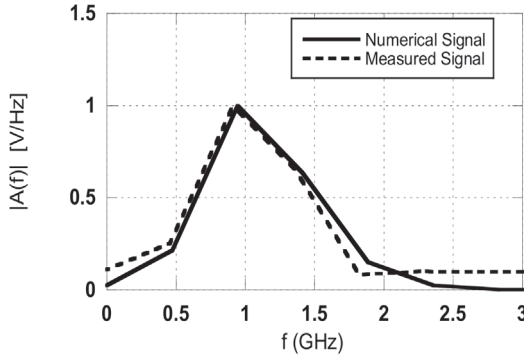


Fig. 5.33. Signal's spectrum for the waveform presented in Fig. 5.32. See legend for the relevant details. Copyright © 2016, IEEE.

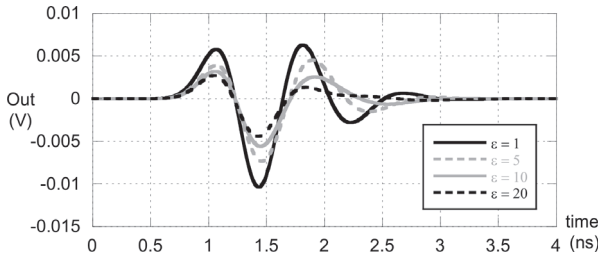


Fig. 5.34. Collected signals for a Ricker pulse radiated through the numerical model of the TR1000 commercial system ( $f_c = 1$  GHz,  $d = 7$  cm) for different values of the permittivity (see legend).

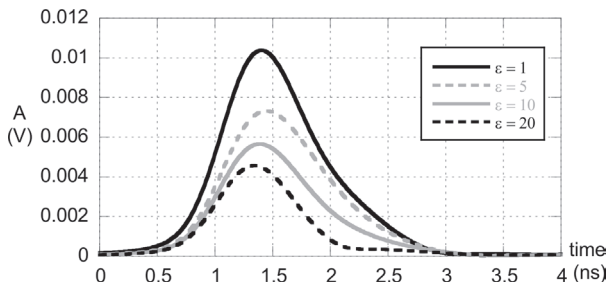


Fig. 5.35. Instantaneous envelope of the received signals (Ricker pulse TR1000,  $f_c = 1$  GHz,  $d = 7$  cm) and different values of the permittivity (see legend).

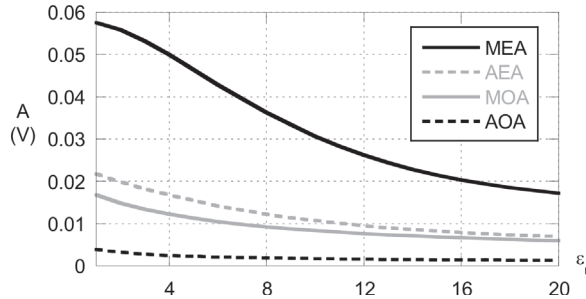


Fig. 5.36. MEA and MOA for a fixed distance between Tx-Rx antenna (TR1000 Ricker pulse,  $d = 7$  cm).

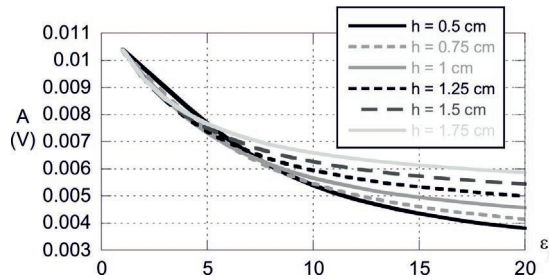


Fig. 5.37. Behavior of the maximum envelope amplitude with respect to permittivity variations for different height of the antenna from the interface (TR1000 Ricker pulse,  $d = 7$  cm). It is clearly visible that the MEA, for higher value of  $\epsilon_r$ , is sensitive to the value of  $h$ .

limited set of results are reported; as expected, a good sensitivity of the instantaneous amplitude of the collected signals can be observed, whereas air and ground wave are overlapping.

Relevant instantaneous envelope are shown in Fig. 5.36, allowing us to assess the true resolution of the waveforms, both in terms of amplitude variation and time occupation. According to the standard definitions and procedures on ETS (see Fig. 5.2) and referring to the relevant figure captions, in Figs. 5.36, different signal attributes are displayed. As a fundamental comment, once again it is seen that, even though an inverse relationship between early-time amplitudes and permittivity always occurs, the actual functional dependence between these quantities is not related to simple formulas, as supposed so far [65]. To complete the scenario in Fig. 5.37 and 5.38 the behavior of the maximum envelope amplitude with respect to permittivity variations for different height and the behavior of the signal energy for a number of heights of the antenna from the interface have been reported.

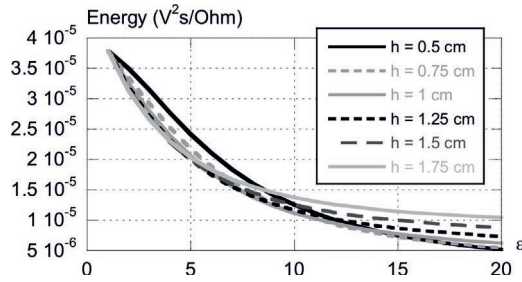


Fig. 5.38. Behavior of the signal energy with respect to permittivity variations for different height of the antenna from the interface (TR1000 Ricker pulse,  $d = 7$  cm).

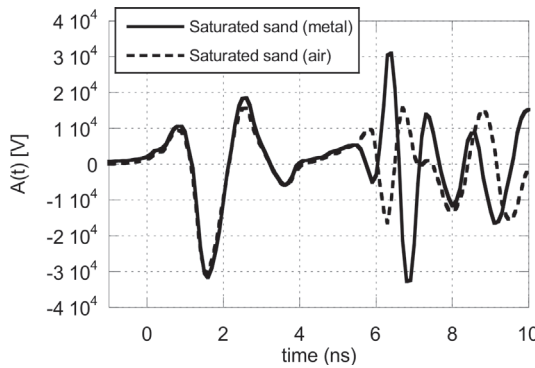
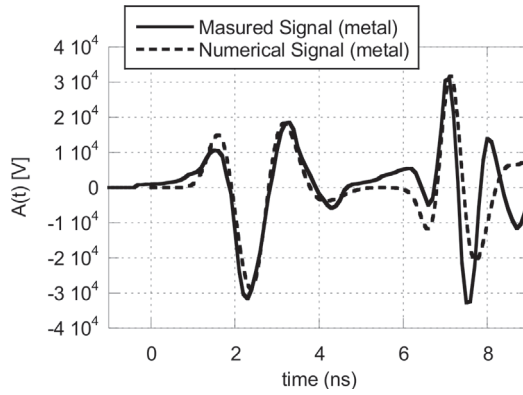


Fig. 5.39. Behavior of a time-domain signal waveform measured by the GPR in the experimental configuration of Fig. 5.3, emphasizing the direct wave (ETS contribution) and two reflected waves due to the presence of a metal sheet and air discontinuities (see legend). The measured traces are in dashed lines. The configuration is the same as in Fig. 5.32, but the ground medium has been saturated with ionized water ( $\epsilon_r = 29$ ).

The same trends outlined in the previous section are confirmed; the numerical model presented here, in conjunction with all the reported results, has allowed to predict and analyze the behavior of early-time attributes in real operative conditions.

### 5.4.3. Numerical analysis of the loss effects

The experimental results obtained by changing the conductivity of the medium under analysis, discussed in the previous section, has also been simulated by means our implementation on the electromagnetic tool. Some results of the signal traces deriving from this simulated environment, as a function of various conductivity values, are presented in Fig. 5.41. From comparisons between the measured and the simulated traces, together with their related envelopes, it is confirmed that the sig-



**Fig. 5.40.** Comparison between time-domain signal waveforms measured by the GPR in the experimental configuration of Fig. 5.3 and simulated with our setup in Fig. 5.31, emphasizing the direct wave (ETS contribution) and the first reflected wave due to the presence of a bottom metal sheet. The configuration is the same as in Fig. 5.32, but the ground medium has been saturated here with ionized water ( $\epsilon_r = 29$ ).

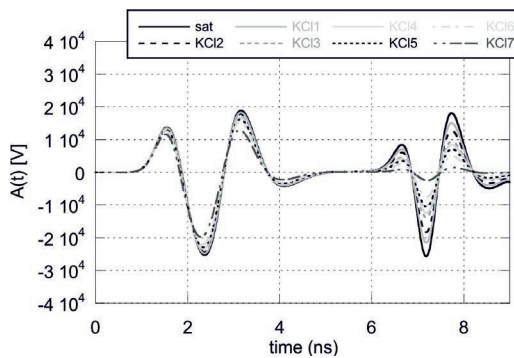


**Fig. 5.41.** Simulated time-domain ETS traces as the medium conductivity is varied through different saline concentrations (KCl) in a water solution, as in the experiments. The subsequent time signal replica is related to the location of a bottom metal screen.

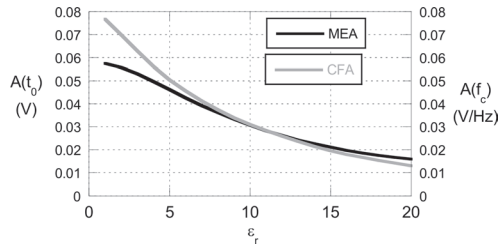


**Fig. 5.42.** Simulated behaviors of ETS ‘alternative’ attributes: the ‘carrier frequency amplitude’ (CFA) vs.  $\epsilon_r$ . The development of suitable interpolation formulas leads to good fitting and prediction of the ETS.

nal amplitudes are consistently affected by the conductivity variations. In these cases, apart from an overall distortion on the gathered trace shape principally related to dispersion for the presence of the water, it is confirmed that the main effect of increasing losses is just on a relatively limited reduction of the signal amplitude. The relevant behaviors of simulated traces for the chosen GPR instrument show again good matching. In fact, the simulated results of Fig. 5.41 agree quite well with those obtained experimentally (see details in Fig. 5.7 and the relevant caption).

#### 5.4.4. Frequency domain elaboration

By proper processing the time-domain data of the traces in the spectral domain, we have also investigated the amplitude of the received signal carrier frequency, as a possible additional ETS observable. An example of the relevance of such analysis is provided referring to the analysis of both permittivity and conductivity effects; as a conclusion of the present study the frequency-domain behaviors of measured data will be provided.

The last considerations refer to the study of other unconventional observable parameters for possible improvement of the sensitivity of the ETS approach and also for proper derivation of useful interpolation formulas able to well predict these behaviors. In fact, if we refer to the spectral content of the signals, it is interesting to monitor the magnitude of the Fourier-transformed (FT) signal at the central operative frequency (what we call here ‘carrier frequency amplitude’, CFA in brief), as a possible descriptive parameter of the main feature of the gathered ETS. This can be easily performed by standard FT processing of the time-domain data (either numerical or experimental ones). It is seen that such alter-

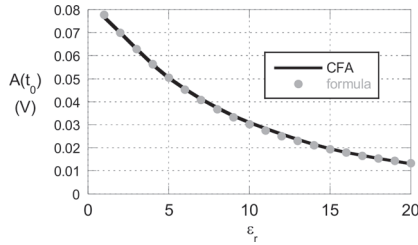


Fig. 5.43. Behavior of the interpolation formulas in equation (5.5).

native attribute presents dependence on the physical and geometrical parameters that is basically similar to those of other observable quantities, but in tested situations the functional relationships look more regular and better predictable. This characteristic can be related to the main signal properties summarized by the carrier frequency, possibly less sensitive to the overall dispersion effects in the investigated scenario. An example of this study is given in Fig. 5.42 for data from the synthetic setup. The curves vs. dielectric constant are given for the usual ETS envelope and for the carrier amplitude. It is manifest a more regular decaying of CFA as  $\epsilon_r$  increases. It is important to note that such consistent behavior makes the derivation of interpolation formulas much simpler. As an example of data fitting, the excellent matching with CFA is also illustrated in Fig. 5.43, according to an empirical formula as a function of the dielectric constant, given by the following closed-form expression of algebraic type:

$$CFA = \frac{a}{b + c\epsilon_r + d\epsilon_r} \quad (5.5)$$

where in this case:  $a = 0.43$ ,  $b = 5$ ,  $c = 0.48$ ,  $d = 0.044$ . In addition to the benefit of achieving valid fitting expressions for the data related to a chosen GPR setup, it should be also emphasized that this method can take advantage of well consolidated approaches that are performed directly in the frequency domain (i.e., in harmonic regime) for canonical Tx/Rx systems of interfacial antennas (particularly, dipoles). Even though these approaches require various approximations and simplifications, the empirical formulas derived through our numerical study give the significant possibility of testing their degree of accuracy and addressing perspectives for improved functional relationships.

The frequency-domain analysis of ETS traces can be accomplished also for the study of the effects of conductivity. The last example of Fig.

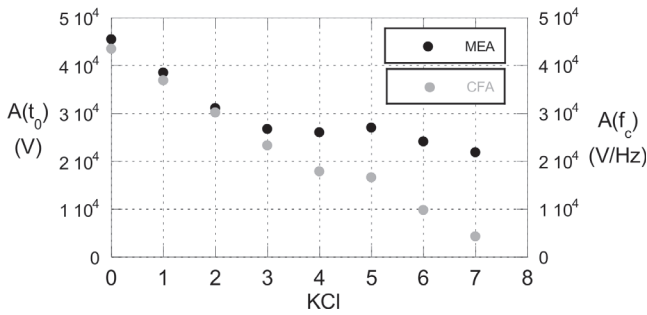


**Fig. 5.44.** Evaluation of the measured behavior of the Carrier Frequency Amplitude (CFA) as an alternative ETS observable quantity, compared with the Maximum Envelope Amplitude (MEA), for a lossy case (different value of a KCl concentration, as in Fig. 5.7). CFA shows a more regular and wide sensitivity with respect to the conductivity variations. Copyright © 2016, IEEE.

5.44 refers again to the changes of salt concentration in the porous material discussed in Section 5.2. The carrier amplitude analysis is applied in this case directly to the data from measurements (see Fig. 5.41). It is interesting to note that, with respect to the already considered maximum envelope amplitude (MEA), the CFA behavior looks again more regularly sensitive to the variation of conductivity, with the consequent considered advantages.

## 5.5. Conclusion

In this chapter, the early-time signal, that is the first-arrival wave collected by a bistatic ground-coupled radar in simple configurations with close fixed antennas, has extensively been tested as a possible advantageous alternative method for monitoring and mapping the permittivity properties of shallow surfaces at small and intermediate scales. This study has shown that, in spite of its conceptual simplicity, the determination of the most effective observable quantities and, above all, the predictability of the relevant functional relationships, as a function of the various involved parameters, represents a rather difficult task to be tackled. Suitable experimental and numerical setups have been employed as the most viable strategy for a systematic analysis of this complex topic. Accurate and wide-ranging parametric surveys have thus been presented, starting from basic test studies. For the first time, a comprehensive and reliable view of the most significant issues influencing the practical use of such technique has been assessed. In connection with the revealed dependence of the ETS amplitude on the permittiv-

ity parameters, it is seen that, for a satisfactory accuracy in evaluating both dielectric constant and conductivity, initial careful calibration procedures should be performed for each specific GPR instrument. Furthermore it is observed that, as the permittivity values tend to increase, the sensitivity of ETS amplitude strongly decreases and can be easily overwhelmed by strong waveform distortion and environmental uncertainties (noise, clutter, inhomogeneities, etc.). Even though involved coupling phenomena occur between the Tx/Rx antennas, it is seen that a 'small offset' configuration is generally preferable for ETS clear detection. On the other side, accurate quantitative predictions of the medium EM parameters have been demonstrated much more delicate and not at all straightforward. The sensitivity of ETS on the type and location of the antennas, the input waveform, and other environmental parameters appear in fact extremely significant and should be treated by means of accurate implementations of numerical methods. Specific behavioral trends of observable quantities have thus been highlighted as a function of different physical and geometric parameters. Particular advantageous choices of original attributes have also been addressed, which allow for suitable polynomial interpolations, deriving empirical but accurate formulas able to adequately evaluate the EM properties of a probed medium and to check the validity of established approaches based on the frequency domain. The results of this analysis can provide a first consistent description both of the potential attractive features and of the critical aspects of the ETS technique. Future research following the strategies delineated in this frame can make this original method increasingly useful in specific operative conditions as a valid alternative to other consolidated approaches.

PART III

INVERSE PROBLEMS



# Introduction

As is well-known the capability of electromagnetic waves to penetrate material objects is dependent on its frequency. Our every-day experience shows that in the range of the optical frequencies, even if an excellent resolution can be obtained, it not possible to penetrate the most common media. On the contrary, frequency lower than few GHz can penetrate low-loss dielectric materials, giving the possibility of inspecting the internal nature of the considered object by means of non-destructive procedures. Generally speaking, when an electromagnetic wave impinges on an object having arbitrary shape and material, it induces conduction or polarization currents, that in turn radiates an electromagnetic field that is dependent on its electrical properties. By suitable measuring and elaborating this scattered field, one is potentially able to obtain unique and valuable information on the investigated scenario. The wide class of problems that aims at recovering electrical and geometrical properties of unknown scatterers embedded in inaccessible regions illuminated by known primary sources are typically named as *inverse problem*. Theoretically, they are said inverse because as they simply represent the counterpart of a class of the problems, called direct, that for historical reasons have been extensively studied. However, from a physical viewpoint, they are not on the same level: the direct problem is often considered 'more important' and for this reason in the past has attracted the attention of the scientific community much more than the inverse one. Anyway a very simple definition can be given: an inverse problem consists in founding an unknown cause (the scatterer in our case) by starting from known consequences (the measured scattered electromagnetic field).

Since we will consider inverse problems in the framework of GPR applications, we will talk in this part of the present thesis of *Microwave Tomography*, being the second term derived from the ancient Greek *tomos*, ‘slice’ or ‘section’ and *graphō*, meaning ‘to write’. The interest in Microwave Tomography (MT) techniques arose contextually with the invention of radar. In fact, by starting from the second half of the 20<sup>th</sup> century it has extensively applied in many applicative contexts wherein non-invasive and non-destructive procedure are required, such as for instance medical diagnostics [69], geophysical and geological probing [70], preservation of cultural heritage [71, 72] and monitoring of sub-surface services [73]-[75].

With regard to general sub-surface applications, MT has demonstrated to be a valuable tool to detect, localize, and reconstruct buried objects by starting from GPR data. Indeed, even if a number of different procedures and algorithms have been already developed [42], they have shown non-trivial limitations. First of all, since the radargram (i.e., the most common outcome for a GPR survey) is usually plotted assuming that velocity of the wave in the investigated medium is constant, it may give rise to misleading results deriving from possible presence of inhomogeneities. In addition, they are not able to provide exhaustive information about shape and electric properties of the investigated target, allowing only detection and rough localization of them; moreover, its interpretation strongly depends on the user’s expertise and on its subjective evaluation. Consequently, as can be easily understood from the above arguments, use of MT technique in the GPR framework, may lead to a remarkable improvement in the interpretation and evaluation of the final outcome. For these reasons, this class of topic has been widely investigated in the past years and various algorithms have been designed and tested.

It is important to note that, to reconstruct the permittivity profile of a probed object, a solution of an inverse scattering problem is required, based on an appropriate model accounting for the electromagnetic interactions between transmitting and receiving antennas, hosting medium and scattering objects. However, we have to consider that the solution of the integral equation usually modeling the inverse scattering problem is not a straightforward task. As a matter of fact, due to particular analytical properties of the kernel of the scattering operators, the problem is inherently ill-posed [76]. A definition of this concept and the consequences on the performances will be discussed in the next sections.

However, various strategies such as the Tikhonov regularization [76] and other ones aimed at exploiting available a priori information [77] have been proposed in the past. The solution of the inverse problem is further complicated by the non-linearity of the relation between data (i.e., the scattered electromagnetic field from the buried object) and unknowns (its permittivity or conductivity profiles). Several linearized models have been proposed in the literature, in the following the Born approximation [88] will be extensively described. It is worth mentioning that applying MT techniques on scattered data from the investigated subsurface to produce images entails many other difficulties. As an example, when inhomogeneous environments have to be tackled, the problem is further complicated by the necessity of accounting for the discontinuities between different layers and the involved interactions with the buried objects. In addition, when data are derived by GPR surveys one has to face with a reduced illumination, that strongly shrinks the amount of information in the data. Moreover, to completely characterize the integral equation modeling the problem at hand, one should have available an analytical model of the antennas that transmit and collect the electromagnetic field radiated by the objects, as well as the Green's function of the problem, which is related to the field scattered by an ideal point target buried in the considered scenario. In recent times various authors have extensively analyzed the capabilities of microwave tomographic algorithms to localize and reconstruct buried objects, both in idealized condition and in more realistic cases [78]. As a matter of fact, it has been seen that, while preventing the possibility of obtaining quantitative information on the dielectric permittivity and electric conductivity of the targets, linear inverse scattering approaches can give well-focused images of the internal structure of the investigated region providing reliable information on the presence, location, and shape of hidden targets.

In this part of the present work, developed in collaboration with the Institute of the Electromagnetic Sensing for the Environment of Naples, a well-established imaging procedure has been applied to both numerical and experimental GPR data presented and discussed in the previous sections. In particular, we aim at testing the capability of this kind of algorithm to localize and provide information about shape and dimension of a buried object in quite challenging operative conditions. Specifically, we consider here targets having size comparable with the dominant wavelength and possibly placed in the near-field region of

the considered antenna. It is worth noting that the electrical parameters of the considered scenario (permittivity of both hosting medium and scatterers) are usually chosen to virtually reproduce a shallow Martian subsurface. Both two-dimensional and three-dimensional versions of the same tomographic algorithm have been applied, with the aim of providing useful information also for 3D more realistic cases. In this way the capabilities of this kind of approach to obtain further useful information with respect to those retrievable from a typical radargrams have been fully addressed.

In conclusion, as a further contribution to the Born-approximation based Microwave Tomography, we investigate here also the potential improvements achievable by taking into account that in general the scattering experiment is not activated by an ideal source, as typically done so far, but through a real transmitting antenna, having its own radiation pattern. To do this, we exploit our full-wave implementation (the same developed for the solution of the relevant direct problem) to numerically model the incident field radiated by the considered antenna. Hence, several examples are provided to assess the benefits reachable if the radiation pattern of the antennas is taken into account in the implementation of the tomographic approach, i.e., in the expression of the incident field and the Green's function, which are the key elements of the imaging problem formulation. Moreover, two figures as the spectral content and the point spread functions are used to carry out a theoretical analysis, which allows us to outline some general considerations on the performance of this advanced approach in terms of reconstruction capabilities, expected when directive antennas are used.

## 6. Microwave Tomography

### 6.1. Scattering equation

As is well-known, the interactions between the electromagnetic signal radiated by a GPR antenna and scattered by a buried target are governed by the Maxwell equations. Consequently, in order to give an overall description of this problem, extensively faced in the next sections, we start here from the very beginning, briefly deriving the scattering equation. Let us assume that the object illuminated by the GPR antenna is characterized by a permittivity  $\varepsilon$  and a permeability  $\mu$  and is buried in a homogeneous and infinite medium, in turns characterized by  $\varepsilon_b$  and  $\mu_b$ . In this context, in addition to the *unperturbed* or *incident* field, usually denoted by  $\mathbf{E}_{inc}$  and  $\mathbf{H}_{inc}$ , also a *perturbed* overall field is present, indicated by  $\mathbf{E}$  and  $\mathbf{H}$ . It is important to note that the perturbed field is the only one that can be measured in the presence of a scatterer, and that the incident electric (or dually magnetic) field is a known quantity, that can be expressed in term of the Green function of the problem as follows

$$\mathbf{E}(\mathbf{r}) = j\omega\mu \int_V \mathbf{J}_0(\mathbf{r}') \cdot \underline{\mathbf{G}}(\mathbf{r}, \mathbf{r}') d\mathbf{r}' \quad (6.1)$$

Additionally, the difference between the perturbed field (i.e., the field when the object is present) and the unperturbed field (i.e., the field when the object is not present) is called the *scattered* field, hence we can write

$$\mathbf{E}_s(\mathbf{r}) = \mathbf{E}(\mathbf{r}) - \mathbf{E}_{inc}(\mathbf{r}) \quad (6.2)$$

$$\mathbf{H}_s(\mathbf{r}) = \mathbf{H}(\mathbf{r}) - \mathbf{H}_{inc}(\mathbf{r}). \quad (6.3)$$

This means that the scattered field can be related to the presence of a target and to the interaction between the incident field and the target

itself. It is finally worth to mention that often the perturbed field  $\mathbf{E}$  is named as *total fields*. As is the case for most of GPR applications, if the target is unknown, one can deduce some piece of information on it starting from a set of measurements of the total field, that anyway can be collected only outside the unknown object, usually along one or more parallel scan lines. This kind of problem is very challenging and belongs to the family of the mentioned *inverse problems*. For a half-space configuration, typical for GPR applications, the incident field and the value of  $\varepsilon_b$  and  $\mu_b$  are assumed known for every  $\mathbf{r}$ . On the contrary, the volume  $V$  and the distributions of  $\varepsilon(\mathbf{r})$  and  $\mu(\mathbf{r})$  are unknown quantities; of course, the total electric and magnetic field,  $\mathbf{E}(\mathbf{r})$  and  $\mathbf{H}(\mathbf{r})$ , are known quantities only outside the volume  $V$  occupied by object. Usually it is measured at a discrete set of points. It has to be noticed that in most applications some *a priori* informations about the objects that one wants to localize and reconstruct could be available, being essential to limit the region of space wherein the solution of the inverse problem is searched. In order to find the equation connecting the scattered field with the dielectric features of the target in a free space region, we can start by the integral form of the Maxwell equation (see [1] and [79] for further details); anyway another interesting strategy, obtained in half-space conditions by starting from the differential form of the Maxwell equation can be found in [80]. Considering a surface  $S$  (whose unit normals  $\mathbf{n}_0$ ) delimited by a contour  $C$ , for a linear, stationary and isotropic medium, it is possible to write in harmonic regime

$$\oint_C \mathbf{E}(\mathbf{r}) \cdot d\mathbf{l} = -j\omega \int_S \mu(\mathbf{r}) \mathbf{H}(\mathbf{r}) \cdot \mathbf{n}_0 ds \quad (6.4)$$

$$\oint_C \mathbf{H}(\mathbf{r}) \cdot d\mathbf{l} = j\omega \int_S \varepsilon(\mathbf{r}) \mathbf{E}(\mathbf{r}) \cdot \mathbf{n}_0 ds + \int_S \mathbf{J}_0(\mathbf{r}) \cdot \mathbf{n}_0 ds \quad (6.5)$$

Analogously, the incident field satisfies the following equations

$$\oint_C \mathbf{E}_{inc}(\mathbf{r}) \cdot d\mathbf{l} = -j\omega \int_S \mu_b(\mathbf{r}) \mathbf{H}_{inc}(\mathbf{r}) \cdot \mathbf{n}_0 ds \quad (6.6)$$

$$\oint_C \mathbf{H}_{inc}(\mathbf{r}) \cdot d\mathbf{l} = j\omega \int_S \varepsilon_b(\mathbf{r}) \mathbf{E}_{inc}(\mathbf{r}) \cdot \mathbf{n}_0 ds + \int_S \mathbf{J}_0(\mathbf{r}) \cdot \mathbf{n}_0 ds \quad (6.7)$$

Subtracting the two previous pair of integral equations we have

$$\oint_C [\mathbf{E}(\mathbf{r}) - \mathbf{E}_{inc}(\mathbf{r})] \cdot d\mathbf{l} = -j\omega \int_S [\mu(\mathbf{r})\mathbf{H}(\mathbf{r}) - \mu_b(\mathbf{r})\mathbf{H}_{inc}(\mathbf{r})] \cdot \mathbf{n}_0 ds \quad (6.8)$$

$$\oint_C [\mathbf{H}(\mathbf{r}) - \mathbf{H}_{inc}(\mathbf{r})] \cdot d\mathbf{l} = j\omega \int_S [\varepsilon(\mathbf{r})\mathbf{E}(\mathbf{r}) - \varepsilon_b(\mathbf{r})\mathbf{E}_{inc}(\mathbf{r})] \cdot \mathbf{n}_0 ds \quad (6.9)$$

Thus, according to equation (6.2), we obtain

$$\oint_C \mathbf{E}_s(\mathbf{r}) \cdot d\mathbf{l} = -j\omega \int_S \mu(\mathbf{r})\mathbf{H}(\mathbf{r}) - \mu_b(\mathbf{r})[\mathbf{H}(\mathbf{r}) - \mathbf{H}_s(\mathbf{r})] \cdot \mathbf{n}_0 ds \quad (6.10)$$

$$\oint_C \mathbf{H}_s(\mathbf{r}) \cdot d\mathbf{l} = j\omega \int_S \varepsilon(\mathbf{r})\mathbf{E}(\mathbf{r}) - \varepsilon_b(\mathbf{r})[\mathbf{E}(\mathbf{r}) - \mathbf{E}_s(\mathbf{r})] \cdot \mathbf{n}_0 ds \quad (6.11)$$

Now, by introducing the equivalent electric and magnetic sources

$$\mathbf{M}_{eq}(\mathbf{r}) = j\omega[\mu(\mathbf{r}) - \mu_b(\mathbf{r})]\mathbf{H}(\mathbf{r}) \quad (6.12)$$

$$\mathbf{J}_{eq}(\mathbf{r}) = j\omega[\varepsilon(\mathbf{r}) - \varepsilon_b(\mathbf{r})]\mathbf{E}(\mathbf{r}) \quad (6.13)$$

we can finally rewrite equations (6.10) as follow

$$\oint_C \mathbf{E}_s(\mathbf{r}) \cdot d\mathbf{l} = -j\omega \int_S \mu_b(\mathbf{r})\mathbf{H}_s(\mathbf{r}) \cdot \mathbf{n}_0 ds - \int_S \mathbf{M}_{eq}(\mathbf{r}) \cdot \mathbf{n}_0 ds \quad (6.14)$$

$$\oint_C \mathbf{H}_{inc}(\mathbf{r}) \cdot d\mathbf{l} = j\omega \int_S \varepsilon_b(\mathbf{r})\mathbf{E}_{inc}(\mathbf{r}) \cdot \mathbf{n}_0 ds + \int_S \mathbf{J}_{eq}(\mathbf{r}) \cdot \mathbf{n}_0 ds \quad (6.15)$$

By comparison of equations (6.4) and (6.14) we can conclude that the scattered field can be considered to be generated by an equivalent electric and magnetic density current, both radiating in free space. Such sources have support coinciding with the space region occupied by scatterers and depend on their dielectric properties and on the total internal field, which in turn depends on the incident field. Since we have defined a new set of source (i.e.,  $\mathbf{M}_{eq}$  and  $\mathbf{J}_{eq}$ ), recalling equation (6.1) the scattered electric field produced by an object occupying a volume  $V$  can be expressed in integral forms as

$$\mathbf{E}_s(\mathbf{r}) = j\omega\mu_b \int_V \mathbf{J}_{eq}(\mathbf{r}') \cdot \underline{\mathbf{G}}(\mathbf{r}, \mathbf{r}') d\mathbf{r}' + \int_V \nabla \times \mathbf{M}_{eq}(\mathbf{r}') \cdot \underline{\mathbf{G}}(\mathbf{r}, \mathbf{r}') d\mathbf{r}' \quad (6.16)$$

Let us suppose that the object that we want to localize and reconstruct is non-magnetic; this means that  $\mu(\mathbf{r}) = \mu_0$  and considering equation (6.12) we deduce that  $\mathbf{M}_{eq}(\mathbf{r}) = 0$ . Consequently, the term on the right side of equations (6.16) containing the equivalent magnetic current

density vanishes. We obtain the following simplified expression for the scattered field

$$\mathbf{E}_s(\mathbf{r}) = j\omega\mu_b \int_V \mathbf{J}_{eq}(\mathbf{r}') \cdot \underline{\mathbf{G}}(\mathbf{r}, \mathbf{r}') d\mathbf{r}' \quad (6.17)$$

Even though an expression for the scattered electric field is now available, the problem at hand is not yet solved, since  $\mathbf{J}_{eq}$  is related to the total electric field  $\mathbf{E}$  and to the permittivity of the target  $\varepsilon$ , which are both unknown function (specifically the total field can be known only on a discrete set of points outside the volume  $V$  of the unknown sought target).

Recalling the first of equation (6.2) and considering (6.17) we can write the total field as follow

$$\mathbf{E}(\mathbf{r}) = \mathbf{E}_{inc}(\mathbf{r}) + j\omega\mu_b \int_V \mathbf{J}_{eq}(\mathbf{r}') \cdot \underline{\mathbf{G}}(\mathbf{r}, \mathbf{r}') d\mathbf{r}' \quad (6.18)$$

Finally, by using equation (6.12), we can write

$$\mathbf{E}(\mathbf{r}) = \mathbf{E}_{inc}(\mathbf{r}) + j\omega\mu_b \int_V \tau(\mathbf{r}') \mathbf{E}(\mathbf{r}') \cdot \underline{\mathbf{G}}(\mathbf{r}, \mathbf{r}') d\mathbf{r}' \quad (6.19)$$

where

$$\tau(\mathbf{r}) = j\omega[\varepsilon(\mathbf{r}) - \varepsilon_b] \quad (6.20)$$

is the so-called *object function*. Of course, in (6.19)  $\mathbf{r}'$  represents the point of the unknown volume  $V$  occupied by the object. Consequently,  $\mathbf{E}(\mathbf{r}')$  is the unknown total field which is penetrated inside the object we want to localize and reconstruct. In direct scattering problem equations (6.19) must be solved for any  $\mathbf{r}$  and the only unknown is the total electric field vector  $\mathbf{E}$ . If the shape of the volume  $V$  is arbitrary, a solution of such equation can be obtained only using a numerical method. In the inverse scattering problem, which is of paramount importance for GPR applications,  $\mathbf{E}(\mathbf{r})$  is assumed to be measurable only outside the volume  $V$ . So, equations (6.19) turns out to be a non-linear integral equation, since both  $\mathbf{E}(\mathbf{r})$  and  $\mathbf{r}$  inside the integral are unknowns; in addition, a variation of  $\tau(\mathbf{r}')$  produces a variation on the value of the field  $\mathbf{E}(\mathbf{r}')$ . It is very important to note that, for the scenario considered here, also the shape of the unknown target is itself not known a-priori. This means that we do not have detailed information about the volume  $V$  occupied by the scatterer; in those cases, it is usual to define an investigation domain  $V_i$ , which by definition includes the support (or volume)  $V$  of the scatterer under test. The scattering formulation reported so far concerns

a general three-dimensional configuration. However, thanks to specific assumptions about the considered object and on the illumination system, the imaging procedure can be simplified by considering a two-dimensional scenario. Specifically, if the object to be localized and reconstructed shows an elongate shape with respect to the space region illuminated by the source, it can be approximated as an infinite cylinder. Of course, this is an assumption that should be carefully verified for each application, but it is highly convenient for many problems faced in this work. In fact, it allows us to manage a 2D scalar problem and to understand which kind of information one can obtain keeping the complexity of the problem low. However, in the next also a 3D configuration will be considered, giving the possibility of analyzing the limitations of such a simplified approach. Under this approximation the cross section of the cylinder can be assumed to be independent of one of the spatial coordinates (e.g., the  $z$  axis), thus we can write

$$\begin{aligned}\varepsilon(x, y, z) &= \varepsilon_0 \varepsilon_r(x, y) \\ \mu(x, y, z) &= \mu_0 \mu_r(x, y)\end{aligned}\quad (6.21)$$

This means that the 2D object has an arbitrary cross section inside the  $xy$  plane. Moreover, we can assume that the incident field is  $z$ -polarized and uniform along  $z$  (TM incident field)

$$\mathbf{E}_{inc}(\mathbf{r}) = E_{inc_z}(\mathbf{r}_t) \mathbf{z}_0 \quad (6.22)$$

where

$$\mathbf{r} = x\mathbf{x}_0 + y\mathbf{y}_0 + z\mathbf{z}_0 = \mathbf{r}_t + z\mathbf{z}_0. \quad (6.23)$$

Now, for symmetry reasons and for a linear and isotropic medium both the scattered and the total electric field turn out to be independent of  $z$  and  $z$ -polarized, allowing us to write

$$\begin{aligned}\mathbf{E}_s(\mathbf{r}) &= E_{s_z}(\mathbf{r}_t) \mathbf{z}_0 \\ \mathbf{E}(\mathbf{r}) &= E_z(\mathbf{r}_t) \mathbf{z}_0\end{aligned}\quad (6.24)$$

Under the previous assumptions equation (6.19) can be rewritten as

$$\mathbf{E}(\mathbf{r}_t) = \mathbf{E}_{inc}(\mathbf{r}_t) + j\omega\mu_b \int_S \int_{-\infty}^{\infty} \tau(\mathbf{r}'_t) \mathbf{E}(\mathbf{r}'_t) \cdot \underline{\mathbf{G}}(\mathbf{r}_t, \mathbf{r}'_t) dz' d\mathbf{r}'_t \quad (6.25)$$

where  $S$  is the cross section of the cylindrical object. Recalling the expression of the free space dyadic tensor [1]

$$\underline{\mathbf{G}}(\mathbf{r}, \mathbf{r}') = -\frac{1}{4\pi} \left[ \mathbf{I} + \frac{1}{k^2} \nabla \nabla \right] \frac{e^{-jk|\mathbf{r}-\mathbf{r}'|}}{|\mathbf{r}-\mathbf{r}'|} \quad (6.26)$$

we have

$$\mathbf{E}(\mathbf{r}_t) = \mathbf{E}_{inc}(\mathbf{r}_t) + j\omega\mu_b \int_S \tau(\mathbf{r}'_t) \mathbf{E}(\mathbf{r}'_t) \cdot \left[ \mathbf{I} + \frac{1}{k^2} \nabla \nabla \right] \int_{-\infty}^{\infty} \frac{e^{-jk_b|\mathbf{r}-\mathbf{r}'|}}{|\mathbf{r}-\mathbf{r}'|} dz' d\mathbf{r}'_t \quad (6.27)$$

Now, since the following relation hold [1], [123]

$$G_{2D}(\mathbf{r}_t, \mathbf{r}'_t) = \frac{j}{4} H_0^{(2)}(k_b|\mathbf{r}_t - \mathbf{r}'_t|) = -\frac{1}{4\pi} \int_{-\infty}^{\infty} \frac{e^{-jk_b|\mathbf{r}-\mathbf{r}'|}}{|\mathbf{r}-\mathbf{r}'|} dz \quad (6.28)$$

we can finally write the 2D scattering equation

$$E_z(\mathbf{r}_t) = E_{inc_z}(\mathbf{r}_t) + j\omega\mu_b \int_S \tau(\mathbf{r}'_t) E_z(\mathbf{r}'_t) G_{2D}(\mathbf{r}_t, \mathbf{r}'_t) d\mathbf{r}'_t \quad (6.29)$$

It is worth mentioning that, when the incident field is a TE field we have that

$$\mathbf{E}_{inc}(\mathbf{r}_t) = E_{inc_x} \mathbf{x}_0 + E_{inc_y} \mathbf{y}_0. \quad (6.30)$$

The problem at hand is still two-dimensional but the vector nature of the integral equations is conserved. In some cases this kind of illumination can provide better results, due to the increased information contained in the measured samples of the new component of the scattered field. However, the simplification provided by the scalar problem is lost. Furthermore, as already described for the 3D formulation of the problem, if the cross section of the object is unknown (as for most of GPR applications), a two-dimensional investigation domain  $D$  which contains a cross section of the illuminated scatterer should be defined, thus we can write

$$E_z(x, y) = E_{inc_z}(x, y) + j\omega\mu_b \iint_D \tau(x', y') E_z(x, x', y') G(x; x', y') dx' dy' \quad (6.31)$$

Finally, if the cylinder under test is made of metal, under a TM illumination equation (6.29) can be rewritten as

$$E_z(\mathbf{r}_t) = E_{inc_z}(\mathbf{r}_t) + j\omega\mu_b \oint_L J_{S_z}(\mathbf{r}'_t) G_{2D}(\mathbf{r}_t, \mathbf{r}'_t) d\mathbf{r}'_t \quad (6.32)$$

where  $L$  is a closed line that determines the profile of the scatterer in the considered transverse plane, and  $J_{S_z}$  is the  $z$  component of the surface current density  $\mathbf{J}_S$  flowing on the metallic profile of the object and representing the unknown of the problem at hand.

### 6.1.1. Contrast function

Very often in the specialized literature the scattering equations is represented in terms of a *contrast function* [80]-[84], defined as follow

$$\begin{aligned}\chi_e(x, y, f) &= \frac{\varepsilon(x, y) - \varepsilon_b}{\varepsilon_b} \\ \chi_m(x, y, f) &= \frac{\mu(x, y) - \mu_b}{\mu_b}\end{aligned}\quad (6.33)$$

where  $\varepsilon_b = \varepsilon_b, \varepsilon_0$  and  $\mu_b = \mu_b, \mu_0$ . In the most general case, because of the dispersion of the medium, the contrast is a function of the frequency, but in many practical applications such a dependence is just neglected, also because it is not easy to predict a reliable dispersion law for the specific case at hand. If we consider again a non-magnetic target we can re-write equations (6.33) as follow

$$\begin{aligned}\chi_e(x, y) &= \frac{\varepsilon(x, y) - \varepsilon_b}{\varepsilon_b} \\ \chi_m(x, y) &= 0\end{aligned}\quad (6.34)$$

It is worth noting that this contrast function is rather similar to the object function consider so far, reported here for convenience

$$\tau(x, y) = j\omega[\varepsilon(x, y) - \varepsilon_b] \quad (6.35)$$

in fact, by suitably recasting the second term (i.e., the scattered electric field) of equation (6.31) we obtain

$$E_s(x, y) = j\omega\mu_b j\omega\varepsilon_b \iint_D G(x, y; x', y') E_z(x, y; x', y') \frac{j\omega[\varepsilon(x, y) - \varepsilon_b]}{j\omega\varepsilon_b} dx' dy' \quad (6.36)$$

thus, recognizing the contrast function in the kernel of the previous integral we can finally write

$$E_{s_z}(x, y) = -k_b^2 \iint_D G(x, y; x', y') E_z(x, y; x', y') \chi_e(x', y') dx' dy' \quad (6.37)$$

This form of the 2D scattering equation is very common and represents the mathematical link among the scattered field, the Green function of the problem, the internal electric field and the dielectric features of the illuminated target.

### 6.1.2. Half-space 2D scattering equations

In the previous section the scattering equation in the more general case (i.e., when a scatterer is illuminated in the free space) has been outlined. However, if we are considering a GPR scenario, a rigorous approach cannot be based on this kind of hypothesis. In simple realistic case the GPR antenna is placed at the interface between two smooth dielectric media, then to give a coherent mathematical representation of the scattering equation we have to consider two different Green functions, one accounting for the field radiated in the upper medium and one for the lower medium, where the object under analysis should be buried. To do this we can directly start by a differential representation of the Maxwell equation, following the procedure outlined in [80] for the 2D case (by considering  $y_s = 0$ , meaning that the source point is on the  $y$  axis). We report here only the final results, which give us the possibility to introduce the distinction between *internal* and *external* Green function.

$$E_z(x_s; x, y) = E_{inc}(x_s; x, y) + k_b^2 \iint_D G_i(x; x', y') E_z(x_s; x', y') \chi_e(x', y') dx' dy' \quad (6.38)$$

$$E_{s_z}(x_s; x_0, y_0) = k_b^2 \iint_D G_e(x_0; x', y') E_z(x_s; x', y') \chi_e(x', y') dx' dy' \quad (6.39)$$

where  $(x, y)$  is the generic point within the *investigation* domain,  $x_s$  is the source point within the *observation* domain (i.e., a line) and  $(x_0, y_0)$  is the receiving point within the *observation* domain.  $G_i$  and  $G_e$  in equation (6.38) and (6.39), respectively, are the dielectric internal and external Green functions. It is important to highlight that this function are proportional to the electric field generated by spatially impulsive source buried in a homogeneous soil. More specifically, the internal one is proportional to the field in the soil, whereas that external is proportional to the field in air. This makes the Green functions square integrable functions, since they are essentially electromagnetic fields generated by finite energy sources.

It is important to note that the scattering equations is outlined here in the frequency domain; this forces us to consider always the total field, because the incident and scattered field are defined at every point of the investigation domain. However real data are collected in time domain, but considering a Fourier Transform operation we can insert the data inside the scattering equations. Consequently, under specific conditions (e.g., if incident and scattered field do not overlap) we can consider only

the scattered contributions, merely subtracting the incident field on both sides of equation (6.38). Unfortunately, this operation in most realistic cases is not feasible, because of non-ideal effects of the illuminated scenario, but also due to the presence of noise and clutter on the data. Anyway, some advanced operations of background removal have been introduced by various author [80] [42]; its description is anyway beyond the scope of the present work.

## 6.2. Ill-posedness and nonlinearity

The solutions of the scattering equations introduced in previous sections belong to the wide class of the *inverse problems*. As outlined so far, in GPR prospecting we want to retrieve some piece of information about the illuminated object by starting from measurements of the electric scattered field data, gathered outside the probed volume and generated by known sources. As said, the reason why this problem is called ‘inverse’ is connected to historical issues: the way to approach the problem is practically reversed with respect to another problem conventionally labeled as ‘direct’ or ‘forward’ scattering problem. It consists in the calculation of the field scattered from a known dielectric permittivity, under the radiation of electromagnetic waves radiated by known sources and is defined *well posed*. Mathematically, this means that for such class of problem the solution *exists*, is *unique*, and has a *continuous* dependence on the data (this definition has been firstly introduced by Hadamard in 1923). The first two conditions are quite intuitive, whereas the last one, if satisfied, involves the fact that a small error on the data must induce small error on the solution. In applications such as GPR prospecting, this means, as an example, that small error in the evaluation of the permittivity of the background medium will produce small error in the evaluations of the scattered field.

A problem is said to be *ill-posed* when at least one of the conditions previously outlined for the well-posedness is not satisfied. With regard to the inverse problem related to GPR data processing, the most relevant issue is the non continuous dependence of the solution on the data. This means that even a small error on the scattered field (e.g., additive thermal noise) can induce meaningful error in the reconstruction of the dielectric characteristics of the background scenario. This does not mean that ill-posed problem do not have physical sense, however to outline a solution an operation of *regularization* is always necessary. There are

endless possibilities to regularize an inverse problem, all based on the general idea to renounce to an ideal solution, looking indeed for suitable, not fully detailed, refined and robust results. Various authors have given a mathematical demonstration of the ill-posedness of an inverse scattering problem [76]-[87], we are not giving here detailed description of this issue. Generally speaking, let us consider a specific class of contrast functions represented by a sinusoidal (i.e.,  $\sin(kx) \sin(ky)$ ) variations inside a finite investigation domain  $D$ . Additionally, let us consider the limit value of the scattering equations when the oscillations of the contrast become faster and faster (i.e., for  $k \rightarrow \infty$ ). Expressing the total field  $E$  in (6.38) in term of the so-called Born series, we will find in every term of such a series the following integral (multiplied by other terms whose kernel are not depending by the incident field)

$$k_b^2 \iint_D G_i E_{inc} \chi_e dx' dy' \quad (6.40)$$

Since this integral is composed of the contrast function times a square integrable function (independent from it), for the Riemann-Lebesgue lemma, we can easily show that it vanishes for  $k \rightarrow \infty$ . Consequently, in this limit (for a detailed demonstration see [88]), it is possible to show that the series decomposition of the total field  $E$  converges uniformly at the incident field  $E_{inc}$ . Therefore, we can state that very fast oscillating and limited contrasts will be transparent to the radiation. This reasoning could be repeated also for a contrast given by the sum of a slow and a fast oscillating contribution: we will find that the internal field is influenced only by the slow varying portion of the contrast profile. Now, considering  $E = E_{inc}$  inside equation (6.39) we have

$$E_{s_z} \approx k_b^2 \iint_D G_e E_{inc_z} \chi_e dx' dy' \quad (6.41)$$

Since both the external Green functions and the incident field are square integrable functions independent from the contrast, we have that in the limit for  $k \rightarrow \infty$  the contrast  $\chi_e$  produces a null scattered field (i.e., it represents an invisible target). To generalize the approach we can consider that any square integrable function  $\chi_e$  can be expanded, within the investigation domain  $D$ , along its Fourier series, then any target can be generically seen (with a certain degree of continuity) as composed by a slow varying part plus a fast varying part. As highlighted previously, at a certain point the fast oscillating part becomes more and more transparent, and in the considered limit completely transparent.

Consequently, due to uncertainties on the data it will become more and more difficult (and eventually impossible) to retrieve the profile of the object. We have finally demonstrated in this way the ill-posedness of the inverse scattering problem, which basically involves the impossibility to retrieve all the details of the considered target.

The non-linearity of the problem can be more simply explained. As is clearly visible in equation (6.38) the electric field inside the investigation domain depends on the contrast function. Consequently, if in (6.38)  $\chi_e$  is multiplied by any arbitrarily constant, the scattered field will be not just multiplied for the same constant, because in meantime the internal field has changed too. Generally speaking, we can say that any mathematical relationship  $f$  between two quantities is said to be linear when, given two value of the independent variable  $x_1$  and  $x_2$  and two scalar quantities  $a$  and  $b$ , the following property holds

$$f(ax_1 + bx_2) = af(x_1) + bf(x_2) \quad (6.42)$$

If this property is not satisfied the physical phenomenon at hand is nonlinear. Unfortunately, the inversion of a nonlinear relationship is in general more difficult than the inversion of a linear one, due to possible presence of false solutions or local minima. In the more general case, one looks for the minimum of nonlinear function by making use of the gradient of the curve in any point, following the direction where the gradient itself vanishes. Of course at a certain point one reaches a minimum of the function: if the starting point of the procedure is in a suitable position the actual global minimum can be obtained; but if the starting point does not lie in the valley of the global minimum (not individualized a priori) the procedure will converge at a local minimum, and it will be erroneously interpreted as the solution of the problem at hand. Just as an example, a method to face the problem of the local minima consists in repeating the minimization procedure starting from several point, chosen and updated by means of ad-hoc stochastic criteria. In this way the probabilities to achieve the global minima increase, at a price of an increased computational burden. By exploiting both *deterministic* or *statistical* minimization procedure, nonlinear approaches can require heavy computational effort, compromising the possibility of applying this technique for large-scale problems. Specifically, GPR data processing involve problems that are very large with respect to the considered wavelength, consequently a class of approximated linear algorithms are usually exploited.

### 6.2.1. Born approximation

If the Born series for the scattered field is truncated to the first term we obtain the first-order Born Approximation (BA) [80, 88], which, as we have seen in previous section, basically means that the internal electric field inside the unknown object is assumed equal to the impinging field. Of course, under the BA the scattering is approximated as a linear phenomenon, thus it is not affected by the problem of local minima. This means that it is possible to carried out faster and easier processing algorithms with respect to actual nonlinear model. Moreover, even though is less intuitive, BA allows a noticeable insight about the characteristics of the expected results, that are essentially based on the spatial filtering properties of the linear scattering operator, that in turns depends on the impulsive response of the considered antenna. It is very interesting to note that from a physical point of view, the BA tends to neglect the mutual interactions between any two different buried target or (which is mathematically the same) between two different parts of the same target. Specifically, if we consider two different very small object, whose contrast is a low norm function, we can assume that each of them, in absence of the other one, would provide a scattered field given by equation (6.39), where the contrast is a function that describes each of the two targets in turn. Consequently, the integral term in the scattering equation (see (6.38)) can be regarded as a negligible perturbation with respect to the incident field. However, if the two targets are present at the same time (so that the contrast is given by the sum of the contrasts relative to each of the two targets separately considered), they interact with each other, and consequently the comprehensive scattered field is not simply given by the sum of the scattered field that each of them would produce in absence of the other. This interaction is the mathematical genesis of the nonlinearity, because it makes the *internal total* field different from the *internal incident* field. Let us conclude highlighting that in framework of GPR a ‘weak scatterer’ is defined as just an object for which the internal field, and (in case of magnetic targets) its first-order spatial derivatives, can be approximated with those of the incident field. The ‘weakness’, in particular, is a feature not only related to the maximum level of the contrast, but also to the electrical size of the buried target (which implies a dependence on the frequency), to the shape and to the nature of the background medium (homogeneous or layered, lossless or lossy). It is important to emphasize that, independently from the validity of the BA in the current situation (with GPR field data, very often BA is not valid),

the secondary sources that generate the scattered field under BA have the same support of the actual secondary sources, and this support is just the extension of the buried targets. Now, assuming that both the incident and the actual internal fields are supported throughout the entire investigation domain, it is clear that, either under the exact model or under the BA, the support of the secondary source is equal to the support of the dielectric contrast, which is just the extension of the buried targets. Therefore, it is licit to expect that in many cases the position, the size, and (under certain limits) the shape of the buried targets can be satisfyingly retrieved under BA, even in cases when the targets are not weak [89, 90]. This has also been widely shown experimentally [91, 92]. Let us also state that ‘satisfyingly’ is a rather generic term: it means that the achievable results are useful for some applications but does not mean that the geometrical reconstruction is ‘perfect’ or resembles those obtainable with an optic system. In particular, the achievable reconstruction is affected by the filtering properties of the linear scattering operator (i.e., related to the antenna and to the observation domain); consequently, in any case, in situations beyond the limits of the BA, we will not achieve a quantitative reconstruction of the electromagnetic characteristics of the buried object.

### 6.3. Microwave tomographic algorithm

The microwave tomographic algorithm considered here has been developed and extensively tested by some authors [83, 93] in the last years assuming a homogeneous half-space and a 2-D geometry as a reference scenario. The adoption of the 2-D geometry is theoretically well suited to simulate only elongated objects, whereas we consider here canonical shaped targets. In addition, it introduces a further approximation for the transmitting and receiving modeled antennas that should be in principle treated as 3-D sources. Anyway a three-dimensional version of the proposed algorithm is also considered, giving the possibility of evaluating the impact of this kind of assumption. The geometry of the problem typically consists of two half-spaces (air and soil) separated by a planar interface. The upper half-space is a free space, whilst the lower one is described by a relative dielectric permittivity  $\epsilon_b$  and conductivity  $\sigma_b$  and is non-magnetic (i.e.,  $\mu = \mu_0$ ). The incident field source is assumed to be a time-harmonic (with  $e^{j\omega t}$  time dependence, where  $\omega = 2\pi f$ ) line current source (TM-polarization), of infinite extent, and

invariant along one of the Cartesian axis ( $z$ ). It radiates within the defined frequency band ( $f_{min}, f_{max}$ ), determined by the bandwidth of the transmitted numerical or experimental pulse and by the antenna system. Both multi-monostatic and multi-bistatic GPR configuration is assumed; in the first case the location of the transmitting and receiving antennas coincides at each observation point, whereas in the other one shows an offset (chosen here as  $d = 0.19$ ) m. The objects are considered invariant along the direction of extension of the line sources, and their section is a priori known to reside within the investigation rectangular domain. The objects are searched by assuming them as actual unknowns of the problem and represented by a relative dielectric permittivity profile  $\varepsilon_t(x, z)$ , and by a conductivity profile  $\sigma_t(x, z)$  inside  $D$ . The problem is then recast in terms of the so-called unknown contrast function, already introduced in section 6.1.1 and reported here for convenience

$$\chi(x', y', f) = \frac{\varepsilon_c(x', y') - \varepsilon_{c_b}}{\varepsilon_{c_b}} \quad (6.43)$$

where

$$\begin{aligned} \varepsilon_c(x', y') &= \varepsilon_0 \varepsilon_t(x', y') - j\sigma_t(x', y')/\omega \\ \varepsilon_b &= \varepsilon_0 \varepsilon_{c_b} - j(\sigma_b/\omega) \end{aligned} \quad (6.44)$$

Under the Born Approximation, as discussed in section 6.2.1, the relationship between the unknowns and the data is provided by the linear integral equation in the frequency domain

$$E_s(x, x_s, \omega) = k_b^2 \iint_D G_e(x_0 = x_s; x', y', \omega) E_{inc}(x_s; x', y', \omega) \chi(x', y') dx' dy' \quad (6.45)$$

where  $E_s$  denotes the scattered electric field probed at  $x_s$  when the source is located at the same point  $x_s$  on in  $x_s + d$  and  $k_s$  is the wavenumber in the lower half-space. The scattered field is collected over an observation domain at the interface at step  $\Delta < \lambda$ . The scattered field  $E_s$  is defined as the 'difference' between the total field and the incident field. The former is the field backscattered by both the buried target and the air/soil interface, while the latter only accounts for the reflection at the air/soil interface. According to the reference scenario outlined previously, the quantities defining the kernel of linear integral equation (6.45) have the following meaning. The external Green's function  $G_e(x_0 = x_s; x', y', \omega)$  accounts for the electric field radiated at the antenna position  $x_s$  by a line source electric current with unit strength located at  $(x', y')$ , while

$E_{inc}(x_s; x', y', \omega)$  is the electric field radiated by the line source located at  $x_s$ , at the generic point  $(x', y')$  of the lower medium, for the case when the target is not present.

In order to achieve the robustness of the solution against the noise on data and the uncertainties of the parameters of the reference scenario, the inversion of the linear operator in (6.45) has been performed thanks to the truncated singular value decomposition (TSVD) expansion [76]

$$\chi = \sum_{n=1}^N \frac{1}{\sigma_n} \langle \mathbf{E}_s, \mathbf{v}_n \rangle \mathbf{u}_n \quad (6.46)$$

where  $[\sigma_n, \mathbf{v}_n, \mathbf{u}_n]_{n=0}^K$  is the singular system of the matrix  $\mathbf{L}$ , arising from the discretization of the operator in equation (6.45),  $\langle \cdot, \cdot \rangle$  denotes the scalar product in the data space and  $K$  denotes the number of measurements, being  $N \leq K$ . By restricting the solution space to the one spanned by the first  $N + 1$  singular functions  $u_n$ , this regularization scheme does not amplify the effect of errors and uncertainties on data, so that the solution is made stable. The choice of the index  $N$  is performed with regard to ‘the degree of regularization’ that one wants to apply in the inversion procedure. In particular, the reconstruction results will be given as a spatial map of the modulus of the retrieved contrast function; the regions where it is significant different from zero indicate the location of the buried objects. As a further simplification, typically considered as appropriate if the antenna is placed in direct contact with the lower medium, the probed scenario can be schematized as homogeneous (i.e., the presence of the two half-spaces is not considered), whose dielectric constant is equal to  $\varepsilon_b$ . We do not give here any result obtained by applying this algorithm to canonical shaped dielectric objects, because in the next chapter a number of interesting reconstruction will extensively discussed to compare performances of this standard approach with those achievable by means of an advanced implementation.

#### 6.4. Reconstruction of PEC scatterers

Shape reconstruction of strongly scattering objects, especially metallic ones, is also an important issues in the frameworks of GPR applications. A number of method have been developed so far, including linearized techniques based on physical optics (PO) or Kirchhoff approximation. It is important to note that under this hypothesis the relationship be-

tween unknown and data is linear, but unlike the case of dielectric target (which is based on the image of the contrast functions) here the reconstruction provides an image corresponding to the support of the induced surface currents distribution on the illuminated region. In the specialized literature, also various nonlinear iterative inverse scattering techniques are proposed as optimization problems, but that based on the PO approximations does not suffer from local minima problem and is computationally less expensive. Of course, as already highlighted in the previous section, absence of local minima favorably affects the reliability of the results and the low computational burden allows us to deal with electrical large investigation domain. However, PO requires that the radii curvature of the illuminated scatterers to be large as compared to the impinging wavelengths, and in case of a complex scenario (in term of number of targets) interactions are not accounted for. Additionally, the considered target should be convex. For all these reasons, PO is usual classified as a *high-frequency single-scattering* model. Under these hypothesis, it has been shown that PO provides good approximations (in terms of small errors) both for *direct problem* and *inverse problem* [94, 95]. Specifically, when a shape reconstruction problem is faced, it possible to relax the previous assumption and a Kirchoff-based inverse approach is able to give useful information even in the case of objects whose extent is comparable to the probing wavelength.

The scattering equation for PEC target, conveniently reported in the following, has been already introduced in section 6.1, where the overall model of the scattering phenomena has been outlined. We consider here an object invariant along the  $y$  axis and a line source oriented along the same direction, thus orthogonal to the investigation domain; indeed the  $z$  axis here represents the vertical extension of the probed target, while the  $x$  axis is the scanning direction of the GPR. Recalling equation (6.32) we can write

$$E_z(\mathbf{r}_t) = E_{inc_z}(\mathbf{r}_t) + j\omega\mu_b \int_L J_{S_z}(\mathbf{r}'_t) G_{2D}(\mathbf{r}_t, \mathbf{r}'_t) d\mathbf{r}'_t \quad (6.47)$$

where  $S$  and  $J_s$  are the unknown to be reconstructed. Within the above hypotheses, under the Kirchhoff approximation, the scattered field  $E_s$  collected in the upper half-space for  $z = 0$  at each  $\omega$ , when the transmitting and receiving antenna are at the source abscissa  $x_s$ , is given as

$$E_z(x_s) = -j\omega\mu_b \int_L J_{PO_z}(x_s, y, x) G_e(x_s, x, y) dL \quad (6.48)$$

where  $L$  denotes the contour of the scattering object and  $G_e$  is the external Green function of the problem for the angular frequency  $\omega$ ; for an half-space geometry we have the following integral expression

$$G(x_s, x, y) = -\frac{j}{2\pi} \int_{-\infty}^{+\infty} \frac{e^{-jk_{y_2}y}}{k_{y_1} + k_{y_2}} e^{-jk_x(x_s-x)} dk_x \quad (6.49)$$

where  $k_{y_i} = \sqrt{(k_i^2 - k_x^2)}$ ,  $k_i$  being the wavenumber of the  $i$ -th medium ( $i = 1, 2$ ) and  $k_x, k_y$  the spectral variable along  $x$  and  $y$  respectively. Moreover,  $J_{PO}$  is the physical-optics surface current density, namely

$$J_{PO}(x_s, x, y) = \begin{cases} (2\mathbf{n}_0 \times \mathbf{H}_i(x_s, x, y)) \cdot \mathbf{z}_0 & \text{on } L_i \\ 0 & \text{on } L_s \end{cases} \quad (6.50)$$

where  $\mathbf{H}_i$  is the incident magnetic field in the lower half-space when there are no objects (i.e., the magnetic field transmitted in the lower region),  $\mathbf{n}_0(x, y) = (n_x(x, y), n_y(x, y))$  is the outward-directed unit vector normal on the scattered surface at the generic point  $r = (x, y)$ , while  $L_i$  and  $L_s$ , being  $L = L_i \cup L_s$ , are respectively the illuminated and shadowed sides of the scatterer. By accounting for the relationship existing among the electric incident field and the magnetic one, the current density  $J_{PO}$  can be expressed as

$$J_{PO}(x_s, x, y) = \begin{cases} \frac{1}{\pi} \int_{-\infty}^{+\infty} [n_x(x, y)k'_x + n_y(x, y)k_{y_2}] \\ \frac{e^{-jk_{y_2}z}}{k_{y_1} + k_{y_2}} e^{-jk'_x(x_s-x)} dk'_x & \text{on } L_i \\ 0 & \text{on } L_s \end{cases} \quad (6.51)$$

By replacing equations (6.49) and (6.50) in equation (6.48), after some algebra, the scattered field can be rewritten as

$$E_s(x_s) = -\frac{\omega\mu_0}{2\pi^2} \int_{-\infty}^{+\infty} \frac{e^{jk_x x_s}}{k_{y_1}(k_x) + k_{y_2}(k_x)} \int_{-\infty}^{+\infty} \frac{e^{jk'_x x_s}}{k_{y_1}(k'_x) + k_{y_2}(k'_x)} \\ \int_D [n_x(x, y)k'_x + n_y(x, y)k_{y_2}(k'_x)] \delta_L(x, y) \\ e^{-j(k_{y_2}(k'_x) + k_{y_2}(k_x))z} e^{-j(k'_x - k_x)x} dx dy dk'_x dk_x \quad (6.52)$$

where the quantity  $\delta_L(x, y)$  denotes a single-layer distribution and allows us to pass from an integral over the contour of the scatterer to the

integral over the investigation domain  $D$  [76]. According to the above scattering model, the reconstruction problem is stated as the inversion of the equation (6.52), which can be rewritten for all the frequencies belonging to the considered range in a synthetic form as

$$E_s(x_s, \omega) = L[\gamma] \quad (6.53)$$

where the unknown is given by the vector distribution (see [96])

$$\gamma(x, y) = (n_x(x, y), n_z(x, y))\delta_L(x, y) \quad (6.54)$$

Equation (6.53) states a linear integral relationship between the meaningful signal, i.e., the field scattered by the targets, and the unknown *object function*  $\gamma(x, y)$ , which is expressed through the compact operator  $L$  [76, 86]. Being the imaging problem faced as the inversion of the relationship in equation (6.54), as already highlighted in section 6.3, an ill-posed linear problem has to be suitably faced through a regularized inversion scheme [86]. A well-known commonly exploited tool to solve this kind of problems is, as said, the truncated singular value decomposition (TSVD) scheme [76]. Thus, an approximate and stable solution of equation (6.54) is given as

$$\tilde{\gamma} = \sum_{n=0}^N \frac{1}{\sigma_n} \langle \mathbf{E}_s, \mathbf{v}_n \rangle \mathbf{u}_n \quad (6.55)$$

where, as already introduced,  $[\sigma_n, \mathbf{v}_n, \mathbf{u}_n]_{n=0}^K$  is the singular system of the matrix  $\mathbf{L}$ , arising from the discretization of the compact operator in equation (6.53),  $\langle \cdot, \cdot \rangle$  denoted the scalar product in the data space and  $K$  denotes the number of measurements, being  $N \leq K$ . The choice of the  $N$  index is performed in order to ensure a trade-off between the contrasting needs for accuracy and resolution from one side (which should push to increase such an index) and for the stability of the solution from the other side (which should push to limit the increase of the index). As result of our inversion approach, we consider  $\tilde{\gamma} = \sqrt{|\tilde{\gamma}_x|^2 + |\tilde{\gamma}_z|^2}$  (modulus of the vector  $\tilde{\gamma}$ ) as the quantity that can be imaged to obtain a tomographic reconstruction. Finally, it is worth noting that the involved computational time mainly depends on the time needed to fill the matrix  $\mathbf{L}$  and to compute its SVD. Such a time grows up with the number of cells discretizing the investigated domain under test ( $N_{cells}$ ); on the other hand, since  $\mathbf{L}$  does not change once the measurement configuration and the features of the investigated domain have been fixed, they can be

computed off-line and stored in a database. In this way, the involved computational time is drastically reduced and real-time results can be achieved.

#### 6.4.1. Inversion with experimental data

The reconstruction capabilities of the tomographic approach on the experimental data presented in section 4.1 are investigated by applying the inverse scheme just introduced. The results are given in terms of the normalized amplitude of the reconstructed function presented by equation (6.55) with respect to its maximum inside the investigation domain  $D$ . It should be reminded that the tomographic reconstructions here manage critical cases of non-penetrable objects, whose dimensions are comparable with the dominant probing wavelength, buried in the shallow region of the lower half-space. In addition, data are gathered under a reflection measurement configuration, hence most of the information achievable is expected relating to the upper illuminated parts of the targets that give rise to the main scattering effects. Accordingly, only the upper side of the objects is expected to be actually well retrieved.

Measurements have been developed thanks to our experimental setup, already presented in section 4.1. In the following, further details about the overall configuration will be given. The GPR commercial system works in bistatic modality with the source and receiver separated by 19 cm, spanning in the range  $[-70;70]$  cm. The antenna system sweeps along the air-soil interface at 61 spatial points with a step of 2 cm. In particular, the Tx antenna moves between  $[-69.5;50.5]$  cm, whereas the Rx antenna moves within  $[-50.5;69.5]$  cm. The working frequency ranges between  $f_{min} = 0.3$  GHz and  $f_{max} = 1.3$  GHz, with 26 frequencies spaced of 40 MHz (this slightly modified frequency range with respect that nominally presented in section 4.1 is related to the specific evaluation of the effective spectrum of the signal transmitted by the GPR instrument when positioned on the ground-medium surface). The first tomographic reconstruction from measured data is shown in Fig. 6.1 and is referred to the case of a pair of metallic targets already presented in Fig. 6.1, with a cube (9-cm side) and a pyramid (10-cm height and 9-cm side square basis), both located at a depth of 9 cm (for the top parts) and spaced side by side along  $x$  axis of 80 cm. From this figure, one can observe a spot at about  $x = -30$  cm, which correctly accounts for the upper side of the cube and provides a good estimation

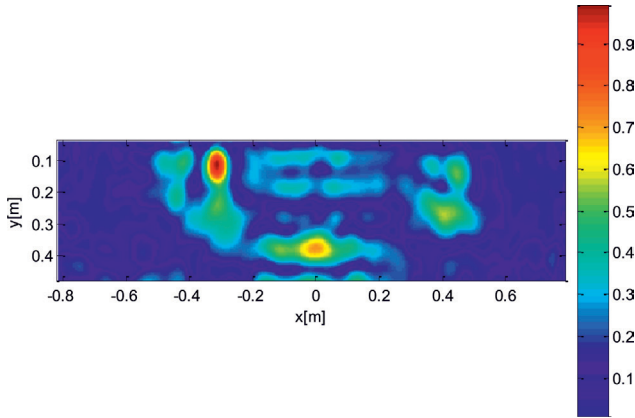


**Fig. 6.1.** Tomographic reconstruction of targets from experimental data for metallic cube and pyramid buried in a sandy soil. Other physical parameters in the text. Copyright © 2013, reproduced courtesy of The Electromagnetics Academy.

of the major reflecting side. The spot at the center of the investigation domain (around  $x = 0$ ), at depth of about 30 cm, is concerned with the reflection from the bottom of the dielectric box (as already emphasized in the radargram of Fig. 6.1). Finally, the spots at about  $x = 50$  cm are concerned with the location of the main reflecting areas of the pyramid shape. A further inversion result from measurements refers to the case of parallelepiped and cylinder targets, whose dimensions were already presented. The scatterers were placed in this case with their major length perpendicular to the scanning direction, and again spaced along the  $x$  axis of about 80 cm and 9 cm deep. The relevant tomographic reconstruction is presented in Fig. 6.2. As in the previous case, the main features of the probed scenario can be enlightened from the tomographic reconstruction. The stronger spot at about  $x = -30$  cm accounts for the upper side of the parallelepiped. As above, the wider spot at the center of the investigation domain is concerned with the bottom of the box. Finally, the spot at about  $x = 50$  cm is concerned with the proper cylinder location, whose scattering effect is correctly less strong than that arising from the parallelepiped (the former presenting a round contour instead of a flat face and edges).

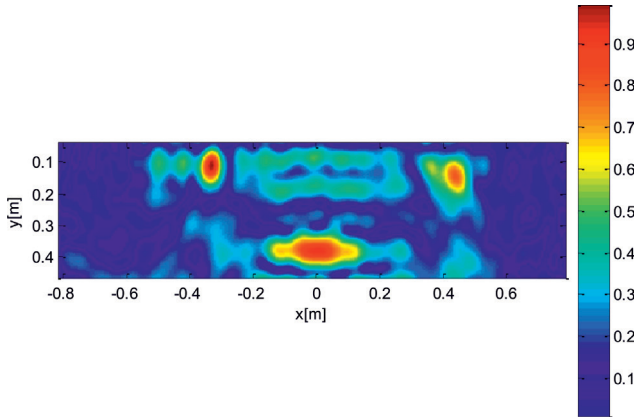


**Fig. 6.2.** Tomographic reconstruction of targets from experimental data for a metallic parallelepiped and a cylinder buried in a sandy soil, with their major lengths perpendicular to the scanning direction. Other physical parameters in the text. Copyright © 2013, reproduced courtesy of The Electromagnetics Academy.

#### 6.4.2. Inversion with numerical data

According to the simulated environment already presented in section 5.3, the investigated domain is in the lower half-space and its half-size along the longitudinal  $x$  axis is equal to  $a = 40$  cm (80 cm overall), while its extent along the depth ranges from  $z_{min} = 1$  cm to  $z_{max} = 50$  cm. The measurement configuration assumes a bistatic modality with source and receiver separated, as said, by an  $offset = 19$  cm. The antenna system is moved along the air-soil interface at 25 spatial points with a uniform step of 3 cm. In particular, the Tx antenna moves between  $[-40; 40]$  cm, whereas the Rx antenna moves within  $[-21; 59]$  cm. The working frequency ranges between  $f_{min} = 0.3$  GHz and  $f_{max} = 1.3$  GHz with 41 discrete frequencies spaced of 25 MHz. The inversion is regularized by the TSVD approach, where the TSVD index  $N$  is chosen to retain in the summation (6.55) the singular values larger than 0.1 times the highest singular value. The first set of results accounts for three buried PEC cubes having different sizes in the simulations (5 cm, 9 cm, and 13 cm) and upper side at depth of 10 cm. Their center is laterally shifted of about 7.5 cm along  $x$  with respect to the center of the investigated domain. The color-plot reconstructions of the 'object function', i.e., the tomographic images, are shown in Figs. 6.3(a,b), and 6.4 for the three cube sizes, respectively. In these figures, as in the following ones, the black lines represent the contour of the actual objects. These corrob-

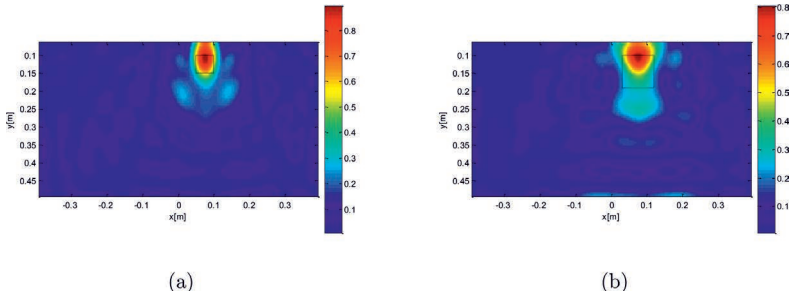


**Fig. 6.3.** Tomographic reconstruction from simulations of three PEC cubes having different sizes (the upper side of the object is at 10 cm depth from the interface): (a) 'small' cube with side 5 cm; (b) 'middle' cube with side 9 cm. Other physical parameters are given in the text. Copyright © 2013, reproduced courtesy of The Electromagnetics Academy.

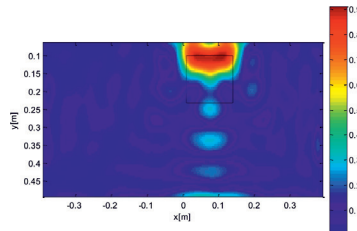


**Fig. 6.4.** As in Fig. 6.3 for a cube having side 13 cm. Copyright © 2013, reproduced courtesy of The Electromagnetics Academy.

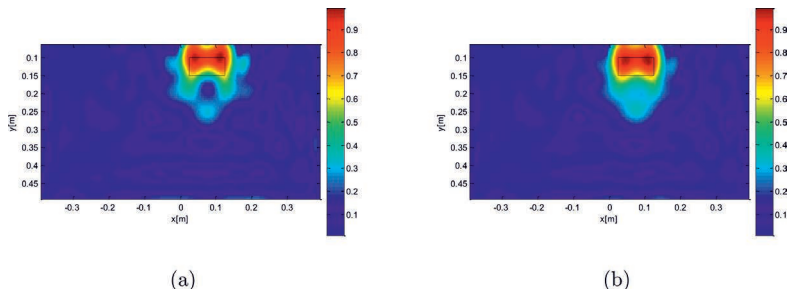


**Fig. 6.5.** Tomographic reconstruction from simulations of buried PEC parallelepiped and cylinder, placed with their major length along the scanning  $x$  direction: (a) parallelepiped; (b) cylinder. Other physical parameters in the text. Copyright © 2013, reproduced courtesy of The Electromagnetics Academy.

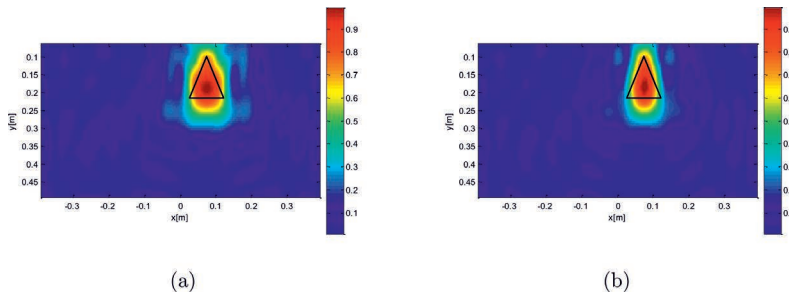


**Fig. 6.6.** Tomographic reconstruction of PEC pyramid and cone from simulations: (a) pyramid; (b) cone. Other physical parameters in the text. Copyright © 2013, reproduced courtesy of The Electromagnetics Academy.

rate that, despite the relevant wavelengths of the signal in the hosting medium are in the range around 15 cm (i.e., actually comparable to the typical dimensions of our scatterers), accurate images are obtained. It is seen that the extents of the upper sides are reconstructed with good accuracy, and this feature is more evident for the larger cubes. Moreover, the main vertical position is properly localized by the peak values of the TSVD reconstructed function. The thickness of the spot along the depth is due to the finite working frequency and is anyway comparable to the ideal resolution limits, given by  $c_0 / (2B\sqrt{\epsilon_b}) = 8.4$  cm, being  $B = 1$  GHz the signal bandwidth. The second set of results concerns two other metallic targets previously introduced: a parallelepiped with length 10 cm and square section with side 5 cm, and a cylinder of the same length and diameter 5 cm, both the objects being 10-cm deep. The two targets are placed with their axis parallel to the scanning  $x$  direction. Fig. 6.5 shows the tomographic reconstructions of the parallelepiped (Fig. 6.5(a)) and of the cylinder (Fig. 6.5(b)). Again, the object function describes quite well the location and size of these scatterers. The third considered numerical data-set is referred to pyramidal and conical metallic targets. Both targets have the same height (10 cm); the pyramid has a square basis with side 9 cm, and the diameter of the conical basis is 9 cm (see Table 4.1); the axis of both targets is placed vertically. Fig. 6.6 gives the tomographic reconstruction of the pyramid (Fig. 6.6(a)) and of the cone (Fig. 6.6(b)). It is interesting to note that the reconstructions are very similar one the other, according to the features of the two shapes in the imaged slice. In particular, the main contribution of the object function appears to be placed slightly below with respect to the upper

edge, due to the reduced scattering effect of the wedge shape.

## 6.5. 3D microwave tomographic algorithm

So far the capabilities of a well-assessed microwave tomographic algorithm to produce two-dimensional images in challenging conditions have been investigated. As discussed, this assumption is well suited only for elongated targets, that keep the same cross-section for distances larger than the probing wavelengths. Even though this hypothesis leads to good results it does not account for the three-dimensional nature of the scattering mechanism. Since we are considering canonical shaped target that do not present any privileged direction of extension, this assumption may be not always adequate to accurately represents more complex configurations of the investigated scenario. Moreover, under this hypothesis, the integral equations modeling the problem is reduced to its scalar version, preventing the possibilities to analyze other components of the scattered electromagnetic (whenever the antenna is able to manage also the components of the field) and to study possible depolarization effects. It is worth mentioning that the 3D imaging procedure outlined in the follow must be clearly distinguishable from a 'pseudo-3D' algorithm, that is simply based on interpolation procedures of a two-dimensional reconstruction developed on different parallel planes sampling the investigated scenario. Incidentally, it has also been demonstrated that this algorithm does not always offer the same performances [97]. The simulated GPR data to be processed have already been described in section 4.5, where a virtual model of a GPR system is placed at the ground interface to derive three-dimensional information on the features of buried dielectric and metallic targets (location, dimension, and shape). Once again the scatterers can have size comparable to the resolution limits and can be placed in the shallow subsurface in the antenna near field. To this aim, the microwave tomographic algorithm presented in section 6.3 has been suitably extended. Data are gathered on a planar surface, along several parallel linear traces. Once again, our approach basically exploits the Born approximation to model the underlining scattering phenomenon [83, 88]. Therefore, the imaging is faced as the solution of a linear inverse scattering problem, wherein the data/unknown relationships account for the dyadic nature of the interaction between the field and the probed materials. In particular, the scattering equations for our 3D scenario has been already introduced in

section 6.1. By suitably recasting equation (6.19) and referring to Fig. 4.23 and 4.24 we can write

$$\mathbf{E}_s^y(\mathbf{r}_r; \mathbf{r}_s, \omega) = k_b^2 \iint_D \underline{\mathbf{G}}_e(\mathbf{r}_r; \mathbf{r}_s, \omega) \mathbf{E}(\mathbf{r}; \mathbf{r}_s, \omega) \chi_e(\mathbf{r}) d\mathbf{r} = \mathcal{L}_{yy}(\chi_e) \quad (6.56)$$

where  $\mathbf{E}_s^y$  is the  $y$  component of the field scattered by the targets,  $\underline{\mathbf{G}}$  is the dyadic Green function, that is the electric field radiated at each point of measurement grid (see Fig. 4.24) by an arbitrary oriented electric dipole located in  $D$ , and  $\mathbf{E}_{inc}^y$  is the incident field in  $D$  due to a  $y$ -oriented electric dipole. Moreover, the vectors

$$\begin{aligned} \mathbf{r}_s &= x_s \mathbf{x}_0 + y_s \mathbf{y}_0 + z_s \mathbf{z}_0 = x_r \mathbf{x}_0 + y_r \mathbf{y}_0 + z_r \mathbf{z}_0 \\ \mathbf{r} &= x \mathbf{x}_0 + y \mathbf{y}_0 + z \mathbf{z}_0 \end{aligned} \quad (6.57)$$

specify the position of the source and of the receiver (that coincide for this monostatic case), and of generic point of the investigated domain  $D$ , respectively. It is worth pointing out that, since the antenna system is very close to the air/ground interface, also in the case the Green function as well as the incident field is herein approximated as those referred to a homogeneous medium having the electromagnetic properties of the ground hosting the targets. Their analytical expression can be found in the next section. This simplification will be removed thanks to our advance approach, when the actual field radiated by transmitting antenna and the actual Green function for the problem will be accounted for in the solution of the scattering equation. The imaging problem is formulated as the inversion of the relationship in 6.56, that is similar to the equation modeling the two-dimensional problem (see equation (6.45) and (6.48) for dielectric and metallic targets, respectively). To regularize the problem and obtain a stable solution, as already described by (6.46) and (6.55), TSVD as a scheme is implemented.

### 6.5.1. Dyadic Green function for a homogeneous medium

As is well-known and discussed, by starting from the Maxwell equation it is possible to express the electric field vector  $\mathbf{E}$  produced by a generic current distribution  $\mathbf{J}$  as follows

$$\mathbf{E}(\mathbf{r}) = j\omega\mu \int \underline{\mathbf{G}}(\mathbf{r}, \mathbf{r}') \cdot \mathbf{J}(\mathbf{r}') d\mathbf{r}'. \quad (6.58)$$

The dyadic Green function can be written as [1]

$$\underline{\mathbf{G}}(\mathbf{r}, \mathbf{r}') = \left[ \mathbf{I} + \frac{\nabla \nabla}{k^2} \right] g(r, r') \quad (6.59)$$

where  $g(\underline{r}, \underline{r}')$  is the scalar Green function for the free space, whose expression is reported here for convenience

$$g(\underline{r}, \underline{r}') = \frac{e^{-jk|\underline{r}-\underline{r}'|}}{4\pi|\underline{r}-\underline{r}'|} \quad (6.60)$$

Incidentally, let us recall that the dyadic Green function and the scalar one are, respectively, solution of the following Helmholtz equations

$$\begin{aligned} \nabla^2 g + k^2 g &= -\delta(\underline{r} - \underline{r}') \\ \nabla \times \nabla \times \underline{\mathbf{G}} - k^2 \underline{\mathbf{G}} &= -\underline{\mathbf{I}}\delta(\underline{r} - \underline{r}') \end{aligned} \quad (6.61)$$

Now, we can demonstrate that the expressions of the gradient and of the gradient of gradient of the Green function (for further details see [1]) have the following forms

$$\begin{aligned} \nabla g &= \left( jk + \frac{1}{4\pi|\underline{r}-\underline{r}'|} \right) g \underline{\mathbf{u}} \\ \nabla \nabla g &= \left[ \left( -k^2 + \frac{3jk}{|\underline{r}-\underline{r}'|} + \frac{3}{|\underline{r}-\underline{r}'|^2} \right) \underline{\mathbf{u}} \underline{\mathbf{u}} \right. \\ &\quad \left. - \left( \frac{jk}{|\underline{r}-\underline{r}'|} + \frac{1}{|\underline{r}-\underline{r}'|^2} \right) \underline{\mathbf{I}} \right] g(\underline{r}, \underline{r}') \end{aligned} \quad (6.62)$$

where

$$\underline{\mathbf{u}} = \frac{\underline{r} - \underline{r}'}{|\underline{r} - \underline{r}'|} \quad (6.63)$$

In addition, considering that

$$\underline{\mathbf{u}} \underline{\mathbf{u}} = \frac{(x-x_m)}{R} \underline{\mathbf{x}}_0 + \frac{(y-y_m)}{R} \underline{\mathbf{y}}_0 + \frac{(z-z_m)}{R} \underline{\mathbf{z}}_0 \quad (6.64)$$

it holds

$$\underline{\mathbf{u}} \underline{\mathbf{u}} = \begin{bmatrix} \underline{\mathbf{x}}_0 & \underline{\mathbf{y}}_0 & \underline{\mathbf{z}}_0 \end{bmatrix} \begin{bmatrix} \frac{(x-x_m)^2}{R^2} & \cdot & \cdot \\ \cdot & \cdot & \cdot \\ \cdot & \cdot & \cdot \end{bmatrix} \begin{bmatrix} \underline{\mathbf{x}}_0 \\ \underline{\mathbf{y}}_0 \\ \underline{\mathbf{z}}_0 \end{bmatrix} \quad (6.65)$$

thus, the sought dyadic Green function can be written as follow

$$\begin{aligned} \underline{\mathbf{G}} &= \begin{bmatrix} 1 & 0 & 1 \\ 0 & 1 & 0 \\ 0 & 0 & 1 \end{bmatrix} g(\underline{r}, \underline{r}') + \frac{1}{k^2} \left[ \left( -k^2 + \frac{3jk}{|\underline{r}-\underline{r}'|} + \frac{3}{|\underline{r}-\underline{r}'|^2} \right) \underline{\mathbf{u}} \underline{\mathbf{u}} \right. \\ &\quad \left. - \left( \frac{jk}{|\underline{r}-\underline{r}'|} + \frac{1}{|\underline{r}-\underline{r}'|^2} \right) \underline{\mathbf{I}} \right] g(\underline{r}, \underline{r}') \end{aligned} \quad (6.66)$$

Finally, the explicit expression of the first terms filling  $3 \times 3$  matrix is reported (we put for convenience  $R = |\mathbf{r} - \mathbf{r}'|$ )

$$G_{xx} = \left[ 1 + \frac{1}{k^2} \left( -k^2 + \frac{3jk}{R} + \frac{3}{R^2} \right) \frac{(x - x_m)^2}{R^2} - \left( \frac{jk}{R} + \frac{1}{R^2} \right) \right] g(\mathbf{r}, \mathbf{r}') \quad (6.67)$$

the remaining term ( $G_{xy}, G_{xz}$  and so on) are not reported here for the sake of brevity, but can be easily found in [1, 80].

### 6.5.2. Dual-pol tomographic algorithm

As is well-known, the dyadic Green function can be written in explicit form as follow

$$\underline{\mathbf{G}} = \begin{bmatrix} G_{xx} & G_{xy} & G_{xz} \\ G_{yx} & G_{yy} & G_{yz} \\ G_{zx} & G_{zy} & G_{zz} \end{bmatrix} \quad (6.68)$$

Once that the scattering equation reported in (6.56) has been discretized into a linear algebraic system using the Method of Moments [98], as usual the imaging is formulated as the solution of the matrix inversion problem

$$\mathbf{E}_s = \overbrace{\underline{\mathbf{G}} \cdot \mathbf{E}_{inc}}^{\mathcal{L}} \chi_e \quad (6.69)$$

by placing  $\mathcal{L} = \underline{\mathbf{G}} \cdot \mathbf{E}_{inc}$  we can write the discretized scattering equation more compactly as

$$\mathbf{E}_s = \mathcal{L}(\chi_e) \quad (6.70)$$

again, by considering equation (6.68) and (6.69) we can write

$$\begin{bmatrix} E_{s_x} \\ E_{s_y} \\ E_{s_z} \end{bmatrix} = \begin{bmatrix} G_{xx}E_x & G_{xy}E_y & G_{xz}E_z \\ G_{yx}E_x & G_{yy}E_y & G_{yz}E_z \\ G_{zx}E_x & G_{zy}E_y & G_{zz}E_z \end{bmatrix} \begin{bmatrix} \chi_e \end{bmatrix} \quad (6.71)$$

now considering that

$$\mathbf{E}_{inc}(\mathbf{r}) = j\omega\mu \int \underline{\mathbf{G}}(\mathbf{r}, \mathbf{r}') \cdot \mathbf{J}(\mathbf{r}') d\mathbf{r}' \quad (6.72)$$

for the incident field we can write

$$\mathbf{E}_{inc} = \begin{bmatrix} E_x \\ E_y \\ E_z \end{bmatrix} = \begin{bmatrix} G_{xx} & G_{xy} & G_{xz} \\ G_{yx} & G_{yy} & G_{yz} \\ G_{zx} & G_{zy} & G_{zz} \end{bmatrix} \begin{bmatrix} J_x \\ J_y \\ J_z \end{bmatrix} = \begin{bmatrix} G_{xx}J_x + G_{xy}J_y + G_{xz}J_z \\ G_{yx}J_x + G_{yy}J_y + G_{yz}J_z \\ G_{zx}J_x + G_{zy}J_y + G_{zz}J_z \end{bmatrix} \quad (6.73)$$

thus, recalling equations (6.69) for the scattered field

$$\mathbf{E}_s = \begin{bmatrix} E_{s_x} \\ E_{s_y} \\ E_{s_z} \end{bmatrix} = \underline{\mathbf{G}} \cdot \mathbf{E}_{inc} = \begin{bmatrix} G_{xx} & G_{xy} & G_{xz} \\ G_{yx} & G_{yy} & G_{yz} \\ G_{zx} & G_{zy} & G_{zz} \end{bmatrix} \begin{bmatrix} G_{xx}J_x + G_{xy}J_y + G_{xz}J_z \\ G_{yx}J_x + G_{yy}J_y + G_{yz}J_z \\ G_{zx}J_x + G_{zy}J_y + G_{zz}J_z \end{bmatrix} \quad (6.74)$$

If as transmitted antenna only a short dipole oriented along  $x$  is considered, we have  $J_x \neq 0$  and equation (6.73) becomes

$$\mathbf{E}_{inc} = \begin{bmatrix} G_{xx} & G_{xy} & G_{xz} \\ G_{yx} & G_{yy} & G_{yz} \\ G_{zx} & G_{zy} & G_{zz} \end{bmatrix} \begin{bmatrix} J_x \\ 0 \\ 0 \end{bmatrix} = \begin{bmatrix} G_{xx}J_x \\ G_{yx}J_x \\ G_{zx}J_x \end{bmatrix} \quad (6.75)$$

hence, for the scattered field we can write

$$\begin{aligned} \mathbf{E}_s &= \begin{bmatrix} E_{s_x} \\ E_{s_y} \\ E_{s_z} \end{bmatrix} = \underline{\mathbf{G}} \cdot \mathbf{E}_{inc} = \begin{bmatrix} G_{xx} & G_{xy} & G_{xz} \\ G_{yx} & G_{yy} & G_{yz} \\ G_{zx} & G_{zy} & G_{zz} \end{bmatrix} \begin{bmatrix} G_{xx}J_x \\ G_{yx}J_x \\ G_{zx}J_x \end{bmatrix} \\ &= \begin{bmatrix} G_{xx}G_{xx}J_x + G_{xy}G_{yx}J_y + G_{xz}G_{zx}J_z \\ G_{yx}G_{xx}J_x + G_{yy}G_{yx}J_y + G_{yz}G_{zx}J_z \\ G_{zx}G_{xx}J_x + G_{zy}G_{yx}J_y + G_{zz}G_{zx}J_z \end{bmatrix} \begin{bmatrix} \chi_e \end{bmatrix} \end{aligned} \quad (6.76)$$

If only  $E_{s_x}$  is measured by the receiving antenna, we have

$$E_{s_x} = G_{xx}G_{xx}I_x + G_{xy}G_{yx}I_x + G_{xz}G_{zx}I_x \quad (6.77)$$

and more compactly, as for the right side of equation (6.56), we can write

$$E_{s_x} = \mathcal{L}_{xx}(\chi_e) \quad (6.78)$$

where the first subscript of  $\mathcal{L}_{xx}$  represents the orientation of the receiving antenna (i.e., the collected component of the electric field), while the second one points out that of the transmitting antenna (i.e., the radiated component). If it is possible to radiate and measure two components of the electric field ( $x$  and  $y$  in this case), we can write

$$\begin{bmatrix} E_{s_x} \\ E_{s_y} \end{bmatrix} = \begin{bmatrix} \mathcal{L}_{xx} \\ \mathcal{L}_{yx} \end{bmatrix} \begin{bmatrix} \chi_e \end{bmatrix} \quad (6.79)$$

where

$$\begin{bmatrix} \mathcal{L}_{xx} \\ \mathcal{L}_{yx} \end{bmatrix} = \begin{bmatrix} G_{xx} & G_{xy} & G_{xz} \\ G_{yx} & G_{yy} & G_{yz} \end{bmatrix} \begin{bmatrix} G_{xx}J_x + G_{xy}J_y \\ G_{yx}J_x + G_{yy}J_y \end{bmatrix} \quad (6.80)$$

that is the operator describing the scattering phenomena when a dual-pol antenna is exploited, both to transmit and receive the scattered electromagnetic field. The expression of each element of the relevant dyadic Green function can be found in (6.67) and in the related bibliography.

## 6.6. Inversion with 3D numerical data

The 3D images obtained by processing the set of forward synthetic data discussed in Sec. 4.5 will be presented in this section. They represent the amplitude of the reconstructed contrast function  $\chi$  as provided by equation (6.56). The investigation domain  $D$  has size  $0.8m \times 0.4 \times 0.5$  m and it is discretized by means of  $N_c = 13090$  cubic cells, whose side is 2.24 cm long. The TSVD truncation threshold is fixed in such a way to filter out all the singular values which are 20 dB lower than the maximum one. The first processed data sets are referred to the buried basalt cube and sphere already analyzed in Fig. 4.29 and 4.30, respectively. The depth slices of the reconstructed contrast functions in color-plot form (related to its intensity according to a proper scale from red to blue) are shown in Fig. 6.7 for the cube and in Fig. 6.8 for the sphere. These figures present 20 planar ( $xy$ ) color plots corresponding to  $z$  values which regularly increase moving from the interface towards the bottom of the ground medium, with a spatial step of 2.24 cm, for an overall investigated height of about 50 cm. The analysis of Figs. 6.7 and 6.8 show that the two dielectric objects are approximately located at the same depth, which is properly retrieved, and allows us to obtain a satisfactory estimation of the upper cross-section size of both targets, while their size along the depth direction is overestimated. This agrees with the fact that the objects are characterized by a larger relative permittivity than the hosting medium and thus by an actual wave propagation velocity  $v$  that is lower than the modeled one (this latter being that corresponding to the background). Moreover, even if the actual shape is not accurately reconstructed and no information on their relative permittivity is available, from Fig. 6.7 and 6.8 it is possible to infer that the objects have different shape and are made by the same material. As a matter of fact, while the reconstructed cross sections for the cube do not significantly vary with  $z$  ranging from about 12 cm to 16 cm, this correctly does not happen for the sphere (in the latter case the radius of the circular scattering section changes as  $z$  varies). In addition, both the reconstructions exhibit similar features as far as their behavior along the  $z$  axis is concerned. To corrobo-

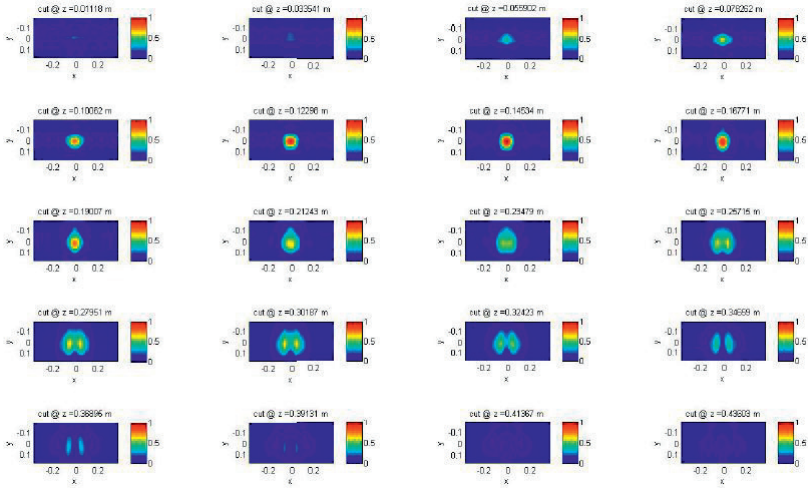


**Fig. 6.7.** Depth slices of the contrast function reconstructed by processing the data set referred to a buried basalt cube as in Fig. 4.29. Copyright © 2013, Hindawi Publishing Corporation, <https://doi.org/10.1155/2013/610389>.

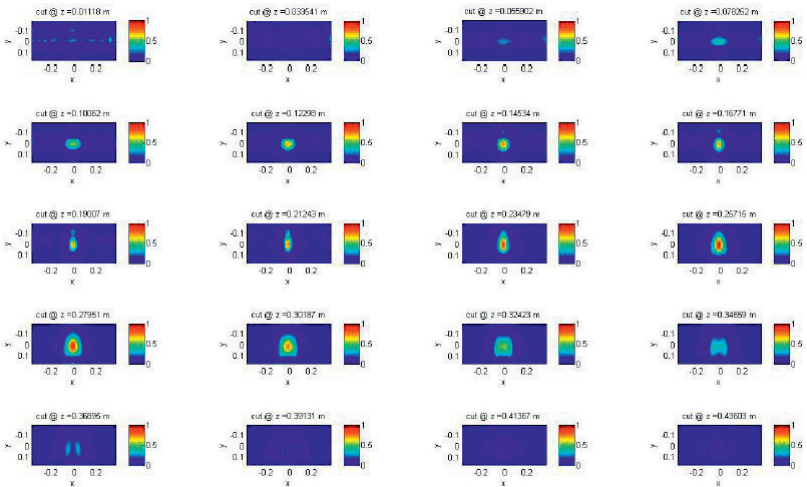


**Fig. 6.8.** Depth slices of the contrast function reconstructed by processing the data set referred to a buried basalt sphere as in Fig. 4.30. Copyright © 2013, Hindawi Publishing Corporation, <https://doi.org/10.1155/2013/610389>.

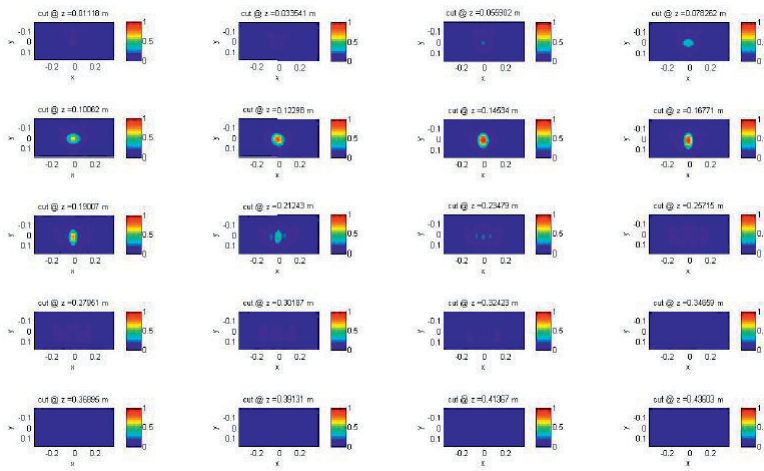


**Fig. 6.9.** Depth slices of the contrast function reconstructed by processing the data set referred to a vacuum cube as in Fig. 4.31. Copyright © 2013, Hindawi Publishing Corporation, <https://doi.org/10.1155/2013/610389>.

rate the previous considerations, Figs. 6.9 and 6.10 show the depth slices of contrast functions retrieved by processing the data sets corresponding to vacuum cubic and spherical objects (with data analyzed in Fig. 4.31 and Fig. 4.32), respectively, which have the same size and location of the already-considered basalt ones. These figures show that the targets depth is again properly retrieved, as well as the size of their upper cross section. Moreover, it is evident that, as in the case of basaltic objects, the reconstructed cross sections of the cubic object do not significantly change for  $z$  ranging from about 12 cm to 16 cm, while this is not true for the sphere. Furthermore, the reconstructions in Fig. 6.11 and Fig. 6.12 referred to a PEC cases have a similar behavior along the  $z$  axis, which is different from that shown in Fig. 6.7 and Fig. 6.8. In this respect, it is worth noting that now the targets size along the depth direction is underestimated in agreement with the lower relative permittivity of the objects than the one of the hosting medium.

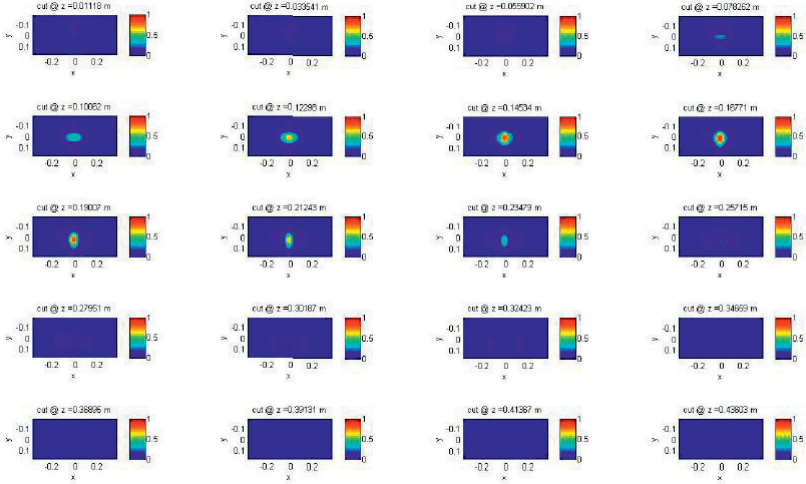


Fig. 6.10. Depth slices of the contrast function reconstructed by processing the data set referred to a buried basalt sphere as in Fig. 4.32. Copyright © 2013, Hindawi Publishing Corporation, <https://doi.org/10.1155/2013/610389>.

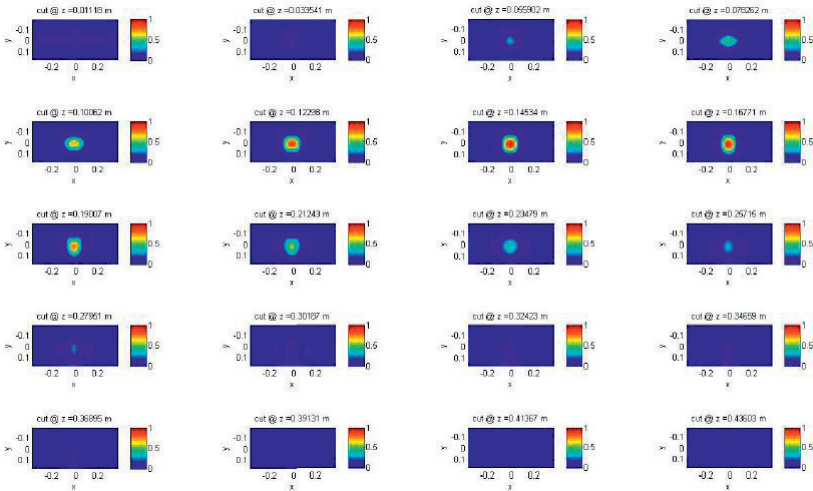


Fig. 6.11. Depth slices of the contrast function reconstructed by processing the data set referred to a PEC cube as in Fig. 4.33. Copyright © 2013, Hindawi Publishing Corporation, <https://doi.org/10.1155/2013/610389>.

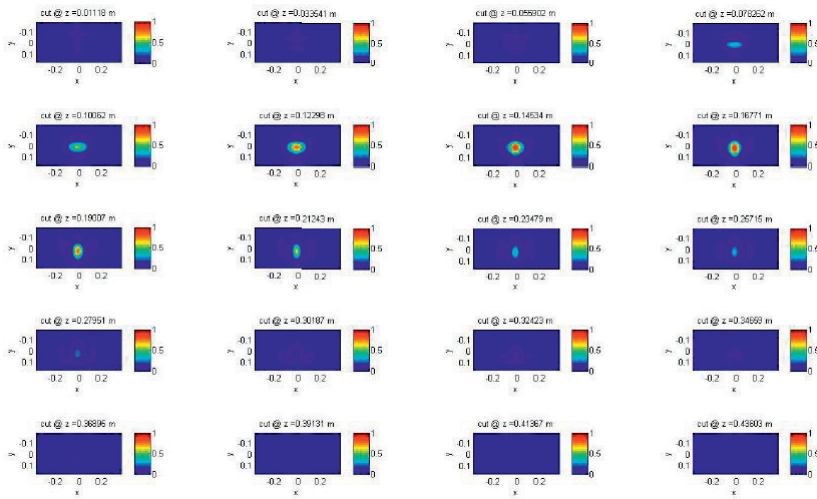


Fig. 6.12. Depth slices of the contrast function reconstructed by processing the data set referred to a buried PEC sphere as in Fig. 4.34.

## 6.7. Conclusion

In this chapter performances achievable applying an inverse tomographic algorithm on data gathered by means of GPR systems were investigated aiming at characterizing specific features of metallic and dielectric targets buried in a ground medium. An efficient inversion technique, developed in the past years at the Institute of the Remote Sensing for the Environment of Naples, was applied by processing and imaging direct ad-hoc data produced from both measurements and simulations. Most of the investigations were performed in challenging practical conditions, with scatterers placed in the near-field region of shallow subsurface and with dimensions comparable to the typical wavelengths of the GPR signals. The results showed a very good capability of proving a correct spatial localization of the targets, in conjunction with a satisfactory prediction of size, shape and depth. This has been observed even for realistic measurements in the presence of noise on data and uncertainties about the background scenario. It is important to note that the intrinsic limits related to the limited range of illumination by the transmitting antenna and the finite bandwidth of the signal spectrum do not anyway allow for the identification of finer geometrical details. Valuable information have been provided to evaluate performances of

the GPR systems designing in the framework of the Exomars mission, since both the permittivity of hosting medium and buried target were chosen to represent the subsurface of the red planet, where basalt rocks of different shape and dimension is proven to be present. The capability of the systems to provide useful 3D image of the considered subsurface has been also investigated. A consistent analysis of results for canonical metallic and dielectric scatterers has been possible by suitably designed a two-dimensional scan domain in our virtual model of a monostatic GPR systems. The angular spread of the radiated field by the GPR antenna, particularly significant when operating in the near-field regions, has been presented and discussed; in conjunction with the critical position and dimension of the considered targets it represents an additional parameter which adversely affects the resolution features of the procedure. Despite these aspects, it has been quantitatively tested that, starting from an accurate set of forward data and using a stable reconstruction algorithm, designed by suitably extending the two-dimensional inversion procedure, this approach possesses a good capability to prove the correct spatial position of the reflecting parts of the targets, in conjunction with a quite satisfactory prediction of its shape and size.

## 7. Advanced Microwave Tomography

### 7.1. Introduction

As discussed in the previous chapters, the main goal of the ExoMars mission to Mars will be to drill the first 2 meters of the Martian subsurface and analyze the extracted samples on site, to look for evidence of past or present life on the red planet. Although the final landing site has not yet been defined, it is likely that the rover will land in the equatorial belt in an area with soil conditions similar to those already examined by other rovers (see the introduction at the Part II of this thesis for further details). Consequently, the most probable geological scenario will be a dry sandy material (as that modeled in the experimental setup described in Section 4.1) whose surface is partially covered by variable-sized rocky blocks. However, it is assumed that a similar density distribution of the blocks also occurs in the shallow subsurface. In order to prevent the dangerous and energy-consuming drilling of hidden hard rocks, the geological nature of the first few meters of the subsoil should be known in detail. As already discussed, among various potential instruments, a GPR is considered as the best candidate to non-destructively investigate the shallow Martian subsoil and to image the electromagnetic discontinuities generated by any lithological variations. Generally speaking the capability to successfully detect the presence of buried rocks will mainly depend on the target/background electromagnetic contrast and on the overall attenuation within the subsurface. Moreover, the evaluation of the depth of such targets, as shown in Sections 4.2 and 4.4, will require the estimation of the electromagnetic properties of the background soil, using some inversion procedure. In this context, the present chapter aims at accurately modeling and numerically predicting

the performances of the tomographic algorithm presented in Chapter 6 to localized and reconstruct buried object in a Martian-like scenario. In particular, the potential improvements achievable by taking into account that the scattering effect is not activated by an ideal source, but through a real transmitting antenna having its own radiation pattern and producing a certain near-field distribution, will be demonstrated. Thanks to our fully numerical implementation based on an high-frequency electromagnetic Computer Aided Design (CAD) package (see Section 4.3), the actual far- and near-field distribution of a Vivaldi antenna (see Section 3.5 for the relevant details) has suitably accounted for in the imaging process. In addition, two figures as the *spectral content* and the *point spread functions* [76],[80] are used to carry out a theoretical analysis, which allows us to trace some general considerations on the expected performances when directive antennas are used. Several examples are provided to assess the benefits obtainable if the field radiated is taken into account to determine the expression of the incident field and the Green function, which are key elements for the model of the imaging problem. The analysis is focused on canonical shapes possibly buried in the near-field region of the considered antenna, with the goal of understanding the effect of the geometry and dimensions of the rocks as well as the effect of target/background electromagnetic contrast. Even though we focus our attention on the numerical model of the Vivaldi antenna developed in the framework of the Exomars mission, the proposed approach has general validity for different antennas and will be applied on both metallic and dielectric objects by acting on the two algorithms presented in Section 6.3 and 6.4. It is worth noting that these procedures are nearly identical, one has only to relate the actual incident electric field (i.e., that produced by the same antenna exploited to solve the direct problem, a Vivaldi in this case) with the contrast function and the incident magnetic field to the current flowing on the unknown metallic target. We initially assume an exact knowledge of the probed medium, then this assumption is removed and also the effects due to a not fully accurate model of the investigated scenario are considered.

## 7.2. 2D numerical model of the incident field

As we have seen in Chapter 6, in the frequency domain the interaction between the electromagnetic field radiated by the transmitting antenna and an object buried in the investigation domain is governed by the scat-

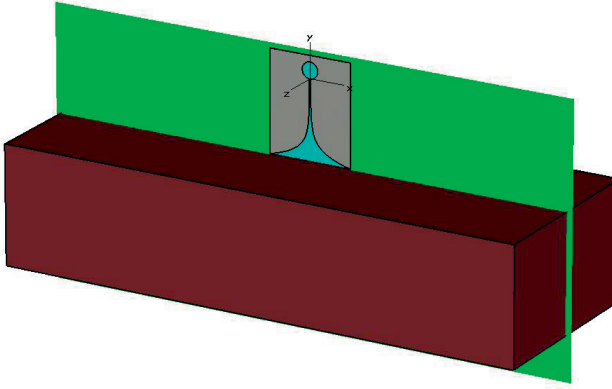


**Fig. 7.1.** 2D section of the 3D numerical domain where the incident field radiated by the Vivaldi antenna is spatially and spectrally sampled. Copyright © 2017, IEEE.

tering equations. Under the Born approximation for a two-dimensional geometry we can write

$$E_s(x, x_s, \omega) = k_b^2 \int \int_D G_e(x; x', y') E_{inc}(x_s, x', y') \chi(x', y') dx' dy'. \quad (7.1)$$

In Section 6.3 the solutions of this equation has been developed following standard approaches, widely studied and described in the specialized literature [83, 84]. So far, the time harmonic incident field has always been assumed as those generated by a line source radiating in free space, since in this way the mathematical complexity of the problem can be kept as lower as possible. However, this choice introduces an approximation that becomes less and less adequate for increasing directional features of the actual antenna involved in the solutions of the direct problem. Additionally, if the medium hosting the buried target is inhomogeneous or the source is placed at a certain distance from the interface, a line source radiating in free space turns out to be inaccurate to mathematically model the actual field impinging on the object. In Chapter 4 a numerical model of a GPR system has been developed and extensively tested for the solution of the direct scattering problem. A number of antennas having different operational bandwidth and directional features have been used as transmitting and receiving systems. Since a full-wave solution makes everywhere available the electromagnetic field inside the investigated medium, in the rectangular domain  $D$  where the solution of the inverse problem is searched for we can spatially and spectrally sampling the electric field radiated by the same antenna ex-

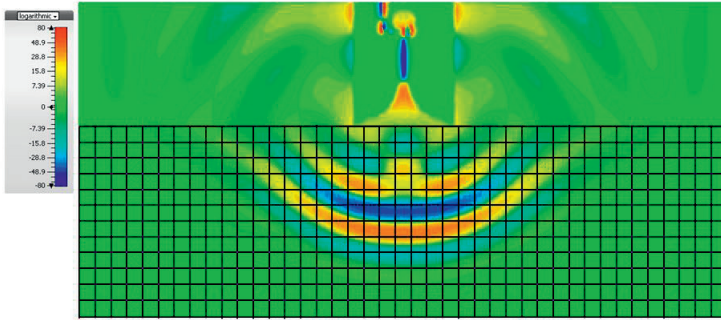


Fig. 7.2. Spatial discretization of the investigated domain. A time-domain pulse radiated by the Vivaldi antenna is shown for a fixed instant  $t_0$  on a vertical section of the 3D domain presented in Fig. 7.1. Copyright © 2017, IEEE.

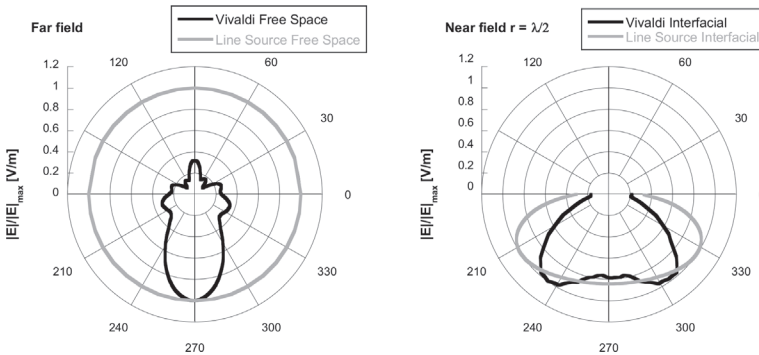


Fig. 7.3. Comparison between the near- and far-field distribution of the considered antenna; see relevant legends for further details.

exploited to solve the relevant direct problem. As shown in Fig. 7.1 for a two-dimensional implementation of the algorithm the longitudinal plane lying just below the antenna is selected; thus the time-domain electric field propagating inside this region is collected for a suitable number of time instants and for each pixel constituting the discretized domain shown in Fig. 7.2. By means of an ad-hoc MatLab routine a 'big' matrix is created and elaborated to achieve the frequency domain electric (or magnetic for non-penetrable targets) field to be placed inside the scattering equation. For the examples presented in the next sections, as said a Vivaldi antenna designed to fulfill constraint imposed by the Exomars Mission project will be always considered. Performances of this advanced implementation of the microwave tomographic algorithm

will be compared with those achieved through standard procedure (see Section 6.3 for all the relevant details). Since the spatial distribution of the electric (or magnetic) field radiated by a Vivaldi and a filamentary antenna are rather different both in the near- and far-field region (see Fig. 7.3 and relevant legend), substantial improvements are expected when the actual field is considered instead of that produced by a line source, simply modeled through an Hankel function [35].

### 7.3. Spectral performance analysis

In this section the effect introduced by the radiative behavior of the transmitting and receiving antenna on the reconstruction capabilities of the advanced version of the microwave tomographic algorithm will be discussed. The spectral content of the object space [80] and the regularized Point Spread Function (PSF) [76] are taken into account to compare the performances achievable by using the Vivaldi antenna with those provided by a line source. Generally speaking, the spectral content  $sp$  is defined as the sum of the modulus of the discrete Fourier transform of the singular vectors  $\mathbf{v}_n$  (see Section 6.3 for further details) corresponding to the singular values that are above the fixed TSVD threshold  $T$ , thus we can write

$$sp(k_x, k_z) = \sum_{n=1}^T |\tilde{\mathbf{v}}_n(k_x, k_z)| \quad (7.2)$$

where  $k_x$  and  $k_z$  are the spectral variables (with respect to  $x$  and  $z$  respectively) and  $\tilde{\mathbf{v}}_n$  the two-dimensional discrete Fourier transform of  $\mathbf{v}_n$ . Once the scenario and the measurement configuration have been fixed, the spectral content gives an indication of the filtering effects introduced by the regularized inversion of the matrix  $\mathbf{L}$ , that in turn is related to antenna (seen as a spatial filter), to the spectrum of the transmitted signals and finally to the measurements configuration. Consequently, it provides a global indication on the spatial harmonics of the targets that can be hopefully retrieved by using the TSVD for a fixed value of the regularization parameter. It is important to note, that the spectral content does not give any information on how the reconstruction capability changes as a function of the actual location of the target inside the investigated region. However, this kind of information can be obtained by means of the regularized PSF, defined as the reconstruction of a point-like target achieved by the TSVD regularization scheme. Accordingly, the regularized PSF of an impulse located at  $(x_0, z_0)$  is given

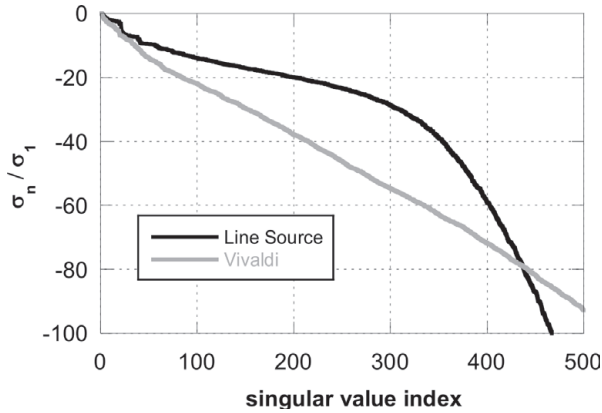
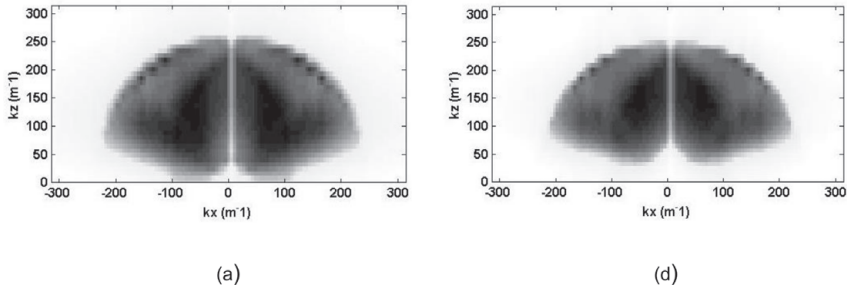


Fig. 7.4. Singular values behavior for a Vivaldi antennas (solid line) and a line source ones (dotted line) for a lossless soil with  $\epsilon_r = 3.2$ . Copyright © 2017, IEEE.

as a function of the spatial variables  $(x, z)$

$$PSF(x, z, x_0, z_0) = \sum_{n=1}^T \mathbf{v}_n^*(x_0, z_0) \mathbf{v}_n(x, z). \quad (7.3)$$

Even though both spectral content and PSF are general tools to assess the reconstruction capabilities of the tomographic algorithm, the dependency of the matrix  $\mathbf{L}$  on the features of the investigated domain as well as on the adopted measurement configuration makes necessary to introduce some hypothesis on the specific case at hand. Let us assume that a homogeneous lossless soil with relative permittivity  $\epsilon_b = 3.2$  is probed by moving an antenna system in  $M = 25$  measurement points evenly spaced of 3 cm along a line close to the air-soil interface. The investigated domain  $D$  is centered with respect to the measurement line and has an extent equal to 0.6 m along the  $x$ -axis and 0.4 along the  $z$ -axis; it is located just below the air-soil interface, that in first approximation is assumed as flat. The systems is monostatic and for each position on the surface data are collected at  $N_f = 21$  frequencies evenly spaced of 125 MHz in the range from 500 MHz to 3 GHz (that coincides with the operative bandwidth of the Vivaldi antenna described in Section 3.5). In Fig. 7.4 the behavior of the singular values of the matrix  $\mathbf{L}$  corresponding to Vivaldi and filamentary antennas have been presented. It is very interesting to note that the curve referred to the line source exhibits a change of slope at  $-30$  dB, whereas that one corresponding to the Vivaldi decreases uniformly. As a consequence, in this second



**Fig. 7.5.** Spectral content referred to filamentary antennas on a lossless soil with  $\epsilon_r = 3.2$ : a) singular values lower than -60 dB filtered out; b) singular values lower than -30 dB filtered out. Copyright © 2017, IEEE.

case, it is much more involved to define the essential dimension of the object space; it is expected that the choice of the SVD threshold affects significantly the achievable spatial resolution. As a first example in Fig. 7.5 the spectral contents, evaluated implementing equation (7.2), have been shown. Specifically, in Figs. 7.5(a) and 7.5(b) the results obtained by filtering out all the singular values lower than -60 dB and -30 dB with respect to the maximum one are presented. Analogously Figs. 7.6(a),(b) show the spectral content for the operator related to the considered Vivaldi antenna. In both cases pictures are normalized to their maximum value in dB scale and allows us to observe that, whatever the antenna system, the matrix  $\mathbf{L}$  acts as a low-pass spatial filtering in the transversal direction (i.e., along the measurements axis) and as a band-pass spatial filter in depth (i.e., along the  $z$ -axis). However, it is very important to note that the use of Vivaldi antennas implies a significant reduction of the spectral plane coverage, involving a loss of the achievable spatial resolution, mainly along the transverse direction. In addition, the spectral plane coverage decreases dramatically when the SVD threshold goes from -60 dB to -30 dB and a significant loss of resolution is expected. This behavior can be understood looking at the near- and far-field distributions for these two kinds of radiators, already reported in Fig. 7.3. Indeed, the directional features of the Vivaldi antenna does not allow us to illuminate and collect the scattered signal for a wide angle of observation; on the contrary, the line source is capable to provide wider range of observations. These properties for the considered antenna in connection with the synthetic aperture principle simply explain the spatial filtering behavior of the discretized operators. To

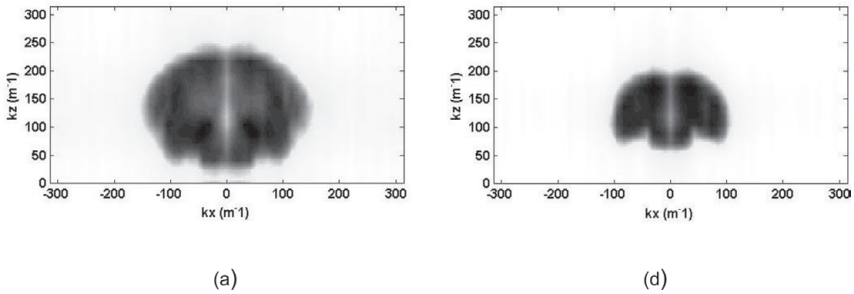


**Fig. 7.6.** Spectral content referred to a Vivaldi antennas on lossless soil with  $\epsilon_r = 3.2$ : a) singular values lower than  $-60$  dB filtered out; b) singular values lower than  $-30$  dB filtered out. Copyright © 2017, IEEE.

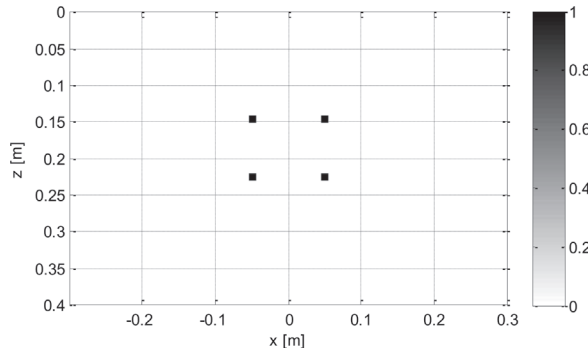


**Fig. 7.7.** Point-like targets for the numerical evaluation of the spread point function.

better understand this issues in the following the point spread function of a group of pixels shown in Fig. 7.7 will be presented and discussed. They represent four point-like target placed at a distance equal to 10 cm along the  $x$ -direction and 8 cm along the  $z$ -direction. By suitably analyzing the images obtained changing the threshold  $T$  of the TSVD regularization scheme and the permittivity of the background medium we are able to outline some interesting properties of the two operators. In particular, in Figs. 7.8(a)-(d) the images of the considered pixels when the line source antenna is illuminating a homogeneous medium described by a dielectric constant  $\epsilon_r = 3.2$  (same value considered in the previous chapter, representing a sandy dry material) for thresholds  $T$  equal to  $-15, -20, -30, -60$  dB, respectively, have been presented; in pictures (e)-(h) the same reconstruction for a background medium made by free space have been reported. Let us highlight that the range resolution (i.e., along the  $z$ -direction) of the systems is related to the

bandwidth of transmitted pulse as follow

$$\delta_z = \frac{c}{2B} \quad (7.4)$$

being  $B$  the bandwidth and  $c$  the velocity of the electromagnetic wave in the medium. On this basis, better resolution are expected for increasing values of the permittivity of the medium and for lower values of the selected threshold. Indeed, the lower is the number of singular values  $\sigma$  that are filtered out, the better will be the resolution of the systems. However, the choice of the threshold  $T$  is strictly related to the noise level and to the degree of regularization that one has to introduced on real data. Here for modeling purposes we consider  $T = -15, -20, -30$  and  $-60$  dB; but we have to consider that in many real cases usually we cannot go beyond  $-30$  dB. As expected the better reconstruction has been obtained in Fig. 7.8(d), i.e., for  $\epsilon_r = 3.2$  and for the lowest value of the threshold  $T = -60$  dB. It is interesting to note that for the case (a) (i.e.,  $\epsilon_r = 3.2$  and  $T = -15$  dB) not enough information is available in the data to successfully reconstruct each of the four pixels; finally, for the results (e)-(g) the resolution of the radiated pulse in conjunction with the chosen threshold  $T$  are not capable to solve the proposed targets. Anyway, by considering a higher number of singular values ( $N \approx 450$  for  $T = -60$  dB in Fig. 7.4) according to the expected resolution provided by the pulse ( $\delta_z = 6$  cm) for the case (h) the four pixels can be finally solved. An overall good result has been obtained along the horizontal direction, whose resolution is controlled by the synthetic aperture principle (i.e., better resolution for wider angles of observation is obtained). In Fig. 7.9 the same pictures illuminating point-like targets with the Vivaldi antenna have been reported. According to the spectral coverage already presented in Fig. 7.6 the results show worse resolution. In case (a) again not enough information is available and in cases (e)-(f) only a single big spot is clearly visible. This is due to a limited angle of observation offered by the directional nature of the considered antenna. It is important to note, finally, that pictures (d) and (h) show reconstruction capabilities comparable with those obtained in the previous cases: indeed, the total number of singular values considered by imposing  $T = -60$  dB is approximately the same for both the discretized operators (see Fig. 7.4). To give further details about this issues Figs. 7.11(a)-(d) show two cuts along  $x$  and  $z$  axis of the regularized PSF, computed in this case for a point-like target centered in the investigated domain, again for the two antenna systems and different SVD thresholds. The numerical

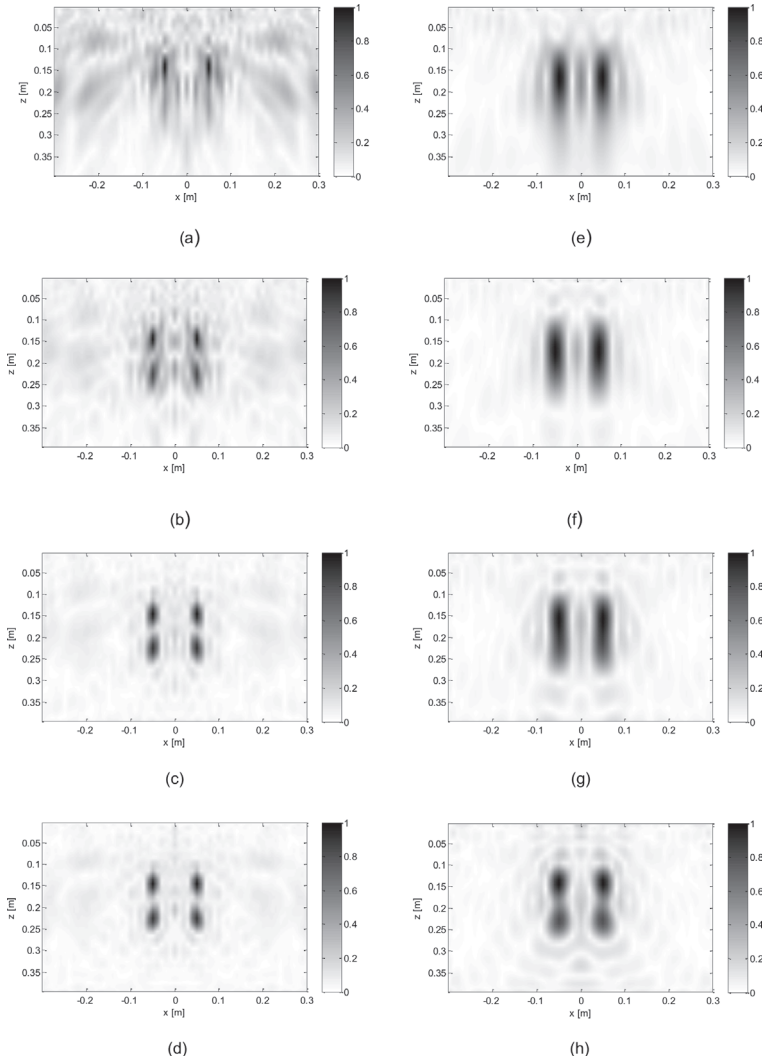
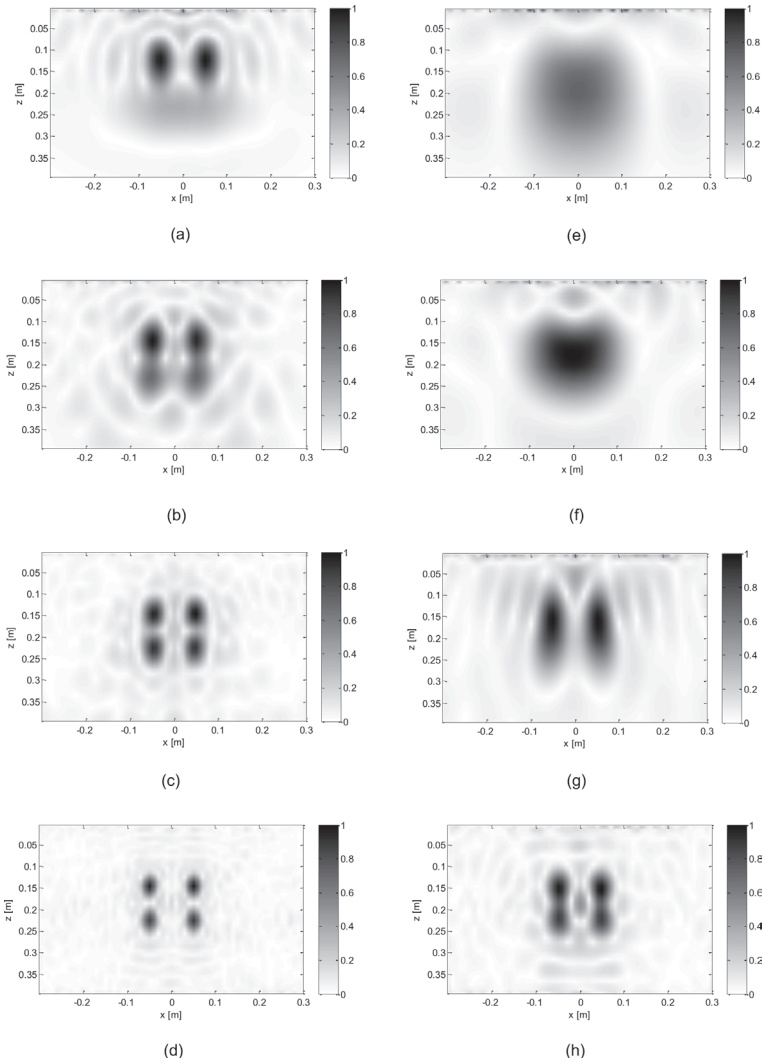
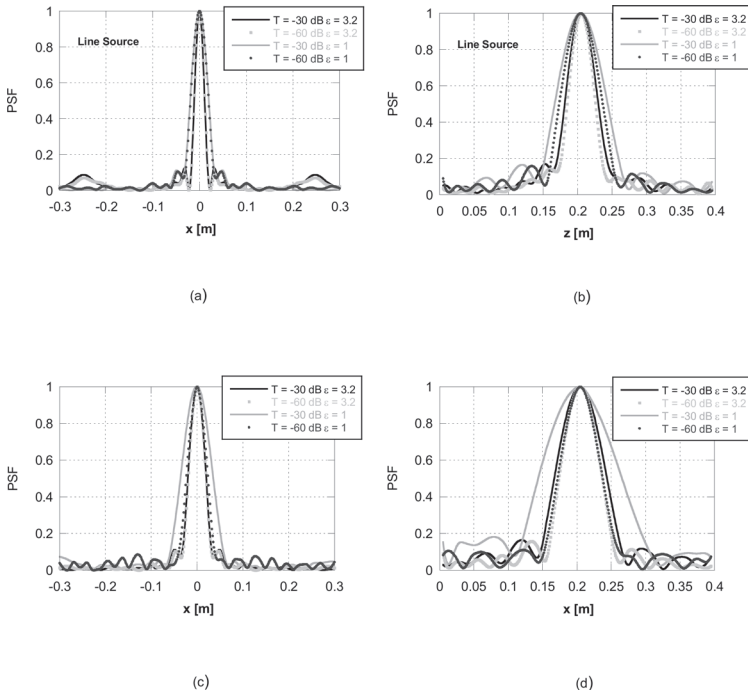


Fig. 7.8. Image of the four pixels in Fig. 7.7 illuminated by a line source antenna: from (a) to (d)  $\epsilon_r = 3.2$  and  $T = -15, -20, -30$  and  $-60$  dB, respectively. From (e) to (h)  $\epsilon_r = 1$ , but  $T$  assumes the same values.



**Fig. 7.9.** Image of the four pixels in Fig. 7.7 illuminated by a Vivaldi antenna: from (a) to (d)  $\epsilon_r = 3.2$  and  $T = -15, -20, -30$  and  $= -60$  dB, respectively. From (e) to (h)  $\epsilon_r = 1$ , and  $T$  has the same values.



**Fig. 7.10.** Horizontal and vertical sections of the PSF of pixel centered in the investigation domain for both antennas working in ground-coupled configuration and in free-space. Copyright © 2017, IEEE.

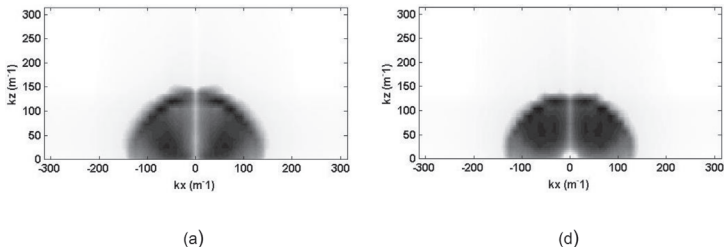


**Fig. 7.11.** Spectral content referred to filamentary antennas - free space: a) singular values lower than -60 dB are filtered out; b) singular values lower than -30 dB are filtered out. Copyright © 2017, IEEE.

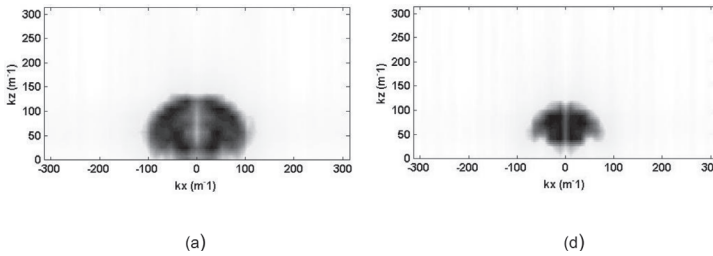


**Fig. 7.12.** Spectral content referred to Vivaldi antennas - free space: a) singular values lower than -60 dB are filtered out; b) singular values lower than -30 dB are filtered out. Copyright © 2017, IEEE.

values of transversal and range resolution can be easily estimated by computing, as an example, the width of the main lobe at 0.5 times its normalized maximum. It is possible to observe that, if data are gathered by means of filamentary antennas, the same values of range and depth resolutions are achieved for the two considered SVD thresholds. Hence, by filtering out all those singular values less than 30 dB with respect to the maximum one, it is possible to obtain a stable solution without affecting the resolution of the reconstruction. On the contrary, when a Vivaldi antennas is used, one should consider as many singular values as possible, and thus the need to assure a stable solution implies a non-negligible loss of resolution, even if data are affected by a low amount of noise. As already discussed, this behavior is related to the directive nature of the Vivaldi radiation pattern and occurs whatever is the permittivity of the probed medium. In Fig. 7.10 also sections of the PSF function are presented for the same antenna radiating in free space; as discussed previously a loss of resolution in any condition is always manifested. To corroborate this results, in Fig. 7.11 the spectral coverage for antennas radiating in free space has been presented. In particular, one can observe that, for the two considered SVD thresholds, the transversal resolution is the same while the range resolution changes slightly if filamentary antennas are adopted. Conversely, in the case of Vivaldi radiator, while a slight variation of the transverse resolution is observed, the other one gets worse significantly.

#### 7.4. Reconstruction of PEC scatterers

To assess the reconstruction capabilities when the real radiation pattern of the antenna is considered in the implementation of the tomo-

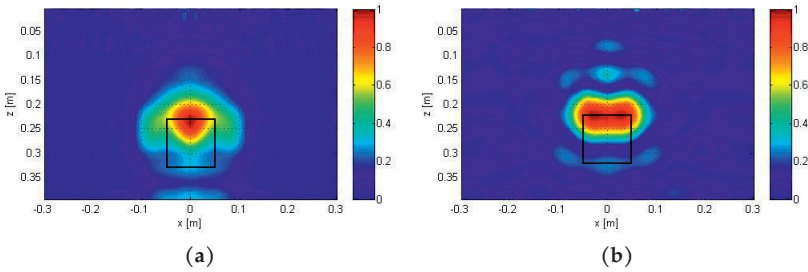


**Fig. 7.13.** (a) Line source processing, depth 22 cm,  $T = -20$  dB; (b) Vivaldi processing, depth 22 cm,  $T = -20$  dB. Copyright © 2017, IEEE.

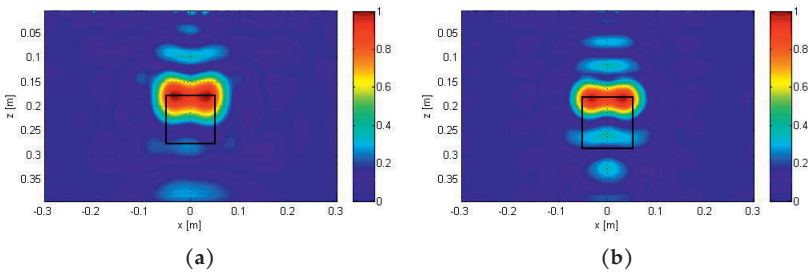


**Fig. 7.14.** (a) PEC cube with our advanced implementation:  $T = -20$  dB (a),  $T = -25$  dB (b). Copyright © 2017, IEEE.

graphic algorithm and to extensively compare the results with those provided by the standard implementation, several tests on metallic and dielectric targets have been developed. In this section different canonical shapes made of perfect electric conductor will be considered, all referred to synthetic data gathered by means of a Vivaldi antennas moved along a straight line in  $M = 25$  measurement points spaced of 3 cm (for further details about the numerical setup see Section 3.5 and 4.3). The antenna works in the frequency range from 0.5 to 3 GHz, evenly sampled with  $N_f = 21$  frequencies ( $\Delta f = 125$  MHz). The background medium is lossless and homogeneous with  $\epsilon_r = 3.2$ ; the imaging procedure is based on the Kirchhoff approximation, further detail can be found in Section 6.4.

A first example is presented in Fig. 7.13, where a PEC cube having side  $l = 13$  cm has been buried at 22 cm from the air/soil interface. Specifically the tomographic images achieved by considering or not the actual radiative behavior of the Vivaldi antenna are shown in Figs. 7.13(a) and (b), respectively. For all the examples outlined here and in the following we will talk about 'Line Source Processing' (LSP) or

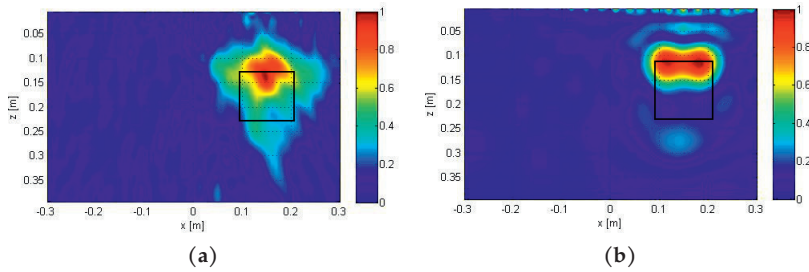


**Fig. 7.15.** (a) Shifted cube, line source processing, depth 12 cm,  $T = -20$  dB (b) Shifted cube, Vivaldi processing, depth 12 cm,  $T = -20$  dB. Copyright © 2017, IEEE.

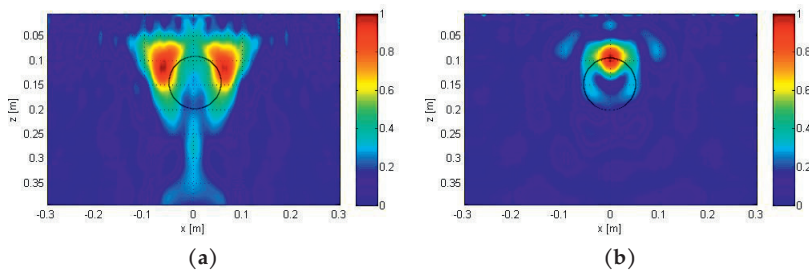


**Fig. 7.16.** (a) PEC cylinder (diameter  $d = 13$  cm, length  $l = 13$  cm)  $T = -20$  dB, conventional algorithm (b) PEC cylinder (diameter  $d = 13$  cm, length  $l = 13$  cm)  $T = -20$  dB. Copyright © 2017, IEEE.

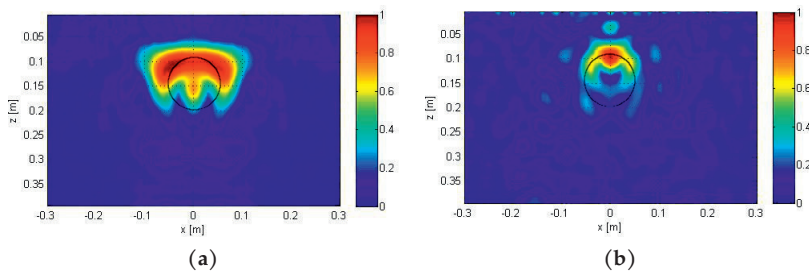


**Fig. 7.17.** Same results as in Fig. 7.16 but for  $T = -30$  dB.

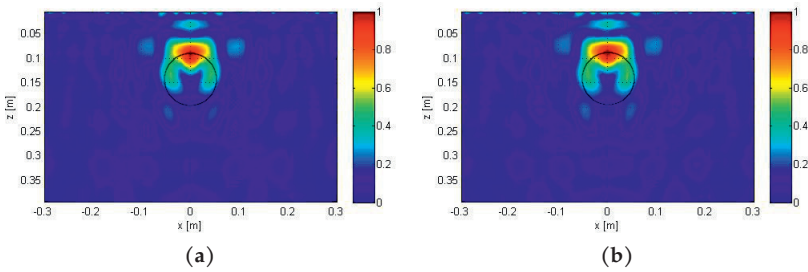


**Fig. 7.18.** (a) Long PEC Cylinder (diameter  $d = 13$  cm, length  $l = 30$  cm)  $T = -25$  dB (b) Long PEC Cylinder (diameter  $d = 13$  cm, length  $l = 30$  cm)  $T = -25$  dB.

‘standard approach’ meaning that synthetic data have been obtained by solving the direct problem with the Vivaldi antenna and putting inside the algorithm (extensively illustrated in Chapter 6) the field radiated by a filamentary source radiating in a homogeneous space, and about ‘Vivaldi Processing’ (VS) or ‘advanced approach’ to indicate that the actual field radiated by the antenna is considered for the imaging procedure (see Section 7.2). For the example at hand it is possible to state that a much better reconstruction of the upper side of the target (the only one illuminated, since the object is not penetrable) has been obtained. It is worth noting that longitudinal and transverse resolutions are the same for both standard and advanced approach and are comparable with the ideal resolution limit  $\delta_z = 3.35$  cm. This is in contrast with what discussed in previous section, since a worse transverse resolution should be found for the advanced approach. However, this loss has been compensated by introducing an accurate model of the incident field inside the scattering equation (7.1), allowing us to rigorously assess the equality between the scattered field and the mathematical model of investigated scenario. In Fig. 7.14 a further example is reported for the same cube buried at 18 cm from the surface, again in the near-field region of the considered antenna. The reconstruction for both pictures (a) and (b) are obtained by means of the advanced approach and are related to different choices of the SVD threshold. As expected an higher value for  $T$  improves the achieved range resolution, becoming closer to the ideal limit  $\delta_z$ . To assess the capabilities of our code to reconstruct also objects placed in the lateral region of the probed area, in Fig. 7.15 reconstructions obtained for a cube buried 12 cm from the interface is presented. Once again, by comparing Figs. 7.15(a) and (b) one can state that the image achieved with the advanced approach

(Fig. 7.15(b)) is manifestly better than those generated by the standard implementation (Fig. 7.15(a)). It is interesting to note that this last result is noticeable worse with respect to those obtained for centered object; this is because the error introduced by filamentary current in the lateral region is bigger than that in the center (just below the antenna); consequently also the distribution of the singular values turn out to be modified. To further analyze the reconstruction capabilities of the proposed advanced approach a metallic cylinder having diameter  $d = 13$  cm and a length  $l = 13$  m is considered in the following. In Figs. 7.16(a) and (b) the reconstruction generated with conventional and advanced approaches have been shown. It is very interesting to note that even for  $T = -20$  dB the results obtained by accounting for the actual distribution of the radiated field are significantly different; in addition by enforcing  $T = -30$  dB (Figs. 7.17(a) and (b)) a further improvement in the reconstruction of the curved shape of the cylinder is clearly visible.

As a final results, in Fig. 7.18 the reconstruction obtained with the advanced approach for a metallic cylinder having again diameter  $d = 13$  cm but length  $l = 30$  cm is presented with aim to analyzing if the three-dimensional nature of the buried object is able to affect the performances of the imaging procedure, that is inherently 2D. As is clearly visible, the results are not affected by this approximation, being the curved section of the cylinder rather well defined or not different from the shorter object just presented.

## 7.5. Reconstruction of dielectric scatterers

In this section images of dielectric targets having the same canonical shapes adopted in the previous section will be presented. All the examples provided are based on the assumption that the background medium is exactly known (homogeneous lossless soil with  $\epsilon_r = 3.2$ ). Once again we refer to the standard algorithm, already introduced and applied to experimental as well as numerical data in Section 6.3, and to an advanced approach. The images achieved for a basalt cube ( $\epsilon_r = 6.7$ ) having side  $l = 13$  cm and placed at 18 cm below the air-soil interface by considering and not the actual field distribution of the antennas are shown in Fig. 7.19. These results corroborate that, also for this new class of objects, the use of an accurate model of the antenna allows for a more defined localization of the upper side of the cube as well as of the lower one, provided that the dielectric contrast between hosting medium and

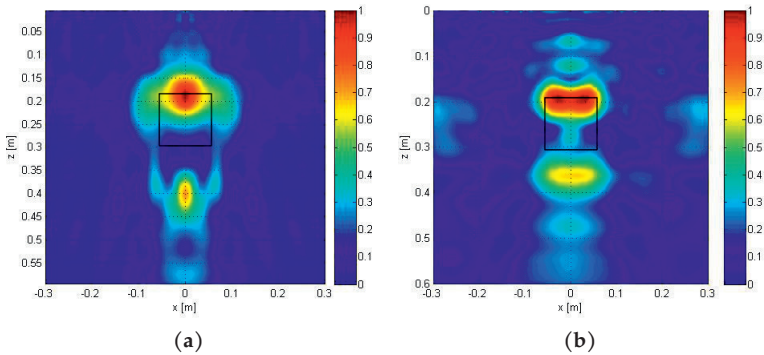


Fig. 7.19. (a) Basalt cube, conventional algorithm, depth 18cm,  $T = -22$  dB (b) Basalt cube, advanced approach, depth 18cm,  $T = -22$  dB. Copyright © 2017, IEEE.

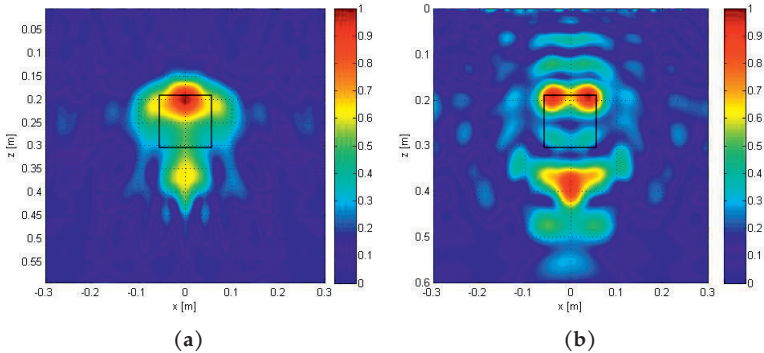
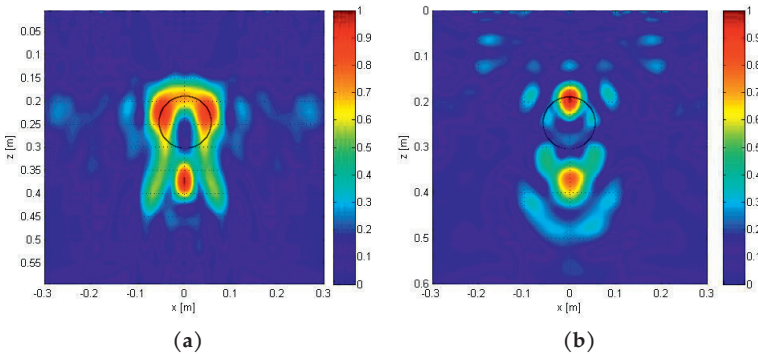


Fig. 7.20. As in Fig. 7.19 but for  $T = -26$  dB.

target are properly taken into account. As for the metallic objects this result suggests that the capability to accurately model the incident field and consequently to rigorously respect the integral scattering equation, allows us to neglect loss of resolution and to better image the most important features of the dielectric inclusions. A further example is reported in Fig. 7.20 for the same basalt cube (same depth and dimension) but modifying the SVD threshold  $T$ , equal to -26 dB in this case. In Fig. 7.21 a basalt cylinder having the same dimension to the one presented in Fig. 7.16 is considered. Figs. (a) and (b) show reconstructions achieved with standard and advanced approach, respectively. As expected, the latter shows a more focused image and a better reconstruction of the curved face of the cylinder. It is finally important to note that in all the reconstructions presented in this section the lower face of the probed object results always down-shifted with respect to its actual position;



**Fig. 7.21.** (a) Basalt cylinder, conventional algorithm, depth 18cm,  $T = -25$  dB (b) Basalt cylinder, advanced approach, depth 18cm,  $T = -25$  dB.

this is because the algorithm ‘see’ a wave that propagates in a dielectric medium having  $\epsilon_r = 3.2$ , hence at a velocity  $v_b = c/\sqrt{(3.2)}$  even when it penetrates the basalt medium, where its actual velocity is lower, being  $v_t = c/\sqrt{(6.7)}$ . This delay cannot be automatically compensated by the algorithm and can be anyway dependent on the shape of the inclusion.

## 7.6. Contact less configuration

For a wide variety of applications the GPR instruments could not be able to operate in ground-coupled configuration. Just to give a practical example, in the framework of the Exomars mission it is likely that the rover will land in an area with soil conditions similar to those already examined by other rovers like Pathfinder, Spirit, and Opportunity [99, 100], and suitably modeled at the geophysics lab of the ‘Rome Tre’ University. Consequently, as said, the most probable geological scenario will be a dry loose material at surface which is partially covered by variable-sized rocky blocks; in this condition the GPR system will presumably operate with an antenna raised from the surface of about 20 cm [46]. However, also for a number of civil and geophysical application such a configuration could be desired, as an example when the system is placed on-board mobile platforms. In this condition if the incident electric field is not properly modeled, detection and localization of the buried object could be not accurately performed. In the framework of the standard approach, a spectral representation for the line source has been considered in the past, resulting anyway inadequate to represent the directional behavior of the Vivaldi antenna. For these reasons our advanced approach has

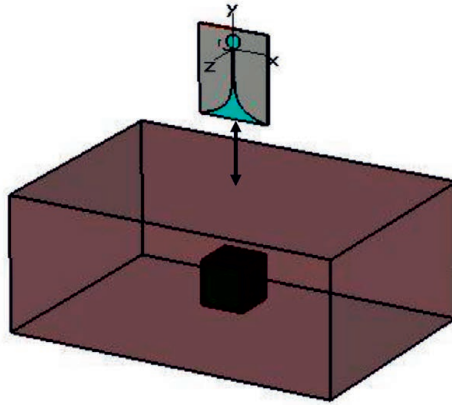


Fig. 7.22. Simulated scenario for a Vivaldi antenna raised of 20 cm from the air-soil interface. A canonical shaped object is buried in the lower half-space.

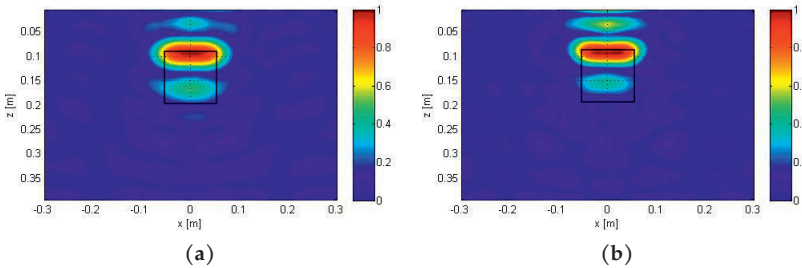


Fig. 7.23. (a) PEC cube, depth 9 cm, advanced implementation: (a)  $T = -20$  dB, (b)  $T = -25$  dB.

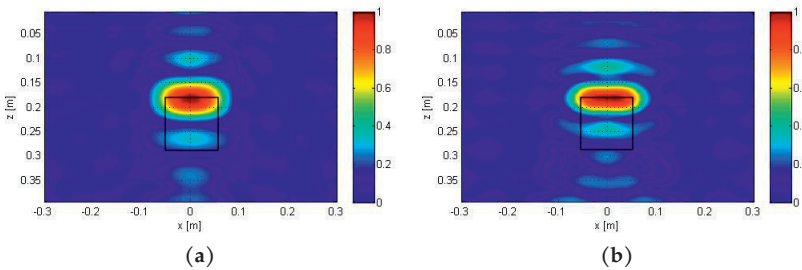
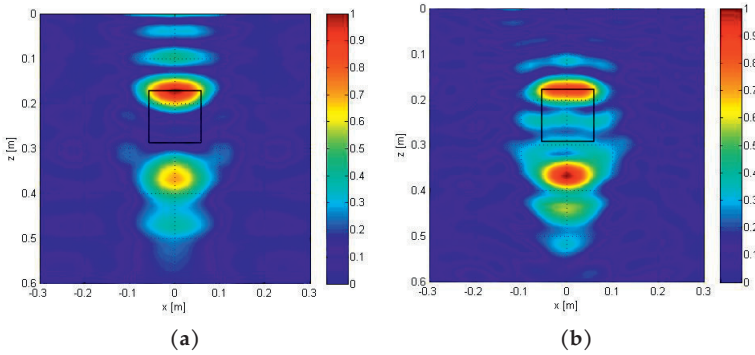


Fig. 7.24. (a) PEC cube, depth 18 cm, advanced implementation: (a)  $T = -20$  dB, (b)  $T = -25$  dB.



**Fig. 7.25.** (a) Basalt cube, depth 18 cm, advanced implementation: (a)  $T = -18$  dB, (b)  $T = -25$  dB.

been extended to this new configuration (see Fig. 7.22). In Figs. 7.23 and 7.24 images of the same metallic cube considered in the previous section is presented for different depths, equal to 9 and 18 cm. In Fig. 7.25 the reconstruction for a basalt cube buried at 18 cm is reported. All the objects have been well located and reconstructed, confirming the accuracy of the proposed advanced algorithm.

## 7.7. Non-ideal effects

Since the assumption of exactly knowing the features of the probed medium may be considered unrealistic, in this Section some examples are provided when several uncertainties in the soil parameters are introduced. Firstly, the effect on the reconstruction of an error of about 10% on the estimation of the dielectric constant of the hosting medium is considered. Practically, the direct problem is solved choosing  $\epsilon_r = 3.2$ , whereas the error is implemented in the evaluation of the incident field. Also a number of rough profiles for the air/soil interface, so far assumed perfectly flat, are designed and implemented. Finally, the presence of one or two buried interfaces to make the hosting medium non-homogeneous (layered) will be investigated.

### 7.7.1. Error on the permittivity estimation

In Fig. 7.26 the image achieved by considering  $\epsilon_{r_n} = 3.2$  (named 'nominal' permittivity) in the solution of the direct problem and  $\epsilon_{r_a} = 2.8$  (named 'actual' permittivity) for the evaluation of the incident field is presented. As expected, both the reconstructions, case (a) for advanced

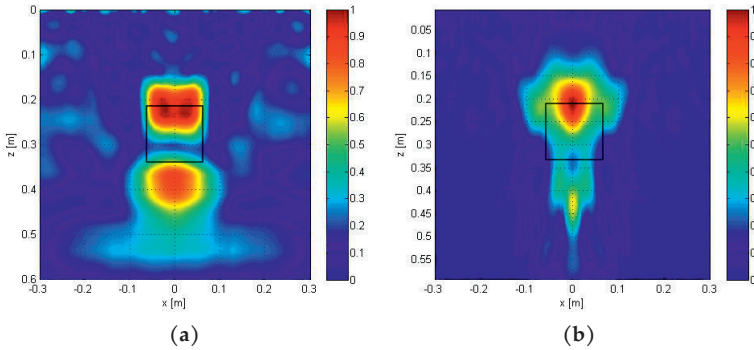


**Fig. 7.26.** (a) Basalt cube, Vivaldi processing. Nominal  $\epsilon_{r_n} = 3.2$  and actual  $\epsilon_{r_a} = 2.8$ . (b) Line processing, nominal  $\epsilon_{r_n} = 3.2$ , actual  $\epsilon_{r_a} = 2.8$ . Copyright © 2017, IEEE.

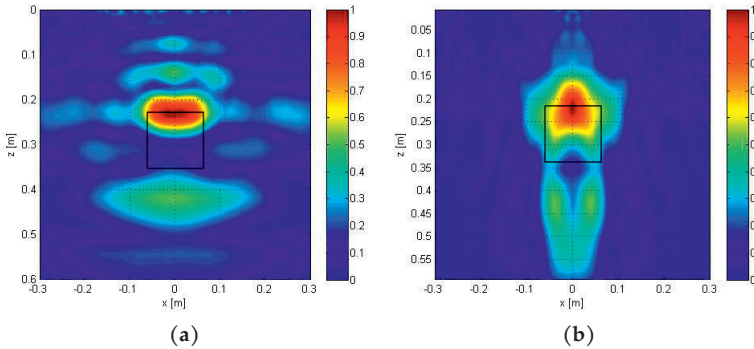


**Fig. 7.27.** (a) Basalt cube, Vivaldi processing. Nominal  $\epsilon_{r_n} = 3.2$  and actual  $\epsilon_{r_a} = 3.6$ . (b) Line processing, nominal  $\epsilon_{r_n} = 3.2$ , actual  $\epsilon_{r_a} = 3.6$ .

implementation and (b) for conventional algorithm, show a loss of range resolution, particularly evident for the first case. Anyway, once again the advanced implementation allows us to obtain a quite satisfactory reconstruction of both lower and upper faces.

In Fig. 7.27 the reconstruction achieved by imposing  $\epsilon_{r_n} = 3.2$  and  $\epsilon_{r_a} = 3.6$  is reported. Being  $\epsilon_{r_a} > \epsilon_{r_n}$  non-appreciable loss of resolution is visible but an important defocusing effect clearly affecting the lower face of the basalt cube is present. It is important to note that for both these results the reconstruction generated by means of the advanced implementation is manifestly better with respect to those related to the conventional algorithm.

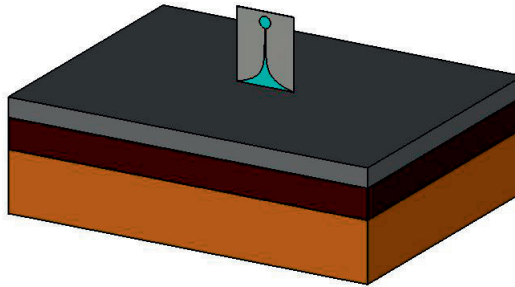
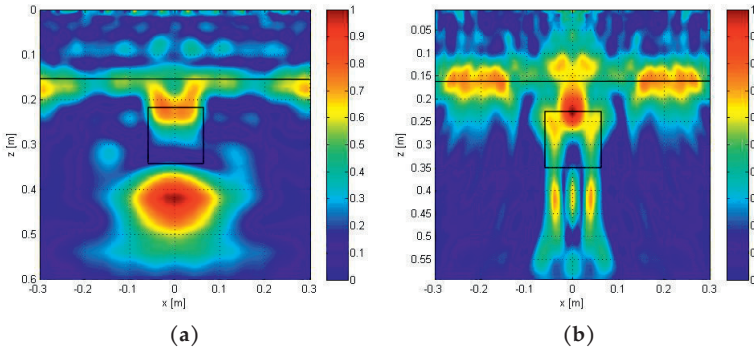


Fig. 7.28. Inhomogeneous background medium made by three interfaced flat layers.

### 7.7.2. Inhomogeneous ground medium

For many real application the background medium cannot be considered as homogeneous. The first step toward a more realistic model is usually made by two or more interfaced dielectric media, whose permittivity and thickness can be gradually varied. Even though this scenario is rather common, the analytical model of the relevant incident field can become much more involved. As a matter of fact, the problem is further complicated by the necessity of accounting for the discontinuities between different layers, which involve additional interactions between the scatterers and all the interfaces, that are not present in the case of a homogeneous background. In addition, the integral equations modeling the problem involve the evaluation of Sommerfeld-like integrals so that the computational burden increases significantly. However, full-wave solutions are not affected by this kind of complication and one can account for arbitrary discontinuities inside the hosting medium. In the following two different cases will be described to assess the overall soundness of the proposed advanced approach when a certain degree of inhomogeneities is considered. As an example in Fig. 7.28 a three-layers configuration is presented, whose dielectric permittivity starting from the highest up to the lowest are equal to 3.2, 2.2 and 4.5, respectively. The first interface (air-soil) is placed at 0 cm, whereas the second and the third one are at 12 and 18 cm, respectively. In Fig. 7.29 two images achieved by considering two media having permittivity  $\epsilon_r = 3.2$  and  $\epsilon_r = 2.2$  are presented; the first interface as for the picture in Fig. 7.28 representing three layers, is placed at 0 cm, the second one at 12 cm. Both the advanced procedure, capable to account for the discontinuities, and the standard implementation have been reported for the same basalt cube considered so far (see Fig. 7.19). Even though the second interface is retrieved in



**Fig. 7.29.** (a) Basalt cube, Vivaldi Processing; (b) Basalt cube line processing. For both results the threshold is  $T = -20$  dB.

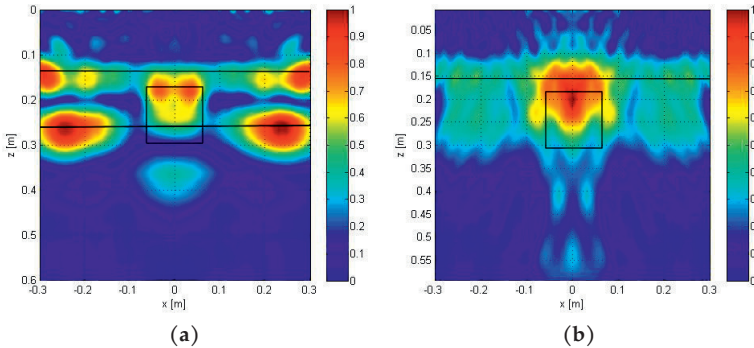


**Fig. 7.30.** (a) Basalt cube, Vivaldi Processing; (b) Basalt cube line processing. For both the results the threshold  $T = -20$  dB.

the right position, as expected the overall results is rather deteriorated and the lower face of the object is clearly defocused. Anyway thanks to our advanced algorithm we are still able to localize and qualitatively reconstruct the shape of the buried object. In Fig. 7.30 the reconstruction of the scenario presented in Fig. 7.28 has been reported. The presence of three layers introduce a much more complex interaction among object and hosting medium. By comparing Figs. 7.29(a) and (b) it is clearly visible that by processing data with the actual incident field allows us to better localize and qualitatively reconstruct the first interface and the upper face of the object. In both cases the lower interface is no longer retrieved but the advanced approach is able to localize even the second interface.

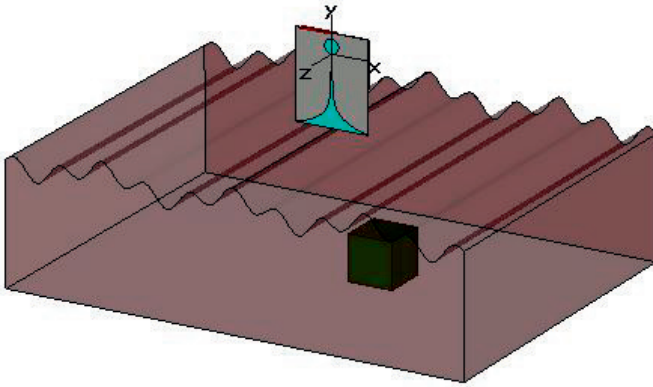


Fig. 7.31. GPR Numerical setup: roughness effects.

### 7.7.3. Surface roughness

To assess the capabilities of the proposed algorithm to locate and reconstruct targets buried under an irregular surface in the following a number of full-wave simulations accounting for a certain degree of roughness will be discussed. In particular two classes of profiles have been designed with a horizontal variation comparable with the probing wavelength ( $\lambda_b \approx 10$  cm for the case at hand). Namely, a case 'A' having a vertical peak-to-peak variation equal to 20 cm and a case 'B' whose vertical peak-to-peak variation is equal to 10 cm have been selected. Inside this class two different horizontal variations have been designed: namely a case A1 and A2 having a horizontal faster and lower variation with respect  $\lambda_b$ . More precisely, for the model A1 a variation of a half-wave occurs in 10 cm, whereas for the A2 a full wave variation occurs in the same interval. Analogously the class B can be split into the two subclasses B1 and B2 associating at each of them the same horizontal variations. To give a practical example in Fig. 7.31 the roughness profile B1 has been applied to the air/soil interface of the numerical model. Also the antenna and a buried basalt cube are clearly visible. In Fig 7.32 a first example is presented. Specifically, in Fig. 7.32(a) the reconstruction of a basalt cube buried at 21 cm from the surface is reported to compare the results shown in Fig. 7.32(b) obtained by applying a rough profile A1 (peak-to-peak vertical variation equal to 20 cm, slow horizontal variation). A loss of resolution is visible as well as defocusing effects at the lower basalt/sand interface. However a rather good result

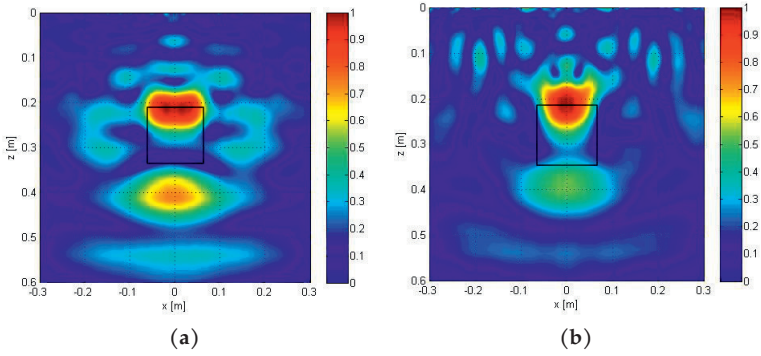


Fig. 7.32. (a) Basalt cube, Vivaldi processing: (a) no roughness, (b) rough profile A1 ( $T = -20$  dB).

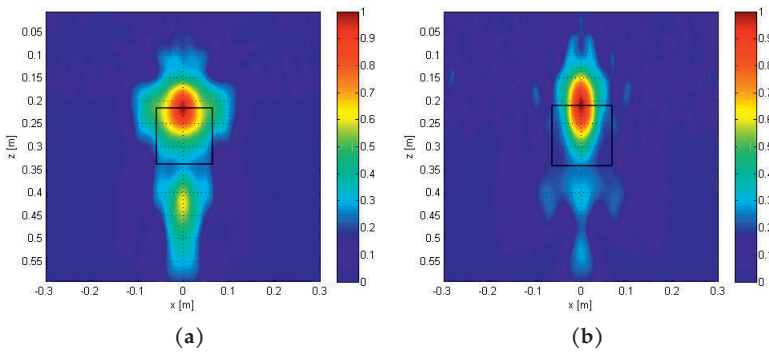
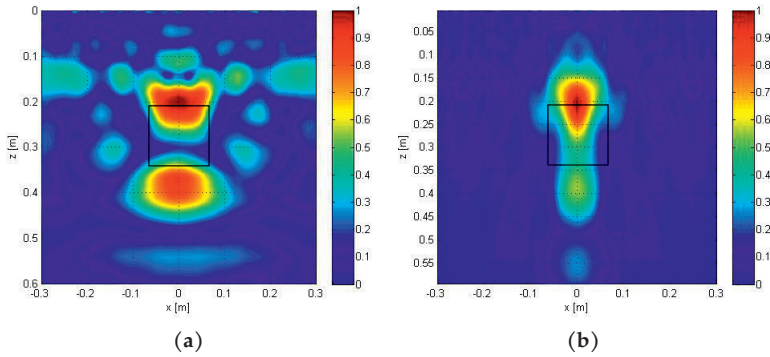
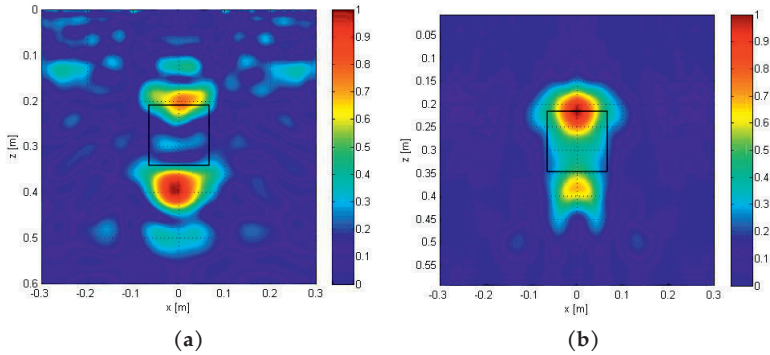


Fig. 7.33. Basalt cube, line source processing : (a) flat interface, (b) rough profile A1 ( $T = -20$  dB).



**Fig. 7.34.** (a) Basalt cube Vivaldi processing, profile A2,  $T = -20$  dB; (b) Basalt cube line source processing, profile A2,  $T = -20$  dB.



**Fig. 7.35.** (a) Basalt cube, Vivaldi processing profile A2,  $T = -25$  dB; (b) Basalt cube, line source processing profile A2  $T = -25$  dB.

has been obtained, allowing us to assess an overall soundness for the proposed algorithm. In Fig. 7.33 the same result are presented for a conventional implementation, showing a manifestly worse results in presence of the rough interface. Similar considerations can be done for the reconstruction presented in Figs. 7.34, 7.35, 7.36 and 7.37 (see captions for all the relevant details). As general comments it is possible to state that the advanced approach, being capable to account for the actual field radiated by the numerical antenna, performs quite well in presence of both light (B1) and heavy (A2) roughness profiles. In addition, the achieved images are always manifestly better than those produced through the conventional implementation.

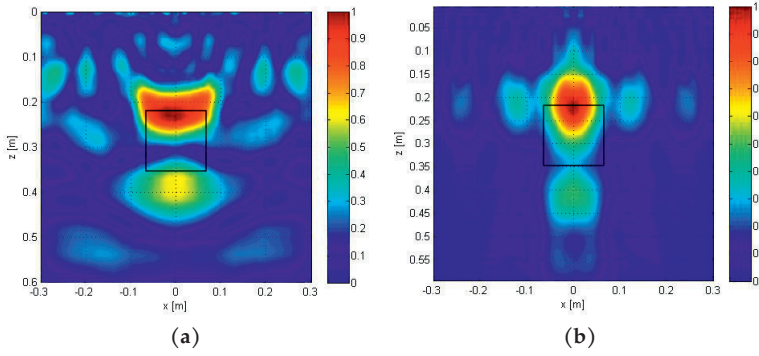


Fig. 7.36. (a) Basalt cube, Vivaldi source processing B1,  $T = -20$  dB; (b) Basalt cube, line source processing, profile B1,  $T = -20$  dB.

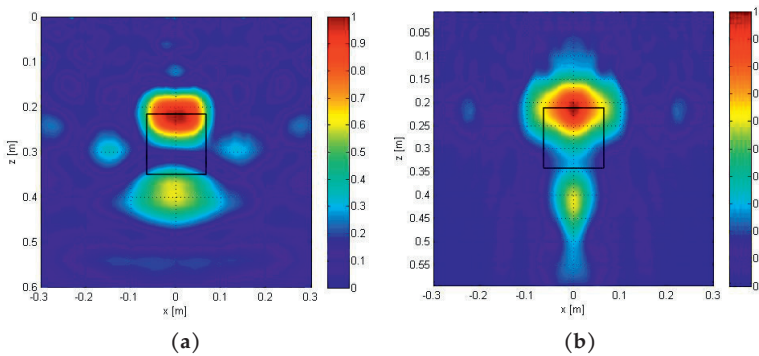


Fig. 7.37. (a) Basalt cube Vivaldi source processing B2,  $T = -20$  dB; (b) Basalt cube line source processing profile B2,  $T = -20$  dB.

## 7.8. Multipath effects

As a further interesting application, let us suppose that two metallic cubes like those ones considered so far are in the investigated domain at a certain distance far one to the other along the measurement direction (i.e.,  $x$ -direction). Two different antennas have been used to solve the direct problem, the Vivaldi antenna considered so far and a folded loaded dipole (see Fig. 7.38), whose design is outlined in Section 3.3, having a radiation pattern very similar to that one of a filamentary source (i.e., nearly omnidirectional). As shown in Fig. 7.38, when two targets are placed at short distance, besides the direct scattered contribute from each of the two objects, also a further signal produced by mutual-coupling phenomena may occur. Since this multipath has an apparent length greater than those of the direct signals, a further deeper fictitious object may be visible inside the investigated domain. To corroborate this hypothesis, in Fig. 7.39 the reconstruction obtained for two metallic cubes having sides  $l = 13$  cm, placed at 25 cm from the surface and at a side-to-side distance equal to 10 cm, is presented. As expected, two main spots in the right position but also a smaller contribution in the central deeper region of the retrieved image are clearly visible. It is due to multipaths that occur in the investigated scenario in conjunction with the omnidirectional nature of the considered antenna, that is able to illuminate buried target for a wide angular region. To better understand this mechanism in Figs. 7.40(a) and (b) two reconstructions obtained for the same scenario but implementing two different side-to-side distances for the buried metallic cubes, equal to 15 and 20 cm respectively, have been presented. As expected, the central deeper spot representing a so-called ‘ghost object’ becomes less strong and more

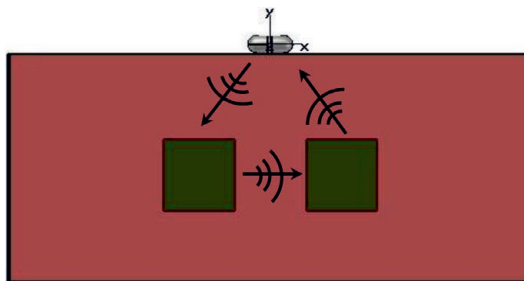
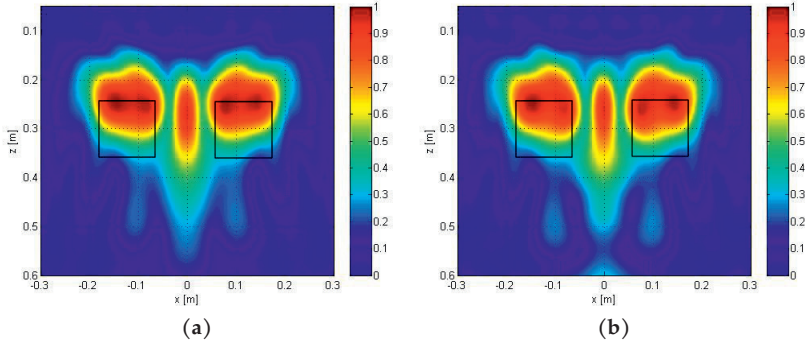
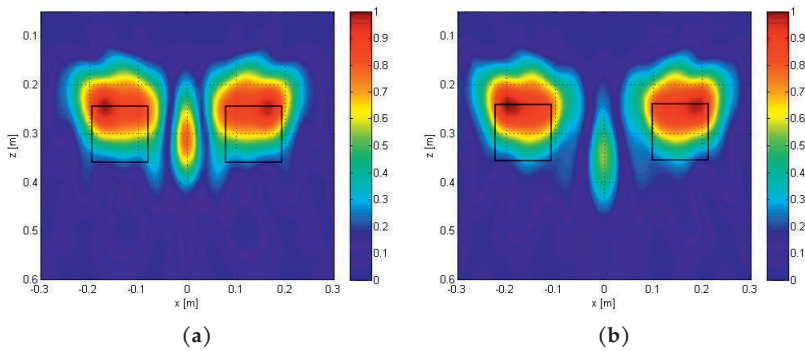


Fig. 7.38. Loaded folded dipole antenna, as those described in Sec. 3.3, placed at the air/soil interface.



**Fig. 7.39.** (a) Reconstruction obtained with a conventional implementation of the tomographic algorithm applied to data generated through folded loaded dipole ( $T = -20$  dB). Two PEC cubes at a distance side-to-side of 10 cm at depth equal to 25 cm are considered; (b) Same configuration but different threshold,  $T = -25$  dB.



**Fig. 7.40.** Reconstruction obtained with a conventional implementation of the tomographic algorithm applied to data generated through folded loaded dipole ( $T = -20$  dB). Two PEC cubes at distances side-to-side of 15 cm (a) and 20 cm (b) are considered.

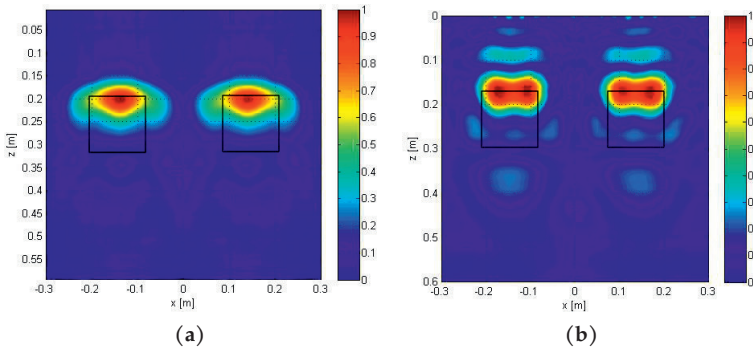


**Fig. 7.41.** Reconstruction obtained considering Vivaldi antenna ( $T = -20$  dB). PEC cubes are at distances side-to-side of 15 cm and at depth equal to 18 cm: (a) Standard implementation, (b) Advanced approach. Copyright © 2017, IEEE.

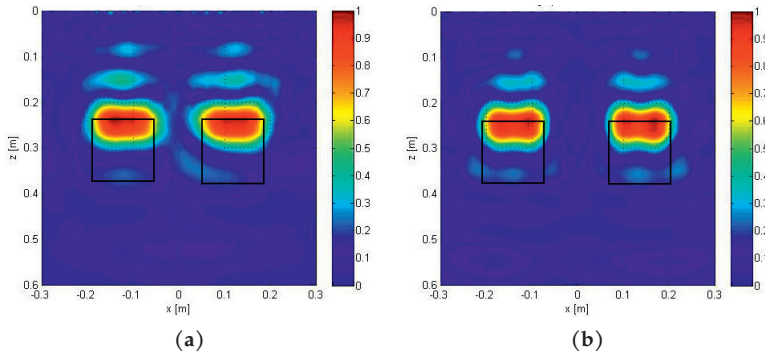


**Fig. 7.42.** Reconstruction obtained with standard implementation of the tomographic algorithm applied to data generated through Vivaldi antenna ( $T = -20$  dB). Two PEC cubes at distances side-to-side of 10 cm (a) and 15 cm (b), as in Fig. 7.40, are considered. Copyright © 2017, IEEE.

deep, confirming the genesis of the observed phenomenon. From a theoretical viewpoint a ghost object may be related to the omnidirectional features of the considered antenna. Indeed, during the scanning procedure, when the transmitting antenna is placed just on the first of the two buried targets it is able to illuminate and collect also the coupled signal produced by the second one. Consequently, if a more directive antenna is exploited, this phenomenon may be drastically reduced. To confirm this assumption in Fig. 7.41(a) and (b) the images generated illuminating with a Vivaldi antenna two cubes buried at 9 cm from the air/soil interface and processing with both standard and advanced implementations are presented. As expected, both the reconstructions do

not show ghost objects; in addition the upper face of the metallic cube is better reconstructed when the actual field radiated by the considered directive antenna is implemented in the scattering equation. In Fig. 7.42, finally, the same result for two cubes buried at 25 cm from the surface is reported. By comparing this reconstruction with those in Fig. 7.40 one can see as an antenna having a rather directive pattern is able to eliminate the contribution due to multipaths phenomena. It is worth noting that these results show different range resolution because of the operative bandwidth of the antennas; namely the folded loaded dipole is matched inside an interval ranging from 0.5 to 1.5 GHz, whereas the other one between 0.5 up to 3 GHz (see Chapter 3 for further details).

### 7.9. 3D numerical model of the incident field

Even though the scattering phenomenon is inherently three-dimensional, as we have done so far, to make simpler the implementation of the algorithm, in first approximation a two-dimensional procedure is developed. In this section, by starting from the relevant 3D implementation outlined in Sections 4.5 and 6.5, an advanced 3D microwave tomographic algorithm will be further developed and tested. As extensively described in Section 7.2 of this Chapter for the 2D case, also here the electric or magnetic field radiated by a Vivaldi antenna is spatially and spectrally sampled on a number of evenly spaced parallel plane, as shown in Fig. 7.43.

Thus an overall ‘big matrix’ representing both the frequency domain incident field and the relevant Green function is suitably arranged to be inserted in the discretized operator modeling the scenario. Further detail about the standard implementation of the 3D microwave tomographic algorithm can be found in Section 6.5. However, as expected, the problem at hand becomes sensibly more complex with respect to the 2D approach; it can be anyway managed by means of a MatLab routine. All details about the numerical implementation on the 3D surveys can be found in Section 4.5, where a printed monopole antenna is considered. As transmitting system we use here a linear polarized Vivaldi antenna, that radiates and collects Gaussian pulses at each point of the 2D grid place just above the air/soil interface, already presented in Fig. 4.24.

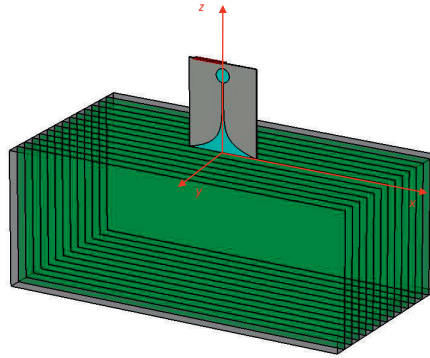


**Fig. 7.43.** 3D numerical domain investigated by the Vivaldi antenna. A discretization is introduced also along the third dimension. The incident field is sampled on each 2D plane both in frequency and spatial domains.

### 7.9.1. Metallic cube

In this subsection 3D tomographic reconstructions achieved with standard and advanced implementations of the algorithm for a metallic cube having side  $l = 13$  cm buried at 18 from the air/soil interface will be presented. In Figs. 7.44 and 7.45 a 3D image and a number of evenly spaced deep slices (section plane along the  $z$  axis) are respectively reported. They have been post-processed by implementing the field produced by an ideal short dipole, that gives only an approximate representation of the field radiated by the actual Vivaldi antenna. Indeed, our advanced implementation give rises to the image presented in Figs. 7.46 and 7.47: as is clearly visible, the upper face (the only one illuminated by the impinging wave) is quite well reconstructed, whereas in the previous case it was just detected and localized. Besides, an analysis of the depth slices allow us to retrieve also some useful information about the internal nature of the probed scatterer, whose rectangular

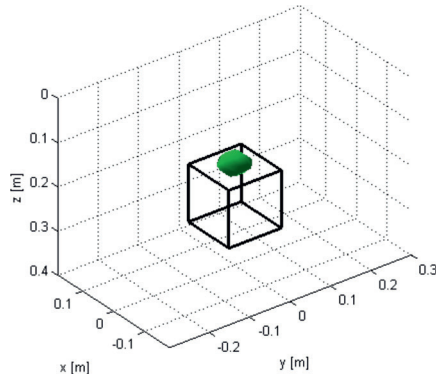


Fig. 7.44. 3D reconstruction of a PEC cube having side 13 cm placed at 18 cm with conventional tomographic algorithm.

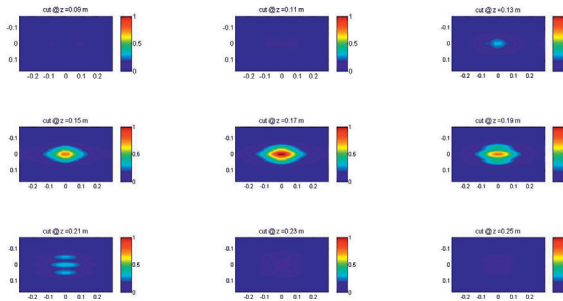


Fig. 7.45. Deep slices (along variable  $z$ ) of a PEC cube having side 13 cm placed at 18 cm with conventional tomographic algorithm.

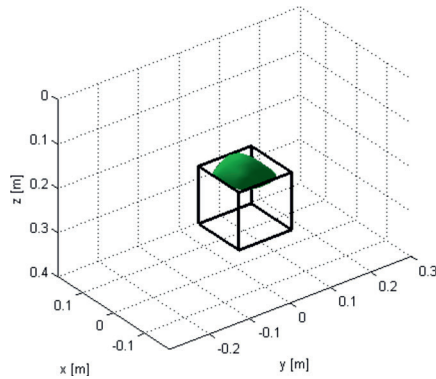
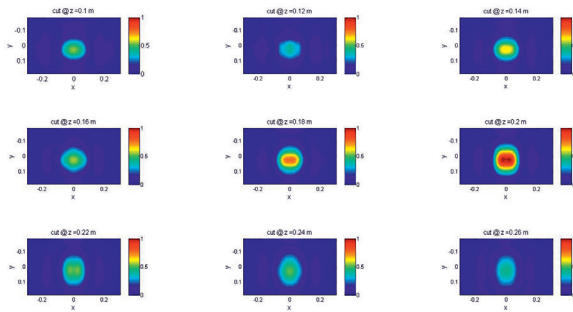


Fig. 7.46. 3D reconstruction of a PEC cube having side 13 cm placed at 18 cm obtained with the advanced implementation of the considered tomographic algorithm.



**Fig. 7.47.** Deep slices (along  $z$ ) of a PEC cube having side 13 cm placed at 18 cm obtained with the advanced implementation of the considered tomographic algorithm.

section in this case is manifest.

### 7.9.2. Dielectric cube

Also a penetrable dielectric target has been investigated. 3D reconstructions achieved with the conventional algorithm for a basalt cube having side  $l = 13$  cm placed at depth equal to 18 cm are presented in Figs. 7.48 and 7.49.

The images generated by accounting for the actual incident field are reported in Figs. 7.50 and 7.51. As for the previous case our advanced approach produces a manifestly better result; indeed both upper and lower sides of the penetrable target are well localized and reconstructed and the cuts along the  $z$ -direction show much more defined sections.

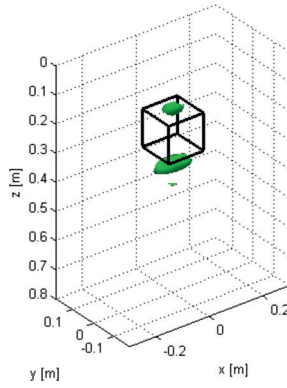


Fig. 7.48. 3D reconstruction of a basalt cube having side 13 cm placed at 18 cm with the conventional tomographic algorithm.

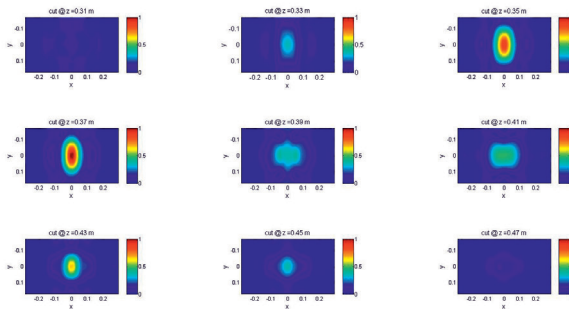
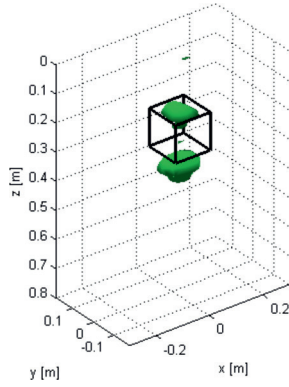
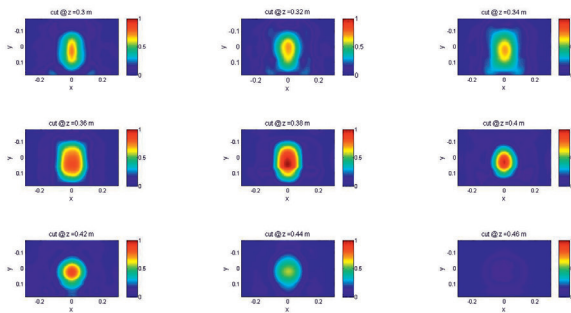


Fig. 7.49. Deep slices (along  $z$ ) of a basalt cube having side 13 cm placed at of 18 cm with the conventional tomographic algorithm.



**Fig. 7.50.** Three-dimensional reconstruction of a basalt cube having side 13 cm placed at 18 cm obtained with the advanced implementation of the considered tomographic algorithm.



**Fig. 7.51.** Deep slices (along  $z$ ) of a basalt cube having side 13 cm placed at 18 cm obtained with the advanced implementation of the considered tomographic algorithm.



PART IV

RECONFIGURABLE LEAKY-WAVE ANTENNAS



# Introduction

In the last years an increasing demand of efficient and reliable mobility connections has led the scientific community to investigate new antenna solutions. Indeed, performances of satellite tracking applications, advanced radars, and telecommunication systems are closely related to the antenna features and performance. Just to give a practical example, one of the most exciting challenges of the last decade is to give wide diffusion of high-quality wide band connections through mobile platforms (trains and airplanes). This challenging goal entails design of communication systems based on cutting-edge technology, most of all concerning the radiation elements, since low-cost and compact antennas capable to perform electronic scanning on both the azimuthal and elevation plane have become indispensable. In this scenario, typical solutions represented by reflector antennas are too bulky and involve problems of mechanical movement, whereas phased array need sophisticated electronic hardware, leading to expensive devices. Additionally, the feeding network can become very lossy at high frequencies, up to reduce the overall gain introduced by the array. For these reasons, Reflectarray and Transmitarray antennas, Metalenses and Reconfigurable Partially Reflecting Surfaces (PRS) for Fabry-Perot cavity antennas are becoming very attractive solutions.

Alternative promising technology are also represented by Micro-Electro-Mechanical Systems (MEMS) and MEMS varactors, since they may represent key components for reconfigurable radiating meta-surfaces. In particular, the latter can be used as tunable elements to obtain continuously tunable capacitance per unit area so as to reconfigure and scan the radiated beam.

It is very interesting to note that diagnosis, modeling and synthesis of reconfigurable antennas are one of the field not yet addressed in a systematic way in the specialized literature. Talking about reconfigurable antenna systems one must think to all kinds of project solutions that provide beam scanning capability with highly directive patterns, capable to keep good performance inside the desired operational bandwidth. A number of different approaches can be exploited to design highly directive antennas; as highlighted previously, the most known and technologically well assessed are reflector antennas. However, as originally shown in [101], high-directional systems can be also obtained by embedding simple sources inside a parallel-plane cavity whose upper wall is made by a Partially Reflecting Surface. This results in Fabry-Perot cavity antennas (FPCAs), a planar class of radiator that has received considerable attention in recent years. In fact, they shows a number of very attractive features, such as feeding simplicity, low profile, low cost and high directivity. Simple printed dipole or a slot etched in the ground plane can be considered as feeding systems, whose role essentially consists in launching a leaky modes responsible for the radiation. Typically, FPCAs are capable to produce pencil beams at broadside, which can be transformed into conical beams with variable scan angle by changing the operating frequency. An open problem in their design is the possibility of scanning the beam at a fixed frequency, or more generally to shape or reconfigure the pattern features. In this thesis a planar structure capable to excite a pair of azimuthally symmetric TE and TM leaky waves with equal values of the phase attenuation constants and of its complex amplitude has been designed, with the aim of obtaining a reconfigurable circularly polarized omni-directional conical beam pointing at a desired angle. We consider a FPCA made by a parallel-plate waveguide in which the upper plate is perturbed by a series of concentric annular rings having slots along both the azimuthal and radial direction. A vertical probe may be used to excite the TM part of the field, whereas a planar current loop can be used to excite the TE: The resulting pair of operating leaky modes would be the perturbed versions of the degenerate  $TM_1/TE_1$  modes of a parallel-plate waveguide (PPW).

Since no modal theory is available for the annular geometry (due to the lack of translational invariance), the antenna design must be based on the analysis of a linearized version of the structure, consisting of a PPW with periodic infinite slots on the upper plate, whose configurations can be suitable chosen to design and equalize the leaky modes

responsible for the radiation. Furthermore, if the period of the PRS is much smaller than the shortest wavelength, the upper plate can be homogenized and represented by an equivalent susceptance. It is worth noting that an ad-hoc Method of Moments has been also developed to efficiently characterize this structure; in particular, an integral-equation formulation for the problem in the presence of an infinite number of slots has been developed, capable to efficiently derive the radiation pattern of the antenna excited by idealized sources. Further details and the mathematical developments can be found in [102]. In the next chapters both modal and radiative properties of the proposed antenna will be presented; specifically, an ad-hoc novel equivalent-network formalism will be introduced to model a PPW partially loaded with a Wire Medium (WM) slab, that has been suitably sized to perturb the propagation of the TEM mode leaving unchanged those of the  $TE_1$  and  $TM_1$  degenerating modes, which is of interest for the realization of FPCA with configurable (in term of polarization features) conical patterns and wide angular scanning ranges. The peculiar anisotropic and spatially dispersive nature of the WM requires a suitable generalization of the standard network approaches in order to take into account the existence of an additional wave inside the WM layers. The proposed transmission-line formulation allows for a convenient determination of the dispersion features, radiation effects, and other characteristics that are not rapidly obtained by other methods based on a standard procedure. All the presented numerical results have been validated by means of a full-wave approach implemented on a commercial CAD tool as well as through a conventional field-matching approach.



## 8. Modal Analysis of a Wire-Medium Loaded Structure

### 8.1. Introduction

It is well known that a parallel plate waveguide (PPW) supports a TEM mode, which always propagates inside the structure. If a Fabry-Perot cavity antennas is derived introducing a High Impedance Surface (HIS) in place of the upper metallic plate, a perturbed version of the TEM mode can become leaky and, whenever properly excited, it radiates in the angular region close to endfire. Hence, if two independent transverse electric and magnetic leaky modes related to the perturbed version of the TE/TM degenerated mode of the relevant PPW are exploited to produce a dual-pol conical beam, undesired radiation of the TEM mode has to be suppressed, at least inside the operational frequency band. An interesting strategy consists in placing a wire medium (WM) slab with vertically aligned wires at the center of the considered structure with the aim of heavily perturbing the transverse field configuration of the TEM mode, leaving almost unchanged those of the  $TE_1$  and  $TM_1$ . Theoretically, as shown in Fig. 8.1, this is possible thanks to the peculiar transverse field configuration of the modes at hand; indeed, being the TEM vertically oriented and constant along the section, it may be effectively perturbed by the presence of a wire medium slab centered instead in the null of the  $TM_1$  modes. In addition, it results uncoupled with the  $TE_1$  mode, whose electric field is normal to the extension of wires.

The class of structures addressed in this thesis are constituted by an air-filled PPW which includes one or more WM layers with vertically aligned wires (see Fig. 8.2). Time-harmonic fields are considered, assuming any relevant wavelength be much larger than the wire periodicity inside the WM layers, hence the resulting model can be homogenized.

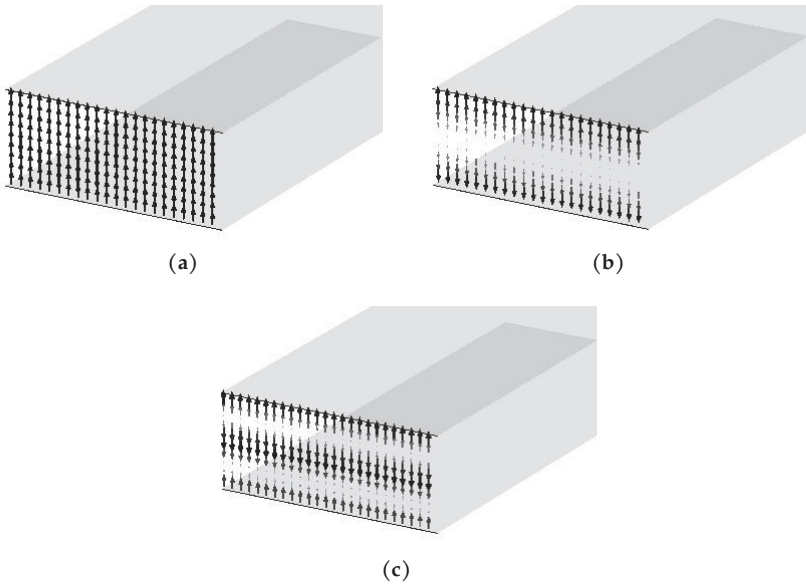


Fig. 8.1. Transverse configuration of the electric field of an air-filled parallel plate waveguide: configuration of the TEM (a),  $TM_1$  (b), and  $TM_2$  (c) modes.

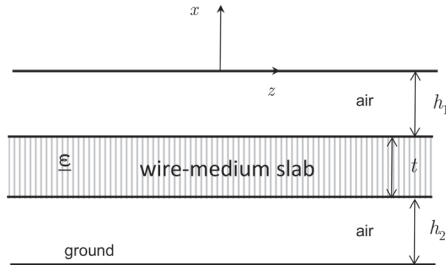


Fig. 8.2. Parallel-plate waveguide having height  $h$  symmetrically loaded with a wire medium slab having thickness  $t$ .

The modal properties of such structures are studied, whilst the related radiative properties will be extensively analyzed in the next chapter by considering excitation by elementary sources. To this aim, the electromagnetic problem related to the structure at hand is solved by considering a full-wave approach, namely by directly enforcing the boundary condition on the Maxwell's equations (applying a so-called field matching technique) as well as by introducing a novel efficient network formalism, representing each air/wire medium interface by means of a three-port equivalent network. In fact, the peculiar anisotropic and spatially dispersive nature of the WM requires a suitable generalization of the standard approaches used for the analysis of multilayered media, in order to take into account the existence of an additional wave inside the WM layers [103]. In this context, the possibility of suppressing TEM mode propagation through WM loading will be addressed. As said, this allows to recast the unimodal regime for obtaining wideband leaky-wave radiation from the  $TM_1$  mode in open configurations. In addition, with reference to an azimuthal symmetric configuration having both radial and annular slots (transversal and longitudinal for the associated linearized structure), the possibility of equalizing the phase constant of the involved TE and TM leaky modes is shown. This is of interest for the realization of FPCA antennas with conical pattern showing reconfigurable polarization features [106].

It is interesting to note that planar structures including wire-medium slabs have received considerable attention in the last decade (see, e.g., [107]-[115]). As first shown in [116], in the largewavelength regime the WM can be considered as a homogeneous anisotropic medium that exhibits unique nonlocal (i.e., spatially dispersive) features. These are in turn responsible for many interesting effects in the interaction of electromagnetic waves with WM slabs, both for propagation across the slab (e.g., canalization regimes of transmission with sub-wavelength imaging applications [107], [108]) and for modal propagation along the slab [109]-[115]. As concerns modal propagation, WM-loaded planar waveguides with different wire orientations have been considered in the literature. Grounded slabs with horizontal wires have been studied, e.g., in [110] and [111], where unexpected omnidirectional propagation features were shown to allow for cylindrical leaky-wave radiation in the form of highly polarized and azimuthally symmetric conical beams. On the other hand, WM slabs with vertical wires find application as constituents of artificial high-impedance surfaces; as such, their modal

properties in both surface-wave and leaky-wave regimes have been studied in [104]. Leaky-wave excitation and radiation in grounded WM slabs with vertically aligned wires has been studied in [113] and [115] for antenna applications.

## 8.2. Field matching technique

To find the dispersion equation of the structure presented in Fig. 8.2 the boundary conditions related to the presence of two air/wire-medium interfaces must be enforced on Maxwell's equations. Since we are dealing with a symmetric structure, as shown in Fig. 8.3, we can simplify the analytical development by bisecting the PPW with a perfect electric or magnetic wall for the TEM and the TM case respectively.

The WM, constituted by perfectly conducting wires aligned in the vertical ( $x$ ) direction and embedded in a host medium with relative permittivity  $\epsilon_{rh}$ , is assumed to be homogenizable and is thus represented as an anisotropic, spatially dispersive medium with dyadic permittivity [105].

$$\begin{aligned}\underline{\underline{\epsilon}} &= \epsilon_0 \left[ \epsilon_{\perp} (\mathbf{u}_x \mathbf{u}_x + \mathbf{u}_y \mathbf{u}_y) + \epsilon_{\parallel} \mathbf{u}_z \mathbf{u}_z \right] \\ &= \epsilon_0 \epsilon_h \left[ \mathbf{u}_x \mathbf{u}_x + \mathbf{u}_y \mathbf{u}_y + \left( 1 - \frac{k_p^2}{\epsilon_h k_0^2 - k_z^2} \right) \mathbf{u}_z \mathbf{u}_z \right]\end{aligned}\quad (8.1)$$

where  $k_p = 2\pi f_p / c$  and an approximate expression for  $f_p$  as a function of the wire radius  $a$  and the wire spacing  $d$  is [116]

$$f_p = \frac{c}{d} \frac{1}{\sqrt{2\pi \left( \ln \frac{d}{2\pi a} + 0.5275 \right)}}\quad (8.2)$$

valid for  $a \ll d \ll \lambda_0$ .

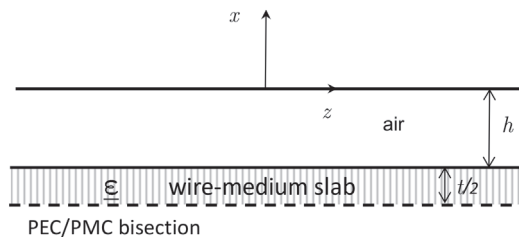


**Fig. 8.3.** Bisected parallel plate waveguide having height  $h$  symmetrically loaded with a wire medium slab having thickness  $t$ .

### 8.2.1. TM modes

In this case only  $H_y, E_x, E_z$  components are present and the closed structure is symmetric; thus, as already shown in Fig. 8.3, the TM modes can be isolated introducing a bisection with a PMC wall. By enforcing the boundary conditions at the upper metallic plate and on the symmetric wall bisecting the structure, for the  $y$  component of the magnetic field inside the waveguide one can write

$$H_y(x, z) = \begin{cases} A \cosh(\gamma_0 x) e^{-jk_z z} & \text{in air} \\ B_{TEM} \sin\left(k_{TEM}\left(x + \frac{h}{2}\right)\right) e^{-jk_z z} + \\ B_{TM} \sinh\left(\gamma_{TM}\left(x + \frac{h}{2}\right)\right) e^{-jk_z z} & \text{in WM} \end{cases} \quad (8.3)$$

where

$$\begin{aligned} k_{TEM} &= k_0 \sqrt{\epsilon_r} \\ \gamma_{TM} &= \sqrt{k_z^2 + k_p^2 - k_{TEM}^2} \\ \gamma_0 &= \sqrt{k_z^2 - k_0^2} \end{aligned} \quad (8.4)$$

are wave numbers of the TM and TEM waves (both with respect to the wires alignment) in the wire medium and the wave number in air, respectively. Moreover,  $k_z$  is the longitudinal wavenumber and represents the unknown of the problem at hand. Again the following quantity

$$k_p^2 = \frac{2\pi/s^2}{\ln \frac{s}{2\pi r_0} + 0.5275} \quad (8.5)$$

is the squared plasma wave number characterizing the wire medium and is of course related to equation (8.2).

The remaining boundary conditions, to be enforced at the air/WM interface, are the continuity of  $\mathbf{E}_\tau$

$$\left. \frac{\partial H_y}{\partial x} \right|_{x=-\left(\frac{h-t}{2}\right)^+} = \frac{1}{\epsilon_r} \left. \frac{\partial H_y}{\partial x} \right|_{x=-\left(\frac{h-t}{2}\right)^-} \quad (8.6)$$

the continuity of  $\mathbf{H}_\tau$

$$H_y \Big|_{x=-\left(\frac{h-t}{2}\right)^+} = H_y \Big|_{x=-\left(\frac{h-t}{2}\right)^-} \quad (8.7)$$

and finally the Additional Boundary Condition (ABC) for the wire medium [103]

$$\left. \frac{\partial^2 H_y}{\partial x^2} \right|_{x=-\left(\frac{h-t}{2}\right)^+} - \left. \frac{\partial^2 H_y}{\partial x^2} \right|_{x=-\left(\frac{h-t}{2}\right)^-} = (\epsilon_r - 1)k_0^2 H_y \Big|_{x=-\left(\frac{h-t}{2}\right)^-}. \quad (8.8)$$

In the previous equations  $\epsilon_r$  represents a dielectric medium in which the wire medium slab can be possibly located,  $h$  is the height of the parallel plate waveguide and  $t$  is the thickness of the WM slab (see Fig. 8.3). After some algebra, an homogeneous  $3 \times 3$  linear system in the unknowns  $A$ ,  $B_{TEM}$  and  $B_{TM}$  is obtained. The determinant of the matrix of the coefficient, reported in the following, equated to zero gives the sought dispersion equation

$$\begin{bmatrix} -\epsilon_r \gamma_0 \sinh\left(\gamma_0 \frac{h-t}{2}\right) & -k_{TEM} \cos\left(k_{TEM} \frac{t}{2}\right) & -\gamma_{TM} \cosh\left(\gamma_{TM} \frac{t}{2}\right) \\ \cosh\left(\gamma_0 \frac{h-t}{2}\right) & -\sin\left(k_{TEM} \frac{t}{2}\right) & -\sinh\left(\gamma_{TM} \frac{t}{2}\right) \\ (k_0^2 - \epsilon_r k_0^2 + \gamma_0^2) \cosh\left(\gamma_0 \frac{h-t}{2}\right) & k_{TEM}^2 \sin\left(k_{TEM} \frac{t}{2}\right) & -\gamma_{TM}^2 \sinh\left(\gamma_{TM} \frac{t}{2}\right) \end{bmatrix}$$

To plot the dispersion diagram of the modes propagating inside the considered closed structure one has to implement a numerical solution of the dispersion equation. Hence, also their transverse field configurations can be analyzed by simply placing values found for  $k_{z_{TM}}$  in the systems and solving for two of the three unknown coefficients.

### 8.2.2. TEM mode

In this case only  $H_y$  and  $E_x$  components are present. Once again the closed structure is symmetric, thus the TEM mode can be isolated introducing a bisection with a PEC wall (see Fig. 8.3). For the  $y$  component of the magnetic field inside the waveguide we can write

$$H_y(x, z) = \begin{cases} A \cosh(\gamma_0 x) e^{-jk_z z} & \text{in air} \\ B_{TEM} \cos\left(k_{TEM}\left(x + \frac{h}{2}\right)\right) e^{-jk_z z} + \\ B_{TM} \cosh\left(\gamma_{TM}\left(x + \frac{h}{2}\right)\right) e^{-jk_z z} & \text{in WM} \end{cases} \quad (8.9)$$

where  $\gamma_{TM}$ ,  $k_{TEM}$ ,  $\gamma_0$  are defined as in the previous subsection and  $A$ ,  $B_{TM}$  and  $B_{TEM}$  are unknown coefficients, related to the unknown eigenvalues  $k_z$  of the considered structure. Thus, by enforcing the boundary conditions at the upper metallic plate and on the symmetric wall bisecting the structure, once again a  $3 \times 3$  matrix, reported in the following, is obtained

$$\begin{bmatrix} -\varepsilon_r \gamma_0 \sinh\left(\gamma_0 \frac{h-t}{2}\right) & k_{TEM} \sin\left(k_{TEM} \frac{t}{2}\right) & -\gamma_{TM} \sinh\left(\gamma_{TM} \frac{t}{2}\right) \\ \cosh\left(\gamma_0 \frac{h-t}{2}\right) & -\cos\left(k_{TEM} \frac{t}{2}\right) & -\cosh\left(\gamma_{TM} \frac{t}{2}\right) \\ (\gamma_0^2 - \varepsilon_r k_0^2 + k_0^2) \cosh\left(\gamma_0 \frac{h-t}{2}\right) & k_{TEM}^2 \cos\left(k_{TEM} \frac{t}{2}\right) & -\gamma_{TM}^2 \cosh\left(\gamma_{TM} \frac{t}{2}\right) \end{bmatrix}$$

Numerically solving the dispersion equation achieved by equating to zero its determinant, it is possible to plot the dispersion diagram for the TEM mode propagating inside the structure at hand. Again, also its transverse field configuration can be obtained by placing the value found for  $k_{z_{TEM}}$  in the systems and solving for two of the three coefficients; in this way all the unknown characterizing equation (8.9) have been found and the behavior of the relevant transverse fields can straightforward be achieved.

### 8.2.3. Generalized structure

If a partially reflecting surface (PRS) is designed on the top of our PPW, as shown in Fig. 8.4, the structure may be able to support a leaky-wave mode. However, it loses its geometrical symmetry with respect to the  $yz$  plane and the problem cannot be simplified by any bisections. The geometry of the upper wall is usually made by periodic longitudinal and traversal slots that can be represented through a frequency-dependent surface transition impedance  $Z_g$ , as described for instance in [119]. A new boundary condition involving this impedance has to be enforced at the  $x = 0$  plane in conjunction with the continuity of the electric field through the partially reflecting surface. In addition, also the second air-WM interface must be considered, and the relevant boundary condition have to be enforced. The picture in Fig. 8.4 allows us to identify four different regions, thus the  $y$ -component of the magnetic field can be written as follows

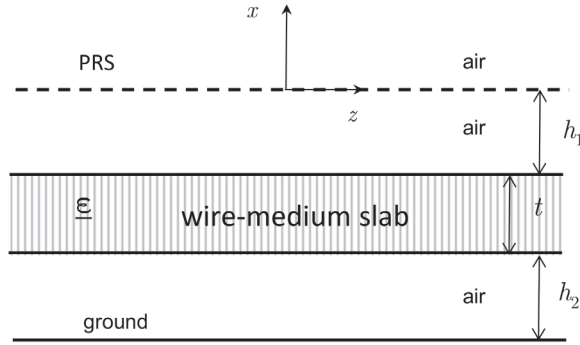


**Fig. 8.4.** Open parallel plate waveguide loaded with a wire medium slab. The structure is no longer symmetric and the boundary condition must be enforced at both the air/WM medium interfaces.

$$H_y(x, z) = \begin{cases} Ae^{-\gamma_0 x} e^{-jk_z z}, & \text{if } x > 0 \\ \left( B^+ e^{-\gamma_0 x} + B^- e^{\gamma_0 x} \right) e^{-jk_z z}, & \text{if } -\frac{h-t}{2} < x < 0 \\ \left( C_{TEM}^+ e^{-jk_{TEM} x} + C_{TEM}^- e^{jk_{TEM} x} + \right. \\ \left. C_{TM}^+ e^{-\gamma_{TM} x} + C_{TM}^- e^{\gamma_{TM} x} \right) e^{-jk_z z}, & \text{if } -\frac{h+t}{2} < x < -\frac{h-t}{2} \\ D \cosh(\gamma_0(x+h)) e^{-jk_z z} & \text{if } -h < x < -\frac{h+t}{2} \end{cases} \quad (8.10)$$

It is important to note that the choice of the hyperbolic cosine in the lower air region allows us to directly satisfy the boundary condition for the magnetic field on the ground. In addition, the continuity of  $\mathbf{E}_\tau$  and the impedance boundary condition have to be enforced at  $x = 0$ . The continuity of  $\mathbf{E}_\tau$  and of  $\mathbf{H}_\tau$  as well as the additional boundary condition have to be also enforced at the two air/wire medium interfaces. All that gives rise to a system of 8 equations in 8 unknowns, namely  $A$ ,  $B^+$ ,  $B^-$ ,  $C_{TEM}^+$ ,  $C_{TEM}^-$ ,  $C_{TM}^+$ ,  $C_{TM}^-$  and  $D$ . In the following, all the conditions are explicitly presented and listed one by one:

1. Continuity of  $\mathbf{E}_\tau|_{x=0}$

$$\left. \frac{\partial H_y}{\partial x} \right|_{x=0^+} = \left. \frac{\partial H_y}{\partial x} \right|_{x=0^-} \quad (8.11)$$

2. Impedance boundary condition at  $x = 0$

$$\frac{1}{j\omega\epsilon_0} \left. \frac{\partial H_y}{\partial x} \right|_{x=0^+} = Z_g \left( H_y|_{x=0^+} - H_y|_{x=0^-} \right) \quad (8.12)$$

3. Continuity of  $\mathbf{E}_\tau$  at the first air/WM interface

$$\left. \frac{\partial H_y}{\partial x} \right|_{x=-\left(\frac{h-t}{2}\right)^+} = \frac{1}{\epsilon_r} \left. \frac{\partial H_y}{\partial x} \right|_{x=-\left(\frac{h-t}{2}\right)^-} \quad (8.13)$$

4. Continuity of  $\mathbf{E}_\tau$  at the second air/WM interface

$$\left. \frac{\partial H_y}{\partial x} \right|_{x=-\left(\frac{h+t}{2}\right)^-} = \frac{1}{\epsilon_r} \left. \frac{\partial H_y}{\partial x} \right|_{x=-\left(\frac{h+t}{2}\right)^+} \quad (8.14)$$

5. Continuity of  $\mathbf{H}_\tau$  at the first air/WM interface

$$H_y|_{x=-\left(\frac{h-t}{2}\right)^+} = H_y|_{x=-\left(\frac{h-t}{2}\right)^-} \quad (8.15)$$

6. Continuity of  $\mathbf{H}_\tau$  at the second air/WM interface

$$H_y|_{x=-\left(\frac{h+t}{2}\right)^+} = H_y|_{x=-\left(\frac{h+t}{2}\right)^-} \quad (8.16)$$

7. ABC at the first air/WM interface

$$\left. \frac{\partial^2 H_y}{\partial x^2} \right|_{x=-\left(\frac{h-t}{2}\right)^+} - \left. \frac{\partial^2 H_y}{\partial x^2} \right|_{x=-\left(\frac{h-t}{2}\right)^-} = (\epsilon_r - 1)k_0^2 H_y|_{x=-\left(\frac{h-t}{2}\right)^-} \quad (8.17)$$

8. ABC at the second air/WM interface

$$\left. \frac{\partial^2 H_y}{\partial x^2} \right|_{x=-\left(\frac{h+t}{2}\right)^+} - \left. \frac{\partial^2 H_y}{\partial x^2} \right|_{x=-\left(\frac{h+t}{2}\right)^-} = (\epsilon_r - 1)k_0^2 H_y|_{x=-\left(\frac{h+t}{2}\right)^-} \quad (8.18)$$

$$\begin{bmatrix}
 \gamma_0 & -\gamma_0 & \gamma_0 & 0 & 0 & 0 & 0 & 0 & 0 & 0 \\
 \frac{\gamma_0}{j\epsilon_0\omega} + Z_g & -Z_g & -Z_g & 0 & 0 & 0 & 0 & 0 & 0 & 0 \\
 0 & -\gamma_0 e^{h_m \gamma_0} & \gamma_0 e^{-h_m \gamma_0} & \frac{jk_{TEM}}{\epsilon_r} e^{jh_m k_{TEM}} & -\frac{jk_{TEM}}{\epsilon_r} e^{-jh_m k_{TEM}} & \frac{\gamma_{TM}}{\epsilon_r} e^{h_m \gamma_{TM}} & -\frac{\gamma_{TM}}{\epsilon_r} e^{-h_m \gamma_{TM}} & 0 & 0 & 0 \\
 0 & 0 & 0 & -\frac{jk_{TEM}}{\epsilon_r} e^{jh_p k_{TEM}} & \frac{jk_{TEM}}{\epsilon_r} e^{-jh_p k_{TEM}} & -\frac{\gamma_{TM}}{\epsilon_r} e^{h_p \gamma_{TM}} & \frac{\gamma_{TM}}{\epsilon_r} e^{-h_p \gamma_{TM}} & -\gamma_0 \sinh[h_m \gamma_0] & 0 & 0 \\
 0 & e^{h_m \gamma_0} & e^{-h_m \gamma_0} & -e^{jh_m k_{TEM}} & -e^{-jh_m k_{TEM}} & -e^{h_m \gamma_{TM}} & -e^{-h_m \gamma_{TM}} & 0 & 0 & 0 \\
 0 & 0 & 0 & e^{jh_p k_{TEM}} & e^{-jh_p k_{TEM}} & e^{h_p \gamma_{TM}} & e^{-h_p \gamma_{TM}} & -\cos[h_m \gamma_0] & 0 & 0 \\
 0 & a_{72} & a_{73} & -k_{TEM}^2 e^{-jh_m k_{TEM}} & -\gamma_{TM}^2 e^{-jh_m k_{TEM}} & -\gamma_{TM}^2 e^{-h_m \gamma_{TM}} & -\gamma_{TM}^2 e^{-h_m \gamma_{TM}} & 0 & 0 & 0 \\
 0 & 0 & 0 & -k_{TEM}^2 e^{jh_p k_{TEM}} & -k_{TEM}^2 e^{-jh_p k_{TEM}} & \gamma_{TM}^2 e^{h_p \gamma_{TM}} & \gamma_{TM}^2 e^{-h_p \gamma_{TM}} & a_{88} & 0 & 0
 \end{bmatrix}$$

After some algebra, a  $8 \times 8$  linear system is obtained, whose related matrix coefficient is entirely shown in the previous page; by equating to zero the relevant determinant it is possible to write the sought dispersion equation, not reported here for space limitation. As in the previous cases, a numerical solution of the equation provides values of the longitudinal wave number for all the modes propagating inside the structure. Since the considered waveguide is open, a complex  $k_z$  is expected, whose real and imaginary parts represent, respectively, the phase and attenuation constant of the involved leaky modes. It is worth noting that in this case the same equation describes the propagation of TM as well as TEM modes: one can plot the wanted solution by referring to a suitable initial point by starting from the cutoff value associated to the unperturbed solution. To write more compactly the  $8 \times 8$  matrix some positions have been suitably introduced. In particular  $h_m = (h - t/2)$  and  $h_p = (h + t/2)$ , being  $t$  the slab thickness and  $h$  the waveguide height. In addition the explicit value of the remaining three elements are reported in the following

$$\begin{aligned} a_{72} &= \gamma_0^2 e^{h_m \gamma_0} - (\epsilon_r - 1) k_0^2 e^{h_m \gamma_0} \\ a_{73} &= \gamma_0^2 e^{-h_m \gamma_0} - (\epsilon_r - 1) k_0^2 e^{-h_m \gamma_0} \\ a_{88} &= -\gamma_0^2 \cosh(h_m \gamma_0) - (\epsilon_r - 1) k_0^2 \cosh(h_m \gamma_0). \end{aligned} \quad (8.20)$$

The values of  $\gamma_0$ ,  $\gamma_{TM}$  and  $k_{TEM}$  are those already presented for the TM and TEM cases related to the symmetric closed structure.

#### 8.2.4. Multi-modal Bloch analysis

In order to validate the homogenized representation of the WM slab, full-wave simulations of the actual periodic structure have been performed with CST Microwave Studio, both for closed and open structures. In particular, a Bloch analysis has been performed on a finite length of a WM-loaded PPW constituted by an integer number of the WM unit cell (i.e., on a *macrocell*), bounded by two waveguide ports that allow for obtaining the scattering parameters for each mode propagating inside the structure. Considering a sufficiently high number of unit cells inside the macrocell allows for accurately evaluating the mutual coupling effects among unit cells; however, it also introduces spurious solutions related to the non-uniqueness of root-extraction operations in the complex plane (see, e.g., [124]). To eliminate such an ambiguity and to extract the transfer matrix of the unit cell ( $T_u$ ) from

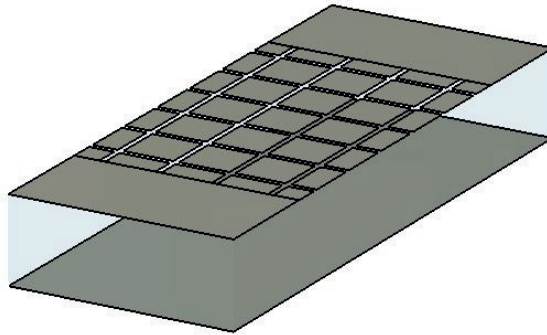
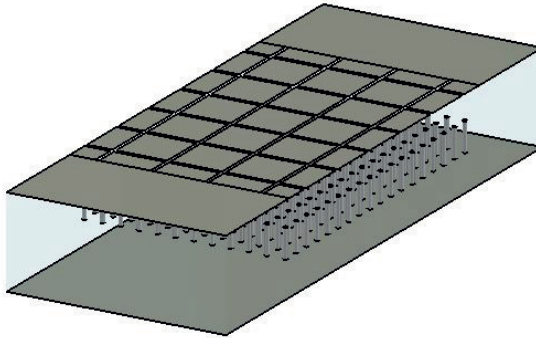


Fig. 8.5. Virtual model of a parallel-plate waveguide whose upper plate is made by a partially reflecting surface. This class of structures are also named Fabry-Perot cavity antennas due to its similarity to the Fabry-Perot interferometer.

that obtained through a full-wave solution of the considered macrocell, a simple approach outlined in [125] has been adopted, which basically allows for evaluating  $T_u$  from the knowledge of two matrices  $T_N$  and  $T_M$ , representing the transfer matrix of macrocells constituted by  $N$  and  $M = N + 1$  unit cells, respectively. Typically, the choice of  $N$  and  $M$  depends on the complexity of the structure; for the case at hand good results have been obtained with  $N = 15$ . It is important to note that two different simulations must be performed, whose structures are made by  $N$  and  $M$  unit cells. The thicker is the WM slab placed inside the waveguide the heavier will be the computational load. Just to give an example, a configuration having a thick  $t = 4$  mm requires about 400.000 tetrahedrons to accurately discretized the overall structure, while for larger value of  $t$ , for instance 9 mm, this number may exceed  $10^6$  tetrahedrons. With regards to the simulation time, it ranges from few hours for thinner slabs up to more than one day for larger value of  $t$ ; computers are equipped with i7 CPU of fourth/fifth generation (8/12 cores), at least 20 Gb of memory is requested. In Figs. 8.5 and 8.6 an example of the simulated structures both loaded and unloaded with a wire medium slab (whose wires for simplicity are suspended in air, but can be easily supported by a foam layer), are presented.

The top plate of the open waveguide is a PRS made by a periodic lattice of square patches: transversal slots (with respect to the direction



**Fig. 8.6.** Virtual model of a Fabry-Perot cavity antenna loaded with a wire medium slab to suppress spurious radiation related to the TEM leaky mode.

of propagation) allow for radiation of TM modes, while the longitudinal that of TE modes. It is important to note that if only TM modes are excited by suitably considering symmetric PMC wall, the longitudinal slots do not affect its radiation since they are not able to sensibly perturb the TM currents distribution. Since we are considering a configuration that supports both TM and TEM modes, namely a multi-modal configuration, a suitable generalization of the proposed approach has been developed recasting the general procedure outlined in [126]. This entails that the dimension of the considered transfer matrix be equal to  $2K \times 2K$ , with  $K$  the total number of propagating modes, that in turn must be suitably arranged inside the matrix. It is finally important to note that the larger is the value of  $K$ , the longer will be the full-wave simulation of the structure at hand, since the solution must be carried out exciting one mode at a time. In the following dispersion curves achieved by means of our full wave multi-modal Bloch analysis will be labeled in the legend as 'CST'.

### 8.3. Results for a closed structure

We consider first a WM-loaded PPW, whose lower and upper plates are assumed to be perfect conductors. The waveguide has thickness  $h$ , is filled with air and is loaded by a WM slab having thickness  $t$  placed symmetrically, i.e., at equal distances from the metal plates.

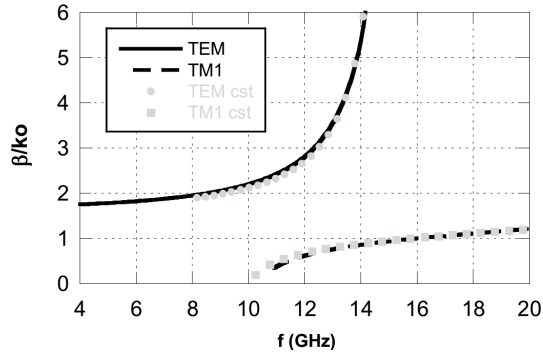


Fig. 8.7. Dispersion curves for the TEM,  $TM_1$  modes supported by an air-filled PPW partially filled with a WM slab (closed configuration). Parameters: PPW thickness  $h = 14.27$  mm; WM slab thickness  $t = 10$  mm; wire radius  $a = 0.14$  mm; wire spacing  $d = 1$  mm; relative permittivity of the wire host medium  $\epsilon_{rh} = 1.06$ . Legend: FMT = Field-Matching Technique; CST = CST Microwave Studio. Copyright © 2015, IEEE.

In Fig. 8.7 dispersion curves are reported for the TEM, and  $TM_1$  modes supported by a structure with  $h = 14.27$  mm and  $t = 10$  mm, in the frequency range from 4 to 20 GHz (the cutoff frequency of the unperturbed  $TM_1$  mode is 10.51 GHz). The WM is constituted by wires with radius  $a = 0.14$  mm arranged in a lattice with period  $d = 1$  mm ( $d = \lambda/10$  at  $f = 30$  GHz), embedded in a medium with  $\epsilon_{rh} = 1.06$  (foam); the resulting plasma frequency is then, from (8.2),  $f_p = 150$  GHz. The results obtained with the field matching technique are in good agreement with those produced with full-wave results obtained through the multimodal Bloch analysis, confirming the accuracy of the homogenized model of the wire medium slab. It can be noted that the presence of the WM strongly perturbs the TEM mode, whose electric field is purely vertical and is thus short-circuited by the metal wires. In particular, the perturbed TEM mode has a normalized phase constant larger than one and thus has become a slow wave. Furthermore, its normalized phase constant has a vertical asymptote, beyond which the mode is suppressed; it has been verified that its existence is due to the transverse resonance of the additional TEM wave inside the WM slab, which occurs when  $f = c/(2t\sqrt{\epsilon_{rh}})$  ( $f = 14.6$  GHz for the structure considered in Fig. 8.7). In Fig. 8.8 a parametric analysis for different values of the thickness  $t$  of the wire medium slab is presented, allowing us to confirm the expected position of the asymptote. Indeed we have the following values for the resonant frequencies:  $f_1 = 14.6$  GHz,  $f_2 = 30$

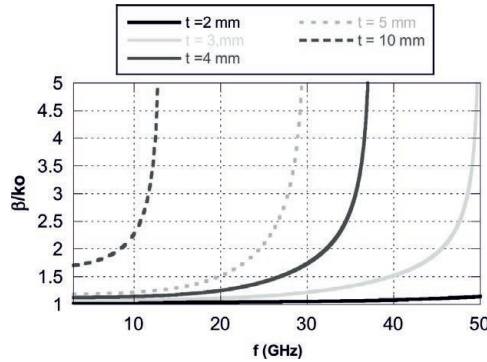


Fig. 8.8. Dispersion curves for the TEM mode supported by the same structure considered in Fig. 8.7 for different values of the slab's thickness  $t$  (see legend).

GHz,  $f_3 = 37.5$  GHz and  $f_4 = 50$  GHz, that are related, respectively, to these values of the thickness  $t_1 = 10$  mm,  $t_2 = 5$  mm,  $t_3 = 4$  mm and  $t_4 = 3$  mm. In Fig. 8.9 a dispersion curves are reported for the TEM,  $TM_1$  and the  $TM_2$  modes supported by the same PPW as in Fig. 8.7, now loaded with a thinner WM slab having  $t = 4$  mm, constituted by wires with radius  $a = 0.19$  mm arranged in a lattice with period  $d = 1.5$  mm ( $d = \lambda/10$  at  $f = 20$  GHz), embedded in a medium with  $\epsilon_{rh} = 1.06$  (foam); the resulting plasma frequency is then, from (8.2),  $f_p = 90$  GHz. Again, the results obtained by numerically solving the dispersion equation are in very good agreement with the full-wave solution. It can be noted that the  $TM_1$  mode is minimally affected by the presence of the WM layer; in fact, the WM interacts with the vertical component of the electric field, which has a null in the middle of the PPW for this mode (see Fig. 8.1). On the other hand, having reduced the thickness of the WM slab, the vertical asymptote of the TEM mode has been shifted to higher frequencies, beyond the WM homogenization regime (not visible in Fig. 8.9); however, the slow-wave nature of the perturbed TEM mode still has remarkable consequences on the radiation properties of open PPW configurations, as discussed in the next sections. As a final example, in Fig. 8.10 dispersion curve obtained again for the same structure considered in Fig. 8.9 (see its label for the relevant details) for the  $TE_1$  mode is presented. The results achieved with a numerical solution of the dispersion equation is reported and validated by means of the presented multimodal full-wave approach. Even though the  $TM_1$  and  $TE_1$  are degenerates in the associated unperturbed waveguide, here

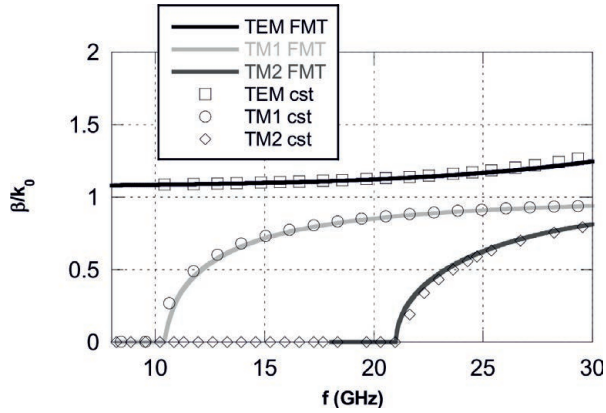


Fig. 8.9. Dispersion curves for the TEM,  $TM_1$  and  $TM_2$  modes supported by a loaded PPW (closed configuration). Parameters: PPW thickness  $h = 14.27$  mm; WM slab thickness  $t = 3$  mm; wire radius  $a = 0.19$  mm; wire spacing  $d = 1.5$  mm; relative permittivity of the wire host medium  $\epsilon_{rh} = 1.06$ . Legend: FMT = Field-Matching Technique; CST = CST Microwave Studio, TLM = Transmission-Line Model. Copyright © 2015, IEEE.

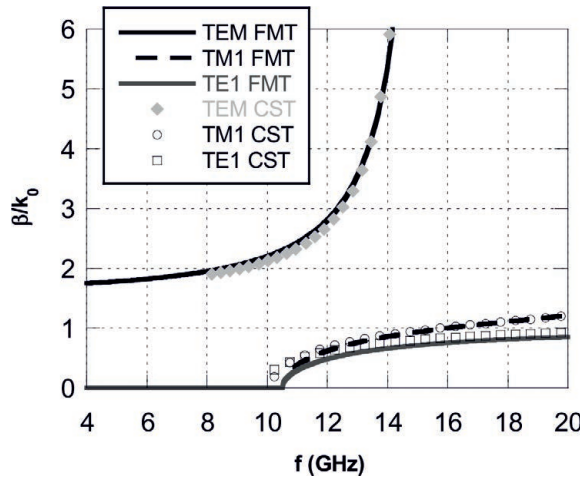


Fig. 8.10. Dispersion equation for the  $TE_1$  mode propagating in the same structure presented in Fig. 8.7. It is not sensibly affected by the wire medium slab due to the E-field orientation; again a full validation has been reported. Copyright © 2015, IEEE.

they show a quite dissimilar behavior due to a different interaction with the wire medium slab filling the structure. Indeed, the TM mode undergoes anyway a small perturbation, while the TE mode is slightly affected by the radial extension of the wires, that strictly speaking cannot be considered null. As will be shown in the following, it is possible to change the dielectric permittivity filling the slab in conjunction with the geometry of the associated open structure to achieve an equalization of the dispersion diagram in a small range of frequencies.

### 8.3.1. Transverse field configuration

As we have seen in the first section of this chapter, by enforcing the boundary condition determined by the nature of the considered structure, it is possible to achieve a  $N \times N$  matrix modeling the problem; its eigenvalues represent the propagation constant of the modes allowed in the guide. When a specific solution is selected, one can straightforwardly evaluate the transverse field configuration by determining  $N - 1$  of the  $N$  total unknowns describing the problem. In this way one can plot e.g., the magnetic field by introducing the relevant frequency and propagation constant. According to the modal results, the field distribution of the TEM mode, that is normally a constant, is expected to be heavily perturbed for increasing value of the thickness  $t$ . In Fig. 8.11 field configurations for the  $y$  component of the magnetic field are reported for the TEM,  $TM_1$  and  $TM_2$  modes supported by the same structure considered so far, loaded with a wire medium having thickness  $t$  equal to 4 mm and 9 mm, at two different frequencies ( $f = 12$  GHz and  $f = 18$  GHz for TEM,  $TM_1$  and  $f = 24$  GHz for  $TM_2$ ). The field configurations of the same modes in the absence of WM loading are also reported for comparison; these are of course independent of frequency. It can be noted that the WM slab has a dramatic effect on the TEM mode, whose unperturbed field configuration is a constant; this is due to the strong interaction between the TEM electric field, which is vertical, and the metal wires of the WM. In particular, the perturbed TEM mode is transversely evanescent in air outside the WM slab. On the other hand, it has a small impact on the  $TM_1$  and  $TM_2$  modes, particularly for the first, whose vertical component of the electric field (the one that interacts with the WM) has a null in the middle of the PPW.

In this section an equivalent transmission-line model will be derived for the electromagnetic fields inside a WM slab assuming an exponential

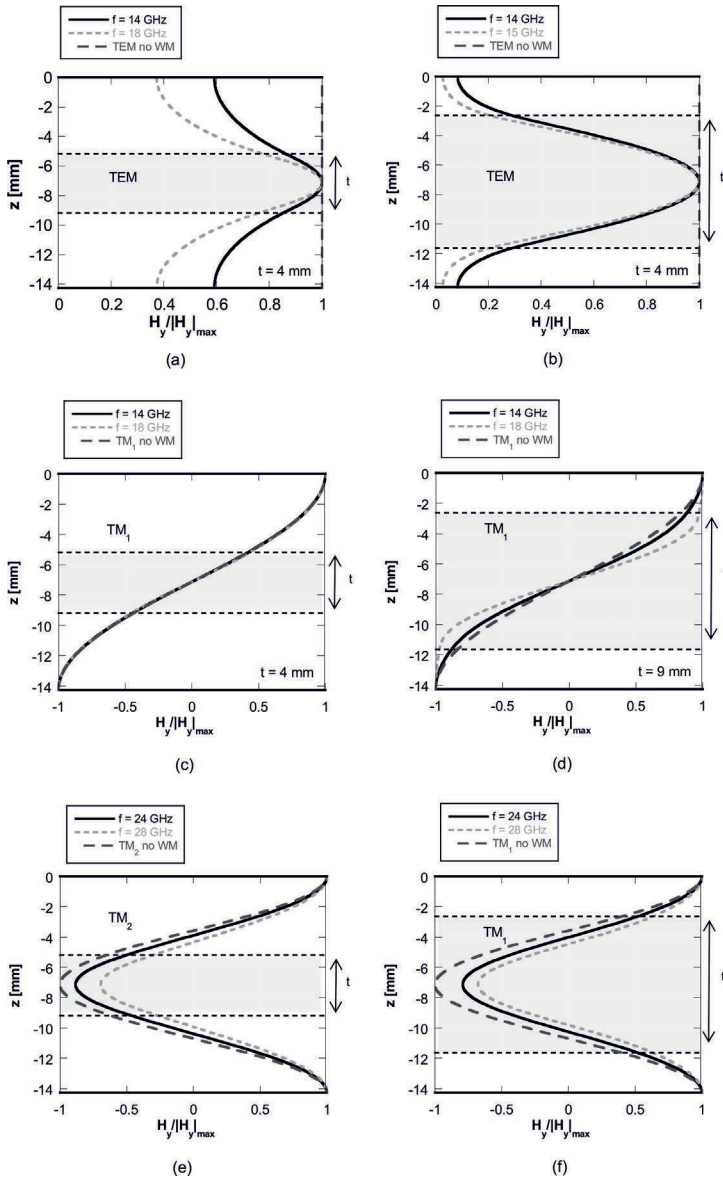


**Fig. 8.11.** Field configurations at different frequencies for the  $y$  component of the magnetic field of the TEM,  $TM_1$  and  $TM_2$  modes supported by a WM-loaded PPW. Parameters: PPW thickness  $h = 14.27$  mm; wire radius  $a = 0.19$  mm; wire spacing  $d = 1.5$  mm. The frequency-independent field configurations of the same modes in the absence of WM loading are also reported for comparison. Copyright © 2015, IEEE.

dependence on the  $x$  and  $y$  coordinates:  $\exp(-j(k_x x + k_y y))$ ; without loss of generality, we may also let  $k_x = 0$ . It is important to note that in this section, as usual, the vertical axis is represented by the  $z$  coordinate, being  $x$  the direction normal to the sheet plane (see Fig. 8.12(a)). Under these assumptions, as known, Maxwell's equations split into two separate sets (we adopt here different axis with respect to Section 8.2), one for  $\text{TE}^z$  fields:

$$\frac{dE_x}{dz} = -j\omega\mu_0 H_y \quad (8.21)$$

$$jk_y E_x = -j\omega\mu_0 H_x \quad (8.22)$$

$$-jk_y H_z - \frac{dH_y}{dz} = j\omega\varepsilon_0 \varepsilon_{\perp} E_x \quad (8.23)$$

and one for  $\text{TM}^z$  fields:

$$-jk_y E_z - \frac{dE_y}{dz} = -j\omega\mu_0 H_x \quad (8.24)$$

$$\frac{dH_x}{dz} = j\omega\varepsilon_0 \varepsilon_{\perp} E_y \quad (8.25)$$

$$jk_y H_x = j\omega\varepsilon_0 \varepsilon_{\parallel} E_z. \quad (8.26)$$

The permittivity dyadic for the wire medium has been introduced in Section 8.2 and is recalled here for convenience

$$\underline{\underline{\varepsilon}} = \varepsilon_0 \left[ \varepsilon_{\perp} (\mathbf{u}_x \mathbf{u}_x + \mathbf{u}_y \mathbf{u}_y) + \varepsilon_{\parallel} \mathbf{u}_z \mathbf{u}_z \right] \quad (8.27)$$

where (see [103, 105])

$$\varepsilon_{\perp} = \varepsilon_h \quad (8.28)$$

$$\varepsilon_{\parallel} = \varepsilon_h \left( 1 - \frac{k_p^2}{\varepsilon_h \beta^2 - k_z^2} \right), \quad (8.29)$$

$k_p^2$  is given by (8.5) and  $\beta^2 = \omega^2 \mu_0 \varepsilon_0$ .

In the  $\text{TE}$  case the electric field is orthogonal to the wires, hence the wave does not interact with them and Maxwell's equations (8.21), (8.22) and (8.23) are the same as in an ordinary isotropic medium having relative permittivity  $\varepsilon_{\perp} = \varepsilon_{\text{rh}}$ . By eliminating  $H_z$  the standard  $\text{TE}$  transmission-line equations are then recovered:

$$\begin{aligned} \frac{dV^{\text{TE}}}{dz} &= -jk_z^{\text{TE}} Z_c^{\text{TE}} I^{\text{TE}} \\ \frac{dI^{\text{TE}}}{dz} &= -jk_z^{\text{TE}} Y_c^{\text{TE}} V^{\text{TE}} \end{aligned} \quad (8.30)$$

where  $V^{\text{TE}} = E_x$ ,  $I^{\text{TE}} = H_y$ ,  $k_z^{\text{TE}} = \sqrt{\epsilon_{\text{rh}}k_0^2 - k_y^2}$  and  $Z_c^{\text{TE}} = 1/Y_c^{\text{TE}} = \omega\mu_0/k_z$ . In the TM case, assuming first  $k_z^2 \neq \epsilon_{\text{rh}}k_0^2$  and eliminating  $E_z$ , from (8.26) we have

$$\begin{aligned}\frac{dV^{\text{TM}}}{dz} &= -jk_z^{\text{TM}}Z_c^{\text{TM}}I^{\text{TM}} \\ \frac{dI^{\text{TM}}}{dz} &= -jk_z^{\text{TM}}Y_c^{\text{TM}}V^{\text{TM}}\end{aligned}\quad (8.31)$$

where  $V^{\text{TM}} = E_y$ ,  $I^{\text{TM}} = -H_x$ , and

$$\begin{aligned}k_z^{\text{TM}} &= \sqrt{\epsilon_{\text{rh}}k_0^2 - k_p^2 - k_y^2} \\ Z_c^{\text{TM}} &= \frac{1}{Y_c^{\text{TM}}} = \frac{1}{\omega\epsilon_0\epsilon_{\text{rh}}k_y} \sqrt{(\epsilon_{\text{rh}}k_0^2 - k_y^2)(k_p^2 + k_y^2)}.\end{aligned}\quad (8.32)$$

When  $k_z^2 = \epsilon_{\text{rh}}k_0^2$  it results  $\epsilon_{\parallel} \rightarrow \infty$ , hence  $E_z \rightarrow 0$ ; the wave is then TEM<sup>z</sup> (it is the additional wave that exists in the WM due to its spatially dispersive nature [116]) and from (8.24), (8.25) and (8.26) we have

$$\begin{aligned}\frac{dV^{\text{TEM}}}{dz} &= -jk_z^{\text{TEM}}Z_c^{\text{TEM}}I^{\text{TEM}} \\ \frac{dI^{\text{TEM}}}{dz} &= -jk_z^{\text{TEM}}Y_c^{\text{TEM}}V^{\text{TEM}}\end{aligned}\quad (8.33)$$

where  $V^{\text{TEM}} = E_y$ ,  $I^{\text{TEM}} = -H_x$ , and

$$\begin{aligned}k_z^{\text{TEM}} &= k_0\sqrt{\epsilon_{\text{rh}}} \\ Z_c^{\text{TEM}} &= \frac{1}{Y_c^{\text{TEM}}} = \sqrt{\frac{\mu_0}{\epsilon_0\epsilon_{\text{rh}}}}\end{aligned}\quad (8.34)$$

#### 8.4. Equivalent network for an air/WM interface

Let us now consider the planar interface  $z = 0$  between the half space  $z > 0$  filled with an ordinary dielectric medium having relative permittivity  $\epsilon_r$  and the half-space  $z < 0$  filled with WM (see Fig. 8.12(a)). In the TE case, the standard boundary conditions that hold at  $z = 0$  (i.e., the continuity of the tangential components of the electric and magnetic fields) require voltages and currents to be continuous at the interface. This results in a two-port representation of the interface consisting in the usual direct connection of the two equivalent transmission lines associated with the TE waves in the two half-spaces.

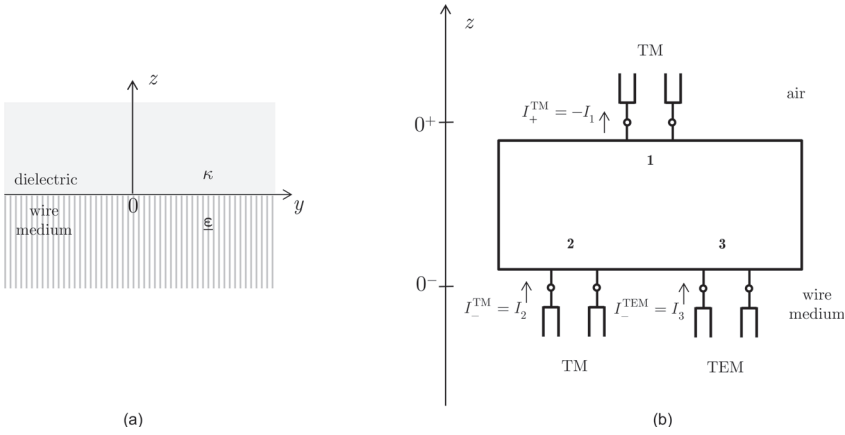


**Fig. 8.12.** (a) Planar interface between a dielectric half space with relative permittivity  $\epsilon_r$  and a WM half space with relative permittivity dyadic  $\hat{\epsilon}$  (see (8.1)), (b) Relevant transverse equivalent network for TM-polarized waves independent of  $x$  and with an  $\exp(-jk_y y)$  dependence on  $y$ . Copyright © 2015, IEEE.

In the TM case instead, the presence of an additional wave in the WM requires the interface to be represented by a *three-port* network. Basically, whenever a TM plane wave is impinging on the interface not only a TM but also TEM wave (again with respect to wire extension) is transmitted in the wire medium. The standard boundary conditions require that the total voltages and currents be continuous at the interface, thus we can write:

1. Continuity of  $\mathbf{E}_\tau = E_y \mathbf{y}_0$  at the air/WM interface

$$E_y|_{z=0^+} = E_y|_{z=0^-} \quad (8.35)$$

2. Continuity of  $\mathbf{E}_\tau = H_x \mathbf{x}_0$  at the second air/WM interface

$$H_x|_{z=0^+} = H_x|_{z=0^-} \quad (8.36)$$

3. ABC at the air/WM interface [103]

$$E_z|_{z=0^+} = \epsilon_h E_z|_{z=0^-} \quad (8.37)$$

It is interesting to note that this last condition, introduced for the first time in [103], must be enforced for the longitudinal component of the

electric field. Using the first of Maxwell's equations, the ABC condition can be rewritten as

$$\left( \frac{dE_y}{dz} - j\omega\mu_0 H_x \right)_{z=0^+} = \epsilon_h \left( \frac{dE_y}{dz} - j\omega\mu_0 H_x \right)_{z=0^-} \quad (8.38)$$

Now, using the transmission-line equation previously introduced, we have

$$E_y|_{z=0^+} = V_+^{TM} \quad E_y|_{z=0^-} = V_-^{TM} + V_-^{TEM} \quad (8.39)$$

$$-H_x|_{z=0^+} = I_+^{TM} \quad -H_x|_{z=0^-} = I_-^{TM} + I_-^{TEM} \quad (8.40)$$

hence the first two boundary conditions can be re-written as

$$V_+^{TM} = V_-^{TM} + V_-^{TEM} \quad (8.41)$$

$$I_+^{TM} = I_-^{TM} + I_-^{TEM} \quad (8.42)$$

while for the last we have

$$\frac{dV_+^{TM}}{dz} + j\omega\mu_0 I_+^{TM} = \epsilon_h \left( \frac{dV_-^{TM}}{dz} + \frac{dV_-^{TEM}}{dz} + j\omega\mu_0 I_-^{TM} + j\omega\mu_0 I_-^{TEM} \right) \quad (8.43)$$

By exploiting the TM and TEM transmission-line equations (see (8.31) and (8.33)), it is possible to express  $dV_+^{TM/TEM}/dz$  in terms of  $I_+^{TM/TEM}$  so that after some algebra (8.43) becomes

$$I_-^{TM} = \frac{\epsilon_{\parallel}}{\epsilon_{\perp}} I_+^{TM} = \zeta I_+^{TM} \quad (8.44)$$

where

$$\zeta = \frac{\epsilon_{\parallel}}{\epsilon_{\perp}} = 1 - \frac{k_p^2}{\beta^2 \epsilon_h - k_z^2} \quad (8.45)$$

but considering equation (8.32) it is finally possible to write

$$\zeta = \frac{k_y^2}{k_p^2 + k_y^2}. \quad (8.46)$$

Now we can re-write (8.42) as

$$I_-^{TEM} = I_+^{TM} - I_-^{TM} = (1 - \zeta) I_+^{TM} \quad (8.47)$$

thus, the air/wire medium interface can be represented by a 3-port network, as shown in Fig. 8.12(a). In particular, referring to Fig. 8.13

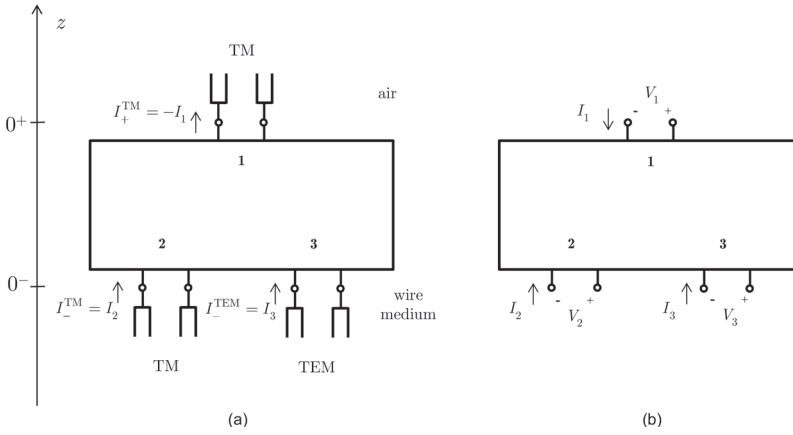


**Fig. 8.13.** (a) Transmission-line equivalent network for an air/wire medium interface, (b) 3-port equivalent network for the considered transmission line. Copyright © 2015, IEEE.

we finally have

$$I_1 = I_+^{TM} \quad I_2 = -I_-^{TM} \quad I_3 = -I_-^{TEM} \quad (8.48)$$

$$V_1 = V_+^{TM} \quad V_2 = V_-^{TM} \quad V_3 = V_-^{TEM} \quad (8.49)$$

Therefore the 3-port network is described by the following equations (where  $I_1$ ,  $V_2$  and  $V_3$  have been selected as independent variables)

$$\begin{cases} V_1 = V_2 + V_3 \\ I_2 = -\xi I_1 \\ I_3 = (\xi - 1)I_1 \end{cases} \quad (8.50)$$

### 8.4.1. Input impedance for the equivalent 3-port network

In this section the input impedance of the 3-port network presented in Fig. 8.13 when it is closed on a given load will be evaluated. Specifically, as shown in Fig. 8.14, here ports 2 and 3 are closed on a 2-port load having impedance  $[Z_L]$  and represented by a  $2 \times 2$  matrix, hence the relation between voltage and current can be written as follow

$$\begin{pmatrix} V_2 \\ V_3 \end{pmatrix} = - [ Z_L ] \begin{pmatrix} I_2 \\ I_3 \end{pmatrix}$$

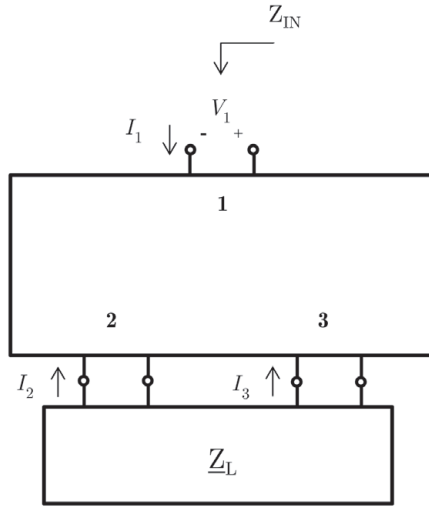


Fig. 8.14. Equivalent 3-port network close on a load impedance.

by exploiting the boundary condition and equations (8.50) we get

$$\begin{aligned}
 V_1 &= \begin{pmatrix} 1 & 1 \end{pmatrix} \begin{pmatrix} V_2 \\ V_3 \end{pmatrix} = - \begin{pmatrix} 1 & 1 \end{pmatrix} \begin{bmatrix} \underline{Z}_L \end{bmatrix} \begin{pmatrix} I_2 \\ I_3 \end{pmatrix} \\
 &= - \begin{pmatrix} 1 & 1 \end{pmatrix} \begin{bmatrix} \underline{Z}_L \end{bmatrix} \begin{pmatrix} -\xi \\ \xi - 1 \end{pmatrix} I_1
 \end{aligned} \tag{8.51}$$

hence, we finally have

$$Z_{IN} = \frac{V_1}{I_1} = - \begin{pmatrix} 1 & 1 \end{pmatrix} \begin{bmatrix} \underline{Z}_L \end{bmatrix} \begin{pmatrix} \xi \\ \xi - 1 \end{pmatrix}. \tag{8.52}$$

If a closed structure is analyzed, a bisection with a perfect electric or magnetic conductor can be exploited and the overall waveguide is represented by an air/wire medium interface whose 3-port model is loaded with two TM/TEM transmission lines having length  $t/2$  and closed on a short/open circuit. In this condition the evaluation of the matrix  $\underline{Z}_L$  is straightforward and leads to the following  $2 \times 2$  matrix

$$\underline{Z}_L = \begin{pmatrix} jZ_{TM} \tan k_z^{TM} t/2 & 0 \\ 0 & jZ_{TEM} \tan k_z^{TM} t/2 \end{pmatrix} \tag{8.53}$$

Having available the input impedance of the equivalent network for a bisected parallel plate waveguide loaded with a wire medium, by means of the transverse resonance method we can easily write the sought dispersion equation. Consequently, a numerical solution gives the dispersion diagram of the relevant TEM and TM modes. In the next subsection the same structure already solved through the field matching technique will be considered and a number of comparisons will be provided. It is important to note that these two alternative methods must lead to exactly the same solution, even though we consider the equivalent network model as more attractive and easier to implement, in particular when stratified structures possibly made by one or more wire medium slabs are designed.

#### 8.4.2. Model validation of the closed structure

In this section the equivalent network model designed for closed and symmetric structures is validated by solving the same waveguide considered in the previous section, whose dispersion results have been presented in Fig. 8.7 (see captions for more details). As shown in Fig.

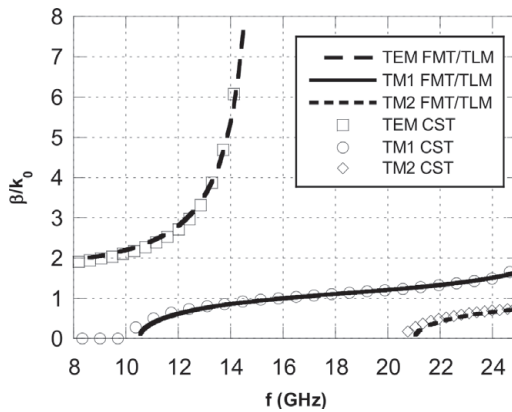


**Fig. 8.15.** Dispersion curves for the TEM,  $TM_1$  and  $TM_2$  modes for the same structure presented in Fig. 8.7. Parameters: PPW thickness  $h = 14.27$  mm; WM slab thickness  $t = 10$  mm; wire radius  $a = 0.14$  mm; wire spacing  $d = 1$  mm; relative permittivity of the wire host medium  $\epsilon_{rh} = 1.06$ . Legend: FMT = Field-Matching Technique; TLM = Transmission Line Model; CST = CST Microwave Studio. Copyright © 2015, IEEE.

8.15 the dispersion curves obtained with the field matching technique and the transmission line are practically superimposed. As a matter of

fact they should give exactly the same values of the propagation constant since, if properly managed, they must lead to the same dispersion equation. In addition, the numerical result is in perfect agreement with the full-wave solution developed by means of multimodal Bloch analysis (see Section 8.2.4 for the relevant details). To better understand the role of the plasma frequency of the wire medium slab, whose dependency on its parameters is outlined by equation (8.2), in Fig. 8.16 dispersion curves produced by three different configurations of the wire medium are presented. The first one, labeled as 'c1', is characterized by the fol-

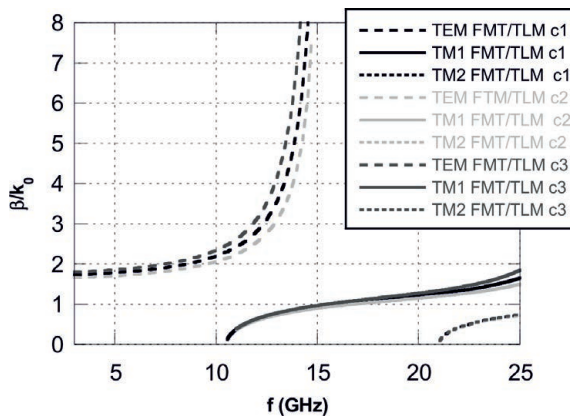


**Fig. 8.16.** Dispersion curves for the TEM,  $TM_1$  and  $TM_2$  modes for three different configurations of a wire medium slab having thickness  $t = 10$  mm. Parameters of c1 configuration: wire radius  $a = 0.14$  mm; wire spacing  $d = 1$  mm, plasma frequency  $f_p = 150$  GHz; c2 configuration:  $a = 0.19$  mm;  $d = 1.5$  mm,  $f_p = 150$  GHz; c3 configuration:  $a = 0.23$  mm;  $d = 1$  mm,  $f_p = 337$  GHz.

low parameters: wire radius  $a = 0.14$  mm; wire spacing  $d = 1$  mm, thus plasma frequency  $f_p = 150$  GHz. For the second and the third one, labeled as 'c2' and 'c3' it is:  $a = 0.19$  mm,  $d = 1.5$  mm,  $f_p = 90$  GHz and  $a = 0.23$  mm,  $d = 1$  mm,  $f_p = 337$  GHz. As expected, the phase constant of the  $TM_1$  and  $TM_2$  modes do not show appreciable differences in the region of frequency where they are fast waves. On the contrary, being the TEM mode always strongly perturbed it is slightly influenced by the plasma frequency of the wire medium; namely, higher values of  $f_p$  correspond to smaller value of the resonant frequency. This means that the formula proposed in the previous sections, that relates the asymptote position to the resonant thickness of the slab must be considered as a first-order approximation, anyway suitable for modeling

purposes. In Fig. 8.17 a series of diagrams have been reported aiming at fully characterizing the behavior of the propagating modes with respect to a selected range of thickness  $t$ . In particular Figs 8.17(a)-(f) present dispersion curves for TEM,  $TM_1$  and  $TM_2$  modes for six different values  $t$ , namely equal to 4, 5, 6, 7, 8 and 9 mm, obtained with the field matching technique as well as the proposed transmission line model. As expected, for growing values of the thickness, the asymptote characterizing the TEM behavior is shifted to lower frequencies; an analogue trend is observed for the  $TM_1$  when  $t$  is larger than 6 mm: indeed for this values of  $t$  an asymptote is shifting towards frequency closer and closer to the considered range. It is important to note that when the curve of the  $TM_1$  becomes slow (i.e.,  $\beta/k_0 > 1$ ) the leaky wave mode associated to open structure, whose modal curves will be a perturbed version of these presented, ends its scansion towards endfire. This means that the thickness  $t$  of the wire medium slab determine the slope of the phase constant of the considered mode and consequently the rate of the scansion with respect to frequency. In particular the configuration of Fig. 8.17(f) shows an asymptote at about 16.6 GHz, thus allowing for a unimodal  $TM_1$  regime between 16.6 GHz and 20 GHz. With regard to the  $TM_2$  mode, it results practically unperturbed in the considered range of frequency. Since the accuracy of the proposed approach has been already validated in the previous section in these picture, only the results for  $t = 4$  mm, namely Fig. 8.17(a), has been validated by means of a multimodal Bloch analysis. A result validating structures having larger values of  $t$  has been already reported in Fig. 8.15.

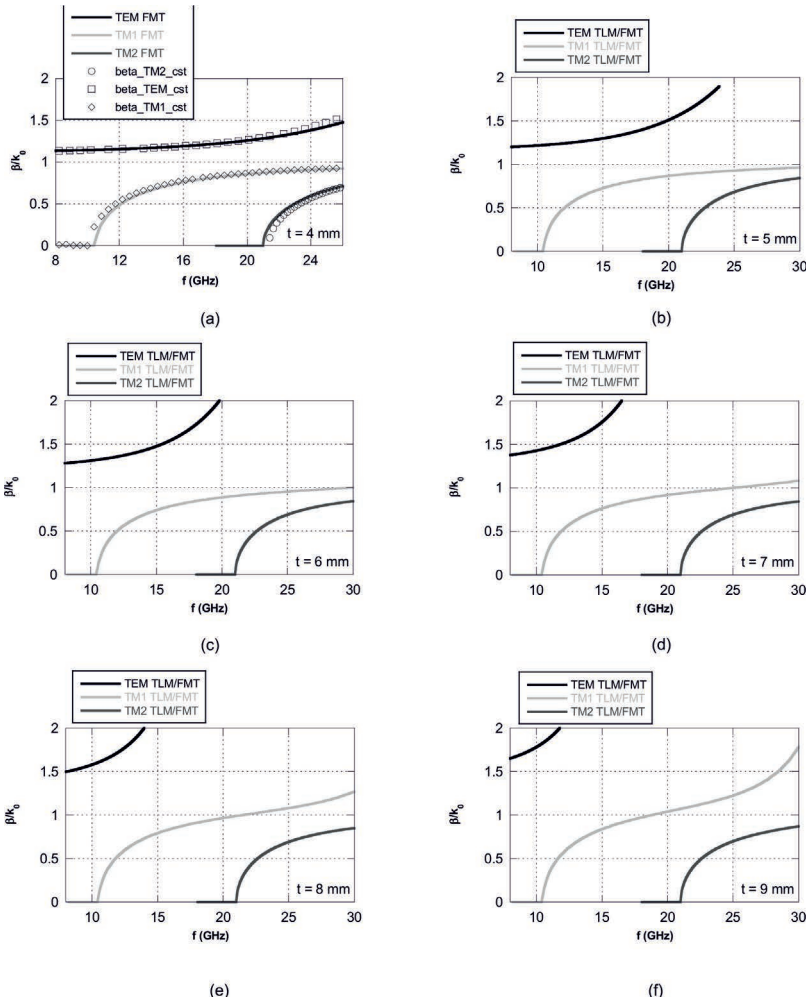


**Fig. 8.17.** Dispersion curves of TEM, TM<sub>1</sub> and TM<sub>2</sub> modes propagating inside a closed PPW loaded with a wire-medium slab for six different thicknesses; all the relevant details have been reported in each sub-figure. Parameters:  $a = 0.19$  mm;  $d = 1.5$  mm,  $f_p = 150$  GHz.

### 8.5. Input impedance of a wire medium slab

If the structure is no longer symmetric, for instance when it is opened to support leaky waves, two air/wire medium interfaces have to be considered. They can be represented by a series of two 3-port network, one mirrored with respect to the other, as shown in Fig. 8.18.

We call  $Z^\downarrow$  the input impedance seen looking downwards at the section  $z = 0^+$  and  $Z^\uparrow$  the input impedance at  $z = -t^-$  looking upwards at the section  $t = 0^-$ . Of course they are coincident for symmetric structures but can differ if multilayer configuration are considered. They coincide if the overall structure is symmetric, namely if above and below the wire medium slab there is the same material. The conditions of transverse resonance reads

$$Z^\uparrow + Z^\downarrow = 0 \quad (8.54)$$

in the following, the expression for  $Z^\downarrow$  as a function of  $Z_L$  and the parameters of the wire-medium slab (i.e., its thickness and its permittivity dyadic reported by (8.1)) will be presented. This is the essential quantity for the application of the transverse resonance technique [127, 128]. Furthermore, as shown below, it allows for directly calculating the  $ABCD$  of the WM slab; this is needed in the reciprocity-based approach to the calculation of the far-field pattern of sources radiating in the presence of the WM-loaded multilayer [121] (see next chapter). The constitutive relations for the three-port network associated with the lower dielectric-WM interface at  $z = -h$  are (see equation (8.50))

$$\begin{aligned} V'_1 &= V'_2 + V'_3 \\ I'_2 &= -\xi I'_1 \\ I'_3 &= (\xi - 1)I'_1 \end{aligned} \quad (8.55)$$

where  $\xi = k_y^2 / (k_y^2 + k_p^2)$ . By letting  $I'_1 = -Y'_L V'_1$  in (8.55) it results

$$I'_2 = Y'_L \xi (V'_1 + V'_3) \quad (8.56)$$

$$I'_3 = (1 - \xi) Y'_L \xi (V'_2 + V'_3). \quad (8.57)$$

Let now the TM and TEM transmission lines inside the WM slab be represented through their ABCD matrices:

$$\begin{pmatrix} V_2 \\ -I_2 \end{pmatrix} = \begin{pmatrix} A_{TM} & B_{TM} \\ C_{TM} & D_{TM} \end{pmatrix} \begin{pmatrix} V'_2 \\ I'_2 \end{pmatrix} \quad (8.58)$$



Let now  $[Z_L'']$  be the impedance matrix at  $z = 0^-$  looking downwards (see Fig. 8.18), defined by

$$\begin{pmatrix} V_2 \\ V_3 \end{pmatrix} = [Z_L''] \cdot \begin{pmatrix} -I_2 \\ -I_3 \end{pmatrix} \quad (8.64)$$

From (8.60), (8.61), it results

$$[Z_L''] = [T] \cdot [Y]^{-1} \quad (8.65)$$

On the other hand, from (8.50) and (8.64) we have

$$\begin{aligned} V_1 = V_2 + V_3 &= \begin{pmatrix} 1 & 1 \end{pmatrix} \begin{pmatrix} V_2 \\ V_3 \end{pmatrix} \\ &= \begin{pmatrix} 1 & 1 \end{pmatrix} [Z_L''] \cdot \begin{pmatrix} \xi \\ 1 - \xi \end{pmatrix} I_1 \end{aligned} \quad (8.66)$$

where  $\xi = k_y^2 / (k_y^2 + k_p^2)$  and  $\varepsilon_l$  is the relative permittivity of the dielectric layer adjacent to the WM interface at  $z = 0$ . Finally, from (8.66) and (8.65), the sought impedance  $Z^\downarrow$  is obtained as

$$Z^\downarrow = \begin{pmatrix} 1 & 1 \end{pmatrix} \cdot [T] \cdot [Y]^{-1} \cdot \begin{pmatrix} \xi \\ 1 - \xi \end{pmatrix} \quad (8.67)$$

from which, performing explicitly the matrix multiplications, the sought quantity is obtained. By enforcing the transverse resonance condition the dispersion equation of a parallel-plate waveguide loaded with a wire medium slab having thickness  $t$  can be straightforwardly achieved, resulting more compact and easy to implement with respect to the determinant of the matrix generated by the more general field matching technique. It is finally important to note that the input impedance just derived is essential for the evaluation the radiated field through reciprocity, as will be illustrated in the next chapter.

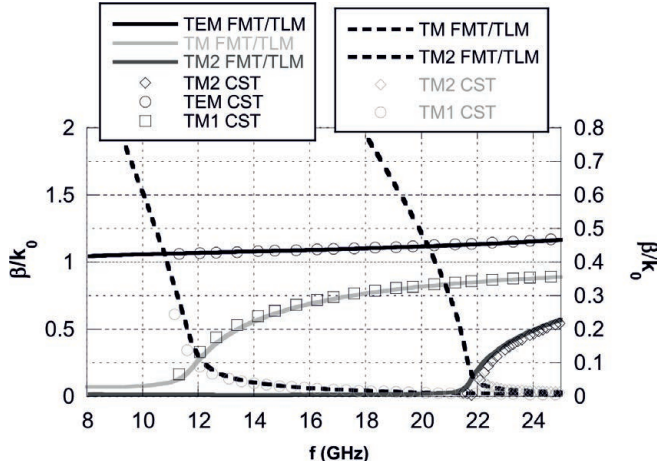


Fig. 8.19. Dispersion and attenuation curves for the TEM,  $TM_1$  and  $TM_2$  modes for an open PPW loaded with a wire medium slab. Parameters: PPW thickness  $h = 14.27$  mm; WM slab thickness  $t = 3$  mm; wire radius  $a = 0.19$  mm; wire spacing  $d = 1.5$  mm; relative permittivity of the wire host medium  $\epsilon_{rh} = 1.06$ . Legend: FMT = Field-Matching Technique; TLM = Transmission Line Model; CST = CST Microwave Studio. The upper plate of the PPW is made by square patches whose unit cell has a slot width  $w = 0.01$  mm. Copyright © 2015, IEEE.

## 8.6. Open structure

Let us now consider a WM-loaded structure in an open configuration, obtained replacing the PPW upper plate with a PRS constituted by an infinitesimally thin metal patterned screen. Since radiation may escape from the waveguiding region, leaky-wave regimes are now expected to occur in the modal spectrum [117, 118]. In Fig. 8.19 the same structure as in Fig. 8.9 is considered, being the PRS modeled as a simple shunt admittance in the relevant equivalent network, whose expression is [119]

$$Y_{\text{PRS}} = \frac{2j\gamma}{\eta_{\text{eff}}} \quad (8.68)$$

where

$$\gamma = \frac{pk_{\text{eff}}}{\pi} \ln \csc \left( \frac{\pi w}{2p} \right) \quad (8.69)$$

and  $\eta_{\text{eff}} = \eta_0 / \sqrt{\epsilon_{\text{eff}}}$ ,  $k_{\text{eff}} = k_0 \sqrt{\epsilon_{\text{eff}}}$ , with  $\epsilon_{\text{eff}} = (\epsilon_r + 1)/2$ .

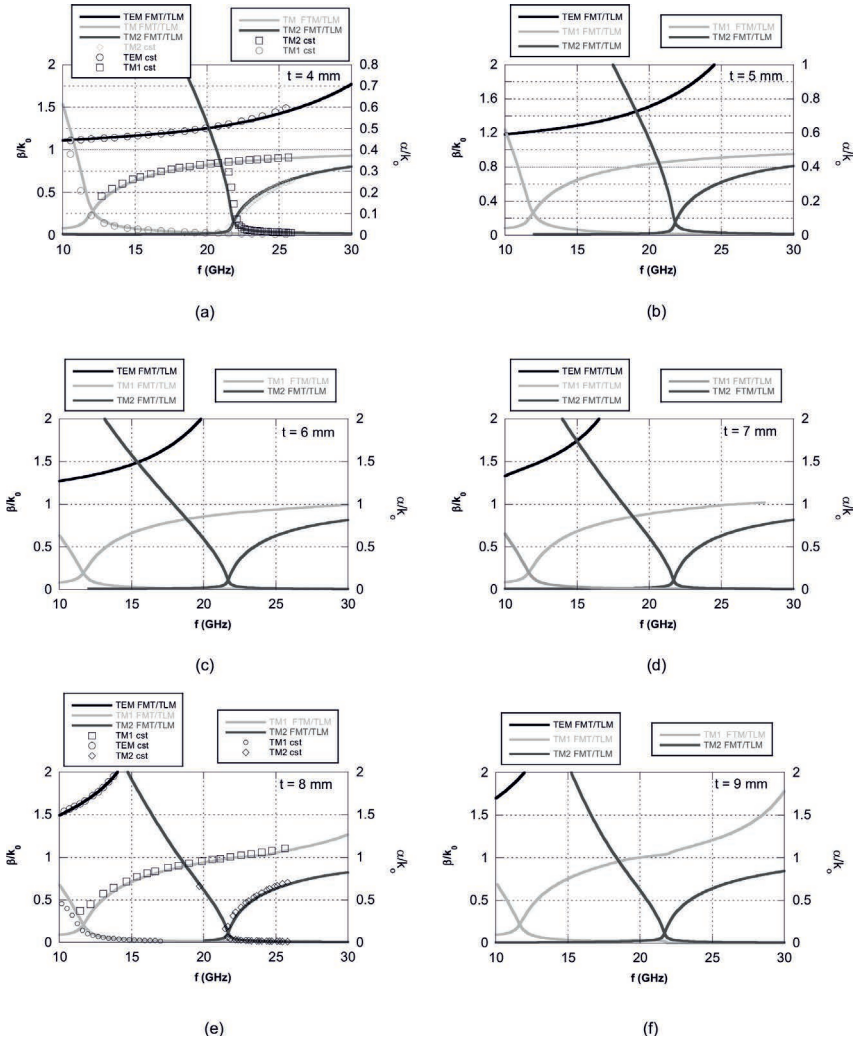


**Fig. 8.20.** Dispersion curves of TEM, TM<sub>1</sub> and TM<sub>2</sub> modes propagating inside an open PPW whose upper plate is made by a homogenized PRS and loaded with a wire-medium slab having six different thicknesses; all the relevant details have been reported in each sub-figure. Parameters:  $a = 0.19$  mm;  $d = 1.5$  mm,  $f_p = 150$  GHz. The PRS is the same presented in Fig. 8.19.

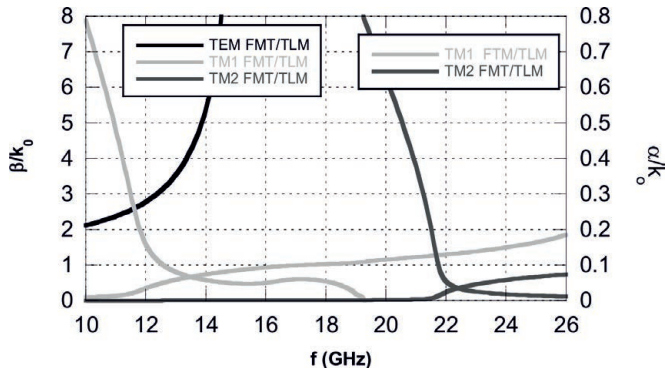


Fig. 8.21. Dispersion and attenuation curves for the TEM,  $TM_1$  and  $TM_2$  modes supported by a structure as in Fig. 8.15, where now the upper PPW plate is a PRS constituted by an array of rectangular metal patches (*open configuration*). Parameters: Patch dimensions 2.95 mm (along  $x$ ), 2.99 mm (along  $y$ ); spatial periods (along  $x$  and  $y$ ) 3 mm.

The results for the TEM and  $TM_1$  modes obtained with the proposed transmission-line model are again superimposed with those achieved with the field matching technique; note that now the  $TM_1$  mode is leaky, with a complex propagation constant  $k_y = \beta - j\alpha$ , where  $\alpha$  is the longitudinal attenuation constant. Comparisons with the results obtained through a full-wave solution carried out on CST Microwave Studio (developed simulating a WM-loaded PPW with finite length made by 15 cells of the periodic PRS) and with the standard field-matching technique are in excellent agreement, confirming the validity of the proposed approach and the advantages in terms of pre-processing and computing time. In Fig. 8.20(a)-(f) dispersion curves ( $\beta/k_0$  vs.  $f$ ) for TEM,  $TM_1$  and  $TM_2$  modes and for increasing values of the wire-medium thicknesses have been reported. For larger values of  $t$  the TEM mode becomes strongly perturbed: in particular when  $t = 9$  mm an asymptote is clearly visible at about 16.6 GHz, allowing us to obtain a unimodal regime in the range of frequencies between 11 GHz up to about 20 GHz. It is also clearly visible that by changing the value of  $t$  it is possible to modulate the slope of the dispersion curve associated to the  $TM_1$ ; consequently the range of frequency that determines the angular scansion of the relevant beam can be suitably controlled. However, as will be shown in the next chapter, larger thicknesses of the wire medium slab allow a better suppression of the unwanted TEM mode, whose constraint on the side-lobe level is anyway application-dependent.

In Fig. 8.21 also the modal curves for a wire-medium slab having

$t = 10$  mm have been shown. The phase constant does not exhibit appreciable differences with respect to those presented in Fig. 8.15, while, as expected, the attenuation constant of the  $TM_1$  is present at low frequencies and vanishes at about 19.5 GHz, in correspondence to the transition region between leaky and surface waves [120].

In Fig. 8.22(a)-(f) finally, the field configuration for the TEM,  $TM_1$  and  $TM_2$  leaky modes have been shown. As expected, the former is transversely evanescent in air outside the WM slab. On the other hand, the WM slab has a small impact on the  $TM_1$  mode, whose vertical component of the electric field (the one that interacts with the WM) has a null in the middle of the PPW. By suitably exciting the proposed structure with a vertical electric dipole placed on the ground plane, only the radiation of the  $TM_1$  mode will be observed, allowing to obtain a well-defined beam inside the designed unimodal bandwidth.

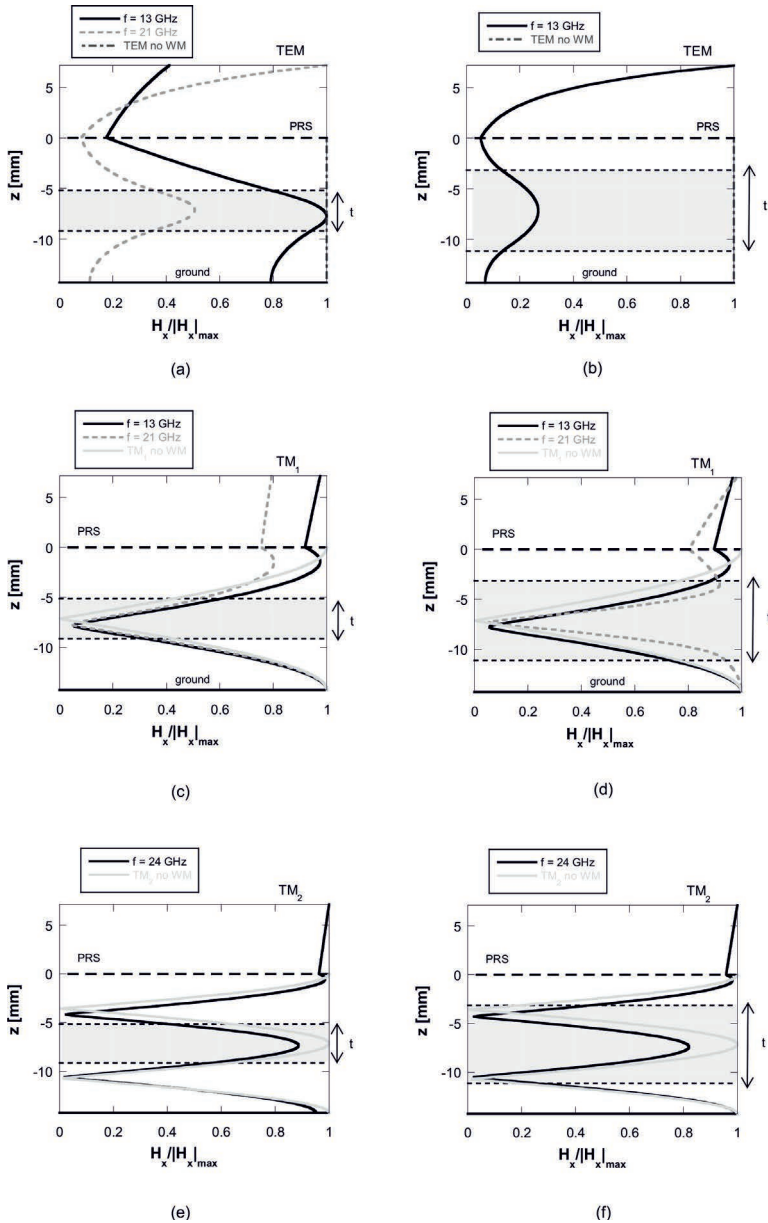


Fig. 8.22. Field configurations at different frequencies for the  $x$  component of the magnetic field of the TEM,  $TM_1$  and  $TM_2$  modes supported by a WM-loaded PPW. Parameters: PPW thickness  $h = 14.27$  mm; wire radius  $a = 0.19$  mm; wire spacing  $d = 1.5$  mm. The frequency-independent field configurations of the same modes in the absence of WM loading are also reported for comparison. Copyright © 2015, IEEE.

## 8.7. Leaky-mode equalization

As discussed in the previous sections, the presence of a wire-medium slab with vertically aligned wires is able to perturb the propagation of the TEM mode leaving almost unchanged those of the  $TE_1$  and  $TM_1$ . Even though these two modes are degenerated inside a simple parallel-plate waveguide (they have the same cutoff and the same dispersion curves but, of course, a different field distribution), by introducing a load, i.e., a wire-medium slab, and by opening the structure to generate a leaky mode, as shown in Fig. 8.10, they result perturbed and not longer coincident. To recast the equalization, at least in a relatively narrow range of frequency, one can think to act on the dielectric filling the wire medium slab and most of all on the geometry of the partially reflecting surface constituting the Fabry-Perot cavity antenna. To give an example in Fig. 8.23 dispersion curves for the  $TE_1$  and  $TM_1$  modes supported by a homogenized PRS made by square patch having period  $p = 3$  mm and slot width on both longitudinal and transverse directions equal to 0.05 mm. The structure is symmetrically loaded with a wire-medium slab having thickness  $t = 10$  mm aiming at designing two leaky modes in the region of frequency where the TEM cannot radiate, namely just after the asymptote. This condition is verified in Fig. 8.23 but the phase and attenuation constant of the two modes are not equalized; this means that the achieved dual-pol beam is made by two independent conical beam pointing in two different directions and having different beamwidth. To overcome this problem and obtain two dispersion curves able to cross each others in the neighborhood of a selected frequency, the geometry of the PRS constituting the upper wall of the structure at hand has been suitable designed. In particular, a rectangular unit cell having two different dimensions for the slots has been introduced, being  $w_y = 0.01$  mm (i.e.,  $w_{TM}$ ) and  $w_x = 0.05$  mm (i.e.,  $w_{TE}$ ) the dimensions along the transversal and longitudinal directions, respectively; in addition the permittivity of the medium filling the WM is fixed to  $\epsilon_r = 1.25$ . In Fig. 8.24 the phase and attenuation constants of the two modes have been reported: both the curves cross each other, allowing to obtain the desired equalized pattern. To better highlight the peculiar features of the designed beam, in Fig. 8.25 and 8.26 both the scanning and the beamwidth behaviors of the proposed antenna with respect to the operating frequency have been reported. It is clearly visible that the equalization has been obtained at about 11.8 GHz, where the TE and

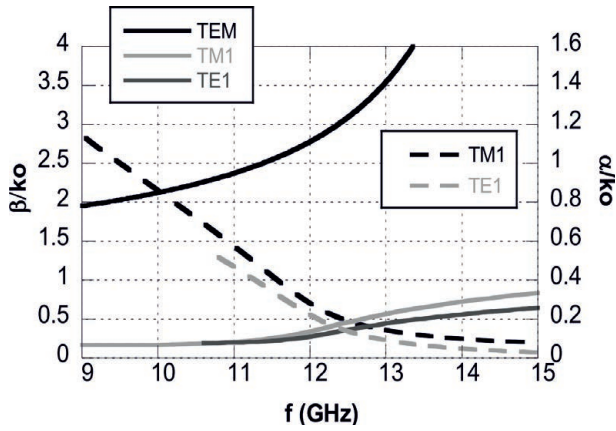


Fig. 8.23. Dispersion equation for the modes propagating inside a wire medium loaded PPW whose upper plate is made by square patch having  $w = 0.05$  mm. The structure is the same considered in Fig. 8.15.

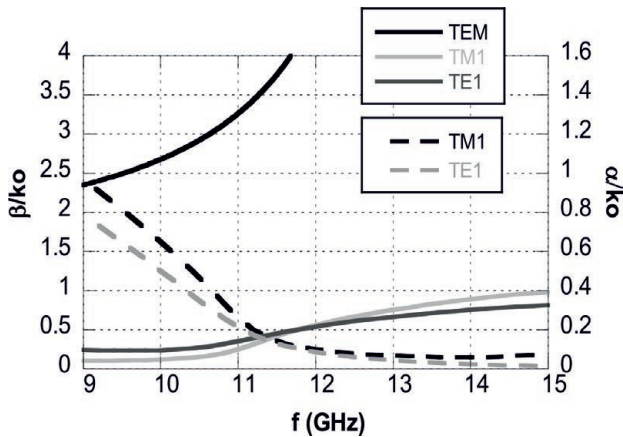
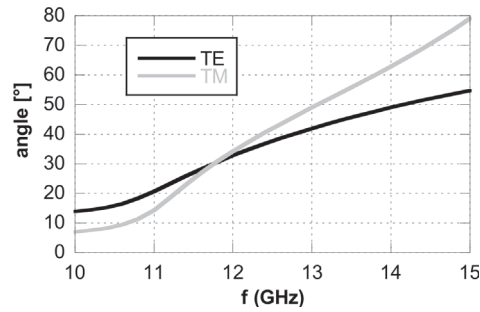
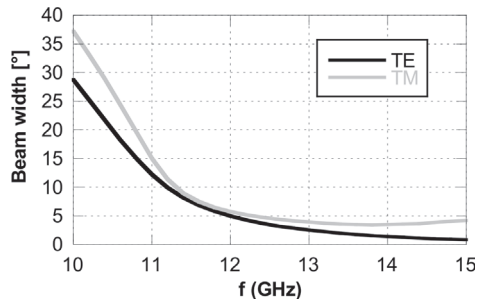


Fig. 8.24. Dispersion equation for the equalized modes: two slots of different width have been considered. Specifically  $w_{TM} = 0.01$  mm and  $w_{TE} = 0.05$  mm.



**Fig. 8.25.** Dispersion equation for the equalized modes: two slots of different width have been considered. Specifically  $w_{TM} = 0.01$  mm and  $w_{TE} = 0.05$  mm.



**Fig. 8.26.** Dispersion equation for the equalized modes: two slots of different width have been considered. Specifically  $w_{TM} = 0.01$  mm and  $w_{TE} = 0.05$  mm.

TM polarized conical beams point in the same direction and present a similar beamwidth. The results outlined in this section assess the possibility of obtaining two independent leaky modes to design a dual-pol leaky-wave antenna capable to reconfigure the polarization. The presented solution should be suitably recast to make more realistic the material filling the guide and to satisfy performances enforced by specific applications. It is important to note, finally, that this class of antennas and their peculiar features represent one of the possible starting point to design fully reconfigurable systems, that should be capable to electronically scan the beam on both elevation and azimuthal planes.



## 9. Radiative Analysis of Wire-Medium Loaded Antennas

### 9.1. Introduction

The radiation pattern produced by elementary sources in the presence of the considered WM-loaded structure can be obtained by using a well-known approach based on the reciprocity theorem [121]. As we will discuss in the following, this method is based on the remarkable properties of the modal solution for guiding structure showing cylindrical symmetry, where for each TM or TE wave the longitudinal dependence of the transverse field can be studied introducing a transmission line. We will start evaluating the far-field pattern of simple planar structure excited by line currents. Hence, a vertical electric dipole will be considered and the capability of a wire-medium slab to suppress spurious radiation will be assessed for both the cases.

### 9.2. Far field via reciprocity

Let us consider a planar antenna obtained introducing periodic perturbations on the upper metallic plate of a parallel-plate wave guide. We can analyze the radiative properties of this kind of structure by exploiting the reciprocity theorem and setting up an equivalent network, whose voltages and currents can be associated to the longitudinal dependences of the transverse components of the impinging electric and magnetic fields. The simplest excitation is represented by an ideal current line, electric to radiate a TE field and magnetic for a TM one. Also vertical or horizontal dipoles, reproducing a more realistic three-dimensional radiation pattern, can be considered. Let us assume that within a linear and isotropic medium there are two sets of source  $\mathbf{J}, \mathbf{M}$  and  $\mathbf{J}^{test}, \mathbf{M}^{test}$  (or more simply  $\mathbf{J}_1, \mathbf{M}_1$  and  $\mathbf{J}_2, \mathbf{M}_2$ ), that can radiate si-

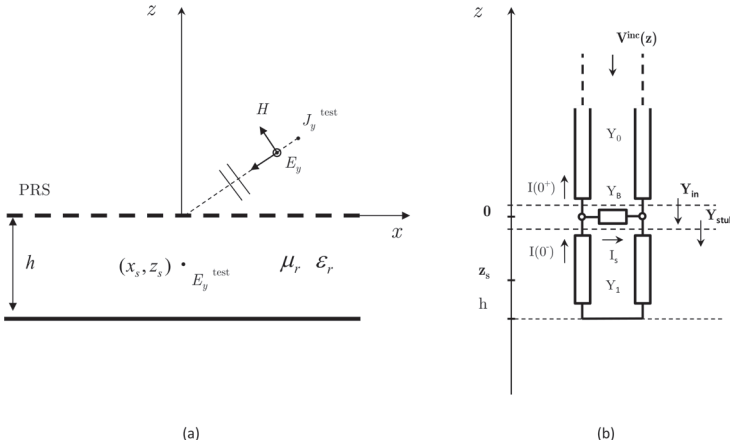


**Fig. 9.1.** (a) Planar structure made by a parallel plate waveguide whose upper plate is periodically perturbed. An incident plane wave radiated by a remote line source is also represented. (b) Equivalent transverse network for the considered planar antenna. Two reference sections for the evaluation of the input admittance have been highlighted.

multaneously or individually at a fixed frequency  $f$ . They produce fields  $\mathbf{E}$ ,  $\mathbf{H}$  and  $\mathbf{E}^{test}$ ,  $\mathbf{H}^{test}$ , respectively. By starting from Maxwell's equation, under these hypotheses, it is possible to demonstrate under general conditions [123] the following integral relation among fields and currents

$$\int_V (\mathbf{E}_1 \cdot \mathbf{J}_2 - \mathbf{H}_1 \cdot \mathbf{M}_2) dv' = \int_V (\mathbf{E}_2 \cdot \mathbf{J}_1 - \mathbf{H}_2 \cdot \mathbf{M}_1) dv'. \quad (9.1)$$

Each integral in (9.1) can be interpreted as a coupling between a set of fields and a set of sources, which produce another set of fields. Typically, these relation, are defined *reactions* and can be denoted in the following way

$$\begin{aligned} \langle 1, 2 \rangle &= \int_V (\mathbf{E}_1 \cdot \mathbf{J}_2 - \mathbf{H}_1 \cdot \mathbf{M}_2) dv' \\ \langle 2, 1 \rangle &= \int_V (\mathbf{E}_2 \cdot \mathbf{J}_1 - \mathbf{H}_2 \cdot \mathbf{M}_1) dv' \end{aligned} \quad (9.2)$$

consequently, from reciprocity we have that

$$\langle 1, 2 \rangle = \langle 2, 1 \rangle \quad (9.3)$$

which states that the reaction (or coupling) of the sources with the corresponding fields must be equal. This interesting results can be suitably exploited to calculate the radiation pattern of the structure investigated e.g. in this thesis. The procedure has been demonstrated

for other kind of antennas for the first time in [121]. In particular, as shown in Fig. 9.1(a), it is convenient to consider a test field (i.e, a plane wave radiated by a source  $J^{test}$  placed in a remote point from the antenna) and evaluating the field produced in  $(x_s, y_s)$ , where the actual line source supporting a current  $J_y$  is located. From equations (9.1) and (9.3), considering that in this simple case  $\mathbf{M}_1 = \mathbf{M}_2 = 0$  and  $\mathbf{E}_1 = E_y^{test}$ ,  $\mathbf{J}_2 = J_y \mathbf{y}_0$ ,  $\mathbf{E}_2 = E_y^{ff}$ ,  $\mathbf{J}_1 = J_y^{test} \mathbf{y}_0$ , we can write

$$\langle E_y^{test}, J_y \rangle = \langle E_y^{ff}, J_y^{test} \rangle. \quad (9.4)$$

where  $E_y^{ff}$  and  $E_y^{test}$  are the electric field produced by the  $J_y$  and  $J_y^{test}$  source currents, respectively. Since  $J_y^{test}$  is a known quantity expressed as a Dirac pulse (one for each direction of propagation) we can write

$$E_y^{ff}(\rho, \theta) = J_y E_y^{test}(x_s, z_s) \quad (9.5)$$

Consequently, the field radiated by the considered antenna can be obtained finding the field  $E_y^{test}(x_s, z_s)$ , namely the field produced by the remote source in the spatial point where the actual source  $J_y$  is located. It is worth to note that when we consider a magnetic line source, by associating the longitudinal dependence of the transverse component of the incident magnetic field to the current of the transmission line, we have to suitable modify the reaction shown by equation (9.1) and (9.4) as follows

$$\langle H_y^{test}, M_y \rangle = \langle H_y^{ff}, M_y^{test} \rangle \quad (9.6)$$

that is again a specific case of that more general represented by equations (9.1).

## 9.2.1. Line source excitation

### 9.2.1.1. TE case

If we consider  $\mathbf{J} = J_y \mathbf{y}_0$ , that is a  $y$ -oriented electric line current, a TE field having  $E_y, H_x, H_z$  components is radiated. Therefore, the incident electric field on the planar structure is given by [35]

$$E_{y,inc}^{test}(x, z) = \frac{-k_0 \eta_0}{4} H_0^{(2)}(k_0 \rho), \quad (9.7)$$

as we can consider  $k_0 \rho \gg 1$ , it is possible to exploit the asymptotic expression of the Hankel function. This means that the cylindrical wave produced by the line current can be locally written as follows

$$E_{y,inc}^{test}(x, z) = E_0^{test} e^{jk_0(x \cos \theta + z \sin \theta)} \quad (9.8)$$

where  $E_0^{test}$  is the complex amplitude of the impinging wave that depends on the initial phase value of the wave excited by the source

$$E_0^{test} = -\eta_0 \sqrt{\frac{jk_0}{8\pi}} \frac{e^{-jk_0\rho}}{\sqrt{\rho}}. \quad (9.9)$$

It is very interesting to note that, as for the case of guided propagation in cylindrical structure (where potentials and fields can be decomposed in a longitudinal and a transverse part), also for the problem at hand we can consider the electric field as made by a transverse and a longitudinal component, as expressed in the following

$$\mathbf{E}(z, x) = \mathbf{E}_t(z, x) + E_z(z, x)\mathbf{z}_0. \quad (9.10)$$

Even though we are considering free-space propagation, such a decomposition is still possible; let us think, as an example, that plane waves can be seen as modal solution of a particular guided structure (i.e., the free space). Additionally, by separating also transverse and longitudinal dependence of the transverse component of the incident electric field, we have

$$\mathbf{E}_t(z, x) = V(z)\mathbf{e}(x) \quad (9.11)$$

and we can finally associate the longitudinal component  $V(z)$  to an equivalent network, whose progressive wave voltage is associated to the longitudinal dependence of the transverse components of the impinging electric field. Specifically, as shown in Fig. 9.1(b), the model is made by two transmission line, one of infinite length (representing the free space) and one closed on a short circuit (representing the ground plane of the structure). These two lines must have a parallel connection with the frequency-dependent equivalent susceptance, that represents a homogenized model of the geometry of the periodic structure; formulas for simple configuration are available in literature [119], as already highlighted in the previous chapter. By starting from equation (9.8) and (9.11), the voltage characterizing the upper transmission line can be written as follows

$$V^{inc}(z) = E_0^{test} e^{jk_{z_0}z} \quad (9.12)$$

where the propagation constants of the two lines are

$$\begin{aligned} k_{z_1} &= \sqrt{\mu_r \epsilon_r - \sin^2 \theta} \\ k_{z_0} &= k_0 \cos \theta \end{aligned} \quad (9.13)$$

and the admittance looking just down the susceptance  $Y_B$  (see lower dotted line in Fig. 9.1) is  $Y_{stub} = -jY_1 \tan(k_{x_1}h)$ . By writing the value of  $V^{inc}(z)$  in  $z = z_s$  it is possible to obtain the field  $E_y^{test}(x_s, z_s)$ , hence thanks to equation (9.5) the sought expression of  $E_y^{ff}(\rho, \theta)$  in the far-field region is obtained. It is worth noting that the  $\theta$ -dependence of the equivalent network is visible in the propagation constant and consequently in the characteristic impedance of the line. This means, actually, that each elevation angle of the impinging wave is associated to an equivalent transverse network. By starting from the transmission-line equation we can write

$$V(z) = V^-(z) + V^+(z) = V_0^- e^{jk_{z_1}z} + V_0^+ e^{-jk_{z_1}z} \quad (9.14)$$

since the progressive wave is propagating in the opposite direction of the positive value of the  $z$ -axis, for the reflection coefficient we have

$$S_v(z) = \frac{V^+(z)}{V^-(z)} = \frac{V_0^+ e^{-jk_{z_1}z}}{V_0^- e^{jk_{z_1}z}} = S_v(0) e^{-j2k_{z_1}z}. \quad (9.15)$$

The voltage propagating in the line can be written in function of the progressive wave and of reflection coefficient as follow

$$V(z) = V_0^- e^{jk_{z_1}z} \left( 1 + \frac{V_0^+}{V_0^-} e^{-j2k_{z_1}z} \right) = V^-(z)(1 + S_v(z)) \quad (9.16)$$

where  $V^-(z) = V^{inc}(z)$ . By considering the previous equation, for the voltage in  $z = 0$  we have

$$V(0) = V(0^+) = V(0^-) = V^{inc}(0)(1 + S_v(0)). \quad (9.17)$$

Recalling that

$$S_v(z) = \frac{Z(z) - Z_0}{Z(z) + Z_0} \quad (9.18)$$

$$S_v(0) = \frac{Z_L - Z_0}{Z_L + Z_0} \quad (9.19)$$

and that  $Y_{in} = Y_B + Y_{stub} = Y_B - jY_1 \cot(k_{z_1}h)$ , for the reflection coefficient seen looking inside the transmission line at the upper reference section we can finally write

$$S_v(0^+) = \frac{Z_{in} - Z_0}{Z_{in} + Z_0} = \frac{Y_0 - Y_{in}}{Y_0 + Y_{in}}. \quad (9.20)$$

Consequently, equation (9.17) can be rewritten in its final form as

$$V(0) = V^{inc}(0) \left( 1 + \frac{Y_0 - Y_{in}}{Y_0 + Y_{in}} \right) = V^{inc}(0) \left( \frac{2Y_0}{Y_0 + Y_{in}} \right) \quad (9.21)$$

where  $Y_{stubb}$  is the input impedance of the line under the considered section and  $V^{inc}(0) = V_0^{inc} = E_0^{test}$  is the complex amplitude of the impinging wave. By considering once again Fig. 9.1(b), for the current on the considered section (i.e.,  $z = 0^-$ , just below the susceptance) we have

$$I(0^-) = I_s + I(0^+) = -V(0)Y_{stubb} = -V^{inc}(0) \left( \frac{2Y_0Y_{stubb}}{Y_0 + Y_{in}} \right); \quad (9.22)$$

it can be associated to the transverse component of the impinging magnetic field, namely  $H_x$ . To accomplish our initial goal, we need now to evaluate the value of the voltage in  $z = z_s$ , where the actual source is located. Since the value of the reflection coefficient in  $z = -h$  is  $S_v(-h) = -1$  we get

$$\begin{aligned} V(z-h) &= V_0^- e^{jk_{z_1}(z-h)} + V_0^+ e^{-jk_{z_1}(z-h)} \\ &= V_0^- e^{-jk_{z_1}h} \left[ e^{jk_{z_1}z} + \frac{V_0^+}{V_0^-} e^{j2k_{z_1}h} e^{-jk_{z_1}z} \right] \end{aligned} \quad (9.23)$$

thus, remembering that  $S_v(-h) = S_v(0)e^{-2jk_{z_1}h} = -1$ , for the voltage in  $z = -h$  we can finally write

$$V(z-h) = V_0^- e^{-jk_{z_1}h} \left( e^{jk_{z_1}h} - e^{-jk_{z_1}z} \right) = -2jV_0^- e^{-jk_{z_1}h} \sin(k_{z_1}z) \quad (9.24)$$

In conclusion, by considering the value of  $V(z-h)$  in  $z = h$  and  $z = h/2$  we can write the sought value of the voltage in  $z = z_s$

$$V(z_s) = V(0) \frac{\sin(k_{z_1}(h + z_s))}{\sin(k_{z_1}h)}. \quad (9.25)$$

Recalling equation (9.8) the field radiated by the remote line source in  $(x_s, z_s)$  can be written as

$$E_y^{test}(x_s, z_s) = V(z_s) e^{jk_0 x_s \sin \theta} \quad (9.26)$$

thus, by considering equation (9.25), (9.21) and (9.9), recalling that  $E_y^{ff}(\rho, \theta) = J_y E_y^{test}(x_s, z_s)$ , the electric field radiated by the structure

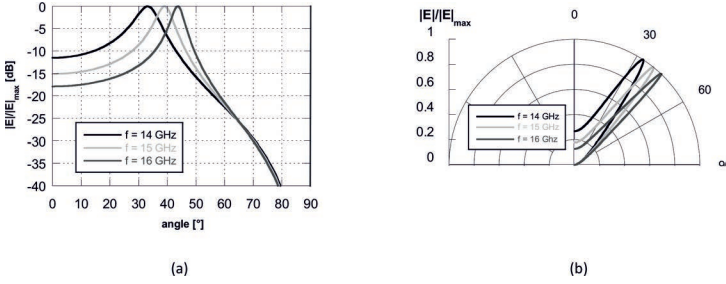


**Fig. 9.2.** Normalized radiation patterns in an arbitrary elevation plane for a Fabry-Perot cavity antenna with a PRS constituted by concentric annular slots represented by its linearized version, excited by a horizontal electric line source placed in the middle of the structure. The patterns are obtained through a homogenized model of the HIS. The linearized structure has the following parameters  $p = 3$  mm,  $w = 0.05$  and  $h = 14.27$  mm. (a) Cartesian plot in dB. (b) Polar plot in linear scale for different values of the frequency (see labels).

at hand, excited by a line source placed in  $(x_s, z_s)$ , is reported in that follows

$$E_y^{ff}(\rho, \theta) = -J_y \eta_0 \sqrt{\frac{jk_0}{8\pi}} \frac{e^{-jk_0\rho}}{\sqrt{\rho}} \left( \frac{2Y_0}{Y_0 + Y_{in}} \right) \frac{\sin(k_{z_1}(h + x_s))}{\sin(k_{z_1}h)} e^{jk_0 z_s \sin \theta}. \quad (9.27)$$

Since the electric field produced by the structure far from the source can be written as

$$E_y(\rho, \theta) \simeq \frac{e^{-jk_0\rho}}{\sqrt{\rho}} F(\theta) \quad (9.28)$$

for the far-field pattern we finally have

$$F(\theta) = -J_y \eta_0 \sqrt{\frac{jk_0}{8\pi}} \left( \frac{2Y_0}{Y_0 + Y_{in}} \right) \frac{\sin(k_{z_1}(h + x_s))}{\sin(k_{z_1}h)} e^{jk_0 z_s \sin \theta}. \quad (9.29)$$

In Fig. (9.2) results have been reported, considering a parallel plate waveguide whose height is equal to  $h = 14.37$  mm. The PRS is made by square patches (period  $p = 3$  mm) where the width of the transverse slot (with respect to the direction of propagation) inside the unit cell is equal to 0.05 mm. The width of the longitudinal slots is equal to 0.01 mm, but it is not able to perturb the currents associated to the TM mode; indeed, as shown in [119], HIS made by a periodic arrangement of strips and patches in this condition are represented by the same susceptance. In Fig. 9.2(a) a Cartesian plot of the far-field pattern for different frequencies has been reported, showing the typical scanning

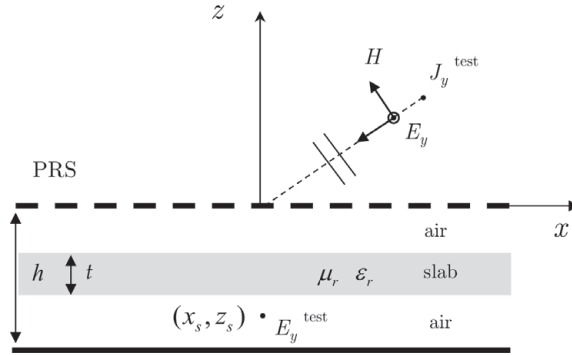


Fig. 9.3. Fabry-Perot cavity antenna excited by an electric line source and symmetrically loaded with a dielectric slab.

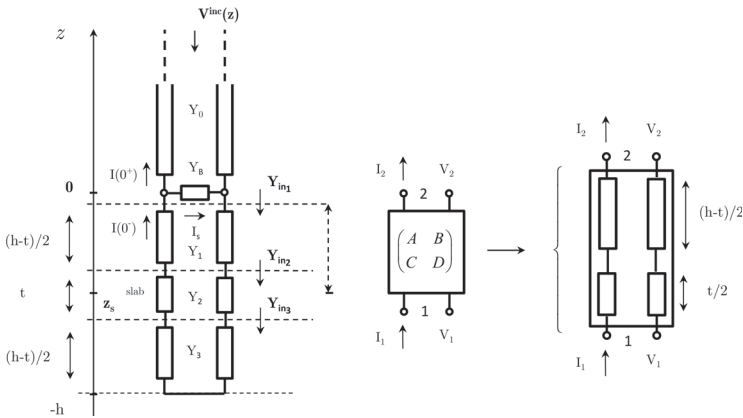


Fig. 9.4. Transmission-line model and relative  $ABCD$  matrix for a PPW loaded with a dielectric slab, terminated by a homogenized PRS.

behavior of the leaky mode. Additionally, in 9.2(b) a polar plot showing a section of the related conical beam is presented.

Since our analysis aims at introducing a wire-medium slab inside the proposed structure, whose wires are possibly inserted in a dielectric medium having permittivity  $\epsilon_r$ , (as shown in Fig. 9.3), a symmetric slab (centered with respect to the median plane) has been considered. In this way the effect on the radiation pattern of the  $TE_1$  can be straightforwardly evaluated. To find the voltage inside and/or below the proposed slab we need to consider the transfer matrix of the structure lying under the shunt susceptance representing the PRS, as shown in Fig. 9.4. The input

admittance  $Y_{in_1}$  seen looking inside the highlighted section is given by

$$Y_{in_1} = Y_1 \frac{Y_{in_2} \cos(k_{x_1} \frac{h-t}{2}) + jY_1 \sin(k_{x_1} \frac{h-t}{2})}{Y_1 \cos(k_{x_1} \frac{h-t}{2}) + jY_{in_2} \sin(k_{x_1} \frac{h-t}{2})} \quad (9.30)$$

whereas the transfer matrix of each line segment is written as (see [122])

$$\begin{pmatrix} \cos(k_x l) & jZ_0 \sin(k_x l) \\ \frac{j}{Z_0} \sin(k_x l) & \cos(k_x l) \end{pmatrix} \quad (9.31)$$

thus, recalling that voltage and current of the involved 2-port network can be written in matrix form as

$$\begin{pmatrix} V_1 \\ I_1 \end{pmatrix} = \begin{pmatrix} A & B \\ C & D \end{pmatrix} \begin{pmatrix} V_2 \\ I_2 \end{pmatrix} \quad (9.32)$$

and that  $V_2 = V(0)$ ,  $I_2 = I(0^-)$ , we finally have the voltage in  $(x_s, z_s)$ , where the actual source is located

$$\begin{cases} V(z_s) = V_1 = AV_2 + BI_2 = AV(0) + BI(0^-) \\ I(z_s) = I_1 = CV_2 + DI_2 = CV(0) + DI(0^-). \end{cases} \quad (9.33)$$

In Fig. 9.5 some results for the structure presented in Fig. 9.3 having the same HIS of the previous example have been reported, introducing a dielectric slab with  $\epsilon_r = 1.5$  and  $\epsilon_r = 2$ , respectively. It is interesting note that for larger value of the permittivity we are able to modulate the tracking angle and the width of the conical beam, giving the possibility to obtain a further degree of freedom to equalize phase and propagation constant of the TE and TM modes responsible for the radiation.

### 9.2.1.2. TM case

Following the same procedure outlined in the previous section, we can straightforwardly evaluate also the far-field pattern generated by a magnetic line source. Two different possibilities are available, since inside the transmission line we can consider the wave voltage associated to the transverse component of the incident electric field, but also the wave current, that in turns must be connected to the magnetic field. As is known, in this case the non-null components of the impinging field generated by the source are  $H_y, E_x, E_z$ , but the equivalent transverse network is the same shown in Fig. 9.1, where a wave voltage  $V_z^{inc}$  has been chosen to link the incident field with the voltage in the section

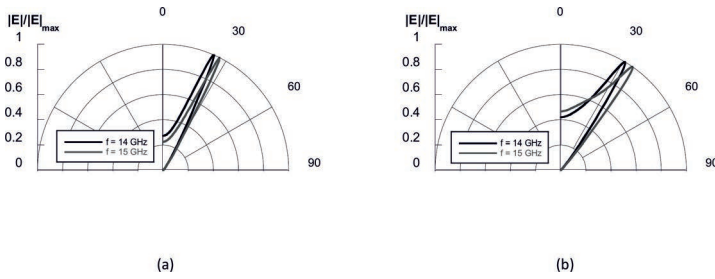


**Fig. 9.5.** Normalized radiation patterns in an arbitrary elevation plane for a dielectric loaded structure. Patterns are obtained with a homogenized model. The linearized structure has the following parameters  $p = 3$  mm,  $w = 0.05$  and  $h = 14.27$  mm. (a) Polar plot in linear scale for  $\epsilon_r = 1.5$ . (b) Polar plot in linear scale  $\epsilon_r = 2$  for two values of the frequency (see labels).

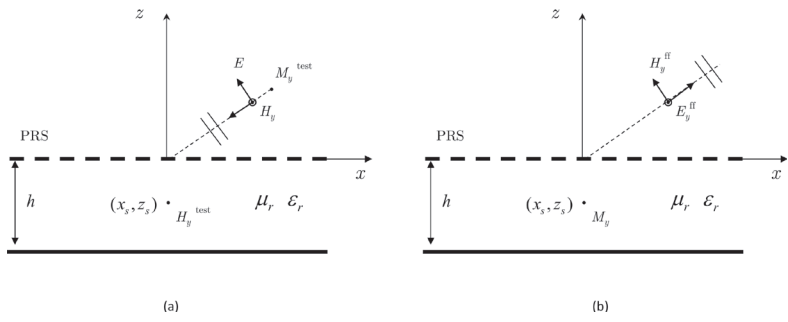


**Fig. 9.6.** (a) Planar structure made by a parallel-plate waveguide whose upper plate is periodically perturbed by slots. Also an incident plane wave radiated by a remote magnetic line source is represented. (b) Associated reciprocal planar structure. In  $(x_s, z_s)$  the actual magnetic source is considered and also the plane wave radiated in far field is reported.

where the actual source is located. However in this case, as shown in Fig. 9.6, the electric field radiated by a magnetic filamentary current in Cartesian coordinates can be written as

$$\mathbf{E} = E_x \mathbf{x}_0 + E_z \mathbf{z}_0 \tag{9.34}$$

where  $\mathbf{E} = E_0 \mathbf{e}_0$ . Consequently, the transverse component of the electric field is  $E_x = E_0 \cos \theta$  and the progressive wave voltage inside the line, as already reported by equation (9.12), reduces to

$$V_z^{inc} = E_0^{test} e^{jk_{z_0} z} \cos \theta. \tag{9.35}$$

Recalling equation (9.22), reported in the following for convenience

$$I(0^-) = I_s + I(0^+) = -V(0) Y_{stub} = -V^{inc}(0) \left( \frac{2Y_0 Y_{stub}}{Y_0 + Y_{in}} \right) \tag{9.36}$$

we have that

$$V^{inc}(0) = E_0^{test} \cos \theta \quad (9.37)$$

with

$$E_0^{test} = \eta_0 \sqrt{\frac{jk_0}{8\pi}}. \quad (9.38)$$

It is worth noting that equation (9.22) provides a link between the impinging magnetic field and the current of the transmission line, although in the starting model we have considered a wave voltage. Following the same procedure outlined in the previous section we can write the expression for the current in  $(x_s, z_s)$ , where the actual source is located

$$I(z_s) = I(0^-) \frac{\cos(k_{z_1}(z_s + h))}{\cos(k_{z_1}h)} \quad (9.39)$$

thus thanks to equation (9.6), for the far-field distribution we have

$$H_y^{ff}(\rho, \theta) = -M_y \eta_0 \sqrt{\frac{jk_0}{8\pi}} \frac{e^{-jk_0\rho}}{\sqrt{\rho}} \left( \frac{2Y_0 Y_{stub}}{Y_0 + Y_{in}} \right) \frac{\cos(k_{z_1}(h + x_s))}{\cos(k_{z_1}h)} \cos \theta e^{jk_0 z_s \cos \theta} \quad (9.40)$$

and recalling that  $Y_0 = \omega \varepsilon_0 / k_{x_1} = 1 / (\eta_0 \cos \theta)$  we can finally write

$$H_y^{ff}(\rho, \theta) = -M_y \sqrt{\frac{jk_0}{8\pi}} \frac{e^{-jk_0\rho}}{\sqrt{\rho}} \left( \frac{2Y_{stub}}{Y_0 + Y_{in}} \right) \frac{\cos(k_{z_1}(h + x_s))}{\cos(k_{z_1}h)} e^{jk_0 z_s \cos \theta}. \quad (9.41)$$

Of course, when a transmission line is associated to the impinging field, we can consider also the incident wave current, giving rise to this expression

$$I_z^{inc} = H_0^{test} e^{jk_{z_0} z}. \quad (9.42)$$

with

$$H_0^{test} = \sqrt{\frac{jk_0}{8\pi}}. \quad (9.43)$$

Following such a dual procedure, a new expression of the current inside the line has to be written, which depends on the impinging magnetic field

$$I(0^-) = I^{inc}(0) \left( \frac{2Y_{stub}}{Y_0 + Y_{in}} \right). \quad (9.44)$$

However, as expected, this formula give rises to the same expression reported in equation (9.41). To give some examples we consider here the same structure described for the TE case, whose PRS has transversal slots have a width equal to  $w_{TM} = 0.01$  mm and longitudinal slots of  $w_{TE} = 0.05$  mm. As shown in Fig. 9.7, the far-field pattern shows two

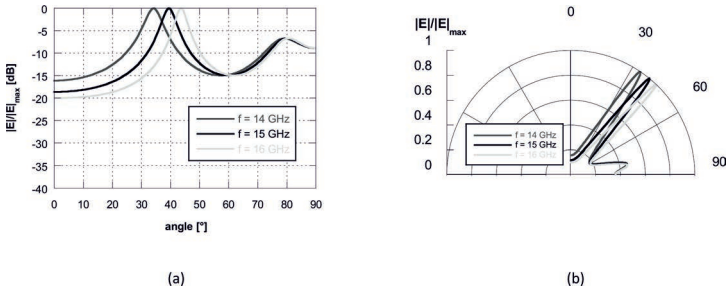


Fig. 9.7. Far-field pattern for the considered structure. Radiation of both TEM and  $TM_1$ , in Cartesian and polar plots, for different frequency values in an arbitrary elevation plane.

main lobes: one generated by the TEM leaky mode propagating inside the structure and having a perturbed transverse field distribution with respect to that of the associated PPW, and the other one produced by relevant  $TM_1$  leaky mode. This simple result confirms the necessity to suppress the unwanted lobe: it can be eliminated by perturbing the field distribution inside the guide but keeping unchanged those of the  $TM_1$  and  $TE_1$  leaky modes. In particular, as shown in the previous chapter, an interesting strategy consists in symmetrically loading the structure by means of a wire-medium slab, just where a null of the transverse field distribution of the  $TM_1$  field is present. Even though a magnetic line source should be placed only on the ground plane, where it is able to model a magnetic current flowing on an etched slot, to test the accuracy of the proposed approach, in Fig. 9.8 the radiation pattern obtained by placing the source in  $z_s = 0.55h$  has been reported. Since field distribution of the  $TM_1$  field shows a null in this section (not properly in  $z_s = 0.5h$  as it represents a perturbed version of the mode propagating inside a PPW), as expected, at the angular direction where a lobe should be present, we clearly see now a null. It is also worth noting that the TEM mode is always well excited (and it will be so for any position along the section) since its distribution is constant along the transverse plane of the guide.

## 9.2.2. Vertical electric dipole

### 9.2.2.1. TM case

A more realistic excitation for the structure at hand is represented by a vertical electric dipole (VED). The equivalent transverse network shown in Fig. 9.9 and the voltage wave propagating inside the network

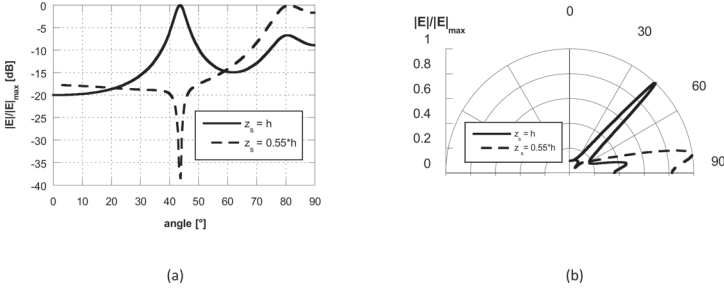


**Fig. 9.8.** Far-field pattern for two particular positions of the excitation, in Cartesian and polar plots. The TEM mode is clearly visible, while in direction where the  $TM_1$  modes should be present a null is clearly visible, since the position of the source coincides with a null of the transverse field configuration.

are the same as introduced in the previous section for an ideal line source; we only need to develop a suitable modification related to the implementation of the reciprocity theorem. Let us consider the following source

$$\mathbf{J} = I_0 l_0 \mathbf{z}_0 \delta(x) \delta(y) \delta(z - z_s) \quad (9.45)$$

that represents a VED placed in  $z = z_s$ . To evaluate the far field  $\mathbf{E}^{ff}$  by means of the reciprocity theorem, we introduce a test dipole placed at  $(r, \theta, \phi = 0)$ , directed along  $\theta_0$ , with

$$\mathbf{J}^{test} = I^{test} l^{test} \theta_0 \delta(\mathbf{r} - \mathbf{r}^{test}). \quad (9.46)$$

The field incident upon the PRS, produced by  $\mathbf{J}^{test}$ , can be approximated at the origin and in the far field as

$$\mathbf{E}^{inc} = -jk_0 \eta_0 \frac{I^{test} l^{test}}{4\pi r} e^{-jkr} \theta_0 = E_0^{inc} \theta_0 \quad (9.47)$$

hence, recalling that  $\theta_0 \cdot \mathbf{x}_0 = \cos \theta$ , the transverse incident field is  $x$ -directed and is given by

$$\mathbf{E}_t^{inc} = E_0^{inc} \cos \theta e^{jk_z z} e^{jk_x x} \mathbf{x}_0 \quad (9.48)$$

where  $k_z = k_0 \cos \theta$  and  $k_x = k_0 \sin \theta$ . Consequently, we may write

$$\mathbf{E}_t^{inc} = V^{inc}(z) \mathbf{e}_t(x) \quad (9.49)$$

with

$$V^{inc}(z) = V_0^{inc} e^{jk_z z} \quad (9.50)$$

$$\mathbf{e}_t(x) = \mathbf{x}_0 e^{jk_x x} \quad (9.51)$$

and  $V_0^{inc} = E_0^{inc} \cos \theta$ . In Fig. 9.9 the transverse equivalent network for this problem is reported, equal to that just introduced for the ideal line source, giving rise to the same formula for voltage and current upon the reference section, reported in the following

$$\begin{cases} V(0) = V^{inc}(0) \frac{2Y_0}{Y_0 + Y_{in}} \\ I(0^-) = -V^{inc}(0) \frac{2Y_0 Y_{stub}}{Y_0 + Y_{in}} \end{cases} \quad (9.52)$$

By exploiting the same considerations outlined in the previous section, the current in  $z = z_s$  can be written as

$$I(z_s) = I(0^-) \frac{\cos(k_{z_1}(z_s + h))}{\cos(k_{z_1}h)} \quad (9.53)$$

consequently, if the VED is placed on the ground plane, as shown in Fig. 9.9(a), we finally have

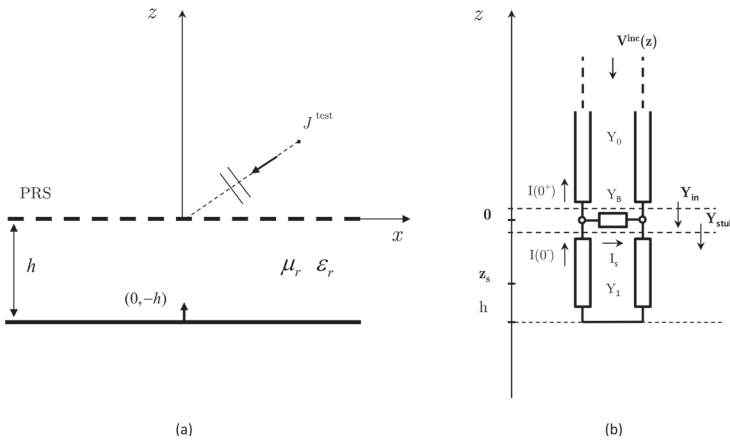


**Fig. 9.9.** Planar structure made by a parallel-plate waveguide whose upper plate is substituted by a HIS, excited by a VED placed on the ground plane. An incident plane wave radiated by a remote dipole is also represented. (b) Equivalent transverse network for the considered planar antenna. Two reference sections for the evaluation of the input admittance have been highlighted.

$$I(-h) = \frac{I(0^-)}{\cos(k_{z_1}h)} = \frac{V^{inc}(0)}{\cos(k_{z_1}h)} \frac{2Y_0 Y_{stub}}{Y_0 + Y_{in}} \quad (9.54)$$

To find the electric field received by the considered vertical dipole (i.e., the  $z$ -component), starting from Maxwell's equations we can write

$$E_z = \frac{1}{j\omega\epsilon} \nabla_t \cdot (\mathbf{H}_t \times \mathbf{z}_0) \quad (9.55)$$

where

$$\mathbf{H}_t(x, z) = I(z)\mathbf{h}_t(x) \quad (9.56)$$

and

$$\mathbf{h}_t(x) = \mathbf{z}_0 \times \mathbf{e}_t(x) = \mathbf{y}_0 e^{jk_x x} \quad (9.57)$$

Thus, the z-component of the electric field can be rewritten as follows

$$\begin{aligned} E_z &= \frac{1}{j\omega\epsilon} I(z) \nabla_t \cdot (\mathbf{h}_t \times \mathbf{z}_0) = \frac{1}{j\omega\epsilon} I(z) \nabla_t \cdot (\mathbf{e}_t) = \\ &= \frac{1}{j\omega\epsilon} I(z) \nabla_t \cdot (e^{jk_x x} \mathbf{x}_0) = \frac{k_x}{\omega\epsilon} I(z) e^{jk_x x} \end{aligned} \quad (9.58)$$

and on the VED we have

$$E_z = \frac{k_x}{\omega\epsilon} I(-h); \quad (9.59)$$

since  $k_x = k_0 \sin \theta$  and  $\omega\epsilon = k_0 \epsilon_r / \eta_0$ , recalling equation (9.54) for the test field on the dipole we finally have

$$E_z^{test} = -\frac{\eta_0}{\epsilon_r} \sin \theta \frac{V^{inc}(0)}{\cos(k_{z_1} h)} \frac{2Y_0 Y_{stub}}{Y_0 + Y_{in}}. \quad (9.60)$$

By considering reciprocity we can write

$$\langle \mathbf{J}_i, \mathbf{E}^{test} \rangle = \langle \mathbf{J}^{test}, \mathbf{E}^{ff} \rangle \quad (9.61)$$

hence

$$I_0 I_0 E_z^{test}(0, 0, z = -h) = E_\theta^{ff}(r, \theta, \phi = 0) I^{test} l^{test} \quad (9.62)$$

introducing (9.60) in the previous equation, we get

$$-I_0 I_0 \frac{\eta_0}{\epsilon_r} \sin \theta \frac{V^{inc}(0)}{\cos(k_{z_1} h)} \frac{2Y_0 Y_{stub}}{Y_0 + Y_{in}} = E_\theta^{ff} I^{test} l^{test} \quad (9.63)$$

thus, recalling equation (9.47) we can finally write the far-field radiated by the considered structure

$$E_\theta^{ff} = jk_0 \eta_0 \frac{I_0 l_0}{4\pi r} e^{-jkr} \frac{\eta_0}{\epsilon_r} \sin \theta \cos \theta \frac{1}{\cos(k_{z_1} h)} \frac{2Y_0 Y_{stub}}{Y_0 + Y_{in}}. \quad (9.64)$$

In Fig. 9.10 some results for the TM modes have been reported; the structure is the same considered previously ( $h = 14.37$  mm,  $p = 3$  mm,  $w = 0.01$  mm). Besides the lobe produced by the radiation of the  $\text{TM}_1$  leaky mode, also a secondary lobe having nearly the same

amplitude is clearly visible; it represents the unwanted radiation of the TEM leaky mode. As said, this mode is always propagating inside a PPW and can be excited for arbitrary position of the considered vertical electric dipole. On the contrary, since the  $TM_1$  field configuration is represented by a sinusoidal wave with a null along the median plane and a maximum both on the upper and lower metallic planes, its excitation will be maximized by means of a VED placed just on the ground plane. As already demonstrated exciting the structure at hand by means of a line source, by placing the VED at  $z_s \approx h/2$  only the TEM mode will be visible, being the transverse field of the TM modes null in that section of the guide.

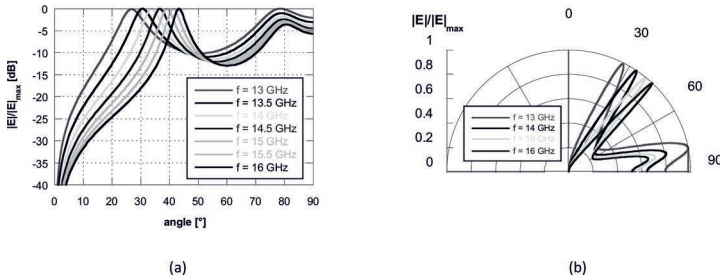
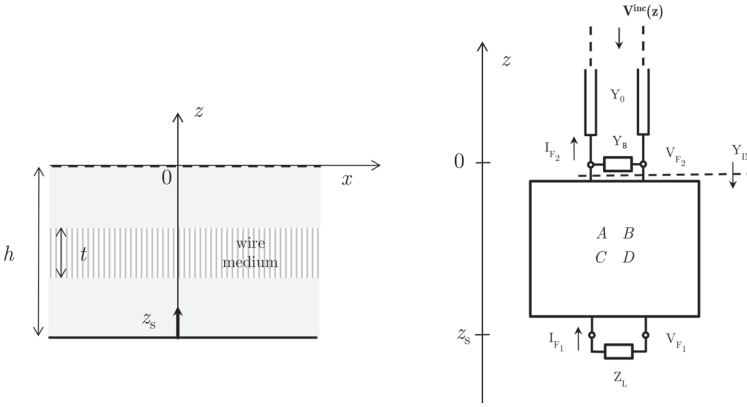


Fig. 9.10. Far-field pattern for the considered structure in arbitrary elevation plane. Radiation of both TEM and  $TM_1$ , in Cartesian and polar plots, (a) and (b) respectively, are visible for different frequency values. Copyright © 2015, IEEE.

### 9.3. Wire-medium slab

Starting from the equivalent network model outlined in section ?? and exploiting one again the reciprocity, we can analyze the radiation of the planar structure considered in previous sections loaded with a wire-medium slab, whose wires are vertically aligned inside the guide. Basically, general features of the structure extensively analyzed in section 8.6 will be discussed, and capability of a WM slab to suppress spurious radiation will be comprehensively outlined. As already shown in Fig. 9.4, following similar procedures, we can design here a transverse network by suitable introducing a transmission matrix for any line segment, and evaluating the input impedance  $Z_{IN}$  of the overall structure. It is worth noting that the input impedance  $Z^\downarrow$  of the equivalent network describing the wire-medium slab has already been carried (see equations (9.65)),



**Fig. 9.11.** (a) Transmission line model of a FPCA loaded with a symmetric wire medium slab. (b) Equivalent transverse network with emphasis on the ABCD matrix representing the wires and the two air/WM interfaces.

and is reported in the following for convenience

$$Z^\downarrow = \begin{pmatrix} 1 & 1 \end{pmatrix} \left[ \underline{Z}'_L \right] \begin{pmatrix} \xi \\ \xi - 1 \end{pmatrix} \quad (9.65)$$

To evaluate the input admittance seen looking downward the reference section, highlighted in Fig. 9.11, by exploiting canonical transmission line theory, we can write

$$Y_{IN} = Y_1 \frac{Y_1^\downarrow \cos(k_{x_1} \frac{h-t}{2}) + jY_1 \sin(k_{x_1} \frac{h-t}{2})}{Y_1 \cos(k_{x_1} \frac{h-t}{2}) + jY_1^\downarrow \sin(k_{x_1} \frac{h-t}{2})} \quad (9.66)$$

where  $Y_1^\downarrow = 1/Z_1^\downarrow$  and  $Y_1$  is the characteristic admittance of the transmission-line, representing the air layer between the WM slab and the PRS, having length  $l = (h - t)/2$  (see Fig. 9.4). As shown in the previous section, to find the radiated field we need to calculate the value of the voltage or the current in the point  $z = z_s$  of the equivalent transverse network. Consequently, we can represent the structure under the reference section by means of an overall transfer matrix, that allows to connect voltage and current as follows

$$\begin{pmatrix} V_{F1} \\ I_{F1} \end{pmatrix} = \begin{pmatrix} A & B \\ C & D \end{pmatrix} \begin{pmatrix} V_{F2} \\ I_{F2} \end{pmatrix}. \quad (9.67)$$

In particular, this ABCD matrix can be simply obtained by respectively introducing the transfer matrices of the line segments constituting the

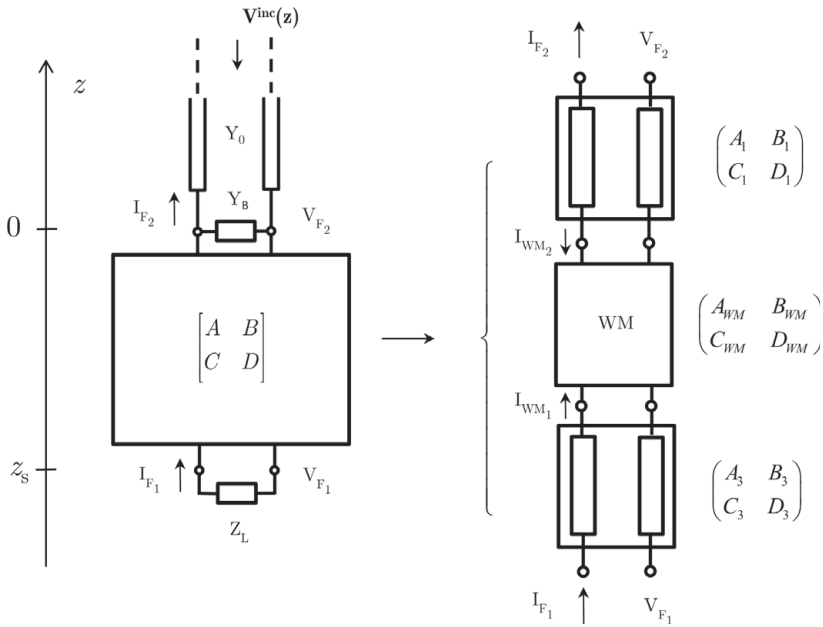


**Fig. 9.12.** Transmission line model of the ABCD matrix representing the wire medium slab. Each region inside the structure must be represented by a suitable transmission line and the relevant transfer matrix. Copyright © 2015, IEEE.

overall network, as shown in Fig. 9.12 and 9.13, where  $Z'_L$  and  $Z_L$  contain information on the structure up and below the considered slab (PRS and ground plane, respectively). Recalling that a series of transfer matrices is the product of the each of them, the ABCD matrix for the structure at hand can be written as follows

$$\begin{pmatrix} A & B \\ C & D \end{pmatrix} = \begin{pmatrix} A_1 & B_1 \\ C_1 & D_1 \end{pmatrix} \begin{pmatrix} A_{WM} & B_{WM} \\ C_{WM} & D_{WM} \end{pmatrix} \begin{pmatrix} A_3 & B_3 \\ C_3 & D_3 \end{pmatrix}, \quad (9.68)$$

while, for the voltage in  $(x_s, z_s)$ , where the actual source is located, we have

$$\begin{cases} V(z_s) = V_{F1} = AV_{F2} + BI_{F2} = AV(0) + BI(0^-) \\ I(z_s) = I_{F1} = CV_{F2} + DI_{F2} = CV(0) + DI(0^-). \end{cases} \quad (9.69)$$

It is important to note that the first and the last matrix of the right-hand term of equation (9.68) are already known, since they represent a simple transmission line segment (see equation (9.31)). We need, instead, to evaluate the central transfer matrix, that is specifically associated to the

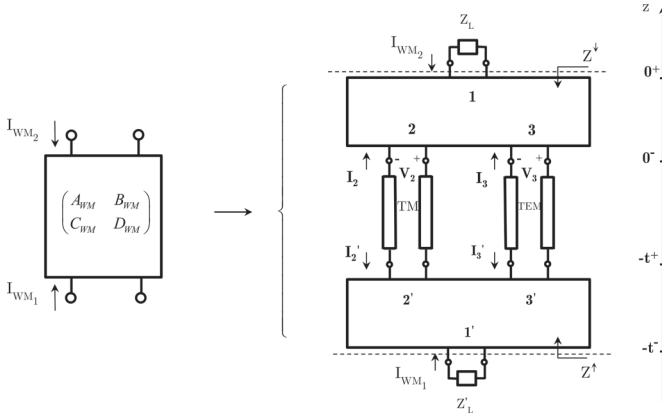


**Fig. 9.13.** Detailed representation of the equivalent network representing the ABCD matrix of the wire medium slab.

wire medium slab. With reference to Fig. 9.12 it is defined as follow

$$\begin{pmatrix} V_{WM1} \\ I_{WM1} \end{pmatrix} = \begin{pmatrix} A_{WM} & B_{WM} \\ C_{WM} & D_{WM} \end{pmatrix} \begin{pmatrix} V_{WM2} \\ -I_{WM2} \end{pmatrix}. \quad (9.70)$$

From standard network analysis (see [122]), with reference to Fig. 9.70 we can write

$$\begin{aligned} Z_{\downarrow} &= \frac{A_{WM}Z_L + B_{WM}}{C_{WM}Z_L + D_{WM}} \\ Z_{\uparrow} &= \frac{A_{WM}Z'_L + B_{WM}}{C_{WM}Z'_L + D_{WM}} \end{aligned} \quad (9.71)$$

in particular, considering the short- and open-circuit terminations  $Z'_L = 0, \infty$  and  $Z_L = 0, \infty$  we have from (9.71)

$$\begin{aligned} Z_0^{\downarrow} &= \frac{B_{WM}}{D_{WM}} & Z_{\infty}^{\downarrow} &= \frac{A_{WM}B_{WM}}{A_{WM}D_{WM} - 1} \\ Z_0^{\uparrow} &= \frac{B_{WM}}{A_{WM}} & Z_{\infty}^{\uparrow} &= \frac{D_{WM}B_{WM}}{A_{WM}D_{WM} - 1} \end{aligned} \quad (9.72)$$

where the input impedances  $Z_{0/\infty}^{\downarrow}$  and  $Z_{0/\infty}^{\uparrow}$  must be calculated by explicitly evaluating equation (9.65) and calculating the two limits. For

the sake of brevity in the following we report only the final results

$$\begin{aligned}
 Z_0^\downarrow = & -\frac{jZ^{TEM^2}(\zeta-1)^2 \sin(k_z^{TEM}t) \sin(k_z^{TM}t)}{(\zeta-1)Z^{TEM} \cos(k_z^{TEM}t) \sin(k_z^{TM}t) - \zeta Z^{TM} \cos(k_z^{TM}t) \sin(k_z^{TEM}t)} \\
 & + \frac{2jZ^{TEM}(\cos(k_z^{TEM}t) \cos(k_z^{TM}t) - 1)(\zeta-1)\zeta Z^{TM}}{(\zeta-1)Z^{TEM} \cos(k_z^{TEM}t) \sin(k_z^{TM}t) - \zeta Z^{TM} \cos(k_z^{TM}t) \sin(k_z^{TEM}t)} \\
 & + \frac{j\zeta^2 \sin(k_z^{TEM}t) \sin(k_z^{TM}t) Z^{TM^2}}{(\zeta-1)Z^{TEM} \cos(k_z^{TEM}t) \sin(k_z^{TM}t) - \zeta Z^{TM} \cos(k_z^{TM}t) \sin(k_z^{TEM}t)}
 \end{aligned}$$

$$Z_\infty^\downarrow = j(Z^{TEM} \cot(k_z^{TEM}t)(\zeta-1) - \cot(k_z^{TM}t)\zeta Z^{TM}). \quad (9.73)$$

Thus, (9.72) can be inverted (using also the reciprocity constraint  $A_{WM}D_{WM} - B_{WM}C_{WM} = 1$ ) to obtain the sought WM ABCD parameters:

$$\begin{aligned}
 A_{WM} &= \sqrt{\frac{Z_0^\downarrow}{Z_0'^\uparrow}} \sqrt{\frac{Z_\infty^\downarrow}{Z_\infty^\downarrow - Z_0^\downarrow}} \\
 B_{WM} &= \sqrt{Z_0^\downarrow Z_0'^\uparrow} \sqrt{\frac{Z_\infty^\downarrow}{Z_\infty^\downarrow - Z_0^\downarrow}} \\
 C_{WM} &= \sqrt{\frac{Z_0^\downarrow}{Z_0'^\uparrow}} \frac{1}{\sqrt{Z_\infty^\downarrow(Z_\infty^\downarrow - Z_0^\downarrow)}} \\
 D_{WM} &= \sqrt{\frac{Z_0'^\uparrow}{Z_0^\downarrow}} \sqrt{\frac{Z_\infty^\downarrow}{Z_\infty^\downarrow - Z_0^\downarrow}}
 \end{aligned} \quad (9.74)$$

If the structure is symmetric, as in our case, equation (9.74) simplify to the final expression

$$\begin{aligned}
 A_{WM} &= D_{WM} = \sqrt{\frac{Z_\infty^\downarrow}{Z_\infty^\downarrow - Z_0^\downarrow}} \\
 B_{WM} &= Z_0^\downarrow \sqrt{\frac{Z_\infty^\downarrow}{Z_\infty^\downarrow - Z_0^\downarrow}} \\
 C_{WM} &= \frac{1}{\sqrt{Z_\infty^\downarrow(Z_\infty^\downarrow - Z_0^\downarrow)}}
 \end{aligned} \quad (9.75)$$

Having available the expression of the transfer matrix for the overall structure shown in Fig. 9.12, we can go back to equation (9.69) to obtain sought values of the voltage and current in the section where the actual source is located.

### 9.3.1. TEM suppression

As widely discussed in the previous sections, by starting from the value of the voltage in a specific point of the equivalent transverse model we can plot the far field of the considered structure. Considering once again equations (9.52)-(9.61) and (9.69) and recalling that

$$E_{\theta}^{ff} = jk_0 \eta_0 \frac{I_0 l_0}{4\pi r} e^{-jkr} \frac{\eta_0}{\epsilon_r} \sin \theta \cos \theta \frac{1}{\cos(k_{z_1} h)} \frac{2Y_0 Y_{stub}}{Y_0 + Y_{in}} \quad (9.76)$$

we can finally investigate the capability of the designed structure to suppress the unwanted contribution generated by the TEM mode. We consider here the same structure as in Fig. 9.10, with longitudinal and transversal slots having dimension  $w_{TM} = 0.01$  and  $w_{TE} = 0.05$  mm. The period of the PRS lattice is  $p = 3$  mm. In Fig. 9.14 the radiation pattern generated by symmetrically loading the open PPW with a wire medium slab having thickness  $t = 4$  mm is presented. Different frequencies have been considered to cover all the expected unimodal bandwidth, ranging from 13 GHz up to 21 GHz (the cut-off frequency of the  $TM_2$  mode is  $f_c = 21.5$  GHz). The characteristics of these diagrams fully corroborate the modal curves reported in Fig. 8.20(a) and the relevant transverse field configuration presented in Fig. 8.22(a). As expected, a residue radiation (see [130, 131] for further details) is still visible in Fig. 9.14. It is less and less visible for higher frequency, also in agreement with the relevant transverse field distribution of the TEM mode, whose value on the lower metal plate, where the VED is placed, decreases for increasing frequency values.

In Fig. 9.15 and 9.16 radiation pattern for  $t = 6$  mm and  $t = 8$  mm have been presented. As expected the residual radiation around  $80^\circ$  is less visible and a well defined beam associated to the  $TM_1$  leaky wave mode has been obtained. It is finally interesting to note that the behavior of the radiation patterns presented in Figs. 9.14-9.16 confirm the prediction of the relevant dispersion curves shown in Fig. 8.20: indeed, the slope of the phase constant of the associated structure is in agreement with the width of angular region swept by the beam. Larger values of  $t$  determine larger values of the this slope, consequently the

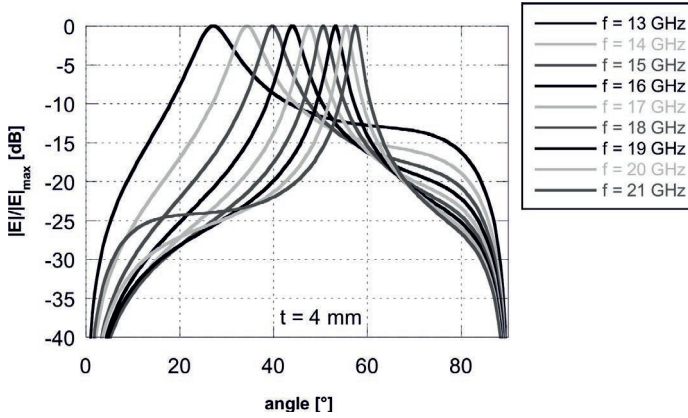


Fig. 9.14. Far-field pattern for the structure excited with a VED in presence of a wire medium slab in arbitrary elevation plane for different frequencies. By suitable dimensioning the thickness we are able to suppress radiation of the TEM mode. WM parameters: wire radius  $a = 0.19$  mm; wire spacing  $d = 1.5$  mm, plasma frequency  $f_p = 90$  GHz. Patch dimensions 2.95 mm (along  $x$ ), 2.99 mm (along  $y$ ); spatial periods (along  $x$  and  $y$ ) 3 mm. Copyright © 2015, IEEE.

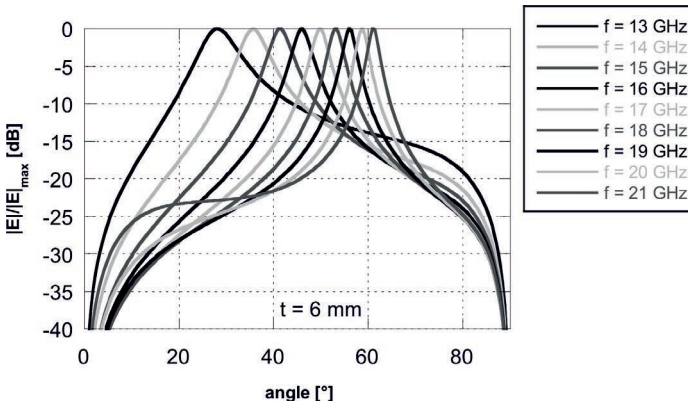
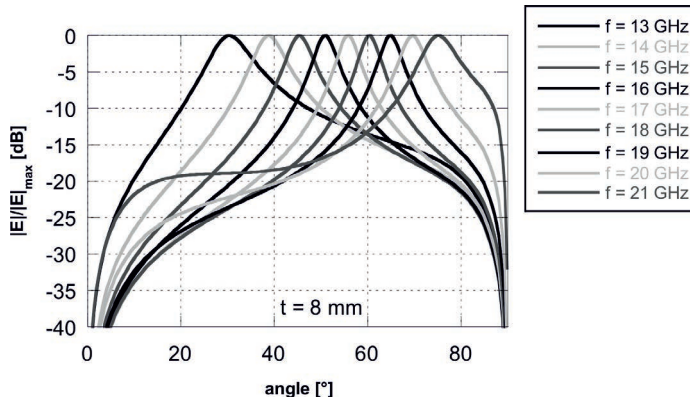


Fig. 9.15. Far-field pattern for the same structure presented in Fig. 9.14 excited with a VED in presence of a wire-medium slab having thickness  $t = 6$  mm in an arbitrary elevation plane for different frequencies. Copyright © 2015, IEEE.



**Fig. 9.16.** Far-field pattern for the same structure presented in Fig. 9.14 excited with a VED in presence of a wire medium slab having thickness  $t = 8$  mm in arbitrary elevation plane for different frequencies. Copyright © 2015, IEEE.

radiation pattern is able to cover wide angles in the same frequency range. The behavior of the attenuation constant is also influenced by the presence of thicker wire medium slab; in fact, as expected, the far-field patterns presented in Fig. 9.16 show larger values of the beamwidth with respect to those presented in Fig. 9.14 and 9.15.

#### 9.4. Conclusion

An efficient network formalism has been presented for the analysis of planar (possibly layered) structures loaded with a vertically aligned wire-medium slab. The equivalent network allows for a rapid determination of the modal dispersion equation and of radiative properties in the presence of elementary sources if compared with the more cumbersome direct approach based on matching the electromagnetic fields at the structure interfaces. Modal and radiative properties of parallel-plate waveguides loaded with symmetrically placed wire-medium slab have been obtained with the proposed method for both closed and open configurations. The modal curves have been validated through a full-wave CAD tool; a multimodal Bloch analysis has been suitably developed to process the scattering parameters provided by the full wave solution. With reference to partially open structures, highly desirable effects on radiative properties due to a line source and to a simple

dipole feed have been observed, related to the strong perturbation of the TEM mode whose radiative spurious contributions is significantly suppressed. These features allow for wideband leaky-wave radiation from the  $TM_1$  mode, which is minimally affected by the presence of the wire medium, in the form of linearly polarized, omnidirectional conical patterns with rather wide angular scanning ranges. The possibility of equalizing the  $TE_1$  and  $TM_1$  leaky mode supported by a Fabry-Perot cavity antenna inside the bandwidth where the radiation of the TEM mode is suppressed has been also discussed. This is of interest for the realization of a dual-pol conical beam. The novel results outlined in this and previous chapters represent a first contribution toward the design of planar radiators having unique reconfigurable features.

PART V

NON-DIFFRACTING BEAMS



# Introduction

The capability of focusing electromagnetic radiation in the near-field region of an antenna is a very attractive feature for a wide variety of applications such as imaging, diagnostic and wireless power transfer. Generally speaking, in optics, solutions of the scalar wave equation that remain confined and do not undergo diffracting spreading are named Bessel beam; they were first proposed in [133] and, as for plane waves, they have a finite energy density but are not square integrable. Having determined free-space and radial propagation constants, namely  $k_0$  and  $k_\rho$ , it is possible to demonstrate that Bessel beams are made by superposition of plane waves whose propagation constants lay on a cone; consequently, they can be either propagating or evanescent. In the last three decades, several generalizations have been proposed to design zero-order Bessel beams (see [133, 134] and their bibliographies) all based on a scalar wave theory, that as is known, is applicable only when the size of the generating aperture is much larger than the operative wavelength, and the cone of the wave vectors describing the Bessel beam (i.e.,  $k_\rho$ ) is narrow with respect to that of the free space. It is important to note that Bessel's beams can be realistically generated through a finite aperture, hence they do not undergo diffraction over a limited range within the Fresnel zone of the structure [135]. In fact, an infinite amount of energy would be required to generate an ideal beam over an entire plane with an infinite non-diffracting range. Even though the capability to generate Bessel beams with narrow beamwidths is particularly important for several applications, a fully vectorial wave analysis is needed, since paraxial approximations cannot be applied. In the last years, the generation of non-diffractive beams using a leaky radial waveguide has

been presented [136, 137] and, more recently, thanks to a customized optimization algorithm [138] the capability of a Radial Line Slotted Array (RLSA) antenna to focus energy in a limited region of space has been also exploited: in [140] slot positions and dimensions required to generate a zero-th order Bessel beam over a certain plane in the near-field region have been evaluated. Specifically, a shaped Bessel beam of zero-th order has been designed, adopting a novel procedure capable to control the normal component of the electric field radiated by the antenna. It is interesting to note that this kind of antenna is centrally fed by a coaxial probe, thus avoiding lossy and cumbersome feeding networks. Following the interesting results achieved so far, in this thesis the possibility of designing and focusing a higher-order Bessel beam is investigated. This kind of beam is very attractive because can be properly designed to obtain also an azimuthal phase variation, that basically allows to produce an 'orbital angular momentum' (OAM) beam, recently receiving a great interest at radio frequencies. Indeed, OAM may be capable, among other application, of an increased capacity of communication channels [141]-[143], and enhanced remote sensing [144].

## 10. Higher Order Bessel Beams

### 10.1. Non-diffracting beams

Diffraction is a physical phenomenon that occurs whenever a wave impacts an obstacle or a slit, whose dimensions are comparable with the probing wavelengths. First references to diffraction phenomena appear in the work of Leonardo da Vinci (1452 - 1519), but the term was originally introduced by the Italian scientist Francesco Maria Grimaldi [132] starting from the latin word *diffringere*, that basically means *to break in several parts*. He was the first who accurately described such a phenomenon in a book published in 1665, even though the possibility of explaining diffraction effects on the basis of the wave theory was introduced at the beginning of the 19th century, when Fresnel showed that diffraction can be explained by the application of Huygens' and interference principles. Diffraction affects all classical fields; even though is one of the physics phenomenon best understood, it is considered as one of the most difficult encountered in optics. Diffraction effects are generally most pronounced for waves with wavelength comparable to the dimensions of the involved object. In addition, its formalism is often considered also to describe the propagation in free space of waves of finite extent. As matter of fact, the expanding profile of a laser beam or the beam shape of a microwave antenna related to an operative wavelength  $\lambda$ , is initially confined to a finite area, but will be subject to diffractive spreading as they propagate outward the transverse plane in the free space; thus also this phenomenon can be studied using diffraction equations.

As is widely known, Helmholtz equation, reported in the following,

governs diffractive phenomena in every area of physics

$$\nabla^2\Phi(\mathbf{r},k) + \kappa^2\Phi(\mathbf{r},k) = 0. \quad (10.1)$$

In optics the scalar function  $\Phi$  is very often named *disturbance* (it represents an electromagnetic radiation intensity) and in the majority of problems encountered in optics an approximate description in terms of a single complex scalar wave function is considered adequate [88]; it is indeed analytically not convenient to consider all the components of the electromagnetic field. Nevertheless, a complete description of the radiation phenomena require the specification of the magnitude of the field vectors as well as their direction (polarization), both as a function of position and time. However, due to the very high frequency values of the optical field, one cannot measure the instantaneous value of these quantities but only time averages over intervals that are large compared to the optical period. Usually for optic phenomena one refers to natural light, that as is known does not show a preferential direction of polarization. Namely, light can be considered as made by a number of elementary monochromatic waves, each having casual direction of propagation and different initial phase, giving rise to a radiation that is called for this reason *not polarized* and *incoherent*.

Plane waves are the most known diffraction-free solution of the Helmholtz equations, but a source of infinite extent should be designed to synthesize this ideal waves. Even though plane waves do not has physical meaning, they can be very useful to represent the field radiated by more complex and realistic sources. However in [133], it has been demonstrated for the first time that Helmholtz equation has got another class of diffraction-free solutions, namely a monochromatic wave propagating in the  $z$  direction with constant field amplitude reported in the following

$$\Phi(x, y, z; k) = \exp(-jk_z z) J_0(k_\rho \rho) \quad (10.2)$$

where  $k_\rho^2 + k_z^2 = k_0^2$ , denoting with  $k_0^2$  the square of free-space propagation constant. Moreover,  $(\rho, z)$  are coordinates in a cylindrical system and  $J_0$  is the zeroth-order Bessel function of the first kind. As a matter of fact, equation (10.2) represents a non-diffracting beam because it shows a constant amplitude distribution in every plane normal to the  $z$  axis. Indeed, the amplitude distribution of the scalar variable (i.e., the electric field for an electromagnetic wave) does not change with the longitudinal coordinate.

## 10.2. Generalized field with invariant section

To achieve the excitation of a  $n^{\text{th}}$  order Hankel function and thus of a focused orbital angular momentum (OAM) beam by means of a RLSA antenna, the synthesis of a properly phased aperture field on its slotted plane along the azimuthal angle is requested. Specifically, in the following the attention will be focused on the analysis of an aperture field capable to radiate a beam whose phase could show such a rotational variation. As demonstrated in [88, 145], the most general field with invariant section can be expressed as a linear combination of the following functions

$$J_n(k_t \rho) \quad e^{jn\phi} \quad e^{-jk_z z} \quad (10.3)$$

thus for the  $z$  component of the electric field we can write

$$E_z(\rho, \phi, z) = 2\pi \sum_{n=-\infty}^{\infty} A_n j^n J_n(k_t \rho) e^{jn\phi} e^{-jk_z z} \quad (10.4)$$

consequently, on the  $z = 0$  plane of an aperture antenna it holds

$$E_z(\rho, \phi) = 2\pi \sum_{n=-\infty}^{\infty} A_n j^n J_n(k_t \rho) e^{jn\phi}. \quad (10.5)$$

If  $n = 0$  an azimuthally symmetric field can be obtained, then  $z$  components of the electric field becomes

$$E_z(\rho, \phi, z) = 2\pi j A_0 J_0(k_t \rho) \quad (10.6)$$

since the wave is TM polarized such a field can be used to derive the remaining components of the electromagnetic field [98, 136, 137].

It is important to note that if in equation (10.5)  $n = 1$  the field is no longer azimuthally symmetric, an angular dependency for the phase can be observed and we can write

$$E_z(\rho, \phi, z) = 2\pi A_1 j J_1(k_t \rho) e^{j\phi} e^{jk_z z} \quad (10.7)$$

that is the more general relation of an aperture field having an azimuthal variation of order  $n = 1$ ; it represents the starting point of our future developments. As an example, in Fig. 10.1 (a) and (b) a two-dimensional representation of an azimuthal phase variation of order  $n = -1$  and  $n = -2$  have been shown.

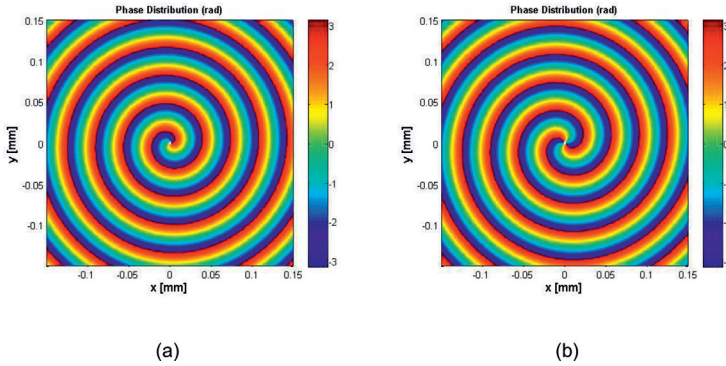


Fig. 10.1. Azimuthal phase variation of a Bessel beam as in equation (10.7) of order  $n = -1$  (a) and  $n = -2$  (b).

### 10.3. Far-field evaluation

In the previous section an aperture field having an invariant section and an azimuthal phase dependency as  $e^{jn\phi}$  has been introduced. Before to design the RLSA slots layout capable to synthesize such a field it is very interesting to evaluate the far field generated by suitably propagating this aperture field. Starting from the procedure outlined in [146], where a closed-form expression for the radiation pattern of cylindrical leaky waves propagating on a planar structure have been derived, here a novel expressions accounting for also an azimuthal variation of the phase of order  $n = 1$ , will be presented. As the structure is invariant in the transverse plane with respect to the  $z$  direction, only the  $z$  component of a magnetic vector potential  $\mathbf{A}$  is exploited to derive the electromagnetic field, considering as specific case an amplitude distribution represented by a Hankel function, as reported in the following

$$A_z(\rho, \phi, z) = \frac{j}{2} H_1^{(2)}(k_t \rho) e^{j\phi} e^{-jk_z z} \quad (10.8)$$

where the factor  $1/2$  is added for convenience. Besides, considering that

$$A_z(\rho, \phi, z) = \frac{j}{2} H_1^{(2)}(k_t \rho) (\cos\phi + j \sin\phi) e^{-jk_z z} \quad (10.9)$$

the calculation can be split in two independent part, the former has been already carried out in [146] but will be briefly synthesized here for the sake of clarity, whereas the latter will be outlined by suitable modifying

the known solution. By starting from equation (10.9) we can write

$$\begin{aligned} A_z(\rho, \phi, z) &= A_{z_1}(\rho, \phi, z) + A_{z_2}(\rho, \phi, z) \\ &= \frac{j}{2} \left[ H_1^{(2)}(k_t \rho) \cos \phi + j H_1^{(2)}(k_t \rho) \sin \phi \right] e^{-jk_z z} \end{aligned} \quad (10.10)$$

thus in the following subsection the first and second potential, namely  $A_{z_1}(\rho, \phi, z)$  and  $A_{z_2}(\rho, \phi, z)$  will be separately evaluated.

### 10.3.1. Derivation of the first term

All the Hankel function reported in this section, if not explicitly indicated, are of the second kind. In the TM case the components of the magnetic field  $\mathbf{H}$  in cylindrical coordinates can be written as follows (see [98] for further details)

$$H_{\rho_1} = \frac{1}{\rho} \frac{\partial A_{z_1}}{\partial \phi} \quad (10.11)$$

$$H_{\phi_1} = -\frac{\partial A_{z_1}}{\partial \rho} \quad (10.12)$$

$$H_{z_1} = 0 \quad (10.13)$$

hence, by considering the equivalence principle, the radiated field may be found from an equivalent current distribution (see [39], Chapter 12)  $\mathbf{J} = \mathbf{z}_0 \times \mathbf{H}$  on the  $z = 0$  plane, assuming zero fields in  $z < 0$ . Replacing the finite aperture plane ( $a \leq \rho \leq b$ ) with a perfect magnetic conductor and exploiting the image theory we can write

$$\mathbf{J} = 2\mathbf{z}_0 \times \mathbf{H} = 2\mathbf{z}_0 \times (H_\rho \boldsymbol{\rho}_0 + H_\phi \boldsymbol{\phi}_0). \quad (10.14)$$

By exploiting elementary radiation theory [123], whose main results are reported in the following for convenience, the radiation pattern of an arbitrary distribution of surface currents is given by the expression

$$\begin{aligned} E_\theta(r, \theta, \phi) &= R(r) N_\theta(\theta, \phi) \\ E_\phi(r, \theta, \phi) &= R(r) N_\phi(\theta, \phi) \end{aligned} \quad (10.15)$$

where in particular

$$\begin{aligned} N_\theta(\theta, \phi) &= \iint_S [J_x \cos \theta \cos \phi + J_y \cos \theta \sin \phi - J_z \sin \theta] e^{jk_r' \cos(\psi)} ds' \\ N_\phi(\theta, \phi) &= \iint_S [-J_x \sin \phi + J_y \cos \phi] e^{jk_r' \cos(\psi)} ds' \end{aligned} \quad (10.16)$$

thus, considering the following Cartesian to cylindrical coordinate transformation

$$\begin{aligned} J_x &= J_\rho \cos \phi' - J_\phi \sin \phi' \\ J_y &= J_\rho \sin \phi' + J_\phi \cos \phi' \end{aligned} \quad (10.17)$$

and recalling that (see [39], pag. 302)

$$kr' \cos \psi = k\rho' \cos(\phi - \phi') = \zeta\rho' \cos(\phi - \phi') \quad (10.18)$$

with  $\zeta = k \sin \theta$  (being  $k$  the free-space wave number), we can finally write

$$\begin{aligned} N_\theta(\theta, \phi) &= \iint_S [(J_\rho \cos \phi' - J_\phi \sin \phi') \cos \theta \cos \phi] e^{j\zeta\rho' \cos(\phi - \phi')} ds' \\ &\quad + \iint_S [(J_\rho \sin \phi' + J_\phi \cos \phi') \cos \theta \sin \phi] e^{j\zeta\rho' \cos(\phi - \phi')} ds' \\ N_\phi(\theta, \phi) &= \iint_S [-(J_\rho \cos \phi' - J_\phi \sin \phi') \sin \phi] e^{j\zeta\rho' \cos(\phi - \phi')} ds' \\ &\quad + \iint_S [(J_\rho \sin \phi' + J_\phi \cos \phi') \cos \phi] e^{j\zeta\rho' \cos(\phi - \phi')} ds'. \end{aligned} \quad (10.19)$$

By recalling equations (10.11) and (10.10) for the  $\mathbf{H}$  field on the  $z = 0$  plane we have

$$H_{\rho_1} = -\frac{1}{2\rho} H_1(k_\rho \rho) \sin \phi \quad (10.20)$$

$$H_{\phi_1} = -\frac{k_\rho}{2} H_1'(k_\rho \rho) \cos \phi \quad (10.21)$$

$$H_{z_1} = 0 \quad (10.22)$$

hence, being  $\boldsymbol{\phi}_0 = \mathbf{z}_0 \times \boldsymbol{\rho}_0$  and  $-\boldsymbol{\rho}_0 = \mathbf{z}_0 \times \boldsymbol{\phi}_0$ , equation (10.14) becomes

$$\begin{aligned} J_{\rho_1} &= k_\rho H_1'(k_\rho \rho') \cos \phi' \\ J_{\phi_1} &= -\frac{1}{\rho} H_1(k_\rho \rho') \sin \phi' \end{aligned} \quad (10.23)$$

finally, the first of the two integrals in (10.19) representing the far-field radiated by a given equivalent current distribution is reported in the

following

$$\begin{aligned}
 N_\theta(\theta, \phi) &= \iint_S \left[ (k_\rho H'_1(k_\rho \rho') \cos \phi' \cos \phi' \right. \\
 &\quad \left. + \frac{1}{\rho} H_1(k_\rho \rho') \sin \phi' \sin \phi') \cos \theta \cos \phi \right] e^{j\zeta \rho' \cos(\phi - \phi') ds'} \\
 &\quad + \iint_S \left[ (k_\rho H'_1(k_\rho \rho') \cos \phi' \sin \phi' \right. \\
 &\quad \left. - \frac{1}{\rho} H_1(k_\rho \rho') \sin \phi' \cos \phi') \cos \theta \sin \phi \right] e^{j\zeta \rho' \cos(\phi - \phi') ds'}.
 \end{aligned} \tag{10.24}$$

By recalling elementary trigonometry (sum identities), after some algebra we can write

$$\begin{aligned}
 N_\theta(\theta, \phi) &= \cos \theta \int_a^b k_\rho H'(k_\rho \rho') \int_0^{2\pi} \cos \phi' \cos(\phi - \phi') e^{j\zeta \rho' \cos(\phi - \phi') ds'} d\phi' \rho' d\rho' \\
 &\quad + \cos \theta \int_a^b -\frac{H(k_\rho \rho')}{\rho'} \int_0^{2\pi} -\sin \phi' \sin(\phi - \phi') e^{j\zeta \rho' \cos(\phi - \phi') ds'} d\phi' \rho' d\rho'
 \end{aligned} \tag{10.25}$$

now, having the two inner integral a period of  $2\pi$  we can write

$$\begin{aligned}
 &\int_0^{2\pi} \cos \phi' \cos(\phi - \phi') e^{j\zeta \rho' \cos(\phi - \phi') ds'} d\phi' \\
 &= \int_0^{2\pi} \cos \phi' \cos(\phi - \phi') e^{j\zeta \rho' \cos(\phi - \phi') ds'} d(\phi - \phi') \\
 &\int_0^{2\pi} \sin \phi' \sin(\phi - \phi') e^{j\zeta \rho' \cos(\phi - \phi') ds'} d\phi' \\
 &= \int_0^{2\pi} -\sin \phi' \sin(\phi - \phi') e^{j\zeta \rho' \cos(\phi - \phi') ds'} d(\phi - \phi')
 \end{aligned}$$

introducing a new variable the computation of these integrals can be simplified, namely by placing  $x = \phi - \phi'$  and  $\phi' = x - \phi$  we have that  $\cos \phi' = \cos(x - \phi) = \cos x \cos \phi + \sin \phi \sin x$ , therefore the previous integrals reduce to

$$\begin{aligned}
 &\int_0^{2\pi} \cos \phi' \cos(\phi - \phi') e^{j\zeta \rho' \cos(\phi - \phi') ds'} d(\phi - \phi') \\
 &= 2 \cos \phi \int_0^\pi \cos^2 x e^{j\zeta \rho' \cos x} + \frac{\sin \phi}{2} \int_0^{2\pi} \sin(2x) e^{j\zeta \rho' \cos x} dx.
 \end{aligned} \tag{10.26}$$

$$\begin{aligned}
 & - \int_0^{2\pi} \sin \phi' \sin(\phi - \phi') e^{j\zeta\rho' \cos(\phi - \phi') ds'} d(\phi - \phi') \\
 & = -2 \cos \phi \int_0^\pi \sin^2 x e^{j\zeta\rho' \cos x} + \frac{\sin \phi}{2} \int_0^{2\pi} \sin(2x) e^{j\zeta\rho' \cos x} dx
 \end{aligned} \tag{10.27}$$

It is important to note that the second integral on the right side of both (10.26) and (10.27) equation is null; moreover thanks to the periodicity, the limits of the first one have been changed.

The solution of the remaining integral of equation (10.26) can be carried out by considering the integral representation of the Bessel functions and its derivative for  $n = 1$  [147, 148], reported in the following

$$\begin{aligned}
 J_n(z) &= \frac{j^{-n}}{\pi} \int_0^\pi \cos(nx) e^{jz \cos x} dx \\
 J_1'(z) &= \frac{1}{\pi} \int_0^\pi \cos^2 x e^{jz \cos x} dx
 \end{aligned} \tag{10.28}$$

thus the integral (10.26) can be rewritten as

$$2 \cos \phi \int_0^\pi \cos^2 x e^{j\zeta\rho' \cos x} dx = 2\pi \cos \phi J_1'(\zeta\rho'). \tag{10.29}$$

Regarding to the remaining integral in (10.27), considering that [148]

$$J_1(z) = \frac{(z/2)^\nu}{\Gamma(\nu + \frac{1}{2}) + \Gamma(\frac{1}{2})} \int_0^\pi \sin^{2\nu} x e^{jz \cos x} dx \tag{10.30}$$

and exploiting some remarkable properties of the Gamma function, we can write

$$2 \cos \phi \int_0^\pi \sin^2 x e^{j\zeta\rho' \cos x} dx = -\frac{2\pi}{\zeta\rho'} \cos \phi J_1(\zeta\rho'). \tag{10.31}$$

Rearranging these results, the final integral can be solved as pointed out in [146, 147], leading to the following final result

$$\begin{aligned}
 N_{\theta_1}(\theta, \phi) &= 2\pi \cos \theta \cos \phi \int_a^b \left[ k_\rho H_1'(k_\rho \rho') J_1'(\zeta\rho') \rho' + \frac{H_1(k_\rho \rho')}{\zeta\rho'} J_1(\zeta\rho') \right] d\rho' \\
 &= \cos \theta \cos \phi P^1(\theta)
 \end{aligned} \tag{10.32}$$

where  $P^1(\theta)$  is a combination of Bessel and Hankel functions that does not depend on the azimuthal angle. Following an analogue procedure and considering the same integral identity, a similar result for the  $\phi$  component of the radiation integral can be obtained

$$N_{\phi_1}(\theta, \phi) = -\sin \phi \frac{2\pi}{\zeta} [H_1(k_\rho \rho') J_1(\zeta\rho')]_{\rho'=a}^{\rho'=b} \tag{10.33}$$

Equations (10.32) and (10.33) represent the sought solution of the radiation integrals associated to the first magnetic potential introduced by equation (10.10).

### 10.3.2. Derivation of the second term

In this case the components of the magnetic field  $\mathbf{H}$  in cylindrical coordinates are reported in the following

$$H_{\rho_2} = \frac{1}{2\rho} H_1(k_\rho \rho) \cos \phi \quad (10.34)$$

$$H_{\phi_2} = -\frac{k_\rho}{2} H_1'(k_\rho \rho) \sin \phi \quad (10.35)$$

$$H_{z_2} = 0 \quad (10.36)$$

thus for the currents we have

$$\begin{aligned} J_\rho &= k_\rho H_1'(k_\rho \rho') \sin \phi' \\ J_\phi &= \frac{1}{\rho} H_1(k_\rho \rho') \cos \phi'. \end{aligned} \quad (10.37)$$

Considering again the radiation formulas and applying the same procedure outlined in the previous section, the following expressions for the radiation integral can be obtained

$$\begin{aligned} N_\theta(\theta, \phi) &= \cos \theta \int_a^b k_\rho H_1'(k_\rho \rho') \int_0^{2\pi} \sin \phi' \cos(\phi - \phi') e^{j\zeta \rho' \cos(\phi - \phi')} d\phi' \rho' d\rho' \\ &\quad + \cos \theta \int_a^b \frac{H_1(k_\rho \rho')}{\rho'} \int_0^{2\pi} \cos \phi' \sin(\phi - \phi') e^{j\zeta \rho' \cos(\phi - \phi')} d\phi' \rho' d\rho' \\ N_\theta(\theta, \phi) &= \cos \theta \int_a^b -k_\rho H_1'(k_\rho \rho') \int_0^{2\pi} \sin \phi' \sin(\phi - \phi') e^{j\zeta \rho' \cos(\phi - \phi')} d\phi' \rho' d\rho' \\ &\quad + \cos \theta \int_a^b \frac{H_1(k_\rho \rho')}{\rho'} \int_0^{2\pi} \cos \phi' \cos(\phi - \phi') e^{j\zeta \rho' \cos(\phi - \phi')} d\phi' \rho' d\rho' \end{aligned} \quad (10.38)$$

that in turn lead to these final results

$$\begin{aligned} N_{\theta_2}(\theta, \phi) &= \cos \theta \sin \phi P^1(\theta) \\ N_{\phi_2}(\theta, \phi) &= \cos \theta C(\theta). \end{aligned} \quad (10.39)$$

where once again  $P^1(\theta)$  and  $C(\theta)$  are combinations of Bessel and Hankel functions that do not depend on the azimuthal angle. Equations (10.39) represent the sought solution of the radiation integrals associated to the second magnetic potential introduced by equation (10.10).

### 10.3.3. Radiation formula for the case $n = 1$

By suitably combining the previous results and recalling equation (10.15), the electric field radiated by an azimuthal-dependent current distribution can be finally written. Specifically, for the electric field produced by the first term of equation (10.10), as outlined in section 10.3.1, we can write

$$\begin{aligned} E_{\theta_1}(\theta, \phi) &= R(r) \cos \theta \cos \phi P^{(1)}(\theta) \\ E_{\phi_1}(\theta, \phi) &= -R(r) \sin \phi C(\theta) \end{aligned} \quad (10.40)$$

while for the second one (see section 10.3.2) we have

$$\begin{aligned} E_{\theta_2}(\theta, \phi) &= R(r) \cos \theta \sin \phi P^{(1)}(\theta) \\ E_{\phi_2}(\theta, \phi) &= R(r) \cos \phi C(\theta). \end{aligned} \quad (10.41)$$

Developing the complex sum among these terms, we can finally write

$$\begin{aligned} E_{tot_\theta}(\theta, \phi) &= E_{\theta_1} + jE_{\theta_2} = R(r) \cos \theta P^{(1)}(\theta) e^{j\phi} \\ E_{tot_\phi}(\theta, \phi) &= E_{\phi_1} + jE_{\phi_2} = jR(r) C(\theta) e^{j\phi} \end{aligned} \quad (10.42)$$

which states that phase rotation (azimuthal dependence for the phase) is still visible in the far field zone.

## 10.4. Radiation formula for a $n$ th-order Hankel function

It may be very useful to make available also a closed-form solution for a generic order  $n$  of the Hankel function and therefore for the phase dependency. This entails that the integrals considered so far should be not carried out introducing a fixed value for  $n$ .

Specifically, for the  $z$ -directed magnetic potential we should write

$$\begin{aligned} A_z(\rho, \phi, z) &= A_{z_1}(\rho, \phi, z) + A_{z_2}(\rho, \phi, z) \\ &= \frac{j}{2} [H_1^{(2)}(k_\rho \rho) \cos(n\phi) + jH_1^{(2)}(k_\rho \rho) \sin(n\phi)] e^{-jk_z z} \end{aligned} \quad (10.43)$$

analogously for the components of magnetic field and current distribution, as reported in the following

$$\begin{aligned} H_\rho &= -\frac{1}{2\rho} H_1(k_\rho \rho) n \sin(n\phi) \\ H_\phi &= -\frac{k_\rho}{2} H_1'(k_\rho \rho) n \cos(n\phi) \\ H_z &= 0 \end{aligned} \quad (10.44)$$

$$\begin{aligned}
 J_\rho &= k_\rho H_1'(k_\rho \rho') \cos(n\phi') \\
 J_\phi &= -\frac{n}{\rho} H_1(k_\rho \rho') \sin(n\phi').
 \end{aligned}
 \tag{10.45}$$

By exploiting again the same procedure outlined in the previous section, the following expression for the radiation formula can be obtained

$$\begin{aligned}
 N_\theta(\theta, \phi) &= \cos \theta \int_a^b k_\rho H_1'(k_\rho \rho') \int_0^{2\pi} [\cos(n\phi') \cos(\phi') \\
 &\quad + \cos(n\phi') \sin(\phi')] \cos(\phi) e^{j\zeta \rho' \cos(\phi - \phi')} d\phi' \rho' d\rho' \\
 &= \cos \theta \int_a^b k_\rho H_1'(k_\rho \rho') \int_0^{2\pi} \cos(n\phi') \cos(\phi - \phi') e^{j\zeta \rho' \cos(\phi - \phi')} d\phi' \rho' d\rho'
 \end{aligned}
 \tag{10.46}$$

thus by changing the variable of the inner integral ( $x = \phi - \phi'$ ) and considering periodicity we should write

$$2 \cos(n\phi) \int_a^b \cos(nx) \cos x e^{j\zeta \rho' \cos x} dx + \sin(n\phi) \int_0^{2\pi} \sin(nx) \cos x e^{j\zeta \rho' \cos x} dx
 \tag{10.47}$$

now, considering again a spectral representation of the Bessel function [148]

$$\begin{aligned}
 J_n(z) &= \frac{j^{-n}}{\pi} \int_0^\pi \cos(nx) e^{jz \cos x} dx \\
 J_n'(z) &= \frac{j^{-n+1}}{\pi} \int_0^\pi \cos(nx) \cos x e^{jz \cos x} dx
 \end{aligned}
 \tag{10.48}$$

we can easily develop the first integral. However, the evaluation of the following integral is not straightforward

$$\sin(n\phi) \int_0^{2\pi} \sin(nx) \cos(x) e^{j\zeta \rho' \cos x} dx.
 \tag{10.49}$$

## 10.5. Radiation formula for a Bessel function

By following the same procedure outlined in the previous sections, it is possible to evaluate also the far-field pattern when the aperture field is represented by a z-directed magnetic potential described through a Bessel function of first kind and  $n = 1$  order. Consequently, the aperture field that is generated has an amplitude distribution defined by a Bessel

function. Namely, we have

$$\begin{aligned}
 A_z(\rho, \phi, z) &= A_{z_1}(\rho, \phi, z) + A_{z_2}(\rho, \phi, z) \\
 &= \frac{j}{2} J_1(k_t \rho) e^{j\phi} e^{-jk_z z} \\
 &= \frac{j}{2} J_1(k_t \rho) (\cos \phi + j \sin \phi) e^{-jk_z z}
 \end{aligned} \tag{10.50}$$

consequently, the components of the magnetic field and of the current associated to the first magnetic potential are reported in the following

$$\begin{aligned}
 H_\rho &= -\frac{1}{2\rho} J_1(k_\rho \rho) \sin(\phi) \\
 H_\phi &= -\frac{k_\rho}{2} J_1'(k_\rho \rho) \cos(\phi) \\
 H_z &= 0
 \end{aligned} \tag{10.51}$$

$$\begin{aligned}
 J_\rho &= k_\rho J_1'(k_\rho \rho') \cos(\phi') \\
 J_\phi &= -\frac{1}{\rho} J_1(k_\rho \rho') \sin(\phi').
 \end{aligned} \tag{10.52}$$

It is important to note that for the integrals considered until now the angular and radial dependency in the magnetic potential have always been separated. This allows us to state that by changing in the magnetic potential the Hankel with a Bessel function does not introduce any different terms in the radiation formula and consequently in the final expression of the radiated electric field.

As an example, for the  $\phi$  component of the radiation integral we can write

$$\begin{aligned}
 N_\theta(\theta, \phi) &= \cos \theta \int_a^b k_\rho J_1'(k_\rho \rho') \int_0^{2\pi} \cos \phi' \cos(\phi - \phi') e^{j\zeta \rho' \cos(\phi - \phi')} d\phi' \rho' d\rho' \\
 &+ \cos \theta \int_a^b -\frac{J_1'(k_\rho \rho')}{\rho'} \int_0^{2\pi} -\sin \phi' \sin(\phi - \phi') e^{j\zeta \rho' \cos(\phi - \phi')} d\phi' \rho' d\rho'
 \end{aligned} \tag{10.53}$$

it is clear that, even if we would not be able to solve the external integral, the solution could be anyway represented by this expression

$$\begin{aligned}
 N_\theta(\theta, \phi) &= \cos \theta \sin \phi Q^{(1)}(\theta) \\
 N_\phi(\theta, \phi) &= \cos \theta Q^{(2)}(\theta)
 \end{aligned} \tag{10.54}$$

where, once again,  $Q^{(1)}(\theta)$  and  $Q^{(2)}(\theta)$  represent the radial and elevation angle dependency for the field. It is interesting to note, finally, that if we consider the most general  $z$ -directed magnetic potential (i.e., a combination of Hankel functions of first and second kind) we obtain

$$A_{tot}(\rho, \phi, z) = \frac{1}{2} [H_1^{(2)}(k_t \rho) \cos \phi + H_1^{(1)}(k_t \rho) \cos \phi] \quad (10.55)$$

and consequently we can write

$$A_{tot}(\rho, \phi, z) = \frac{1}{2} [(J_1(k_t \rho) - jY_1(k_t \rho)) \cos \phi + (J_1(k_t \rho) + jY_1(k_t \rho)) \cos \phi] \quad (10.56)$$

for the second term of the this equation we have

$$H_1^{(2)}(k_t \rho) = (J_1(k_t \rho) + jY_1(k_t \rho)) = (J_1(k_t^* \rho) - jY_1(k_t \rho))^* \quad (10.57)$$

and finally

$$H_1^{(1)}(k_t \rho) = [H_1^{(2)}(k_t^* \rho)]^*. \quad (10.58)$$

By starting from these results it is possible to suitably modify the involved integral to demonstrate once again that the angular dependency remains unchanged. In particular, no complex quantities are involved other than the exponential, which can easily be taken into account by considering  $k_0 = -k_0$ . All these properties allow us to write

$$A_{tot}(\rho, \phi, z) = \frac{1}{2} [H_1^{(2)}(k_t \rho) \cos \phi + H_1^{(2)}(k_t^* \rho) \cos \phi] \quad (10.59)$$

which finally states that no variation is expected for the azimuthal variable.

## 10.6. Aperture field

By starting from the results outlined in the previous sections, it is finally possible to write an aperture field capable to radiate a Bessel beam with an azimuthal phase rotation, whose far-field behavior can be evaluated in closed form. From equations (10.20) and (10.34), representing the magnetic field related to the initial decomposition of the magnetic potential (see (10.10)), the total field  $\mathbf{H}_{tot}$  can be defined as

follows

$$\begin{aligned}
 \mathbf{H}_{tot} &= H_\rho \boldsymbol{\rho}_0 + H_\phi \boldsymbol{\phi}_0 = (H_{\rho_1} + H_{\rho_2}) \boldsymbol{\rho}_0 + (H_{\phi_1} + H_{\phi_2}) \boldsymbol{\phi}_0 = \\
 &= \left[ -\frac{1}{2\rho} H_1(k_\rho \rho) (\cos \phi + j \sin \phi) \right] \boldsymbol{\rho}_0 + \left[ \frac{k_\rho}{2} H'_1(k_\rho \rho) (-j \cos \phi + \sin \phi) \right] \boldsymbol{\phi}_0 \\
 &= -\frac{1}{2\rho} H_1(k_\rho \rho) e^{j\phi} \boldsymbol{\rho}_0 - j \frac{k_\rho}{2} H'_1(k_\rho \rho) (\cos \phi + j \sin \phi) \boldsymbol{\phi}_0
 \end{aligned} \tag{10.60}$$

therefore, we finally have

$$\mathbf{H}_{tot} = -\frac{1}{2\rho} H_1(k_\rho \rho) e^{j\phi} \boldsymbol{\rho}_0 - j \frac{k_\rho}{2} H'_1(k_\rho \rho) e^{j\phi} \boldsymbol{\phi}_0. \tag{10.61}$$

In the next chapter to synthesize this aperture field, following a similar procedure outlined in [138, 140], an RLSA antenna will be designed and optimized. In particular, an outward cylindrical wave is launched inside the structure, thus exploiting the holographic principle in conjunction with an iterative procedure, the slots position and dimension capable to sampling the incident field propagating inside the radial open waveguide will be determined.

## 10.7. RLSA antenna design

To design a higher-order collimated Bessel beam with an azimuthal phase variation, we may exploit the aperture field carried out in the previous chapter and the overall method outlined in [140]. Basically, in that paper, a RLSA antenna has been shown to be capable to produce a shaped and a focused Bessel beam, azimuthally symmetric and without particular requirement on the phase distribution. The procedure is based on the holographic principle and on ad-hoc optimization scheme, developed for the first time in [138]: specifically, in this paper, a RLSA prototype has been designed showing good performance in term of efficiency and directivity.

To synthesize the wanted focused beam the method is based on a procedure that for a given field aperture automatically generates the relevant slot layout. Accordingly to the so-called *Bethe theory* [139], the radiation from a slot cut into a metallic plane can be modeled by an equivalent magnetic dipole sitting on a ground plane, whose dipole moment must be proportional to the magnetic field generated by the feeding wave in the considering structure (a parallel-plate waveguide

in our case) through a dyadic polarizability. These properties allow us to write

$$\mathbf{M} = \underline{\alpha}_m \cdot \mathbf{H}^{inc}. \quad (10.62)$$

It is important to note that Bethe theory also introduces an equivalent electric dipole, but its radiation effect is negligible with respect to that of the magnetic dipole for slots whose length is much greater than their width (as will be for the considered structure). For a single slot oriented along  $\mathbf{u}_0$ , the dyadic polarizability is given by  $\underline{\alpha}_m = \alpha_m \mathbf{u}_0 \mathbf{u}_0$ , where the amplitude of  $\alpha_m$  grows with the slot length up to the resonant length [138].

Since we want to synthesize a specific aperture field, the design methodology of the RLSA antenna can be developed by means of a *holographic technique*, that allows to obtain the size and position of the slots composing the array. Basically, holography predicts that a certain antenna aperture, represented by an equivalent current distribution, can be generated by interference between an input feeding wave and a hologram, which in the case at hand is given by the slotted surface of the RLSA structure. By suitably sampling the incident field launched inside the radial parallel plate waveguide by a coaxial probe, it is possible to synthesize the holographic interference pattern, this entails that position and length of each slot must satisfy the following equations

$$|\underline{\alpha}_m(\rho_i) \cdot \mathbf{H}^{inc}(\rho_i)| = C|A(\rho_i)| \quad (10.63)$$

and

$$\angle \left\{ (\mathbf{M})_0^*(\rho_i) \underline{\alpha}_m(\rho_i) \cdot \mathbf{H}^{inc}(\rho_i) \right\} = \gamma \quad (10.64)$$

where  $\underline{\alpha}_m$  is the dyadic polarizability of the considered slot,  $\mathbf{H}^{inc}(\rho_i)$  is the incident field inside the structure and  $\mathbf{M}_0(\rho_i) = A(\rho_i) \mathbf{u}_0$  is ideal-target aperture magnetic current, namely the holographic image, directed along the generic direction  $\mathbf{u}_0$ .  $C$  and  $\gamma$  are arbitrary real constants.

It is worth noting that enforcing such condition assures that, for each slot, the equivalent magnetic dipole  $\mathbf{M}$  is parallel to the ideal target aperture. Specifically, (10.63) is the key equation that controls the correct slot positioning, which ensures the target aperture phase distribution, whilst (10.64) imposes the amplitude distribution on the radiating aperture which can be achieved by properly choosing the slot length. Consequently, thanks to a quasi-orthogonality properties between slot lengths

and positions, it is allowed to set up independent actions on the two different variables. Basically it is assumed here, as suggested in [138], that a variation in slot length mainly affect the associated equivalent magnetic moment amplitude, allowing us to consider variation of the phase as an higher-order effect; in a similar way, variations of slot positions mainly affects the phase of the associate moment, while magnitude remains almost unchanged.

Since we are considering a radial PPW excited by a  $TM_{0,0}^z$  cylindrical mode (see [123] Chapter 9), it holds

$$\mathbf{H}^{inc}(\rho) = H^{inc} H_1^{(2)}(k_d \rho) \boldsymbol{\phi}_0 \quad (10.65)$$

where  $H_1^{(2)}$  denotes, as usual, the first-order Hankel function of second kind, and  $k_d = 2\pi/\lambda_d$  the wavenumber inside the guide. It remains to evaluate the amplitude of the polarizability, that starting from (10.64) and considering (10.65) reduces to

$$|\alpha_m(\rho)| = \frac{C |A(\rho)|}{|H_1^{(2)}(k_d \rho)|}. \quad (10.66)$$

This expression is exploited to evaluate the slot length profile taking care to consider that, even if the constant  $C$  does not affect the shape of the amplitude aperture, it has to be chosen to keep the slot length within a proper range. Namely, if the value of the constant is too large, the power of the feeding wave is entirely radiated by the slots close to the antenna center; on the other hand, when is too small, the desired aperture shape is easily achieved but a considerable amount of power is not radiated and remains trapped in the PPW, resulting in a low radiation efficiency.

If we consider a linear polarized RLSA antenna, whose slots are always orthogonal to the considered radius, it holds

$$\underline{\alpha}_m = \alpha_m \mathbf{u}_0 \mathbf{u}_0 = \alpha_m \boldsymbol{\phi}_0 \boldsymbol{\phi}_0 \quad (10.67)$$

thus, recalling the magnetic field produced by a vertical probe inside a radial PPW and considering the ideal target distribution carried out in previous sections, highlighted in (10.65) and (10.61) respectively, by starting from (10.64) we can finally write

$$\begin{aligned} \angle \left\{ \left( -\frac{1}{2\rho} H_1^{(2)}(k_\rho \rho) e^{j\phi} \boldsymbol{\rho}_0 - j \frac{k_\rho}{2} H_1^{(2)'}(k_\rho \rho) e^{j\phi} \boldsymbol{\phi}_0 \right) \cdot \right. \\ \left. \alpha_m \boldsymbol{\phi}_0 \boldsymbol{\phi}_0 \cdot H^{inc} H_1^{(2)}(k_d \rho) \boldsymbol{\phi}_0 \right\} = \gamma \end{aligned} \quad (10.68)$$

exploiting relevant properties of the dyadic product, equation (10.68) can be simplified as follows

$$\angle \left\{ -j \frac{k_\rho}{2} H_1^{(2)'}(k_\rho \rho) e^{j\phi} \alpha_m H^{inc} H_1^{(2)}(k_d \rho) \right\} = \gamma. \quad (10.69)$$

considering that [123]

$$H_1^{(2)'}(k_\rho \rho) = \frac{1}{2} \left( H_0^{(2)}(k_\rho \rho) - H_2^{(2)}(k_\rho \rho) \right) \quad (10.70)$$

equation (10.68) becomes

$$\angle \left\{ -j \frac{k_\rho}{2} H_1'(k_\rho \rho) e^{j\phi} \alpha_m H^{inc} H_1^{(2)}(k_d \rho) \right\} = \gamma \quad (10.71)$$

thus, by exploiting the asymptotic large argument expansion of the Hankel function [123], reported in the following

$$H_p^{(2)}(x) \approx \sqrt{\frac{2}{\pi x}} e^{-j[x - p(\pi/2) - \pi/4]} \quad (10.72)$$

equation (10.69) results in a spiral slot arrangement, whose relation between radius and angle is governed by the simply equation

$$\rho = \frac{\cos t}{k_\rho - k_d} \phi \quad (10.73)$$

Therefore, as for any RLSA antenna design, the equations governing the slot length profile  $l(\rho)$  and the position of the slot pair centers have been defined. Specifically, the curve is defined by equation (10.73), where the slot centers are distributed uniformly. It is important to note that the sampling step  $\Delta s$  along the curve is arbitrary, and its value is a design parameter constrained between a minimum and a maximum value. This result is different with respect to those obtained in [140], where no azimuthal variation of the phase were considered and consequently the slots were arranged along concentric circumferences. To give a practical example, in Fig. 10.2 the holographic pattern for a linear and circular polarized RLSA antenna, obtained by modulating the incident field generated by the coaxial probe inside the radial waveguide with the desired aperture field having an azimuthal phase variation of order  $n = -1$ , has been presented. In both cases, the spiral arrangement of the slot constituting the RLSA profile are clearly visible. Theoretically the proposed layout is able to radiate a focused Bessel beam with an azimuthal phase variation, whose non-diffracting range is determined

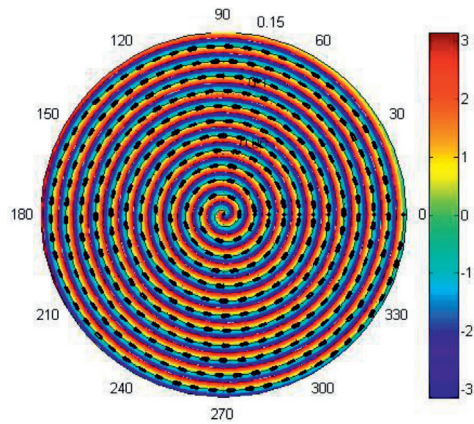


**Fig. 10.2.** Phase pattern of the holographic principle: the resulting spiral curve determines the particular slots arrangement. Copyright © 2017, IEEE.

by the size of the aperture. However, to maximize the efficiency of the antenna one has to make as bigger as possible the dimension of each slots: this results in a strong mutual coupling between adjacent slots. To contrast this phenomenon an iterative optimization procedure that suitably changes at each step the slot dimension and position must be accurately designed. In Fig. 10.3 a CAD model of a linear polarized RLSA

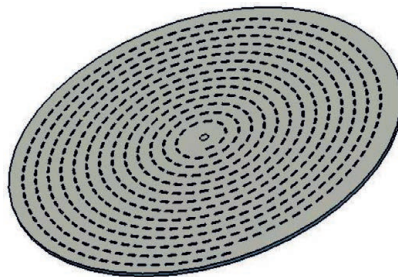


**Fig. 10.3.** Virtual prototype of a RLSA antenna, slots are arranged along an Archimedes spiral. Copyright © 2017, IEEE.

has been reported. Indeed, at the end of the optimization procedure the final slot layout has been designed on a commercial CAD tool to validate the result and optimize the feeding systems of the proposed antenna. As usual, it will be considered matched where the reflection coefficient at the input port is under -10 dB.

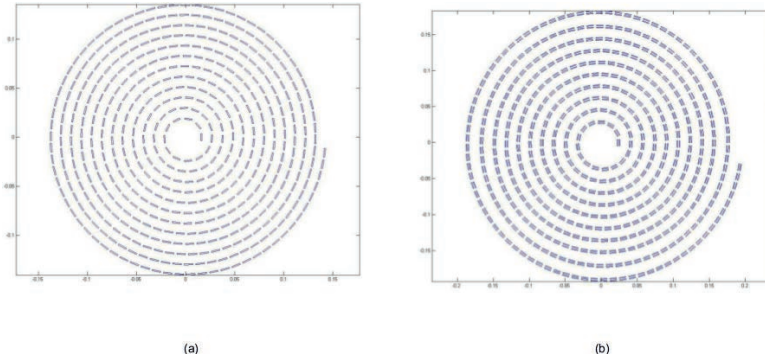


**Fig. 10.4.** Layout of the designed RLSA antenna: (a) configuration having a single slot along the spiral profile, (b) configuration for the double-slot profile.

### 10.7.1. Optimization procedure

The design of the optimization procedure follows the same steps outlined in [138] and [140]. As said, the derived aperture field distribution corresponds to an equivalent magnetic current distribution oriented along  $\phi_0$  that must be synthesized by using the slots of the RLSA antenna: each of them is equivalent to a magnetic dipole oriented along the slot length. In turn, the dipole moment is proportional to the feeding mode within the parallel-plate waveguide of the RLSA structure and is function of the position and size of the corresponding slot. The dielectric permittivity filling the guide is  $\epsilon_r = 1$ ; at the first step of the optimization procedure the slot have same length ( $l_i$ ) and are uniformly spaced. Their width remain constant throughout all the process. For each slot of the RLSA the equivalent magnetic dipole moment  $\mathbf{M}(\rho_i) = M(\rho_i)\phi_0$  is derived with an in-house MoM [149], [150]. Two different slots layouts have been considered, one made by a single slot sampling the spiral curve and another made by two slots shifted of a distance equal to  $\lambda/4$  from its center. This is of interest as the relevant scattering mechanism, occurring when the cylindrical wave propagating inside the radial waveguide impinges on the slots, can be exploited to suppress spurious radiation of unwanted higher-order modes [138]. In particular, if a double-slot configuration is exploited (see Figs. 10.4(a),(b), where a comparison between the involved configuration has been presented)  $\mathbf{M}_1(\mathbf{a}_i)$  and  $\mathbf{M}_2(\mathbf{a}_i)$  are the magnetic dipole moments of the inner and outer slot in the pair, respectively. Consequently,  $\mathbf{M}(\mathbf{a}_i) = \mathbf{M}_1(\mathbf{a}_i) + \mathbf{M}_2(\mathbf{a}_i)$  is dipole moment of the  $i$ -th slot pair of

center  $\mathbf{a}_i$ ; for each of them a complex fitness function  $F_i$  is introduced as follows

$$F_i = \frac{\boldsymbol{\phi}_0 \cdot \mathbf{M}(\mathbf{a}_i) \bar{A}}{A(\rho_i) \bar{M}} \quad (10.74)$$

where

$$\begin{aligned} \bar{A} &= \sum_{i=1}^{N_p} \frac{|A(\rho_i)|}{N_p} \\ \bar{M} &= \sum_{i=1}^{N_p} \frac{|\boldsymbol{\phi}_0 \cdot \mathbf{M}(\rho_i)|}{N_p} \end{aligned} \quad (10.75)$$

are the *target* and the *achieved* average copolar dipole moment amplitude, respectively, with  $N_p$  denoting the total number of slot pairs. It is important to note that  $\angle F_i$  and  $|F_i|$  indicate the phase and amplitude errors between the target and the actual dipole moment distribution, that have to be compensated by adjusting slot pair position and length. To make the solution more stable, one representative slot for a complete round of spiral is adjusted; this is possible thanks to an interpolation procedure of the spiral curve, further details can found in [138]. The RLSA layout is parameterized by defining the parameters  $P_n^{(s)}$  and  $L_n^{(s)}$ , hence at each step  $s$  of the optimization procedure a full-wave analysis of the entire antennas is performed and the equivalent magnetic dipole moments  $\mathbf{M}(\mathbf{a}_i)$  are calculated. Consequently, the values control parameters  $P_n^{(s)}$  and  $L_n^{(s)}$  are updated according to the following empirical formulas

$$\begin{aligned} P_n^{(s+1)} &= P_n^{(s)} - \chi_p \angle F_i / k_d \\ L_n^{(s+1)} &= [1 + \chi_l (1 - |F_i| \sqrt{\eta})] L_n^{(s)} \end{aligned} \quad (10.76)$$

where  $\eta$  is the antenna efficiency, that has to be considered in the optimization process to achieve slots large enough to radiate all the energy injected inside the radial waveguide, and  $\chi_{p,l}$  are two damping factors that can be suitable tuned to prevent oscillation and make more stable the optimization process. The first of equations (10.76) corrects the slot position minimize the local average phase error, whereas the second one corrects the slot length to minimizing the local amplitude error. The optimization loop is repeated until the efficiency is greater than a fixed threshold (typically  $\eta > 90\%$ ) and the average aperture distribution error

$$\varepsilon_\Delta = \frac{1}{N_p} \sum_{i=1}^{N_p} \left| \frac{\boldsymbol{\phi}_0 \cdot \mathbf{M}(\mathbf{a}_i)}{\bar{M}} - \frac{A(\rho_i)}{\bar{A}} \right| = \frac{1}{N_p} \sum_{i=1}^{N_p} \left| \frac{A(\rho_i)}{\bar{A}} \right| |F_i - 1| \quad (10.77)$$

is sufficiently small (e.g.,  $\epsilon_{\Delta} < 0.05$ ).

## 10.8. Numerical results

In this section some results achieved by optimizing an RLSA antenna made by a double-slots layout will be presented and discussed. The main features of the proposed antenna are synthesized in Table 10.1.

frequency	12.5 GHz
antenna diameter	300 mm
waveguide thickness	3.125 mm
slots number	1558
slots width	0.6 mm
slots length	8.8 – 11.3 mm

Tab. 10.1. Antenna's optimized parameters.

In Fig. 10.5 and 10.6 the 2D amplitude and phase distributions of the near-field focused beam achieved by means of the optimization procedure have been reported; the choice of the focused plane has been made by considering the criteria outlined in [151]. In particular Figs. 10.5(a) and 10.6(a) show a rather well-defined focused beam, having the typical 2D distribution of a Bessel beam [136, 140], whereas the expected azimuthal phase variation is visible in Figs. 10.5(b) and 10.6(b). In Figs. 10.7(a),(b) the amplitude and phase behavior of the fitness function defined by equation (10.74) have been presented. In particular, in Fig. 10.7(a) the phase distribution is significantly different from zero, but at the end of the optimization procedure, whose relevant plot is reported in Fig. 10.7(b), an average convergence has been obtained. This overall behavior is corroborated by the results reported in Fig. 10.8(a),(b) where a comparison between the target aperture field (solid blue line) and the dipole moments of each slot constituting the RLSA profile (black dots) is shown. It is clearly visible that the phase distribution is rather mismatched in the first plot and well superimposed at the end of the optimization procedure. On the contrary, the amplitude profile perform quite well from the begin: when the algorithm runs size and position of slots are gradually modified, thus efficiency increases and the mutual coupling among adjacent slots has to be neutralize. It is finally important to note that the near-field distribution presented in Figs. 10.5 and 10.6

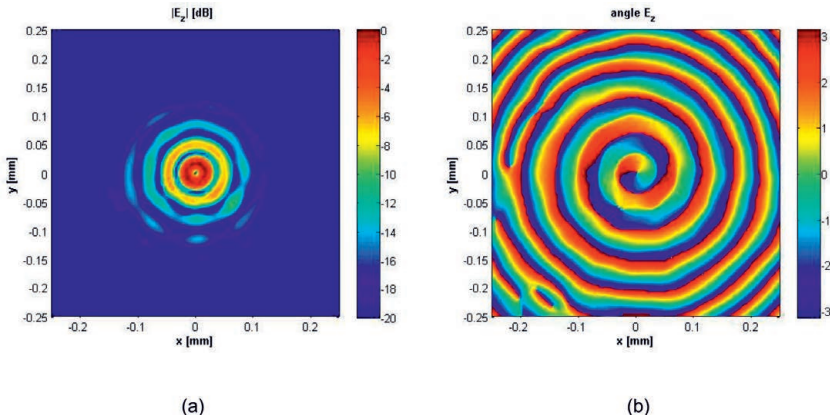


Fig. 10.5. 2D Normalized  $E_z$  components of the electric field in dB at the focusing plane (distance  $d = 35$  cm from the RLSA aperture) evaluated with the in-house MoM code. (a) Amplitude, (b) phase of the synthesized Bessel beam. Copyright © 2017, IEEE.

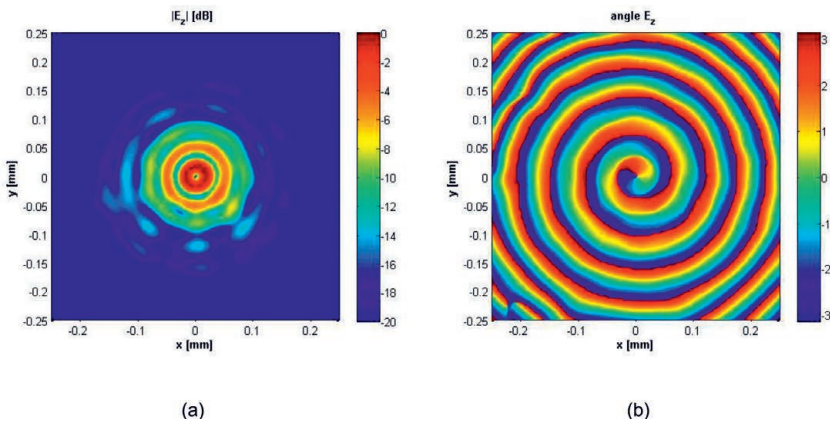
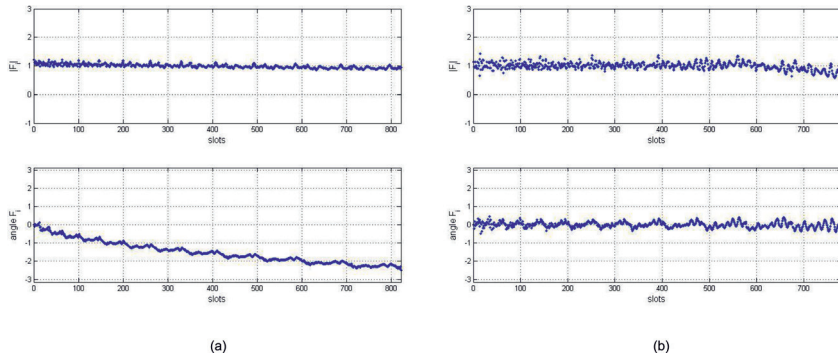
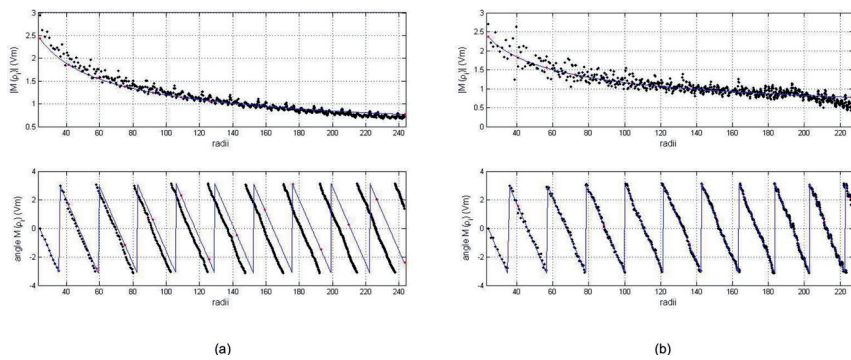


Fig. 10.6. As in Fig. 10.5 on the plane  $d = 45$  cm. Copyright © 2017, IEEE.



**Fig. 10.7.** Behavior of the amplitude and phase of the fitness function along the optimization process. (a) Initial step, (b) final step of the procedure.



**Fig. 10.8.** Evolution of amplitude (above) and phase (below) of the dipole moment of each slot pair during the optimization procedure. Black dots represent the value of the synthesized dipole moments, solid curve the wanted aperture field. (a) Initial design, (b) final design of the slots layout.

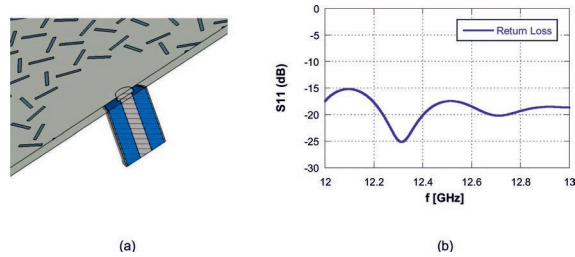


**Fig. 10.9.** (a) Virtual prototype of the optimized feeding system for the designed antenna, (b) Return loss for the realized prototype inside the operational bandwidth. Copyright © 2017, IEEE.

can be improved, most of all for what concerns the side-lobe level; it has been demonstrated, indeed, that due to the spiral slots arrangement in conjunction with the peculiar scattering mechanism generated when the cylindrical wave impinges on the slots etched on the metallic plane, a series of unwanted higher-order modes are excited. However, by operating a second-order optimization procedure, based on an ad-hoc fitness function, it could be theoretically possible to prevent the generation of this spurious radiation.

### 10.8.1. Feeding design

In order to validate the optimized prototype and to design the feeding system for the considered antenna, a full-wave implementation on a commercial CAD tool (CST microwave studio [56]) has been introduced. Due to the very large amount of slots, all with different size and position, an automatic design procedure was suitably developed. Specifically, an ad-hoc macro capable to read a 'txt' file and to automatically plot the slots layout constituting the upper plate of the RLSA antenna has been implemented. The designed feeding system is shown in Fig. 10.9(a), whilst the obtained return loss for the final prototype is highlighted in Fig. 10.9(b), showing an excellent impedance matching.

# List of Publications

## National Conferences

1. **D. Comite**, A. Galli, F. Soldovieri, G. Valerio, P. M. Barone, S. E. Lauro, E. Mattei, and E. Pettinelli, "Estimation of the geometrical features of buried objects from GPR Analysis," *Atti della XIX Riunione Nazionale di Elettromagnetismo (RiNEm)*, Rome, Italy, 10–14 Sep. 2012, 3 pp.
2. **D. Comite**, A. Galli, I. Catapano, and F. Soldovieri, "A numerical microwave tomographic algorithm to improve reconstruction of buried objects," *Atti della XX Riunione Nazionale di Elettromagnetismo (RiNEm)*, Padua, Italy, 15–18 Sep. 2014, 3 pp.

## International Conferences

3. G. Valerio, F. Soldovieri, P. M. Barone, S. E. Lauro, E. Mattei, E. Pettinelli, **D. Comite**, and A. Galli, "Shape reconstruction of scatterers by suitable inverse processing of GPR data," *Proc. European Conference on Antennas and Propagation (EuCAP)*, Prague, Czech Republic, 26–30 Mar. 2012, 3 pp.
4. F. Soldovieri, **D. Comite**, A. Galli, G. Valerio, P.M. Barone, S. E. Lauro, E. Mattei, and E. Pettinelli, "Retrieval of shape characteristics for buried objects with GPR monitoring," *Proc. European Geosciences Union General Assembly (EGU)*, Vienna, 22–27 Apr. 2012, Abstract, 1 p.
5. A. Galli, **D. Comite**, G. Valerio, P. M. Barone, S. E. Lauro, E. Mattei, E. Pettinelli, and G. Vannaroni, "Theoretical and experimental

- investigations on the performance of Ground Penetrating Radars in challenging operational condition," *Proc. European Microwave Week (EuMW)*, Amsterdam, Netherland, 28 Oct.–2 Nov. 2012, 4 pp.
6. A. Galli, **D. Comite**, G. Valerio, and E. Pettinelli, "Numerical study on the critical detection of subsurface dielectric scatterers with GPR system," *Proc. European Conference on Antennas and Propagation (EuCAP)*, Göteborg, Sweden, 8–12 Apr. 2013, 5 pp.
  7. P. Baccarelli, P. Burghignoli, **D. Comite**, D. Di Ruscio, and A. Galli, "Annular reconfigurable metasurface for omnidirectional Dual-Pol Leaky-Wave antennas," *Proc. European Conference on Antennas and Propagation (EuCAP)*, Göteborg, Sweden, 8–12 Apr. 2013, 2 pp.
  8. **D. Comite**, A. Galli, F. Soldovieri, I. Catapano, and E. Pettinelli, "Three-dimensional characterization of buried metallic targets via a tomographic algorithm applied to GPR synthetic data," *Proc. European Geosciences Union General Assembly (EGU) - Vienna, Austria* 8–12 Apr. 2013, Abstract, 1 p.
  9. C. Ferrara, **D. Comite**, P.M. Barone, S.E. Lauro, E. Mattei, G. Vanaroni, A. Galli, and E. Pettinelli, "An evaluation of the Early-Time GPR amplitude technique for electrical conductivity monitoring," *Proc. International Workshop on Advanced Ground Penetrating Radar (IWAGPR)*, Nantes, France, 2–5 Jul. 2013, 4 pp.
  10. G. Valerio, A. Galli, **D. Comite**, and E. Pettinelli, "Analysis on the GPR detection of dielectric scatterers in shallow subsurface," *IEEE International Symposium on Antennas and Propagation and USNC-URSI National Radio Science Meeting*, Orlando, Florida, U.S.A., 7–13 Jul. 2013, Abstract, 1 p.
  11. P. Baccarelli, P. Burghignoli, **D. Comite**, D. Di Ruscio, A. Galli, P. Lampariello, and D. R. Jackson, "Printed annular metasurface for omnidirectional Dual-Pol Leaky-Wave antenna," *Proc. European Microwave Week (EuMW)*, Nuremberg, Germany, 6–11 Oct. 2013, 4 pp.
  12. **D. Comite**, A. Galli, E. Pettinelli, and G. Valerio, "Numerical analysis of the detection performance of Ground Coupled Radars for

- different antenna systems and signal feature," *Proc. European Conference on Antennas and Propagation (EuCAP)*, The Hague, Netherlands, 6–11 Apr. 2014, 3 pp.
13. **D. Comite**, A. Galli, C. Ferrara, and E. Pettinelli, "Relations between GPR Early-Time signal attributes and ground permittivity: A numerical investigation," *Proc. European Conference on Antennas and Propagation (EuCAP)*, The Hague, Netherlands, 6–11 Apr. 2014, 3 pp.
  14. A. Galli, **D. Comite**, I. Catapano, and F. Soldovieri, "Implementation of a synthetic imaging technique for GPR non-destructive testing," *Proc. European Geosciences Union General Assembly (EGU)*, Vienna, 27 Apr.–2 May 2014, Abstract, 1 p.
  15. **D. Comite**, A. Galli, C. Ferrara, S.E. Lauro, E. Mattei, G. Vannaroni, and E. Pettinelli, "Numerical and experimental surveys on the GPR Early-Time signal features for the evaluation of shallow-soil permittivity," *Proc. 15th Ground Penetrating Radar Conference (GPR)*, Brussels, Belgium, 30 Jun.–4 Jul. 2014, 5 pp.
  16. **D. Comite**, A. Galli, I. Catapano, and F. Soldovieri, "An improved tomographic approach for accurate target reconstruction from GPR numerical data," *Proc. 15th Ground Penetrating Radar Conference (GPR)*, Brussels, Belgium, 30 Jun.–4 Jul. 2014, 5 pp.
  17. **D. Comite**, I. Catapano, A. Galli, and F. Soldovieri, "A customized numerical procedure for accurate target reconstruction through GPR Survey," *Proc. European Microwave Week (EuMW)*, Rome, Italy, 5–10 Oct. 2014, 4 pp.
  18. **D. Comite**, A. Galli, S. E. Lauro, E. Mattei, and E. Pettinelli, "GPR Early-Time signal features for the evaluation of Shallow-Soil Permittivity," *Proc. European Conference on Antennas and Propagation (EuCAP)*, Lisbon, Portugal, 12–17 Apr. 2015, 2 pp., accepted for presentation.
  19. **D. Comite**, P. Baccarelli, P. Burghignoli, D. Di Ruscio, and A. Galli, "Modal analysis of planar structures loaded with wire-medium slabs using a transmission-line approach," *Proc. European Conference on Antennas and Propagation (EuCAP)*, Lisbon, Portugal, 12–17 Apr. 2015, 2 pp., accepted for presentation.

20. **D. Comite**, A. Galli, I. Catapano, and F. Soldovieri, "An advanced numerical imaging procedure accounting for non-ideal effects in the simulated scenario," *Proc. European Geosciences Union General Assembly (EGU)*, Vienna, 12–17 Apr. 2015, Abstract, 1 p., accepted for presentation.
21. **D. Comite**, A. Galli, S. E. Lauro, E. Mattei, and E. Pettinelli, "A numerical evaluation of the Early-Time GPR amplitude technique for permittivity and conductive estimation," *Proc. International Workshop on Advance Ground Penetrating Radar (IWAGPR)*, Florence, Italy, 7–10 Jul. 2015, 2 pp., under review.
22. **D. Comite**, A. Galli, I. Catapano, and F. Soldovieri, "An advanced imaging procedure for shallow GPR surveys," *Proc. International Workshop on Advance Ground Penetrating Radar (IWAGPR)*, Florence, Italy, 7–10 Jul. 2015, 2 pp., under review.
23. **D. Comite**, A. Galli, I. Catapano, F. Soldovieri, and E. Pettinelli, "Implementation of an advanced tomographic algorithm for GPR realistic sounding," *Proc. International Symposium on Antennas and Propagation and USNC-URSI Radio Science Meeting*, Vancouver, Canada, 19–25 Jul. 2015, 2 pp., under review.
24. **D. Comite**, P. Burghignoli, P. Baccarelli, and A. Galli, "Wideband Leaky-Wave radiation from wire-medium loaded Fabry Perot cavity antennas," *Proc. International Symposium on Antennas and Propagation and USNC-URSI Radio Science Meeting*, Vancouver, Canada, 19–25 Jul. 2015, 2 pp., under review.
25. M. T. Falconi, **D. Comite**, A. Galli, P. Lombardo, and F. S. Marzano, "Forward scatter radar modeling: Effects of near field for canonical targets," *Proc. International Symposium on Antennas and Propagation and USNC-URSI Radio Science Meeting*, Vancouver, Canada, 19–25 Jul. 2015, 2 pp., under review.
26. **D. Comite**, P. Burghignoli, P. Baccarelli, and A. Galli, "Wire-medium loaded planar structures: A novel transmission-line model and relevant dispersion properties," *Proc. European Microwave Week (EuMW)*, Paris, France, 6–11 Sep. 2015, 4 pp., under review.
27. M. T. Falconi, **D. Comite**, F. S. Marzano, A. Galli, and P. Lombardo, "Analysis of canonical targets in near field for forward scat-

ter radar applications," *Proc. European Microwave Week (EuMW)*, Paris, France, 6–11 Sep. 2015, 4 pp., under review.

### Journal papers

28. S. E. Lauro, E. Mattei, P. M. Barone, E. Pettinelli, G. Valerio, G. Vannaroni, **D. Comite**, and A. Galli, "Estimation of subsurface dielectric target depth for GPR planetary exploration: Laboratory measurements and modeling," *Journal of Applied Geophysics*, vol. 93, pp. 93–100, Jul. 2013.
29. F. Soldovieri, I. Catapano, P. M. Barone, S. E. Lauro, E. Mattei, E. Pettinelli, G. Valerio, **D. Comite**, and A. Galli, "GPR estimation of the geometrical features of buried metallic targets in testing conditions," *Progress in Electromagnetics Research B*, vol. 49, pp. 339–362, 2013.
30. A. Galli, **D. Comite**, I. Catapano, G. Gennarelli, F. Soldovieri, and E. Pettinelli, "3D imaging of buried dielectric targets with a tomographic microwave approach applied to GPR synthetic data," *International Journal on Antennas and Propagation*, vol. 2013, 11 pp., Jul. 2013.
31. D. Di Ruscio, P. Burghignoli, P. Baccarelli, **D. Comite**, and A. Galli, "Spectral method of moments for planar structures with azimuthal symmetry," *IEEE Transaction on Antennas and Propagation*, vol. 62, no. 4, pp. 2317–2322, Apr. 2014.
32. **D. Comite**, A. Galli, S. E. Lauro, E. Mattei, and E. Pettinelli, "Analysis of GPR early-time signal features for the evaluation of soil permittivity through numerical and experimental surveys," *IEEE Journal of Selected Topics in Applied Earth Observations and Remote Sensing*, vol. 9, no. 1, pp. 178–187, Oct. 2017.
33. **D. Comite**, P. Baccarelli, P. Burghignoli, D. Di Ruscio, and A. Galli, "Equivalent-network analysis of propagation and radiation features in wire-medium loaded planar structures," *IEEE Transaction on Antennas and Propagation*, vol. 63, no. 12, pp. 5573–5585, Dec. 2015.
34. **D. Comite**, I. Catapano, A. Galli, and F. Soldovieri, "The Role of the antenna radiation pattern in the performance of a microwave

tomographic approach for GPR imaging," *IEEE Journal of Selected Topics in Applied Earth Observations and Remote Sensing*, vol. 10, no. 10, pp. 4337-4347, Dec. 2017.

# Bibliography

- [1] W. C. Chew, "Waves and fields in inhomogeneous media," *Wiley-IEEE Press*, 1999.
- [2] L. Felsen and N. Marcuvitz, "Radiation and scattering of waves," *IEEE Press*, New York, NY, 1994.
- [3] A. Sommerfeld, "Partial differential equations in physics," New York: Academic, 1949.
- [4] T. Tamir and A. A. Oliner, "The spectrum of electromagnetic waves guided by a plasma layer," *Proc. IEEE*, vol.51, no.2, pp.317–332, Feb. 1963.
- [5] T. Tamir and A. A. Oliner, "Guided complex waves. Part I: Fields at an interface. Part II: Relation to radiation patterns," *Proc. IEE*, vol. 110, no. 2, pp. 310–334, 1963.
- [6] N. Marcuvitz, "On field representation in terms of leaky modes or eigenmodes," *IRE Transaction on Antennas and Propagation*, vol. 4, pp. 192–194, 1951.
- [7] J. Zenneck, "Propagation of plane EM waves along a plane conducting surface," *Annals of Physics*, vol. 28, pp. 846–866, 1907.
- [8] A. N. Sommerfeld, "Propagation of waves in wireless telegraphy," *Annals of Physics*, vol. 28, pp. 665–737, 1909.
- [9] K. A. Norton, "The propagation of radio waves over the surface of the earth and in the upper atmosphere. Part I," *Proc. IRE*, vol. 24, no. 10, pp. 1367–1387, Oct. 1936.

- [10] K. A. Norton, "The physical reality of space and surface waves in the radiation field of radio antennas. Part I," *Proc. IRE*, vol. 25, no. 9, pp. 1192–1202, Sep. 1937.
- [11] K. A. Norton, "The propagation of radio waves over the surface of the earth and in the upper atmosphere. Part II," *Proc. IRE*, vol. 25, no. 9, pp. 1203–1236, Sep. 1937.
- [12] J. R. Wait, "Radiation from a vertical electric dipole over a stratified ground," *IRE Transaction on Antennas and Propagation*, vol. 1, no. 1, pp. 9–11, Jul. 1953.
- [13] J. R. Wait, "Excitation of surface waves on conducting, stratified, dielectric-clad, and corrugated surfaces," *Journal of Research of the National Bureau of Standards*, vol. 59, no. 6, pp. 365–377, Dic. 1957.
- [14] J. R. Wait, "Electromagnetic surface waves," *Advances in Radio Research*, J. A. Saxton, Ed. New York: Academic, vol. 1, pp. 157–217, 1964.
- [15] A. Banos, "Dipole radiation in the presence of a conducting half-space," New York: Pergamon, 1966.
- [16] R. J. King, "Electromagnetic wave propagation over a constant impedance plane," *Radio Science*, vol. 4, no. 3, pp. 255–268, Mar. 1969.
- [17] J. R. Wait, "The ancient and modern history of EM ground-wave propagation," *IEEE Antennas and Propagation Magazine*, vol. 40, no. 5, pp. 7–24, Oct. 1998.
- [18] R. E. Collin, "Hertzian dipole radiating over a lossy earth or sea: Some early and late 20th-century controversies," *IEEE Antennas Propagation and Magazine*, vol. 46, no. 2, pp. 64–79, Apr. 2004.
- [19] R. M. Sorbello, et al., "The horizontal-wire antenna over a dissipative half-space: generalized formula and measurements," *IEEE Transaction on Antennas and Propagation*, vol. 25, no. 6, pp. 850–854, Nov. 1977.
- [20] G. S. Smith, "Directive properties of antennas for transmission into a material half-space," *IEEE Transaction on Antennas and Propagation*, vol. 32, no. 3, pp. 232–246, Mar. 1984.

- [21] A. P. Annan, "Radio interferometry depth sounding: Part I - Theoretical discussion," *Geophysics*, vol. 38, no. 3, pp. 557–580, Jun. 1973.
- [22] J. R. Rossiter, G. A. Latorraca, A. P. Annan, D. W. Strangway, and G. Simmons, "Radio interferometry depth sounding: Part II - Experimental results," *Geophysics*, vol. 38, no. 3, pp. 581–599, Jun. 1973.
- [23] S. A. Arcone, "Numerical studies of the radiation patterns of resistively loaded dipoles," *Journal of Applied Geophysics*, vol. 33, pp. 39–53, 1995.
- [24] S. A. Arcone, "Spatial attenuation rates of interfacial waves: Field and numerical tests of Sommerfeld theory using ground-penetrating radar pulses," *Journal of Applied Geophysics*, vol. 81, pp.122–129, 2012.
- [25] S. J. Radzevicius, J. J. Daniels, and C. C. Chen, "GPR H-plane antenna patterns for a horizontal dipole on a halfspace," *Proc. of Eighth International Conference on Ground Penetrating Radar*, Apr. 2000.
- [26] E. Slob and J. Fokkema, "Interfacial dipoles and radiated energy," *Subsurface Sensing Technologies and Applications*, vol. 3, pp. 347–367, Oct. 2002.
- [27] E. Slob and J. Fokkema, "Coupling effects of two electric dipoles on an interface," *Radio Science*, vol. 37, pp. 6-1–6-10, 2002.
- [28] B. Lampe and K. Hollinger, "Resistively loaded antennas for ground-penetrating radar: A modeling approach," *Geophysics*, vol. 70, no. 3, pp. k23–k32, Jun. 2005.
- [29] S. Lambot, F. André, E. Slob, and H. Veerecken, "Effect of antenna-medium coupling in the analysis of ground-penetrating radar data," *Near Surface Geophysics*, vol. 10, pp. 631–639, 2012.
- [30] D. A. Hill, "The transient fields of a Hertzian dipole in the presence of a dielectric half-space," *Radio Science*, vol. 6, no. 8-9, pp. 787–794, Aug. 1971.

- [31] K. I. Nikoskinen and I. V. Lindell, "Time-Domain analysis of the sommerfeld VMD problem based on the exact image theory," *IEEE Transaction on Antennas and Propagation*, vol. 38, no. 2, pp. 241–250, Feb. 1990.
- [32] K. I. Nikoskinen, "Time-Domain analysis of horizontal dipoles in front of planar dielectric interface," *IEEE Transaction on Antennas and Propagation*, vol. 38, no. 12, pp. 1951–1957, Dic. 1990.
- [33] S. J. Radzevicius, C. C. Chen, L. Peters Jr., J. J. Daniels, "Near-field dipole radiation dynamics through FDTD modeling," *Journal of Applied Geophysics*, vol. 52, pp. 75–91, 2003.
- [34] A. J. Ishimaru, "Electromagnetic wave propagation, radiation and scattering," *Prentice Hall*, 1991.
- [35] D. G. Dudley, "Mathematical foundation for electromagnetic theory," *IEEE Press*, New York, NY, 1994.
- [36] N. Engheta, C. H. Papas, and C. Elachi, "Interface extinction and subsurface peaking of the radiation pattern of a line source," *Applied Physics B*, vol. 26, pp. 231–238, Aug. 1981.
- [37] R. F. Harrington, "Time-Harmonic electromagnetic field," *IEEE Press*, New York, NY, 2001.
- [38] N. Engheta, C. H. Papas, and C. Elachi, "Radiation patterns of interfacial dipole antennas," *Radio Science*, vol. 17, pp. 1557–1556, Jun. 1982.
- [39] C. A. Balanis, "Antenna Theory: Analysis and Design," *John Wiley & Sons Inc*, 3th Edition, 2005.
- [40] G. Picardi et al., "The Mars advanced radar for subsurface and ionosphere sounding (MARSIS): concept and performance," *Geoscience and Remote Sensing Symposium, IGARSS'99 Proc.*, vol. 5, pp. 2674–2677, 1999.
- [41] R. Seu et al., "SHARAD sounding radar on the Mars Reconnaissance Orbiter," *Journal of Geophysical Research: Planets*, pp. (1991–2012), 112(E5), 2007.
- [42] D. J. Daniels, "Ground Penetrating Radar," *The Institution of Electrical Engineers*, London, UK, 2004.

- [43] H. M. Jol, "Ground Penetrating Radar: Theory and applications," *Elseviers*, London, UK, 2009.
- [44] J. Kim, T. Yoon, J. Kim, and J. Choi, "Design of an ultra wide-band printed monopole antenna using FDTD and genetic algorithm," *IEEE Microwave Components Letters*, vol. 15, no. 6, pp.395–397 Jun. 2005.
- [45] T. T. Wu, and R. W. P.King, "The cylindrical antenna with non-reflecting resistive loading," *IEEE Transaction on Antennas and Propagation*, vol. 13, no. 3, pp.369–373, May 1965.
- [46] V. Ciarletti, C. Corbel, D. Plettemeier, P. Cais, S. M. Clifford, and S. E. Hamran, "WISDOM GPR Designed for Shallow and High-Resolution Sounding of the Martian Subsurface," *Proc. of IEEE*, vol. 99, no. 5, pp.825–836, May 2011.
- [47] S. E. Hamran, T. Berger, L. Hanssen, M. J. Oyan, V. Ciarletti, C. Corbel, and D. Plettemeier, "A prototype for the WISDOM GPR on the ExoMars mission," *Proc. of International Workshop on Advanced Ground Penetrating Radar*, pp. 252–255, Jun. 2007.
- [48] D. Plettemeier, V. Ciarletti, S. E. Hamran, C. Corbel, P. Cais, W. F. Benedix, K. Walf, S. Linke, and S. Roddecke, "Full Polarimetric GPR Antenna System Aboard the ExoMars Rover," *Proc. of IEEE Radar Conference*, pp. 1–6, May 2009.
- [49] P. J. Gibson, "The Vivaldi Aerial," *Proc. of the 9<sup>th</sup> European Microwave Conference*, Brighton, U.K., pp. 101–105, May 1979.
- [50] *PulseEkko Pro User Guide*. Sensors and Software Inc., Canada, 2006.
- [51] D. A. Robinson and S. P. Friedman, "The effective permittivity of dense packing of glass beads, quartz sand and their mixtures immersed in different dielectric backgrounds," *J. Non-Crystalline Solids*, vol. 305, no. 1–3, 261–267, Jul. 2002.
- [52] G. C. Topp, J. L. Davis, and A. P. Annan, "Electromagnetic determination of soil water content: Measurements in coaxial transmission lines," *Water Resources Res.*, vol. 16, 574–582, Mar. 1980.
- [53] E. Pettinelli, A. Cereti, A. Galli, and F. Bella, "Time domain reflectometry: Calibration techniques for accurate measurement of

- dielectric properties of various materials," *Review of Scientific Instruments*, vol. 73, pp. 3553–3562, 2002.
- [54] E. Mattei, A. De Santis, A. Di Matteo, E. Pettinelli, and G. Vannaroni, "Time-domain reflectometry of glass beads/magnetite mixtures: A time and frequency domain study," *Applied Physics Letters*, vol. 86, no. 22, 224102–3, May 2005.
- [55] J. R. Taylor, "An introduction to error analysis: the study of uncertainties in physical measurements," University Science Books, 1997.
- [56] CST, *CST Microwave Studio Manual*, Germany, www.cst.com.
- [57] A.P. Annan, "Ground Penetrating Radar: Principles, procedures and applications," *Sensors and Software Inc.*, Missisauga, Canada, 2004.
- [58] L. W. Galagedara, G. W. Parkin, J. D. Redman, P. von Bertoldi, and A. L. Endres, "Field studies of the GPR ground wave method for estimating soil water content during irrigation and drainage," *Journal of Hydrology*, vol. 301, no. 1–4, pp. 182–197, Jan. 2005.
- [59] J. A. Huisman et al., "Measuring soil water content with ground penetrating radar: a review," *Vadose Zone Journal*, vol. 2, pp 476–491, Nov. 2003.
- [60] S. Laurens et al., "Influence of concrete relative humidity on the amplitude of Ground-Penetrating Radar (GPR) signal," *Materials and Structures*, vol. 35, pp. 198–203, 2002.
- [61] Z. M. Sbartai et al., "Ability of the direct wave of radar ground-coupled antenna for NDT of concrete structures," *NDT & E International*, vol. 39, pp. 400–407, 2006.
- [62] J. A. Huisman et al., "Monitoring temporal development of spatial soil water content variation: comparison of ground penetrating radar and time domain reflectometry," *Vadose Zone Journal*, vol. 2, pp 519–529, Nov. 2003.
- [63] E. Pettinelli et al., "Correlation between near-surface electromagnetic soil parameters and early-time GPR signals: an experimental study," *Geophysics*, vol. 72, no. 2, pp. A25–A28, Mar-Apr. 2007.

- [64] E. Pettinelli et al., "A controlled experiment to investigate the correlation between early-time signal attributes of ground-coupled radar and soil dielectric properties," *Journal of Applied Geophysics*, vol. 101, pp. 68–76, 2014.
- [65] A. Di Matteo, E. Pettinelli, and E. C. Slob, "Early-time GPR signal attributes to estimate soil dielectric permittivity: a theoretical study," *IEEE Transaction on Geoscience and Remote Sensing*, vol. 51, no. 3, pp 1643–1654, Mar. 2013.
- [66] A. V. Oppenheim and R. W. Schaffer, "Discrete-time signal processing," *Prentice-Hall*, Jan. 1999.
- [67] C. Ferrara et al., "Comparison of GPR and Unilateral NMR for water content measurements in a laboratory scale experiment," *Near Surface Geophysics*, vol. 11, no. 2, pp. 143–153, Apr. 2013.
- [68] C. E. Baumann and E. E. S. Sampaio., "Electric field of a horizontal antenna above a homogeneous half-space: Implications for GPR," *Geophysics*, vol. 65, no. 3, pp. 823–835, Jun. 2000.
- [69] A. J. Devaney, "Principles of computerized tomographic imaging," *Society for Industrial and Applied Mathematics*, 2001.
- [70] A. J. Devaney, "Geophysical diffraction tomography," *IEEE Transaction on Geoscience and Remote Sensing*, vol. 22, pp. 3–13, Jan. 1984.
- [71] C. Maierhofer and S. Leipold, "Radar investigation of masonry structure," *NDT E Int* , vol. 34, pp. 139–147, 2001.
- [72] J. Hugenschmidt, "Concrete bridge inspection with a mobile GPR system," *Construction and Building Materials*, vol. 16, pp. 147–154, 2002.
- [73] E. L. Miller, M. Kilmer, and C. Rappaport, "A New shape-based method for object localization and characterization from scattered field data," *IEEE Transaction on Geoscience and Remote Sensing*, vol. 38, pp. 1682–1696, Jul. 2000.
- [74] P. M. van den Berg and A. Abubakar, "Linear and nonlinear inversion of GPR data," *2nd International Workshop on advanced Ground Penetrating Radar* , pp. 156–163, Delft, The Netherlands, 2003.

- [75] J. C. Bolomey, "Recent European developments in active microwave imaging for industrial, scientist and medical applications," *IEEE Transaction on Microwave Theory and Technique*, vol. 37, pp. 2109–2117, Dec. 1989.
- [76] M. Bertero and P. Boccacci, "Introduction to inverse problems in imaging," *Institute of Physics Publishing*, London, UK, 1998.
- [77] L. Crocco and T. Isernia, "Inverse scattering with real data: detecting and imaging homogeneous dielectric objects," *Inverse Problems*, vol. 17, pp. 1573–1583, 2001.
- [78] E. Pettinelli, A. Di Matteo, E. Mattei, L. Crocco, F. Soldovieri, J. D. Redman, and A. P. Annan, "GPR response from buried pipes: measurement on field site and tomographic reconstructions," *IEEE Transaction on Geoscience and Remote Sensing*, vol. 47, no. 8, pp. 2639–2645, Aug. 2009.
- [79] M. Pastorino, "Microwave imaging," *John Wiley & Sons Inc*, 1th Edition, 2010.
- [80] R. Persico, "Ground Penetrating Radar: Inverse scattering and data processing," *John Wiley & Sons Inc*, 1st Edition, 2014.
- [81] L. Chommeloux, C. Pichot, and J. C. Bolomey, "Electromagnetic modeling for microwave imaging of cylindrical buried inhomogeneities," *IEEE Transaction on Microwave Theory and Technique*, vol. 34, no. 10, pp. 1064–1076, Oct. 1986.
- [82] T. B. Hansen and P. M. Johansen, "Inversion scheme for ground penetrating radar that takes into account the planar air–soil interface," *IEEE Transaction on Geoscience and Remote Sensing*, vol. 38, no. 1, pp. 496–506, Jan. 2000.
- [83] G. Leone and F. Soldovieri, "Analysis of the distorted Born approximation for subsurface reconstruction: Truncation and uncertainties effects," *IEEE Transaction on Geoscience and Remote Sensing*, vol. 41, no. 1, pp. 66–74, Jan. 2003.
- [84] F. Soldovieri and R. Persico, "Reconstruction of an embedded slab from multifrequency scattered field data under the distorted Born approximation," *IEEE Transaction on Antennas and Propagation*, vol. 52, no. 9, pp. 2348–2356, Sep. 2004.

- [85] F. Cakoni and D. Colton, "Qualitative methods in inverse scattering theory," *Springer-Verlag*, Berlin, Germany, 2006.
- [86] A. N. Tikhonov and V. Y. Arsenin, "Solution of ill-posed problems," *Winston and Wiley*, Washington, DC, USA, 1977.
- [87] D. Colton and R. Kress "Inverse acoustic and electromagnetic scattering theory," *Springer*, 3th Edition, 2013.
- [88] M. Born and E. Wolf, "Principles of optics," *Cambridge University*, 7th Edition, 1999.
- [89] M. Slaney, A. C. Kak, and L. E. Larsen, "Limitations of imaging with first-order diffraction tomography," *IEEE Transaction on Microwave Theory and Technique*, vol. 32, no. 8, pp. 860–874, Aug. 1984.
- [90] M. Idemem and I. Ackduman, "Two dimensional inverse scattering problem connected with bodies buried in a slab," *Inverse Problem*, vol. 6, pp. 749–766, 1990.
- [91] P. Meincke, "Linear GPR inversion for lossy soil and a planar air–soil interface," *IEEE Transaction on Geoscience and Remote Sensing*, vol. 39, no. 12, pp. 2713–2721, Dic. 2001.
- [92] I. Catapano, L. Crocco, R. Persico, M. Pieraccini, and F. Soldovieri, "Linear and non-linear microwave tomography approaches for subsurface prospecting: Validation on real data," *IEEE Antennas and Wireless Propagation Letters*, vol. 5, pp. 49–53, 2006.
- [93] F. Soldovieri, J. Hugenschmidt, R. Persico, and G. Leone, "A linear inverse scattering algorithm for realistic GPR applications," *Near Surface Geophysics*, vol. 5, no. 1, pp. 29–42, Feb. 2007.
- [94] F. Pierri, A. Liseno, and F. Soldovieri, "Shape reconstruction from PO multifrequency scattered fields via the singular value decomposition approach," *IEEE Transaction on Antennas and Propagation*, vol. 49, no. 9, pp. 1333–1343, Sep. 2001.
- [95] F. Soldovieri, A. Brancaccio, G. Prisco, G. Leone, and F. Pierri, "A Kirchhoff-based shape reconstruction algorithm for the multi-monostatic configuration: The realistic case of buried pipe," *IEEE Transaction on Antennas and Propagation*, vol. 46, no. 10, pp. 3031–3038, Oct. 2008.

- [96] R. Solimene, A. Buonanno, F. Soldovieri, and R. Pierri, "Physical optics imaging of 3D PEC objects: Vector and multipolarized approaches," *IEEE Transaction on Geoscience and Remote Sensing*, vol. 48, no. 4, 1799–1808, Apr. 2010.
- [97] I. Catapano, A. Affinito, G. Gennarelli, F. Di Maio, A. Loperte, and F. Soldovieri, "Full three-dimensional imaging via ground penetrating radar: assessment in controlled conditions and on field for archaeological prospecting," *Applied Physics A*, vol. 115, no. 4, 1415–1422, Nov. 2013.
- [98] R. F. Harrington, *Field Computation by Moment Methods*, *IEEE Press*, 1993.
- [99] R. E Arvidson et al., "Overview of the Spirit Mars exploration rover mission to Gusev Crater: landing site to Backstay rock in the Columbia Hills," *Journal of Geophysical Research*, vol. 111, 22 pp., 2006.
- [100] S. W Squyres et al., "Overview of the opportunity Mars exploration rover mission to Meridiani Planum: Eagle Crater to Purgatory Ripple," *Journal of Geophysical Research*, vol. 111, 19 pp., 2006.
- [101] G. von Trentini, "Partially reflecting sheet array," *IRE Transaction on Antennas and Propagation*, vol. 4, pp. 666–671, Oct. 1956.
- [102] D. Di Ruscio, "Studio di metasuperfici a simmetria azimutale e di plasmoni artificiali in guida d'onda," PhD Thesis, Rome, Italy, Feb. 2015.
- [103] M. G. Silveirinha, "Additional boundary condition for the wire medium," *IEEE Transaction on Antennas and Propagation*, vol. 54, no. 6, pp. 1766–1780, Jun. 2006.
- [104] A. B. Yakovlev, M. G. Silveirinha, O. Luukkonen, C. R. Simovski, I. S. Nefedov, and S. A. Tretyakov, "Characterization of surface-wave and leaky-wave propagation on wire-medium slabs and mushroom structures based on local and nonlocal homogenization models," *IEEE Transaction on Microwave Theory and Technique*, vol. 77, no. 11, pp. 2700–2714, Nov. 2009.
- [105] P. A. Belov, R. Marqués, S. I. Maslovski, M. Silveirinha, C. R. Simovski, and S. A. Tretyakov, "Strong spatial dispersion

- in wire media in the very large wavelength limit," *Physical Review B*, vol. 67, pp. 113103-1–113103-4, 2003.
- [106] P. Baccarelli, P. Burghignoli, D. Comite, D. Di Ruscio, A. Galli, P. Lampariello, and D. R. Jackson, "Annular reconfigurable metasurface for omnidirectional dual-pol leaky-wave antennas," *Proc. 7th European Conference Antennas and Propagation (EuCAP)*, Gothenburg, Sweden, 2 pp., 8–11 Apr. 2013.
- [107] P. A. Belov, C. R. Simovski, and P. Ikonen, "Canalization of sub-wavelength images by electromagnetic crystals," *Physical Review B*, vol. 71, 193105, 2005.
- [108] A. Ono, J. Kato, and S. Kawata, "Subwavelength optical imaging through a metallic nanorod array," *Physical Review Letters*, vol. 95, 267407, 2005.
- [109] I. S. Nefedov and A. J. Viitanen, "Guided waves in uniaxial wire medium slab," *Progress In Electromagnetic Research*, vol. 51, pp. 167–185, 2005.
- [110] P. Burghignoli, G. Lovat, F. Capolino, D. R. Jackson, and D. R. Wilton, "Modal propagation and excitation on a wire-medium slab," *IEEE Transaction on Microwave Theory and Technique*, vol. 56, no. 5, pp. 1112–1124, May 2008.
- [111] P. Burghignoli, G. Lovat, F. Capolino, D. R. Jackson, and D. R. Wilton, "Directive leaky-wave radiation from a dipole source in a wire-medium slab," *IEEE Transaction on Antennas and Propagation*, vol. 56, no. 5, pp. 1329–1339, May 2008.
- [112] M. G. Silveirinha, C. A. Fernandes, and J. R. Costa, "Additional boundary condition for a wire medium connected to a metallic surface," *New Journal of Physics*, vol. 10, 053011, 2008.
- [113] Y. Li, A. Alú, and H. Ling, "Investigation of leaky-wave propagation and radiation in a metal cut-wire array," *IEEE Transaction on Antennas and Propagation*, vol. 60, no. 3, pp. 1630–1634, Mar. 2012.
- [114] M. Silveirinha and S. I. Maslovski, "Radiation from elementary sources in a uniaxial wire medium," *Physical Review B*, vol. 85, pp. 155125-1–155125-10, 2012.

- [115] M. G. Silveirinha and S. I. Maslovski, "Radiation from a Hertzian dipole embedded in a wire-medium slab," *IEEE Antennas and Wireless Propagation Letters*, vol. 12, pp. 401–404, 2013.
- [116] P. A. Belov, R. Marqués, S. I. Maslovski, M. Silveirinha, C. R. Simovski, and S. A. Tretyakov, "Strong spatial dispersion in wire media in the very large wavelength limit," *Physical Review B*, vol. 67, pp. 113103-1–113103-4, 2003.
- [117] T. Tamir and A. A. Oliner, "Guided complex waves. Part 1: Fields at an interface," *IEE Proc.*, vol. 110, no. 2, pp. 310–324, Feb. 1963.
- [118] T. Tamir and A. A. Oliner, "Guided complex waves. Part 2: Relation to radiation patterns," *IEE Proc.*, vol. 110, no. 2, pp. 325–334, Feb. 1963.
- [119] O. Luukkonen, C. Simovski, G. Granet, G. Goussetis, D. Lioubtchenko, A. V. Räisänen, and S. A. Tretyakov, "Simple and accurate analytical model of planar grids and high-impedance surfaces comprising metal strips or patches," *IEEE Transaction on Antennas and Propagation*, vol. 56, no. 6, pp. 1624–1632, Jun. 2008.
- [120] P. Lampariello, F. Frezza, and A. A. Oliner, "The transition region between bound-wave and leaky-wave ranges for a partially dielectric loaded open guiding structure," *IEEE Transaction on Microwave Theory and Technique*, vol. 38, pp. 1831–1836, Dec. 1990.
- [121] D. R. Jackson and N. G. Alexópoulos, "Gain enhancement methods for printed circuit antennas," *IEEE Transaction on Antennas and Propagation*, vol. AP-33, pp. 976–987, Sep. 1985.
- [122] D. M. Pozar, "Microwave Engineering," *John Wiley & Sons Inc*, 4th Edition, 2011.
- [123] C. A. Balanis, "Advance engineering electromagnetics," *John Wiley & Sons Inc*, 1st Ed., 1989.
- [124] G. Valerio, S. Paulotto, P. Baccarelli, P. Burghignoli, and A. Galli, "Accurate Bloch analysis of 1-D periodic lines through the simulation of truncated structures," *IEEE Transaction on Antennas and Propagation*, vol. 59, no. 6, pp. 2188–2195, Jun. 2011.

- [125] N. Apaydin, L. Zhang, K. Sertel, and J. L. Volakis, "Experimental validation of frozen modes guided on printed coupled transmission lines," *IEEE Transaction on Microwave Theory and Technique*, vol. 60, pp. 1513–1519, Jun. 2012.
- [126] F. Bongard, J. Perruisseau-Carrier, and J. R. Mosig, "Enhanced periodic structure analysis based on a multiconductor transmission line model and application to metamaterials," *IEEE Transaction on Microwave Theory and Technique*, vol. 57, pp. 2715–2726, Nov. 2009.
- [127] R. Sorrentino, "Transverse Resonance Technique," in *Numerical Techniques for Microwave and Millimeter-wave Passive Structures*, T. Itoh, Ed.: Wiley, New York, U.S.A., Ch. 11, 1989.
- [128] G. Valerio, D. R. Jackson, and A. Galli, "Formulas for the number of surface waves on layered structures," *IEEE Transaction on Microwave Theory and Technique*, vol. 58, no. 7, pp. 1786–1795, Jul. 2010.
- [129] D. Di Ruscio, P. Burghignoli, P. Baccarelli, and A. Galli, "Radiation from vertical dipoles in the presence of homogenized omnidirectional metasurfaces," *8th European Conference on Antennas and Propagation*, The Hague, Netherlands, 6–11 Apr. 2014, pp. 1710–1711.
- [130] P. Baccarelli, P. Burghignoli, F. Frezza, A. Galli, and G. Lovat, "Representation of the continuous spectrum excited by a dipole in a multilayer configuration through weighted cylindrical leaky waves," *Proc. of European Microwave Conference*, Milan, Italy, pp. 1–4, Sep. 2002.
- [131] P. Baccarelli, P. Burghignoli, F. Frezza, A. Galli, G. Lovat, and D. R. Jackson, "Approximate analytical evaluation of the continuous spectrum in a substrate–superstrate dielectric waveguide," *IEEE Transaction on Microwave Theory and Technique*, vol. 50, no. 12, pp. 2690–2701, Dic. 2002.
- [132] F. M. Grimaldi, "Physico mathesis de lumine, coloribus, et iride, aliisque annexis libri duo," *Bernia Ed.*, pp. 1–11 (in Latin), 1665.
- [133] J. Durnin, "Exact solutions for non-diffracting beams. I. The scalar theory," *Journal of the Optical Society of America A*, vol. 4, no. 4, pp. 651–654, Apr. 1987.

- [134] S. R. Mishra, "A vector wave analysis of a Bessel beam," *Optics Communications*, vol. 85, no. 2–3, pp. 159–161, Sep. 1991.
- [135] J. Durnin, J. J. Miceli, Jr., and J. H. Eberly, "Diffraction-free beams," *Physical Review Letters*, vol. 58, no. 15, pp. 1499–1501, Apr. 1987.
- [136] M. Ettore and A. Grbic, "Generation of propagating bessel beams using leaky-wave modes," *IEEE Transaction on Antennas and Propagation*, vol. 60, no. 8, pp. 3605–3613, Aug. 2012.
- [137] M. Ettore, S. M. Rudolph, and A. Grbic, "Generation of propagating bessel beams using leaky-wave modes: Experimental validation," *IEEE Transaction on Antennas and Propagation*, vol. 60, no. 6, pp. 3605–3613, Jun. 2012.
- [138] M. Albani, A. Mazzinghi, and A. Freni, "Automatic design of CP-RLSA antennas," *IEEE Transaction on Antennas and Propagation*, vol. 60, no. 12, pp. 5538–5547, Dec. 2012.
- [139] H. A. Bethe, "Theory of diffraction by small holes," *Phys. Rev.*, vol. 66, no. 7–8, pp. 163–182, 1944.
- [140] M. Ettore, M. Casaletti, G. Valerio, R. Sauleau, L. Le Coq, S. C. Pavone, and M. Albani, "On the near-field shaping and focusing capability of a radial line slot array," *IEEE Transaction on Antennas and Propagation*, vol. 62, no. 4, pp. 1991–1999, Apr. 2014.
- [141] S. V. Mohommadi, L. K. Daldorff, J. E. Bergaman, R. L. Karlesson, B. Thidé, K. Forozesh, T. D. Carozzi, and B. Isham, "Orbital angular momentum in radio - A system study," *IEEE Transaction on Antennas and Propagation*, vol. 58, no. 2, pp. 565–572, Feb. 2010.
- [142] F. Tamburini, E. Mari, A. Sponselli, B. Thidé, A. Bianchini, and F. Romanato, "Encoding many channels on the same frequency through radio vorticity: first experimental test," *New Journal of Physics*, vol. 14, 18 pp., Mar. 2012.
- [143] F. Tamburini, E. Mari, A. Sponselli, B. Thidé, C. Barbieri, and F. Romanato, "Experimental verification of photon angular momentum and vorticity with radio techniques," *Applied Physics Letter*, vol. 99, 4 pp., Nov. 2011.

- [144] N. Urribe-Patarroyo, A. Fraine, D. S. Simon, O. Minaeva, and A. V. Sergienko, "Object identification using correlated orbital angular momentum states," *Quantum Physics*, 5 pp., Sep. 2012.
- [145] F. Gori, "Elementi di ottica," *Accademica*, 1st Edition, 1995.
- [146] A. Ip and D. R. Jackson, "Radiation from cylindrical leaky waves," *IEEE Transaction on Antennas and Propagation*, vol. 38, no. 4, pp. 3605–3613, Apr. 1990.
- [147] G. N. Watson, "A Treatise on the Theory of Bessel Functions," UK: *Cambridge Univ. Press*, 2th Edition, p. 148, 1944.
- [148] I. S. Gradshteyn, and I. M. Ryzhi, "Table of Integrals, Series, and Products," *New York: Academic*, p. 479, 1980.
- [149] M. Casaletti, R. Sauleau, M. Ettore, and S. Maci, "Efficient analysis of metallic and dielectric posts in parallel plate waveguide structures," *IEEE Transaction on Microwave Theory and Technique*, vol. 60, no. 10, pp. 2979–2989, Oct. 2012.
- [150] M. Casaletti, G. Valerio, J. Seljan, M. Ettore, and R. Sauleau, "A full-wave hybrid method for the analysis of multilayered SIW-based antennas," *IEEE Transaction on Antennas and Propagation*, vol. 61, no. 11, pp. 5575–5588, Nov. 2013.
- [151] M. Albani, S. C. Pavone, M. Casaletti, and M. Ettore, "Generation of non-diffractive Bessel beams by inward cylindrical traveling wave aperture distributions," *Optic Express*, vol. 22, no. 15, pp. 18354–18364, Jul. 2014.





## COMITATO PREMIO TESI DI DOTTORATO 2016

*Coordinatore*

GIUSEPPE CICCARONE

*Membri*

BEATRICE ALFONZETTI

GAETANO AZZARITI

ANDREA BAIOCCHI

MAURIZIO DEL MONTE

SILVIA MEZI

VITTORIO LINGIARDI

Il Comitato editoriale assicura una valutazione trasparente e indipendente delle opere sottoponendole in forma anonima a due valutatori, anch'essi anonimi. Per ulteriori dettagli si rinvia al sito: [www.editricespienza.it](http://www.editricespienza.it)

## COLLANA STUDI E RICERCHE

Per informazioni sui precedenti volumi in collana, consultare il sito:  
[www.editricesapienza.it](http://www.editricesapienza.it)

80. «Pendono interrotte le opere»  
Antichi monumenti incompiuti nel mondo greco  
*Massimiliano Papini*
81. La disabilità tra riabilitazione e abilitazione sociale  
Il caso dei Gudat Akal a Mekelle e Wukro  
*Virginia De Silva*
82. I Consoli del Mare di Firenze nel Quattrocento  
*Eleonora Plebani*
83. Le categorie flessive nella didattica del tedesco  
Un confronto tra grammatiche Deutsch als Fremdsprache internazionali  
e per italofoni  
*Claudio Di Meola e Daniela Puato*
84. Il corpo degli altri  
*a cura di Anna Belozorovitch, Tommaso Gennaro, Barbara Ronchetti,  
Francesca Zaccone*
85. El largo viaje de los mitos  
Mitos clásicos y mitos prehispánicos en las literaturas latinoamericanas  
*edición de Stefano Tedeschi*
86. Analysis and Design of Antennas and Algorithms for Near-Field Sensing  
*Davide Comite*
87. Synthesis and biological evaluation of 1,5-diphenylpyrrole derivatives  
as COX-2 selective inhibitors and NO-releasing agents and development  
of a novel BRD9 chemical probe  
*Sara Consalvi*
88. New Techniques for Adaptive Program Optimization  
*Daniele Cono D'Elia*
89. La spiegazione delle disuguaglianze attraverso modelli generativi  
Un contributo alla comprensione della mobilità sociale nella prospettiva  
della sociologia analitica  
*Pasquale di Padova*
90. La dinamica degli opposti  
Ricerca letteraria, cultura mediatica e media in Georges Perec  
*Loredana Fiorletta*

91. Seismic Performance of Masonry Cross Vaults  
Learning from historical developments and experimental testing  
*Angelo Gaetani*
92. What's behind neuropathic pain?  
Neurophysiological diagnostic tests investigating mechanisms  
underlying neuropathic pain  
*Caterina Maria Leone*
93. Getting ready to act  
Neurocognitive aspects of action preparation  
*Rinaldo Livio Perri*
94. Trust e Impresa in Crisi  
*Elena Signori*



This volume collects the main results of the Author's Ph.D. course in Electromagnetics and Mathematical Models for Engineering, attended at 'Sapienza' University of Rome from November 2011 to February 2015, in the Electromagnetic Fields 1 Lab of the Department of Information Engineering, Electronics and Telecommunications, under the tutoring of Prof. Alessandro Galli.



**Davide Comite** received the master's degree (cum laude) in Communications Engineering in 2011 and the Ph.D. degree in Electromagnetics and Mathematical Models for Engineering in 2015, both from 'Sapienza' University, Rome, Italy, where he is currently a Postdoctoral Researcher. He was a visiting PhD student at the Institute of Electronics and Telecommunications of Rennes, University of Rennes 1, France, in 2014 and a Postdoctoral Researcher at the Center of Advanced Communications, Villanova University, PA, USA, in 2015.

His scientific interests currently involve the study of the scattering from natural surfaces, the GNSS reflectometry over the land, and the microwave imaging. He is also interested in the study and design of leaky-wave antennas and in the generation of non-diffracting waves and pulses.

Davide has been the recipient of a number of awards at national and international conferences. He is an Associate Editor of the IET Microwaves, Antennas and Propagation, the IET Journal of Engineering, and IEEE ACCESS. He is an IEEE Senior member and an URSI Senior Member.

Winner of the Competition "Prize for PhD Thesis 2016" arranged by Sapienza University Press.

